
This version is not the official one and is only provided for the convenience of international communication. The content of the paper was translated by Chat-GPT, and there may be some errors or deviations from academic expression standards. If any confusion arises, please refer to the Chinese version. Both the Chinese and English LaTeX source files have been uploaded to my [GitHub](#), and you can also translate it yourself using the LaTeX source. If you have any questions, please feel free to contact me via email: wjl14@mail.ustc.edu.cn.

Regardless of the version used, please cite the publisher's Chinese version to avoid copyright issues. The LaTeX source code is modified from the USTC thesis template. If you need to modify or reference the LaTeX source, please refer to <https://github.com/ustctug/ustcthesis/releases> .

中国科学技术大学

博士学位论文



面向核电荷半径测定的氢原子 $2^3S - 2^3P$ 跃迁精密光谱实验研究

作者姓名： 温金录

学科专业： 物理化学

导 师： 胡水明 教授

完成时间： 二〇二五年三月七日

University of Science and Technology of China

A dissertation for doctor's degree



**Precision spectroscopy of the
 $2^3S - 2^3P$ transition of atomic
helium toward a determination of
the nuclear charge radius**

Author: Jinlu Wen

Speciality: Physical Chemistry

Supervisor: Prof. Shuiming Hu

Completion date: March 7, 2025

ABSTRACT

Precision spectroscopy measurements of few-electron systems have driven the development of modern physics. Due to the relatively simple structure of energy levels, it is possible to obtain high-precision theoretical results from the fundamental physical constants by ab initio calculation using quantum electrodynamics. By comparing the results of precision spectroscopy experiments and theoretical calculations, quantum electrodynamics can be verified, and the fundamental physical constants can be determined. In recent years, the difference in the charge radius of the nucleus (proton) obtained by precision spectroscopy of hydrogen and muonic hydrogen atoms has given rise to the “proton size puzzle.” The study of other few-electron systems can also help solve this puzzle. The helium atom is the simplest multi-electron atom, and its experimental and theoretical accuracy is better than 10^{-11} , which makes it an ideal system for verifying quantum electrodynamics and testing the fundamental physical constants. Moreover, the helium nucleus has a much larger radius, and the muon interacts more strongly with the nucleus. So, if the deviation of the hydrogen and muonic hydrogen results originates from nucleus-related effects, it will be more pronounced in the helium and muonic helium systems. This thesis focuses on measuring precision spectroscopy of $2^3S - 2^3P$ transition of helium, combined with quantum electrodynamics calculations to determine the nuclear charge radius. By comparing the results with measurements of other transitions in helium atoms and those of muonic helium, the Standard Model can be tested and help solve the “proton size puzzle.” The main research contents and results of this thesis are summarized as follows:

1. The atomic beam setup has been improved to obtain a high-brightness and continuously velocity-adjustable sub-stable helium atomic beam, which lays the foundation for high-precision spectral measurement. Meanwhile, the SCTOP measurement scheme is proposed, which utilizes a traveling-wave instead of a standing-wave laser field for detection and effectively eliminates the first-order Doppler effect. Compared with the standing-wave measurement scheme, which includes the cat’s eye method and the active fiber-based retroreflector method, the SCTOP method extends the spectroscopy measurement range and reduces the influence of detection laser power on the results.

2. The influence of spatial effects on frequency results in atomic beam spectroscopy experiments is further investigated. By measuring the spectroscopy and beam distribution under different conditions, combined with theoretical analysis and simula-

ABSTRACT

tions, the influence of post-selection effects on the results of atomic beam spectroscopy experiments is revealed.

3. Based on the above improvement of the setup and method, under the condition of confirming no influence of post-selection effect, the measurement of the $2^3S - 2^3P$ transition frequency of ^4He atom with sub-kHz accuracy has been realized. Combining the results of the same transition measurement for ^3He in the literature, the isotope shift of the helium atom turns out to be $1.0733(21) \text{ fm}^2$. This result is consistent with the recent $2^3S - 2^1S$ transition result but deviates from the muonic helium result by nearly three times the standard deviation.

4. The atomic beam setup has been improved to realize a preliminary measurement of the $2^3S - 2^3P$ transition frequency of ^3He atoms. There are still some problems in the ^3He measurement due to the post-selection effects, and it is expected to give an independent isotope shift result of helium after the improvement of the setup. In addition, some new experimental methods have been tried and prospected, including Ramsey spectroscopy, photoexcitation of helium atoms with free-electron laser, and ionization detection schemes.

KEY WORDS: Helium, Precision Measurement, QED, Proton Size Puzzle, Isotope Shift

Contents

Chapter 1	Introduction	1
1.1	Precision Spectroscopy of Few-Electron Systems	1
1.2	Proton Size Puzzle	5
1.2.1	Electron Elastic Scattering	7
1.2.2	Hydrogen Atom Spectroscopy	9
1.2.3	Muonic Hydrogen Atomic Spectroscopy	10
1.2.4	Other Systems Spectroscopy	11
1.3	Helium Precision Spectroscopy and Nuclear Charge Radius Measurement	13
1.3.1	History of the Development of Helium Atomic Precision Spectroscopy	13
1.3.2	Development History of Theoretical Calculations of Helium Atomic Energy Levels	15
1.3.3	Helium Atomic Nucleus Charge Radius	17
1.3.4	Spectral Measurement of Nuclear Charge Radius in Muonic Helium Atoms	19
1.4	Thesis Structure	20
Chapter 2	Experimental Setup	22
2.1	Experimental Plan	22
2.2	Preparation of Metastable Helium Atomic Beam	24
2.2.1	Preparation of Metastable Helium Atoms	24
2.2.2	Beam Deceleration, Collimation, and Deflection	26
2.2.3	Beam Performance Evaluation	33
2.3	Atomic Single-Quantum State Preparation and Detection	36
2.3.1	Optical Pumping	37
2.3.2	Magnetic Shielding and Bias Magnetic Field	39
2.3.3	Gradient Magnetic Field Detection of Single Quantum States	41
2.4	Optical System	42
2.4.1	Frequency Metrology	43
2.4.2	Cooling Beam Laser	46
2.4.3	Pump and Probe Lasers	47
2.4.4	Laser Power and Polarization Locking	47

2.5	SCTOP Measurement Method	48
2.5.1	Background Introduction	48
2.5.2	Experimental Scheme	53
2.5.3	Evaluation of Effectiveness	55
2.6	Summary and Discussion	60
Chapter 3	^4He Atom $2^3S - 2^3P$ Transition Measurement	62
3.1	Measurement Method	62
3.1.1	Spectral Scan Timing	62
3.1.2	Spectral Data Processing	64
3.2	Measurement Results	65
3.3	Post-Selection Effect	68
3.3.1	Light-Force-Induced Shift Effect	69
3.3.2	Experimental Phenomenon	71
3.3.3	Theoretical Explanation and Numerical Simulation	75
3.3.4	Post-selection Phenomena under Different Experimental Conditions ...	84
3.3.5	Summary and Discussion	93
3.4	$2^3S - 2^3P$ Transition Frequency Measurement Error Analysis	95
3.4.1	Doppler Effect	95
3.4.2	Zeeman Effect	96
3.4.3	Laser Power	101
3.4.4	Quantum Interference Effect	104
3.4.5	Recoil Effect	108
3.4.6	Frequency Standard	109
3.4.7	Other Systematic Errors	109
3.4.8	Total Error Table	109
3.5	$2^3S - 2^3P$ Transition Frequency and Nuclear Charge Radius	110
3.6	Impact of Post-Selection Effect on the 2^3P_J Interval	112
3.6.1	Experimental Scheme	113
3.6.2	Measurement Results and Discussion	114
3.7	Summary and Discussion	116
Chapter 4	^3He Atom $2^3S - 2^3P$ Transition Preliminary Measurement	119
4.1	Experimental Scheme	119
4.1.1	Transition Selection	119
4.1.2	Calculation of the Zeeman Shift Coefficient	120

4.2 Experimental Setup Improvements	124
4.2.1 Gas Flow Path Improvements	124
4.2.2 Determining the Detected Substate	126
4.2.3 Optical Pumping Modification	127
4.2.4 Beam Incidence Direction	129
4.3 Preliminary Measurement Results	131
4.3.1 Experimental Results	132
4.3.2 Post-selection Effect in the ${}^3\text{He}$ Experiment	133
4.3.3 Results Comparison	135
4.4 Summary and Discussion	136
Chapter 5 Summary and Outlook	138
5.1 Summary	138
5.2 Outlook	139
5.2.1 Elimination of Post-Selection Effects	139
5.2.2 FEL Excitation and Ionization Detection	141
5.2.3 Ramsey Spectroscopy Attempt	143
Bibliography	151

Chapter 1 Introduction

1.1 Precision Spectroscopy of Few-Electron Systems

Due to their simple structure, few-electron systems (such as hydrogen and helium atoms) allow for highly precise energy level calculations based on quantum electrodynamics. By accurately measuring the energy levels of these systems using spectroscopic and microwave techniques and comparing the experimental results with theoretical calculations, researchers can validate computational methods, physical laws, and fundamental constants. Therefore, precision spectroscopy of few-electron systems has played a crucial role in advancing modern physics.

In 1853, A. J. Ångström and others identified the hydrogen H- α spectral line by comparing gas discharge spectra with the solar spectrum. Over the following two decades, physicists discovered additional hydrogen atomic spectral lines through spectroscopic observations of celestial bodies^[1]. In 1885, J. J. Balmer formulated an empirical equation, $1/\lambda = R(1/m^2 - 1/n^2)$, to describe the positions of the then-known hydrogen spectral lines^[2]. Interestingly, despite the equation's simplicity, its physical significance remained unclear for a long time. It was not until 1913 that N. Bohr introduced the concept of quantization, providing an explanation for the discrete spectral lines of hydrogen^[3]. According to the Bohr model, the energy levels of the hydrogen atom are given by:

$$E_n = -\frac{R_\infty}{n^2} \quad (1.1)$$

However, the Bohr model, which applies classical mechanics to microscopic atoms and electrons, inevitably encounters certain issues, such as its inability to explain the photoelectric effect and Compton effect. In 1916, Sommerfeld extended the Bohr model by considering elliptical orbits and introducing relativistic corrections^[4], successfully explaining the doublet structure of the H- α line observed by Michelson et al. in 1896. However, further research revealed that the H- α line actually consists of seven components, indicating that Sommerfeld's explanation was merely coincidental. To correctly describe the fine structure of spectra, it became necessary to completely abandon the concept of electron orbits.

In 1924, de Broglie, building upon Einstein's theory of the photoelectric effect, proposed that all microscopic particles exhibit wave-particle duality. In an atom, bound electrons form standing waves, restricting their rotational frequencies to discrete val-

ues, thereby reproducing the discrete energy levels of the Bohr model^[5]. In 1926, Schrödinger, with the assistance of Hermann Weyl, derived results consistent with the Bohr model using a non-relativistic wave equation^[6]. However, since this approach did not account for electron spin, it failed to match Sommerfeld's model and could not explain the seven spectral components of the H- α line. In 1927, Dirac introduced quantum electrodynamics (QED) for the first time, describing the radiation field in a vacuum as a set of harmonic oscillators^[7]. The following year, he formulated the relativistic equation for electrons—now known as the Dirac equation—successfully explaining the fine structure of the hydrogen spectrum^[8]. Shortly thereafter, Fermi developed an elegant formalism for quantum electrodynamics, establishing a theoretical framework that, in principle, allowed for the calculation of all physical processes involving photons, neutral particles, and charged particles^[9]. However, in 1930, Oppenheimer pointed out that higher-order perturbative calculations in quantum electrodynamics inevitably led to infinities, rendering the results physically meaningless^[10]. Furthermore, with the advancement of microwave technology, Lamb and Rutherford discovered in 1947 that the energy levels of the 2S and 2P states in hydrogen exhibited a small discrepancy, a phenomenon now known as the Lamb shift^[11]. These findings clearly revealed that unresolved issues remained in the theoretical framework of the time.

In 1947, H. Bethe introduced a finite mass and charge framework, disregarding photons with energies exceeding the electron mass, and successfully calculated a correction consistent with Lamb's experimental results^[12]. Subsequently, Tomonaga^[13], Schwinger^[14-15], Feynman^[16-17], and Dyson^[18-19] developed a covariant and gauge-invariant formulation of quantum electrodynamics (QED), rendering perturbation series finite at any order. Using QED, any observable involving electroweak interactions can be expressed as a power series expansion in the fine-structure constant α , enabling physicists to compute its expected value. With the advent of renormalization and Feynman diagram techniques, physicists came to believe that, in the absence of strong interactions, QED and quantum field theory could describe, explain, and even predict all microscopic physical phenomena. A well-known example is the anomalous magnetic moment of the electron, where the theoretical prediction from QED remains consistent with experimental measurements to 12 significant digits to this day^[20].

Quantum electrodynamics (QED) serves as the foundation and prototype for all subsequent quantum field theories. In 1954, Yang Chen-Ning and Robert Mills extended QED to establish a non-Abelian gauge field theory, now known as Yang-Mills theory^[21]. In 1971, 't Hooft demonstrated that this theory is renormalizable^[22-23].

Building on earlier developments, in 1967, Weinberg incorporated the mechanism of spontaneous symmetry breaking via the Higgs boson^[24] to construct a theory describing electroweak interactions among leptons^[25]. This theory was later extended to quarks by Glashow and others^[26]. In 1973, Fritzsch and collaborators found that Yang-Mills theory could also account for certain strong interaction phenomena, leading to the development of quantum chromodynamics (QCD)^[27]. These theoretical advancements collectively formed the Standard Model, which has successfully explained all fundamental interactions except gravity. A major milestone in the Standard Model was reached in 2012, when CERN confirmed the existence of the Higgs boson^[28-29], marking the discovery of the last predicted fundamental particle. However, the Standard Model remains incomplete, as it fails to fully explain several fundamental physical phenomena, including gravity^[30], dark matter and dark energy^[31], and the nonzero mass of neutrinos^[32]. As a result, the search for new physics beyond the Standard Model has become one of the most active frontiers in modern physics research.

With the advancement of theoretical precision and experimental techniques, the energy level structure of the hydrogen atom has been studied in greater detail. Based on the latest bound-state quantum electrodynamics (QED) theory, the hydrogen energy levels can be expressed as^[33-34]:

$$E_{n,l,j} = hcR_\infty \left(-\frac{1}{n^2} + f_{n,l,j} \left(\alpha, \frac{m_e}{m_p}, \dots \right) + \delta_{l,0} \frac{C_{NS}}{n^3} r_p^2 \right) \quad (1.2)$$

Among these terms, $f_{n,l,j}$ can be expanded as $\alpha^2 X_{20} + \alpha^3 X_{30} + \alpha^3 \ln \alpha X_{31} + \alpha^4 X_{40} + \dots$. This term includes corrections such as relativistic effects and recoil effects. The coefficient C_{NS} represents the leading-order finite nuclear size effect, while higher-order effects are incorporated within $f_{n,l,j}$. By comparing Equations 1.1 and 1.2, it becomes evident that as our understanding of natural laws deepens, physicists have been able to calculate and measure atomic energy levels with high precision based on fundamental physical constants. The experimental results from precision spectroscopy are used to continuously test and challenge existing theoretical models, a process known as the precision test of bound-state QED. However, due to the computational complexity of multi-electron systems, high-precision studies are currently primarily focused on few-electron systems.

Unlike QED describing the non-bound state lepton systems, the computational methods for bound-state QED vary depending on the system due to differences in the contributions of various effects, and the complexity of the calculations increases accordingly^[35]. In low Z -value (atomic number) systems, where the binding energy is lower

than the orbital rest energy, and under relatively weak coupling conditions, the expansion method based on the Coulomb strength $Z\alpha$ can be used. These systems, due to their relatively simple calculations, serve as ideal candidates for studying bound-state QED. As the Z -value increases, the contributions from nuclear-related effects gradually become more significant. Therefore, high- Z ionized atoms are often used to test nuclear theory models. For systems with moderate Z -values, they provide crucial information on higher-order $Z\alpha$ terms, making them important subjects for testing higher-order bound-state QED calculations.

The bound-state QED calculation involves the interactions between electrons. For high- Z -value ionized systems, the electron-electron interaction is proportional to α , while the interaction between electrons and the atomic nucleus is proportional to $Z\alpha$. Therefore, the electron-electron interaction can be treated as a perturbation, and only a $1/Z$ expansion is required in the calculation. However, for low- Z -value systems, due to the comparable strengths of both interactions, relativistic treatment of electrons is necessary, requiring more complex QED theory calculations. As a result, in systems such as He and Li, the errors in QED calculations limit the precision of theoretical and experimental comparisons. For light nuclear atomic-molecular systems (i.e., low- Z systems), a generalized method has been developed that extends up to the $\alpha^6 m$ order^[36], and the energy levels can be expressed as:

$$E\left(\alpha, \frac{m}{M}\right) = \alpha^2 E^{(2)}\left(\frac{m}{M}\right) + \alpha^4 E^{(4)}\left(\frac{m}{M}\right) + \alpha^5 E^{(5)}\left(\frac{m}{M}\right) + \alpha^6 E^{(6)}\left(\frac{m}{M}\right) + \dots \quad (1.3)$$

here, the expansion coefficients $E^{(i)}$ may contain $\ln \alpha$ terms and can be further expanded as a function of the electron-proton mass ratio:

$$E^{(i)}\left(\frac{m}{M}\right) = E^{(i,0)} + \frac{m}{M} E^{(i,1)} + \left(\frac{m}{M}\right)^2 E^{(i,2)} + \dots \quad (1.4)$$

here, the leading term $E^{(2,0)} \equiv E_0$ represents the non-relativistic energy, corresponding to the eigenvalue of the non-relativistic Hamiltonian H_0 . Taking the helium atom as an example, H_0 can be expressed as:

$$H_0 = \frac{p_1^2}{2} + \frac{p_2^2}{2} - \frac{Z}{r_1} - \frac{Z}{r_2} + \frac{1}{r} \quad (1.5)$$

the second term $E^{(4)}$ is the leading term of relativistic corrections, which is the expectation value of the Breit Hamiltonian; the third term $E^{(5)}$ is the leading term of QED effect corrections; and the $E^{(6)}$ term includes radiation corrections and others, with corresponding expressions for calculating transition central frequencies, fine structures,

hyperfine structures, etc. For systems like He and Li^+ , results have been expanded up to $\alpha^7 m$ order, which are consistent with experimental results^[37-38].

In recent years, research on exotic systems composed of exotic particles (such as muons, pions, etc.) and normal particles has gradually become a hot topic. Taking the muon as an example, its properties are similar to those of an electron, but its mass is 207 times that of the electron, allowing it to bind more tightly with protons. This makes such systems more sensitive to nuclear structure. Comparing the results of these exotic systems with those of normal systems with high precision helps to further test the Standard Model and explore new physics.

In addition to using traditional precision spectroscopy methods, physicists have also proposed some new methods to test QED theory in atomic and molecular systems. For example, the use of tune-out wavelengths for QED testing, proposed by J. Mitroy and Tang Liyan et al. in 2013^[39]. Through high-precision comparison between theory and experiment, this method was successfully implemented in 2022^[40].

1.2 Proton Size Puzzle

Protons, neutrons, and electrons constitute the various forms of matter in the world. In 1911, E. Rutherford proposed the Rutherford model based on the scattering of α particles^[41]. Between 1917 and 1925, he conducted a series of experiments using α particles to bombard light nuclei, demonstrating the presence of hydrogen nuclei within other heavier atomic nuclei, leading to the discovery of the proton^[42-44]. In 1933, O. Stern and others, while measuring the magnetic moment of the proton, discovered that it was unexpectedly large, suggesting that the proton might not be a fundamental particle^[45]. In 1955, R. Hofstadter, in an experiment involving electron scattering off hydrogen targets, found that, contrary to the prediction of the proton being a point charge, the proton's charge distribution extended to a range of 10^{-13} cm ^[46]. In 1964, M. Gell-Mann and G. Zweig proposed the quark model, which was the first step toward understanding the structure of the proton^[47-48]. In 1969, M. Breidenbach and others observed that the inelastic scattering of electrons with protons at high excitation energies was independent of energy transfer^[49]. In the same year, Feynman introduced the parton model to explain the phenomena observed in deep inelastic electron-nucleus scattering experiments^[50-51]. However, the conflict between quark confinement and the lack of interaction between partons led to contradictions between these two models. With the proposal of asymptotic freedom in 1973^[52-53], Quantum Chromodynamics (QCD)

gradually developed into the theory describing the strong interactions between particles. Nevertheless, understanding all the properties of the proton from the first principles of QCD remains an extremely challenging task.

Researchers have been continuously exploring not only the microscopic structure of protons but also more macroscopic questions, such as whether protons can decay and how large protons actually are. Over the past few decades, physicists have conducted extensive research on these topics^[55]. Currently, the study of the proton's charge radius primarily relies on two methods: one is based on subatomic physics involving proton-electron elastic scattering, and the other is based on atomic physics methods involving hydrogen atomic spectra. With the continuous advancement of experimental techniques, both methods have provided a wealth of data, which was ultimately summarized by the Committee on Data of the International Science Council (CODATA) in 2006^[56]. Among these, the result from elastic scattering is 0.895(18) fm, and the result from hydrogen spectroscopy is 0.8760(78) fm, with both values being in close

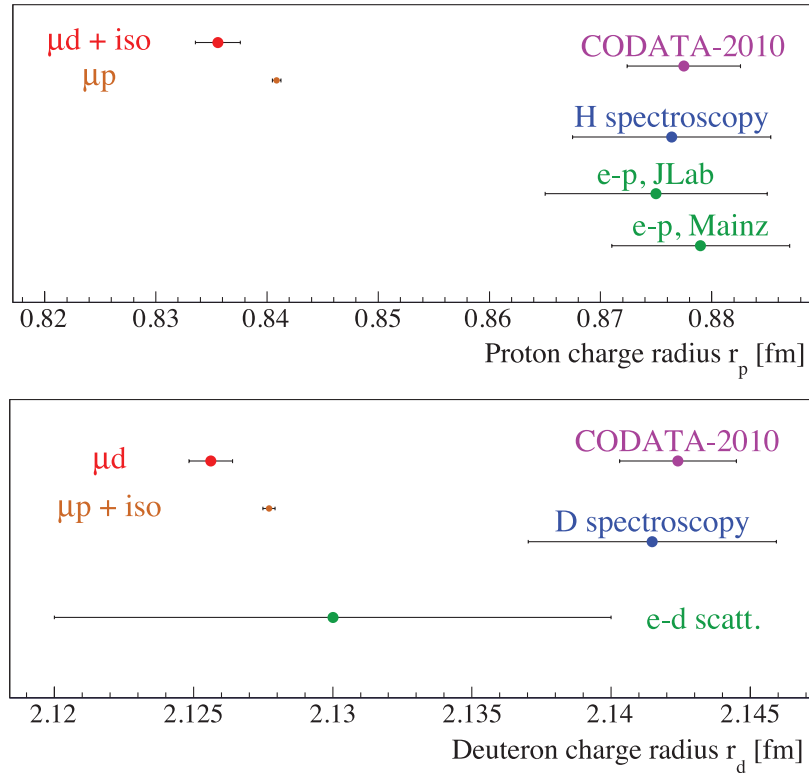


Figure 1.1 By 2016, the measurements and analysis results for the radii of the proton and deuteron were taken from the literature^[54]. In the figure, the red points represent the results from muonic hydrogen and muonic deuterium spectra, the brown points indicate the results derived from combining isotope shifts (marked as “+ iso”), where the values for muonic hydrogen and muonic deuterium are mutually deduced, the purple points represent the CODATA2010 reference values, and the blue and green points represent the reference values for hydrogen/deuterium atomic spectra and the results from electron elastic scattering experiments, respectively, as given by CODATA2010.

agreement.

In 2010, the CREMA collaboration group at the Swiss PSI measured the Lamb shift of the muonic hydrogen atom and obtained a proton charge radius of $0.84184(67)$ fm^[57]. This result was smaller than those from electron elastic scattering and hydrogen atom spectroscopy, with a deviation from the hydrogen atom spectroscopy result that was 4 standard deviations. However, in the same year, the MAM1 collaboration group using the electron elastic scattering method obtained results consistent with the summary of CODATA2006^[58]. As a result, when CODATA2010^[59] and CODATA2014^[60] provided reference values for the proton charge radius, they did not consider the muonic hydrogen results. Subsequently, the CREMA results were supported by new muonic hydrogen^[61] and muonic deuterium^[54] atomic spectroscopy results, confirming that the muonic hydrogen spectra deviated from the results obtained from traditional electron elastic scattering and hydrogen atom spectroscopy. The muonic hydrogen result showed a 6.7σ deviation from the proton charge radius reference value given by CODATA2010^[62], and this deviation is known as the “proton size puzzle.” The discrepancy between the hydrogen and muonic hydrogen systems may imply a violation of lepton universality, suggesting that the differences in the interactions between the electron and the proton, as well as the muon and the proton, could be caused by a new force beyond the Standard Model. This puzzle has attracted a great deal of attention from physicists who are working to resolve it.

1.2.1 Electron Elastic Scattering

The method of electron elastic scattering primarily measures the internal electromagnetic characteristics of the proton by observing the angular distribution of electrons after their electromagnetic interaction with the proton in scattering experiments. Among these, the proton charge radius is obtained by measuring the slope of the electric form factor $G_E(Q^2)$ at the four-momentum transfer square $Q^2 = 0$ ^{①[63]}:

$$r_p = \sqrt{-6 \frac{dG_E(Q^2)}{dQ^2} \Big|_{Q^2=0}} \quad (1.6)$$

Since it is not practically possible to reach $Q^2 = 0$, experiments usually measure the G_E values within a certain Q^2 range and then fit the slope at $Q^2 = 0$. In most electron elastic scattering experiments, a magnetic spectrometer is used as the main detector, which has the advantage of accurately measuring the kinetic energy of scattered

^①Different notations for the proton charge radius are used in the literature, such as r_p , r_E , $\langle r_E^2 \rangle^{1/2}$, etc. In this thesis, the notation r_p is used consistently.

electrons. However, the range of a single measurement by the magnetic spectrometer is limited, requiring multiple adjustments of the incident electron beam energy and spectrometer settings, which may introduce systematic errors related to Q^2 , affecting the final results. Additionally, due to experimental limitations, it is currently difficult to reduce the systematic errors caused by the number of electrons and the proton density of the target to below 1 %. To accurately fit the slope at $Q^2 = 0$, measurements must be taken at low Q^2 conditions, meaning that small scattering angles are involved, which can be affected by small-angle scattering from non-proton materials along the electron beam path, thereby increasing background noise. Also, since the scattered electron energy is relatively low, higher energy resolution from the detector is required. Therefore, although the elastic scattering cross-section at high Q^2 intervals has been repeatedly measured with high precision through various experimental techniques since Hofstadter's experiment^[46], these data are mostly limited to the $Q^2 > 0.01 \text{ GeV}^2$ region, and there are discrepancies among different experimental results, posing challenges for the final global fitting^[64-74]. Related analyses show that different methods used to process the raw elastic scattering data may lead to significant differences in the results^[75-83]. As of CODATA2014, the final reference value for elastic scattering is $r_p(\text{scatt.}) = 0.879(11)\text{fm}$ ^[60], primarily based on the 2010 measurements from the MAM1 group^[58], and it incorporates previous experimental and theoretical analyses.

In 2019, the PRad collaboration improved the experimental setup by adopting a hybrid calorimeter (HyCal), which allowed for higher precision over a broader range and avoided the need for multiple adjustments of experimental conditions. Additionally, a new design was employed to minimize background noise as much as possible^[84]. The experiment also simultaneously measured electron-electron elastic scattering, a result that can be precisely calculated using QED, allowing the product of the incident electron number and target proton density to be inferred, thereby reducing systematic errors. With these improvements, the PRad collaboration measured the proton charge radius in the $Q^2 = 0.0002 \rightarrow 0.06 \text{ GeV}^2$ range, yielding $r_p = 0.831 \pm 0.007(\text{stat.}) \pm 0.012(\text{syst.}) \text{ fm}$. This result is consistent with the CREMA group's muonic hydrogen result. However, this result shows a significant deviation from previous elastic scattering measurements, with a difference of 2.7 standard deviations from the CODATA2014 reference value. Therefore, further experimental and theoretical results are still needed for cross-validation.

1.2.2 Hydrogen Atom Spectroscopy

From Equation 1.2, it can be seen that a set of $\{R_\infty, r_p\}$ results can be obtained using the transition frequencies of two hydrogen atom transitions. The commonly used approach is to input the result of the $1S - 2S$ transition, which has a precision of less than 5×10^{-15} ^[85-86], and then input the experimental result of another transition to measure the proton charge radius. The reason for adopting this approach is that if there were an unknown error in the $1S - 2S$ transition experiment that led to a deviation in the proton charge radius, it would imply that the deviation in the experimental result reached 4000 standard deviations, which is nearly impossible to occur^[87]. In contrast, other transitions, such as $2S - 2P$ ^[88], $2S - 8D$ ^[89], and $1S - 3S$ ^[90], typically have lower measurement precision historically, and their deviations are usually only in the range of 1 to 3 standard deviations, which is more likely to occur. Therefore, since the introduction of the “proton size puzzle,” physicists have remeasured these transitions with higher precision.

In 2017, A. Beyer and colleagues measured the $2S - 4P$ transition in a low-temperature hydrogen atomic beam^[33]. Compared to previous experiments, this study used a $1S - 2S$ photoexcitation scheme instead of the traditional discharge excitation, allowing atoms in the $2S_{1/2}^{F=0}$ state to be nearly completely excited by a Doppler-free two-photon transition, avoiding additional momentum changes. Moreover, hydrogen atoms were cooled using a 5.8 K cryogenic source and an actively fiber-coupled feedback optical path method^[91], reducing the impact of Doppler effect from 16 kHz to just 2.13 kHz. Combining the $1S - 2S$ result^[85-86], the experiment yielded a proton radius of $r_p = 0.8335(95)$ fm, consistent with the muonic hydrogen result. In 2018, Fleurbaey et al. measured the $1S - 3S$ two-photon transition^[92]. Since the experiment used a room-temperature beam, second-order Doppler shifts exceeding 100 kHz needed to be corrected. The final result for the proton radius was $r_p = 0.877(13)$ fm, consistent with the CODATA2014 value^[60]. In 2019, Bezginov et al. improved the separated cavity method to measure the Lamb shift^[93]. This experiment used a proton beam (with an energy of about 55 keV) to collide with hydrogen molecules, producing about 4 % of 2S-state hydrogen atoms for measurement. The proton radius obtained was $r_p = 0.833(10)$ fm. In 2020, Grinin et al. again measured the $1S - 3S$ two-photon transition in a cold beam^[34]. The statistical error was only 110 Hz, and the final proton radius result was $r_p = 0.8482(38)$ fm, lying between the CODATA2014 and muonic hydrogen results. In 2022, Brandt et al. measured the $2S_{1/2} - 8D_{5/2}$ transition in a cold

beam^[94], obtaining a proton radius of $r_p = 0.8584(51)$ fm, also falling between the CODATA2014 and muonic hydrogen results.

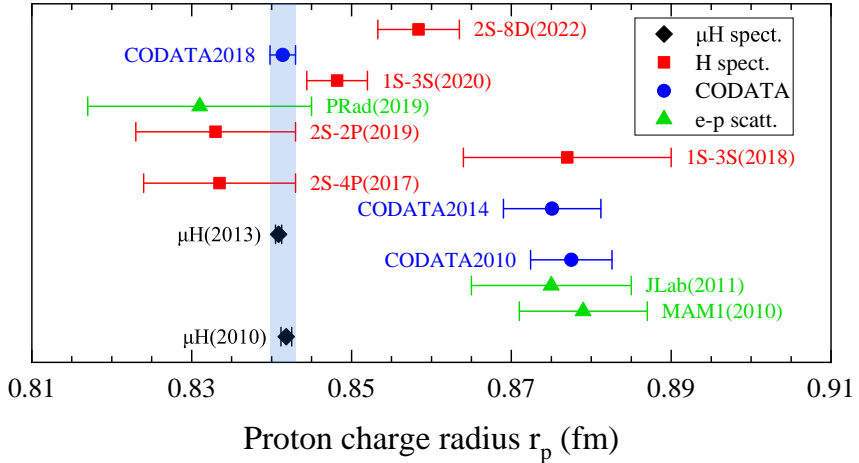


Figure 1.2 Summary of Proton Radius Measurements and Analysis Results from 2010 to 2022.

These new experiments have significantly improved the measurement precision of the existing transitions. However, due to discrepancies between the results, some are consistent with the muonic hydrogen results, while others align with the hydrogen spectral results. Therefore, the proton size puzzle has not been completely resolved, and more experimental verification is still required. In the latest CODATA 2018, the results of the muonic hydrogen experiments have been included. However, due to the large discrepancies between the different results, when compared to over 60 other experimental results, the uncertainty of the muonic hydrogen results needs to be increased by a factor of 1.6 in order to ensure that the normalized residuals of all results after least-squares fitting are less than 2^[95]. The final CODATA2018 result is $r_p = 0.8414(19)$ fm.

1.2.3 Muonic Hydrogen Atomic Spectroscopy

In 2010, Pohl et al. first measured the proton charge radius using muonic hydrogen atoms^[57]. In the experiment, muons were injected into a high-pressure hydrogen gas chamber, forming muonic hydrogen atoms, with approximately 1 % de-exciting to the $2S$ metastable state (with a lifetime of about 1 μ s). Then, the Lamb shift was detected using a pulsed laser with a wavelength of approximately 6 μ m. Since the lifetime of the $2P$ state is only 8.5 ps, the muonic hydrogen atom quickly de-excited to the $1S$ ground state, emitting a 1.9 keV $K\alpha$ X-ray. By recording the number of X-ray events at different frequencies, the spectrum could be fitted. The measured proton radius was $r_p = 0.84184(67)$ fm. In 2013, they expanded the laser scan range and si-

multaneously measured the singlet and triplet transitions^[61], with the final result being $r_p = 0.84087(39)$ fm. This result not only agrees with the 2010 measurement but is also the most precise measurement of the proton radius to date.

In 2016, Pohl et al. measured the three transitions corresponding to the Lamb shift in μ D atoms^[54], ultimately determining the muonic deuterium radius as $r_d = 2.12562(13)_{\text{exp}}(77)_{\text{theo}}$ fm. Compared to the CODATA2010 reference value of $r_d = 2.1424(21)$ fm, the difference is 7.5 times the standard deviation. When CODATA2018 provided the deuteron radius, it incorporated the experimental results of muonic deuterium and similarly amplified the uncertainty of the muonic deuterium result in the fitting, yielding a final reference value of $r_d = 2.12799(74)$ fm.

The theoretical calculation precision for muonic atomic systems has also been continuously improving. Pachucki et al. summarized these advances in their 2024 review^[96]. It is worth noting that, due to the cancellation of some errors in the subtraction process, the isotope shift between hydrogen and deuterium, $r_d^2 - r_p^2$, has higher precision than for individual nuclei. Currently, the result for the muonic hydrogen-muonic deuterium system is $3.8200(7)_{\text{exp}}(30)_{\text{theo}}$ fm², which is in excellent agreement with the result for the electronic hydrogen-deuterium system, $3.8207(3)$ fm². However, since the individual results for hydrogen and deuterium are still not the same, the “proton size puzzle” remains unresolved, requiring further experimental and theoretical research for deeper exploration.

1.2.4 Other Systems Spectroscopy

The proton radius r_p is closely related to the Rydberg constant R_∞ . Therefore, although only a few systems can directly measure r_p , many few-electron systems can measure the Rydberg constant with high precision. Research on these systems is valuable in addressing the “proton size puzzle”^[35,63]. As shown in Figure 1.3, an overview of the research status of several few-electron systems suitable for solving this puzzle is provided^[63].

Certain hydrogen-like exotic atoms, such as positronium ($\text{Ps} \equiv e^+e^-$) and muonium ($\text{M} \equiv \mu^+e^-$), are pure lepton systems that are not affected by nuclear effects. These systems can independently measure the Rydberg constant and are highly sensitive to new physics beyond the Standard Model. Currently, experiments on positronium are being conducted at institutions like ETH Zurich^[97], the University of California Riverside^[98], University College London^[99-103], with the goal of improving the precision of $1S - 2S$, $2S - 2P$ transitions, and measuring narrow transitions from 2^3S_1 to high Ry-

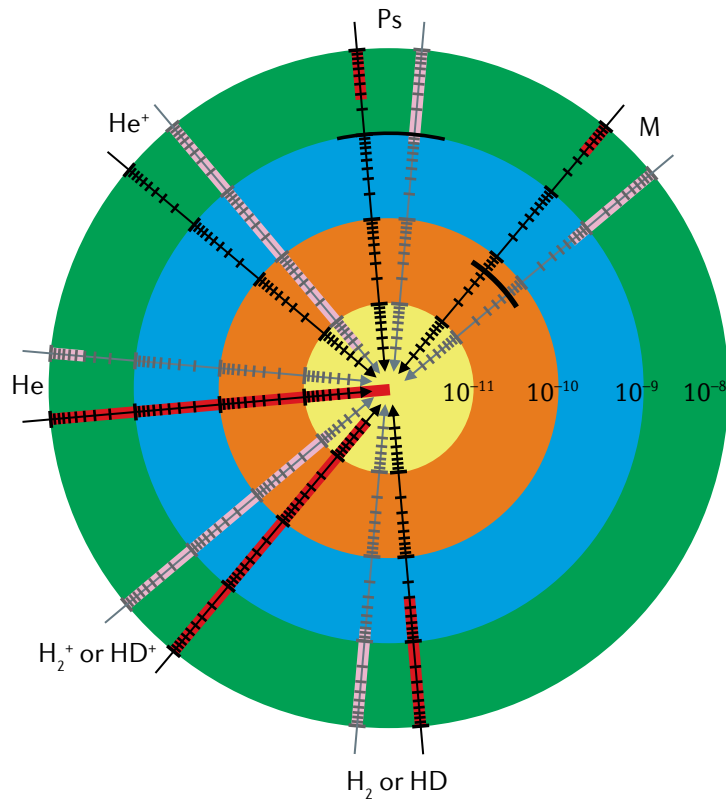


Figure 1.3 Current research status of few-electron systems suitable for solving the “proton size puzzle,” excerpted from reference^[63]. The red bands for each system represent experimental precision, and the pink bands represent theoretical precision. The closer the bands are to the target center, the higher the precision. The data shown in the figure are up to 2020.

dberg states. The precision is expected to reach the ppt level. Due to the equal masses of the two particles in positronium, QED calculations are more complex than for hydrogen, and the theoretical precision is currently lower, but it is expected to improve to below 10 ppt in the future^[104]. For muonium, related experiments are conducted at PSI, with the main objective being to improve the precision of the $1S - 2S$ transition. The Lamb shift measurement in muonium has already been completed^[105-106], and future experiments will compare spectroscopic results from hydrogen and perform a series of transition measurements in muonium.

The simplest molecules (such as H_2 , HD)^[107] and molecular ions (H_2^+ , HD^+)^[108] are ideal systems for measuring the Rydberg constant, the proton-electron mass ratio, and other physical constants. As of 2020, in molecular ion systems, Doppler-free spectroscopic methods have advanced the experimental precision to the 10^{-12} level^[109-110], surpassing the theoretical calculation^[111] by nearly three times. In neutral molecular systems, both theoretical and experimental precision have reached the 10^{-10} level^[112-115].

Due to the more significant higher-order QED effects in helium ions (He^+) ($\Delta\text{QED} \propto Z^k \alpha^n$), the results from helium ions can be used to test the QED theoretical calculations for hydrogen atoms. However, this system still faces challenges in improving experimental and theoretical precision. Experimentally, there is a need to develop high-precision deep ultraviolet optical frequency combs^[116], while theoretically, it is limited by the calculations of second-order radiation corrections^[117]. Additionally, the helium nuclear radius obtained from the helium ion and neutral helium atom systems, compared with the results from muonic helium, helps to further solve the “proton size puzzle.” The mass of the helium nucleus is greater than that of the hydrogen nucleus, and the interaction strength between the muon and the nucleus is approximately ten times that in the muonic hydrogen system. If the deviation in the hydrogen and muonic hydrogen results originates from nucleus-related effects, these effects will be more pronounced in helium and muonic helium. A detailed discussion of this will be provided in Section 1.3.

In recent years, with the improvement of QED theoretical calculation precision, precision spectroscopic measurements in hydrogen-like and helium-like systems have gradually become a research hotspot^[118-120]. At the same time, the CREMA collaboration has been conducting or has completed spectroscopic experiments on systems such as muonic helium, muonic lithium, and muonic beryllium^[121]. The comparison of these experimental results not only verifies QED theory but also provides new perspectives on solving the nuclear radius problem for related systems, and has important implications for understanding the structure of light nuclei.

1.3 Helium Precision Spectroscopy and Nuclear Charge Radius Measurement

1.3.1 History of the Development of Helium Atomic Precision Spectroscopy

Since Janssen’s discovery of the helium atomic spectrum through solar eclipse observations in 1868^[122], helium atoms have been a key focus in spectroscopic research. Before the invention of atomic beam technology and laser technology in the 1950s, the absorption spectrum of helium was the only data source. In 1917, Merrill studied the $2^1S - 5^1P$ transition^[123]. Starting in 1922, physicists investigated transitions from the 2^1S_0 state to the n^1P_1 states (where $n < 20$), and also explored other transitions involving the 1^1S , 2^1S , and 2^3S states. These early works were summarized in the review^[124].

W. F. Meggers first measured the wavelength of the $2^3S - 2^3P$ transition in 1935^[125]. Between 1958 and 1962, G. Herzberg and others measured the binding energies of the 1^1S , 2^1S , and 2^3S states^[126-128]. These results have been widely used, but their precision has remained relatively low. It was not until 1993 that Eikema and colleagues successfully measured a series of deep ultraviolet transitions from the 1^1S state^[129-131], improving the experimental precision of the binding energy and Lamb shift for the 1^1S state^[132-133].

Due to pressure and Doppler effects, the linewidth of spectral lines observed in classical absorption spectra is usually tens to thousands of times broader than the natural linewidth, making it difficult to accurately obtain the center of transition frequencies. Lamb et al. introduced the molecular beam method into atomic spectroscopy^[11], alleviating this issue. However, due to limitations in laser technology, early helium atomic beam experiments primarily focused on the microwave and visible light bands. For example, in the 1970s, V. Hughes and E. Hinds conducted a series of microwave experiments^[134-137], studying the fine structure of the 2^3P state of ${}^4\text{He}$ and the hyperfine structure of the 2^3S and 2^3P states of ${}^3\text{He}$. During the same period, dye laser technology gradually developed and was used in the spectral measurements of atomic systems like hydrogen. In 1982, Biraben et al. conducted the first laser spectroscopy experiment on helium^[138], measuring the $2^3S - n^3S$ and $2^3S - n^3D$ ($n = 3 - 6$) transitions of ${}^4\text{He}$. The experiment did not use the molecular beam method but was conducted in a weak radiofrequency discharge chamber; however, the transitions measured were all two-photon transitions, with the atom absorbing two counter-propagating photons, canceling out the first-order Doppler effect, and significantly reducing the spectral linewidth. Still, since the experiment was carried out in a chamber with relatively high gas pressure, the results were still limited by pressure shifts. In 1983, Hlousek et al. also measured the $2^3S - n^3S$ and $2^3S - n^3D$ ($n = 4, 5$) two-photon transitions in a gas chamber and used the saturated absorption method to measure the $2^3P - 3^3D$ one-photon transition^[139].

Before the development of LNA ($\text{La}_{1-x}\text{Nd}_x\text{MgAl}_{11}\text{O}_{19}$) lasers, the frequency of the $2^3S - 2^3P$ transition could not be directly measured and could only be indirectly calculated from other transition frequencies. In 1985, D. Bloch et al. used a single laser beam passing through both ${}^4\text{He}$ and ${}^3\text{He}$ gas chambers to study the isotope shift of the $2^3S - 2^3P$ transition for the first time^[140]. In 1989, P. Zhao et al. directly measured the $2^3S - 2^3P$ transition in a gas chamber^[141], and updated the isotope shift results in 1991^[142]. In 1994, D. Shiner et al. measured the $2^3S - 2^3P$ transition of ${}^4\text{He}$ ^[143] and ${}^3\text{He}$ ^[144] in an atomic beam. Later, Cancio Pastor et al. used the saturated fluorescence

method to measure the $2^3S - 2^3P$ transition of both ^4He ^[145-146] and ^3He ^[147]. A detailed discussion of these two sets of experiments will be given in Section 2.1. Meanwhile, transitions from 2^3S to 3^3P , 3^3D , etc.^[148-153], as well as other transitions in the singlet state, are continuously being measured, with measurement precision steadily improving^[154-158]. In addition, microwave methods are also continually improving^[159-162], with the most significant achievement being Hessels et al.'s improvement of the precision of the $2^3P_2 - 2^3P_1$ interval to a record 25 Hz^[163]. Ionization energy measurements are also ongoing. For example, the F. Merkt group measured the ionization energies of the 2^1S and 2^3S states in 2021 and 2023^[164-165].

The development of cold atomic physics has provided new opportunities for spectral measurements. In 2001, F. P. D. Santos et al. observed the Bose-Einstein condensation (BEC) of the 2^3S state in ^4He ^[166]. From 2004 to 2007, L. B. Wang and P. Mueller et al. observed the spectra of ^6He and ^8He in a magneto-optical trap (MOT) and, for the first time, measured the nuclear radii of ^6He and ^8He ^[167-168]. In 2009, S. S. Hodgman et al. measured the lifetime of the 2^3S state in MOT, finding it to be 7870(510) s^[169]. In 2011, V. Rooij et al. transferred ultracold ^4He and ^3He atomic ensembles to an optical dipole trap (ODT) and observed the forbidden transition $2^3 - 2^1S$ for the first time^[170]. Subsequently, this research group remeasured the $2^3S - 2^1S$ transition of ^4He ^[171] and ^3He ^[172] in an optical dipole trap at the magic wavelength, improving the measurement precision and correcting some systematic errors. Additionally, forbidden transitions such as $2^3S - 2^1P$ have also been observed in ultracold ensembles^[173]. The BEC group at the Australian National University (ANU), led by A. Truscott, also conducted high-precision measurements of transitions like $2^3S - 3^3S$ ^[174-175], and, in collaboration with Li-Yan Tang et al., used the tune-out wavelength to achieve an independent test of QED^[40].

1.3.2 Development History of Theoretical Calculations of Helium Atomic Energy Levels

Helium atoms are the simplest multi-electron atoms, but compared to hydrogen atoms, the Coulomb interaction between the two electrons makes solving the helium atom using non-relativistic methods more complex. From 1929 to 1932, G. Breit developed a relativistic model to describe the helium atom, approximately extending the Dirac equation from the single-electron case, which led to the Breit equation^[179-181]. With the development of quantum electrodynamics (QED), Bethe and Salpeter proposed a fully covariant treatment method for the helium atom in 1951, known as the Bethe-

Salpeter equation^[182], which provided the theoretical foundation for QED calculations of helium atomic energy levels. In 1960, Pekeris et al. calculated the binding energies of the 1^1S , 2^1S , and 2^3S states^[127-128], taking into account relativistic effects and other corrections, but did not calculate the Lamb shift. Combining the Lamb shift results from Suh and Zaidi et al., the theoretical results of Pekeris et al. were consistent with the experimental results of G. Herzberg et al.^[126]. In 1970, Accad, Pekeris, and Schiff calculated the energies of low-energy S and P states, but as the principal quantum number n increased, the calculation accuracy significantly decreased^[183-184]. Since the 1970s, G. W. Drake at the University of Windsor began helium atom research, developing a variational calculation method based on a double basis set, which improved the accuracy of non-relativistic energy calculations for the $2S$ state to within 10 kHz^[185-187], and, in collaboration with Zong-Chao Yan et al., conducted high-precision calculations on the fine structure of the $2P$ state^[188-190]. J. Morgan et al. at the University of Delaware also independently developed a calculation method and computed the non-relativistic energy of the helium atom^[191]. In the 21st century, K. Pachucki et al. gradually improved the accuracy of helium atom QED calculations^[192-205], and in 2021, completed a calculation of the 2^3S and 2^3P state energies of ${}^4\text{He}$ to the order of ma^7 ^[37], which is the most

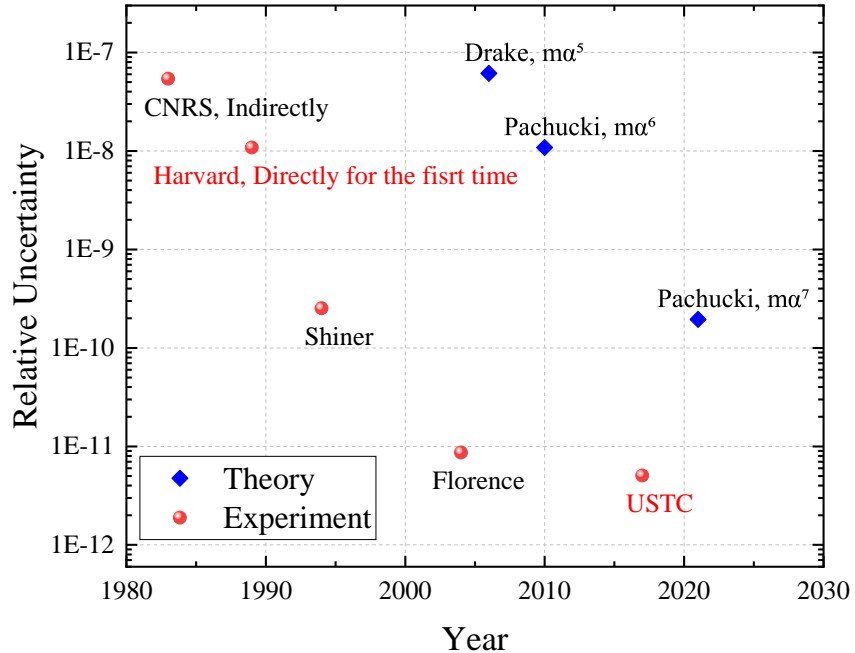


Figure 1.4 Development History of Experimental Measurements and Theoretical Calculations of the $2^3S - 2^3P$ Transition Frequency of Helium Atoms. Due to limitations in laser technology, measurements prior to 1989 were only indirect. For example, in 1983, CNRS indirectly determined the $2^3S - 2^3P$ transition frequency by comparing the $2^3S - 3^3D$ and $2^3P - 3^3D$ transition frequencies^[176]. As of 2023, the latest experimental accuracy is 1.6 kHz^[177-178], and the theoretical accuracy is 54 kHz^[37].

accurate theoretical result for low-electron systems to date. The Precision Measurement Science and Technology Innovation Research Institute of the Chinese Academy of Sciences, led by Tingyun Shi, Li-Yan Tang, and Zhenxiang Zhong of Hainan University, also developed a B-spline-based calculation method and conducted high-precision calculations for lithium ions^[120,206-207], helium tune-out wavelengths^[39-40,208-211], and magic wavelengths^[212].

1.3.3 Helium Atomic Nucleus Charge Radius

Currently, there are two main methods for precise optical spectroscopic measurements of the helium atomic nucleus charge radius: one is by using the transition frequency of ${}^4\text{He}$, combined with theoretical calculations of the helium nucleus radius; the other is by measuring the same transition frequency for ${}^3\text{He}$ and ${}^4\text{He}$ to obtain the isotope shift. Under the point charge approximation, the theoretical transition frequency can be calculated, and the difference between the theory and experimental results arises from the finite nuclear size effect, $E_{\text{FNS}} = C \cdot r_\alpha^2$, where the coefficient C is determined through high-precision theoretical calculations. Therefore, the helium nucleus radius can be obtained from a transition frequency in ${}^4\text{He}$ using the formula $r_\alpha = \sqrt{\Delta E/C}$. For the $2^3S - 2^3P$ transition, the finite nuclear size effect is estimated as $\Delta E_{\text{FNS}}/h \approx 3450 \text{ kHz}$ ^[199]. If the nuclear radius precision requirement is below one-thousandth, both the theoretical and experimental precisions must be better than 7 kHz:

$$\begin{aligned} \delta E_{\text{FNS}}/E_{\text{FNS}} &= 2 \delta r_\alpha/r_\alpha \\ \delta E_{\text{FNS}} &< 2 \times 1 \times 10^{-3} \times 3450 \text{ kHz} \approx 6.9 \text{ kHz} \end{aligned} \quad (1.7)$$

In 2017, our research group improved the measurement precision of this transition to 1.6 kHz^[177-178], meeting the aforementioned requirement. On the theoretical side, Pachucki et al. in 2021 extended the calculation of the energy level structure of helium atom triplet states to the $m\alpha^7$ level^[37], which is currently the highest precision result for energy level calculations in few-electron systems. For the $2^3S - 2^3P$ transition, the theoretical precision is 54 kHz, corresponding to a nuclear radius precision of 7.8×10^{-3} , which is still not comparable to the results from muonic helium ions (with a precision better than 5×10^{-4}). Therefore, due to limitations in theoretical precision, it is currently not possible to directly obtain a sufficiently high-precision helium nuclear radius from the $2^3S - 2^3P$ transition frequency of ${}^4\text{He}$.

However, for the isotope shift $\delta r^2 = r_h^2 - r_\alpha^2$, the calculation only needs to consider the contributions from operators dependent on nuclear mass and size. Since only the

spin-averaged centroid frequency is used, the contributions from nuclear and electronic spins are not considered, greatly simplifying the calculation and significantly improving precision. At the same time, nuclear effects contribute much more to the isotope shift than to the transition frequency. Especially for the $2^3S - 2^3P$ transition, the finite nuclear effect contributes approximately 5×10^{-9} to the transition frequency, while it contributes 4×10^{-5} to the isotope shift. Similar to the method of calculating nuclear radius from absolute frequency, the deviation between theoretical and experimental results for the isotope shift can still be expressed in the form $\Delta E = C \cdot \delta r^2$, where the coefficient C is determined through theoretical calculations. According to the latest theoretical calculations^[199], for the $2^3S - 2^3P$ and $2^3S - 2^1S$ transitions, the point charge theory calculation precision is better than 3×10^{-8} , and the calculation precision of the coefficient C is better than 1×10^{-4} , allowing for high-precision isotope shift results. As of 2016, two sets of isotope shift results for the $2^3S - 2^3P$ transition were $1.061(3) \text{ fm}^2$ ^[143-144] and $1.069(3) \text{ fm}^2$ ^[145-147], while the isotope shift result for the $2^3S - 2^1S$ transition was $1.027(11) \text{ fm}^2$ ^[170]. These two transition results showed a deviation of 4 standard deviations. Compared to the results of elastic electron scattering summarized by I. Sick in 2014, $1.066(60) \text{ fm}^2$ ^[213-214], the isotope shift precision obtained by spectroscopy is higher. Theoretically, these two transitions should yield consistent nuclear charge radii, but the actual measurement results showed a significant discrepancy, prompting further experimental efforts to resolve the discrepancy in helium atom radius measurements.

In 2017, our research group measured the $2^3S - 2^3P$ transition of ${}^4\text{He}$ in an atomic beam^[177], and combined the 2012 results of ${}^3\text{He}$ by Cancio Pastor et al.^[147], yielding an isotope shift result of $1.028(2) \text{ fm}^2$. Due to a near 50kHz deviation between the ${}^4\text{He}$ result and the results of Cancio Pastor et al.^[145-146], a significant discrepancy appeared in the isotope shift results, although they were consistent with the 2011 measurement by V. Rooij et al. for the $2^3S - 2^1S$ transition^[170]. In 2018, Renglink et al. re-measured the $2^3S - 2^1S$ transition of ${}^4\text{He}$ in an optical dipole trap (ODT) at the magic wavelength, improving the measurement precision and correcting some systematic errors^[171]. Combining the 2011 result of V. Rooij for ${}^3\text{He}$, the isotope shift obtained was $1.041(7) \text{ fm}^2$. In 2020, Y. J. Huang et al. measured the $2^1S - 3^1D$ transitions for both ${}^3\text{He}$ and ${}^4\text{He}$, and, using singlet state theory calculations^[215], derived an independent isotope shift result of $1.059(25) \text{ fm}^2$ ^[157-158]. In 2023, Y. van der Werf et al. re-measured the $2^3S - 2^1S$ transition for ${}^3\text{He}$ in an ODT at the magic wavelength, and found a discrepancy of five times the standard deviation with the 2011 result^[172]. They suggested that

this discrepancy might be due to large non-uniform differential ac-Stark shifts caused by the ODT for the ^3He Fermi gas in previous experiments at non-magic wavelengths. Additionally, the measurement results of muonic helium ions (μHe^+) have also been published^[216-217]. As of the end of 2023, the summarized results of the isotope shift measurements are shown in Figure 1.5.

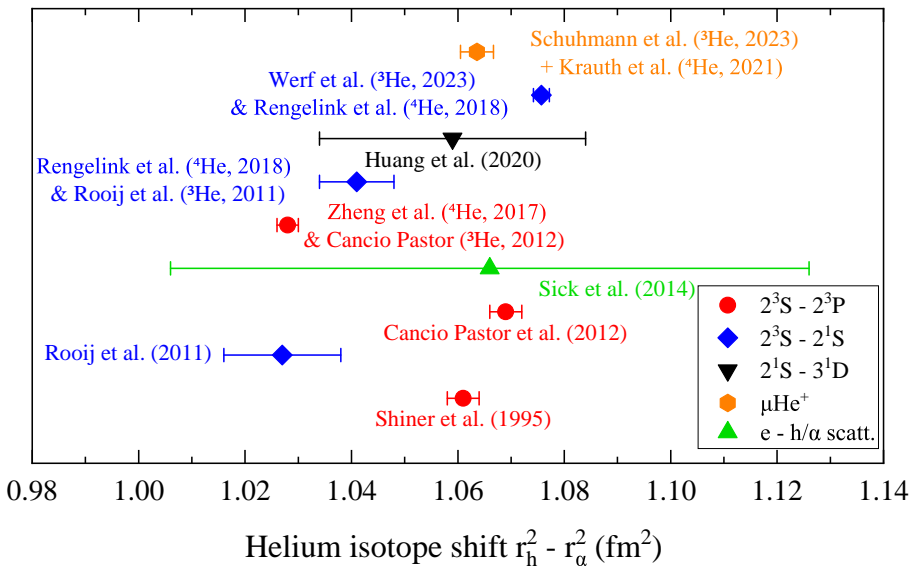


Figure 1.5 Measurement of isotope shifts for helium atoms as of the end of 2023

1.3.4 Spectral Measurement of Nuclear Charge Radius in Muonic Helium Atoms

Since the introduction of the “proton size puzzle,” the PSI research group has studied the size of atomic nuclei by measuring the spectra of muonic helium, muonic lithium, and other systems. In the muonic helium experiment, high-energy protons collide with a graphite target to produce π^- mesons, about 30 % of which decay into muons μ^- . The muon beam then collides with helium gas at 2 mbar inside the detection cavity, generating muonic helium ions, with about 1 % of them in the $2S$ metastable state (with a lifetime of approximately 1.7 μs). When the laser is resonant with the $2S - 2P$ transition frequency, the muonic helium ions are excited to the $2P$ state (with a lifetime of about 0.5 ps), and they quickly decay to the $1S$ ground state, emitting X-rays. By scanning the laser frequency and recording the number of detected X-ray events, the spectrum can be fitted.

The main experimental error comes from statistical uncertainty, which is approximately 15 to 20 GHz. The impact of the Doppler effect has been calculated in detail, and the error is less than 1 GHz, which can be virtually ignored given the current experimental precision. The experimental detection region has a magnetic field of 5 T,

causing a Zeeman shift of about 0.3 GHz, which has been corrected through calculations. For $\mu^3\text{He}^+$, quantum interference effects also need to be considered, contributing a shift of approximately 0.2 GHz.

The final measured nuclear radii are as follows:

$$\begin{aligned} r_h &= 1.97007(12)_{\text{exp}}(93)_{\text{theo}} \text{ fm} = 1.97007(94) \text{ fm} \\ r_\alpha &= 1.67824(13)_{\text{exp}}(82)_{\text{theo}} \text{ fm} = 1.67824(83) \text{ fm} \end{aligned} \quad (1.8)$$

To make a comparison with the spectroscopic experiments, the results need to be converted to isotope shifts. Since certain nuclear structure contributions cancel out during the subtraction process, the experimental frequency values can be directly used for calculation to achieve higher precision results:

$$r_h^2 - r_\alpha^2 = -\frac{E_{\text{LS}}^{\text{exp}}(\mu^3\text{He}^+)}{103.383 \text{ meV/fm}^2} + \frac{E_{\text{LS}}^{\text{exp}}(\mu^4\text{He}^+)}{106.209 \text{ meV/fm}^2} + 0.2585(30) \text{ fm}^2 \quad (1.9)$$

Finally, the isotope displacement result for the muonic helium system^[216-217] is:

$$r_h^2 - r_\alpha^2 = 1.0636(6)_{\text{exp}}(30)_{\text{theo}} \text{ fm}^2 = 1.0636(31) \text{ fm}^2 \quad (1.10)$$

This result is consistent with the isotope displacement result obtained by D. Shiner et al. in 1995 from the beam measurement of the $2^3S - 2^3P$ transition^[143-144], but there is a 3.6 standard deviation deviation when compared with the latest result for the $2^3S - 2^1S$ transition^[171-172]. This seems to indicate a significant discrepancy between the helium and muonic helium systems. However, due to the large discrepancies between different measurements of the $2^3S - 2^3P$ transition, and the significant revisions to the $2^3S - 2^1S$ transition results, a clear conclusion cannot yet be drawn from the helium isotope displacement results.

1.4 Thesis Structure

This thesis mainly introduces the latest experimental progress in precision spectroscopy measurements of metastable helium atomic beams. By improving the experimental setup and detection optical path methods, we have achieved sub-kHz level measurements of the $2^3S - 2^3P$ transition of ${}^4\text{He}$ atoms, and explored the impact of post-selection effects on precision spectroscopy experiments in the beam. Based on this, preliminary measurements of the same transition in ${}^3\text{He}$ atoms were also conducted, and new experimental methods were explored.

The structure of the thesis is arranged as follows: Chapter 1 briefly reviews the history of precision spectroscopy in few-electron systems, introduces the “proton size

puzzle”, and discusses the progress in precision spectroscopy of helium atoms and the measurement of the helium nuclear charge radius. Chapter 2 introduces the beam apparatus and optical system, and briefly describes the traveling wave measurement method. Chapter 3 provides a detailed explanation of the measurement methods, results, and error analysis for ^4He , with a special focus on the impact of post-selection effects on the experimental results. Chapter 4 introduces the preliminary measurement results for ^3He . Chapter 5 discusses attempts at new experimental methods and future prospects.

Chapter 2 Experimental Setup

2.1 Experimental Plan

The goal of this research is to measure the absolute frequency of the $2^3S - 2^3P$ transition in ${}^4\text{He}$ and ${}^3\text{He}$ atoms. Prior to this work, the measurement of this transition frequency was mainly conducted using two methods: one was the single quantum state detection method based on helium atomic beams developed by D. Shiner's team at the University of North Texas^[143]; the other was the saturated absorption fluorescence modulation spectroscopy method developed by the University of Florence in Italy^[145]. Taking the ${}^4\text{He}$ experiment as an example, in Shiner's method, metastable helium atoms were generated via direct current discharge, and then a Stern-Gerlach magnet was used to select the $2^3S_1, M_J = 0$ state atoms. In the detection region, these atoms were excited to the 2^3P state and returned to the 2^3S state. After the detection region, another Stern-Gerlach magnet spatially separated the three sublevels, and the experiment detected only the $M_J = +1$ and -1 states by blocking the $M_J = 0$ state. Since the beam was not decelerated, despite the use of a corner-cube reflector to return the laser along the original path, there was still a first-order Doppler effect of approximately 15 kHz in the experiment. Additionally, due to the limitations of the experimental period, optical frequency combs were not used as frequency references, which led to an uncertainty as high as 50 kHz, and systematic errors such as quantum interference effects were not considered^[218]. In contrast, the method used by the University of Florence involved a simpler beam apparatus, which did not require single quantum state selection. Although helium atoms were not decelerated in this experiment either, the Doppler effect was less than 2 kHz due to the use of saturated absorption spectroscopy. The application of optical frequency combs significantly reduced the errors associated with the frequency reference. However, the undetected atoms led to a substantial broadening of the spectral line width. Furthermore, to achieve saturated absorption conditions, higher detection power was used, which introduced significant power broadening effects. Therefore, a theoretical model needed to be established to compute corrections for second-order Doppler shifts, light shifts, recoil effects, etc. The results of the calculations showed that corrections of 40 to 200 kHz were required for the three sublevels of the transition from 2^3S to 2^3P . Subsequent studies also indicated that this method was highly sensitive to quantum interference effects^[219-220], especially factors such as the polarization of the

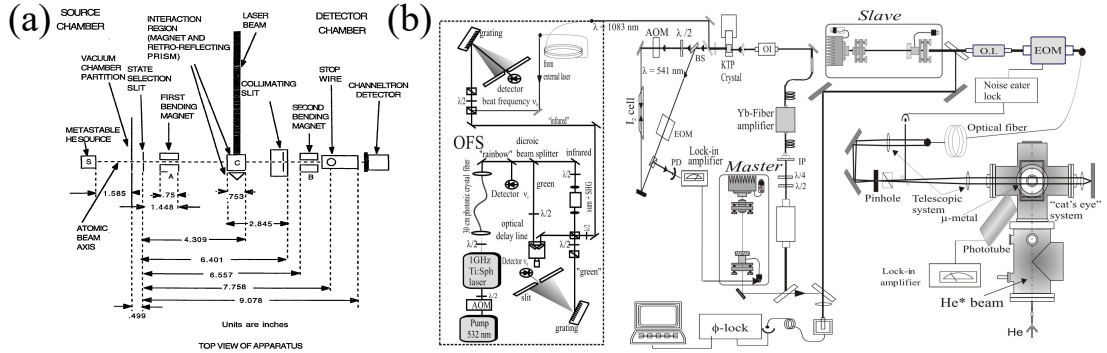


Figure 2.1 (a) Schematic of the single quantum state detection method using a helium atomic beam by the Shiner group, adapted from the doctoral thesis^[221]. (b) Schematic of the saturated fluorescence method by the University of Florence, adapted from the reference^[222].

probe laser and the spatial position of the detector, which required further correction through complex models.

Since 2010, our research group has been conducting measurements of helium atomic spectra^[224]. The initial experimental goal was to measure the intervals between $2^3 P_J$ levels, and during these measurements, the Doppler effect could be eliminated by switching the laser. Therefore, the initial setup^[223] did not involve slowing down the longitudinal velocity of the atomic beam. Drawing on the group's experience with rare gas detection, such as Kr and Ar, a similar experimental setup to that of the Shiner group was adopted^[224-225]. Metastable helium atoms were produced via radio frequency discharge, followed by transverse cooling using laser beams. Optical pumping, combined with Stern-Gerlach magnets, was used for single quantum state detection. However, it was observed that the discharge process generated significant background noise, so the

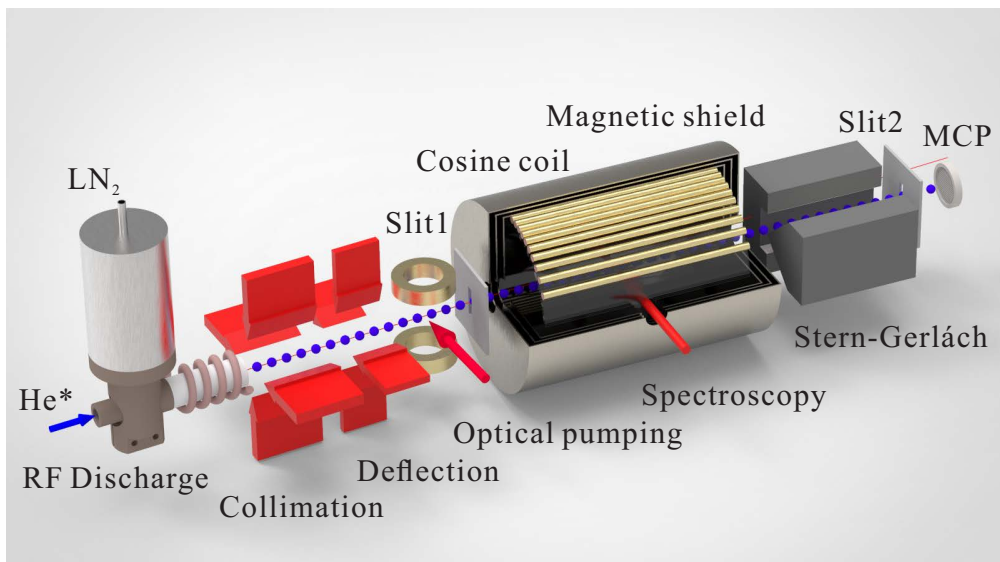


Figure 2.2 The initial setup of our research group, excerpted from the doctoral thesis^[223].

force of light on the atoms was used to actively deflect the metastable helium atoms, thereby improving the signal-to-noise ratio. After completing the measurement of the 2^3P_J intervals^[226-227], and in light of the “proton size puzzle,” our group decided to extend the current setup to measure the absolute frequency of the $2^3S - 2^3P$ transition. In the 2017 measurements, the largest systematic error was the first-order Doppler effect due to the high longitudinal velocity of the beam^[177]. Therefore, a Zeeman cooler was added in the new generation setup, and various issues encountered in the experiment were explored and improved. The current experimental setup was mainly constructed by Dr. Chen Jiaojiao^[228-229], and I later made modifications based on this, including improvements to the detection light path (Section 2.5) and the closed-loop gas circuit (Section 4.2). Further details can be found in the previous doctoral theses from our group^[223,229]. The following will introduce the current experimental setup in two main parts: the beamline device and the optical system.

2.2 Preparation of Metastable Helium Atomic Beam

2.2.1 Preparation of Metastable Helium Atoms

The low-energy states of helium atoms are shown in Figure 2.3. The energy gap between the 2^3S state and the 1^1S state is about 20 eV (equivalent to a 58 nm photon energy), and since the two states have opposite spin symmetries, electric dipole selection rules make it nearly impossible to directly optically excite and prepare metastable helium atoms. Currently, metastable helium atom beams can only be produced through electron collisions, which are categorized into electron beam collisions^[230-232] and dis-

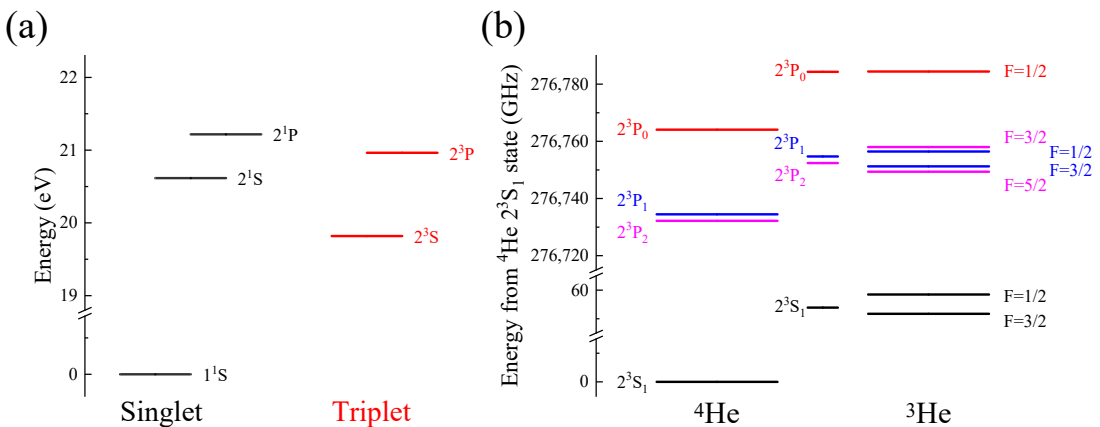


Figure 2.3 Energy level diagram of helium atoms involved in the experiment. (a) The experiment excites helium atoms in the 1^1S state to the 2^3S metastable state via radio-frequency discharge, and probes the $2^3S - 2^3P$ transition at a wavelength of 1083 nm. (b) Comparison of the sublevels of the 2^3S and 2^3P states for ${}^4\text{He}$ and ${}^3\text{He}$. Data from the literature^[215].

charge methods^[233-235]. Due to momentum transfer during the collision process that alters the direction of the atomic beam, the electron beam collision method requires compensation using electrostatic or magnetostatic fields, making the device structure more complex. The discharge method can be further divided into direct current (DC) discharge and radio-frequency (RF) discharge. DC discharge requires a higher excitation electric field strength, typically in the range of tens to hundreds of kV/cm, and higher gas pressure, leading to increased collisions between metastable atoms and background gas, which results in lower overall excitation efficiency. In this experiment, the RF discharge method^[236-237] is used, where electrons are inductively coupled into a helical coil resonator and collide with the gas to generate metastable helium atoms. The RF discharge method requires lower gas pressure, typically in the 10^{-6} Torr range, which reduces losses due to background gas collisions.

Due to the high excitation energy of helium gas, low ionization energy gases (such as krypton gas) can be introduced. These low ionization energy gases dissociate into ions through interactions with electrons, which then collide with helium gas to increase the yield of metastable helium atoms. In the experiment, the flow of helium and krypton gases is controlled by two separate microleak valves. The ratio of the two gases affects the beam intensity. Figure 2.4 shows the variation in beam intensity when the pressure of one gas is fixed and the pressure of the other gas is varied. In the flow gas state, where the molecular pump stage is maintained by a mechanical pump, the helium gas

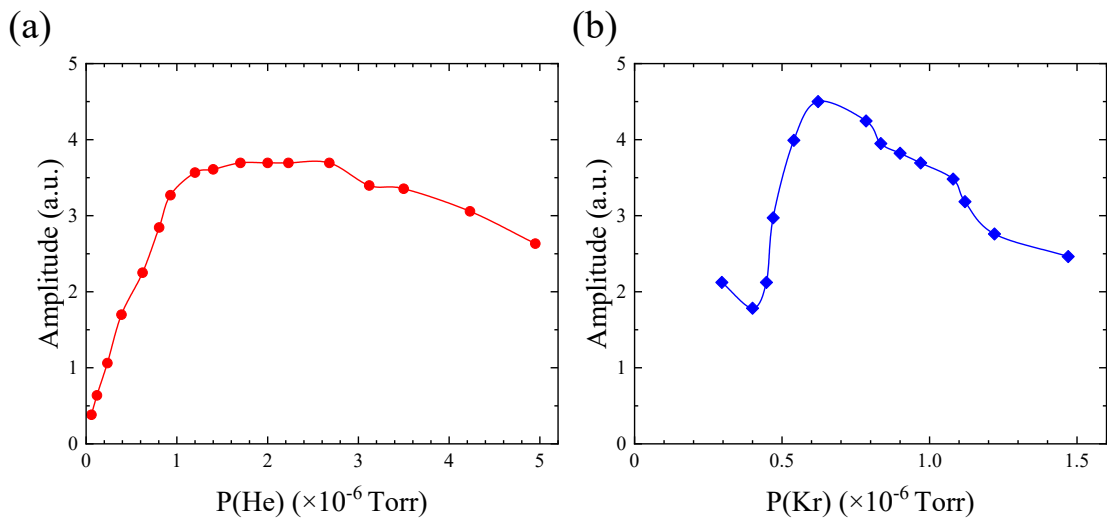


Figure 2.4 The relationship between the atomic beam intensity and the gas pressure during the flow gas measurement. In figure (a), the Kr pressure is fixed at 9.7×10^{-7} Torr while the He pressure is varied; in figure (b), the He pressure is fixed at 2.0×10^{-6} Torr while the Kr pressure is varied. The gas pressure readings correspond to the gas indicators measured by the residual gas analyzer (RGA) in the source chamber, and the beam intensity has been normalized.

pressure in the source chamber is typically in the range of $1.5 \sim 2.0 \times 10^{-6}$ Torr, and the krypton gas pressure is in the range of $0.6 \sim 0.8 \times 10^{-6}$ Torr, where the beam intensity is maximized. When measuring ^3He , due to the rarity of the gas sample, a closed-loop treatment is applied, where the molecular pump stage is directly connected back to the source chamber. In this case, the total pressure in the source chamber increases, and the optimal gas ratio range is helium $1.1 \sim 1.3 \times 10^{-6}$ Torr and krypton $0.9 \sim 1.1 \times 10^{-6}$ Torr.

After the gases are sufficiently mixed, they enter the resonance cavity, which consists of an aluminum nitride tube, a helical coil, and a shielding shell. In the experiment, the third harmonic of the resonance cavity's fundamental frequency is used for excitation to obtain a stronger and more stable atomic beam than the excitation at the fundamental frequency^[236]. The radio frequency is approximately 288 MHz, and after amplification by a power amplifier, the power coupled into the resonance cavity is about 50 W. However, the high-power radio frequency discharge heats the gas, which increases the atomic velocity and reduces the effectiveness of laser cooling. To address this, the experiment uses a liquid nitrogen dewar to cool the resonance cavity^[225], with the dewar connected to the aluminum nitride tube via an oxygen-free copper adapter. In the thermal equilibrium state, the platinum resistance thermometer on the aluminum nitride tube reads about 138 K. The velocity distribution of the atomic beam exiting the resonance cavity satisfies the formula^[238]:

$$f(v) = \frac{v^3}{2u^4} \exp\left[-\frac{v^2}{2u^2}\right] \quad (2.1)$$

Here, $u = \sqrt{k_B T/M}$. When the temperature drops from room temperature (approximately 300 K) to 138 K, the most probable velocity of the beam ($v_{\text{mp}} = \sqrt{3}u$) decreases from 1370 m/s to 927 m/s.

2.2.2 Beam Deceleration, Collimation, and Deflection

In order to maximize the atomic count rate in the final beam, it is necessary to compress and collimate the metastable helium atomic beam generated by radio-frequency discharge excitation. Additionally, to obtain a beam with adjustable velocity, deceleration of the atomic beam is required. Moreover, to avoid interference from singlet-state atoms or high-energy electrons produced during excitation, it is essential to actively deflect the 2^3S metastable atoms. Therefore, in this experiment, laser cooling is used to decelerate, collimate, and deflect the atomic beam.

2.2.2.1 Interaction between Laser and Atoms

When a laser interacts with an atom, each absorbed photon imparts momentum to the atom in the opposite direction of its motion. Since spontaneous emission is isotropic, after interacting with multiple photons, this scattering force reduces the atom's velocity:

$$F_{\text{scatt}} = \frac{\hbar k \Gamma}{2} \frac{I/I_{\text{sat}}}{1 + I/I_{\text{sat}} + 4\delta^2/\Gamma^2} \quad (2.2)$$

where Γ is the upper-state decay rate, $\delta = \omega - \omega_0$ represents the laser frequency detuning, ω is the laser frequency, ω_0 is the two-level resonance frequency, I is the laser intensity, and $I_{\text{sat}} = \pi hc\Gamma/(3\lambda^3)$ is the saturation intensity. When the laser intensity is sufficiently high and exactly resonant, the maximum acceleration produced by the scattering force is:

$$a_{\max} = \frac{F_{\max}}{m} = \frac{\hbar k \Gamma}{2m} = \frac{v_r \Gamma}{2} \quad (2.3)$$

where $v_r = \hbar k/m$ is the change in velocity caused by the recoil momentum from a single photon scattering, known as the recoil velocity. For the $2^3S - 2^3P$ transition studied in this experiment, the upper-state lifetime $\tau \approx 98$ ns, decay rate $\Gamma = 1/\tau \approx 2\pi \times 1.62$ MHz, saturation intensity $I_{\text{sat}} \approx 1.67$ W/m², recoil velocities are $v_r(^4\text{He}) \approx 0.092$ m/s and $v_r(^3\text{He}) \approx 0.122$ m/s, and the maximum accelerations are $a_{\max}(^4\text{He}) \approx 4.7 \times 10^5$ m/s² and $a_{\max}(^3\text{He}) \approx 6.2 \times 10^5$ m/s².

When the atom is decelerated, the change in frequency detuning is given by $\delta' = \delta - \vec{k} \cdot \vec{v}$. To ensure continuous deceleration of the atom by the laser, the laser frequency must be adjusted accordingly, or compensation can be made using a magnetic field or other methods. For example, in a Zeeman decelerator, a magnetic field is used to match the changes in atomic velocity, thereby achieving longitudinal deceleration of the atomic beam.

When the atom is in a standing wave field formed by two laser beams that are identical except for their opposite directions, i.e., in optical molasses, the resultant scattering force acting on the atom is:

$$F_{\text{mol}} = F_{\text{scatt}}(\delta - kv) - F_{\text{scatt}}(\delta + kv) \approx -2k \frac{\partial F_{\text{scatt}}}{\partial \omega} v = -\alpha v \quad (2.4)$$

where the damping coefficient α is given by:

$$\alpha = 2k \frac{\partial F_{\text{scatt}}}{\partial \omega} = -4\hbar k^2 \frac{I}{I_{\text{sat}}} \frac{2\delta/\Gamma}{(1 + 4\delta^2/\Gamma^2)^2} \quad (2.5)$$

When $\delta < 0$, i.e., when the laser is red-detuned, the resulting force is opposite to the velocity direction, and the laser acts to decelerate the atom. This principle is used in

this experiment for transverse cooling, which reduces the divergence of the atomic beam and increases the atomic flux.

When the incident and reflected lasers are left- and right-handed circularly polarized, respectively, and an external magnetic field is applied using anti-Helmholtz coils, i.e., when the atom is in a Magneto-Optical Trap (MOT), the total force acting on the atom is:

$$\begin{aligned} F_{\text{MOT}} &= F_{\text{scatt}}^{\sigma^+}[\omega - kv - (\omega_0 + \beta z)] - F_{\text{scatt}}^{\sigma^-}[\omega + kv - (\omega_0 - \beta z)] \\ &\approx -2k \frac{\partial F_{\text{scatt}}}{\partial \omega} v + 2\beta \frac{\partial F_{\text{scatt}}}{\partial \omega_0} \approx -\alpha v - \frac{\alpha \beta}{k} z \end{aligned} \quad (2.6)$$

Where z is the atomic position, and $\beta = \frac{g u_B}{\hbar} \frac{dB}{dz}$, with the magnetic field at $z = 0$ being zero in the anti-Helmholtz coils. The second term is a position-dependent attenuation function, and the final effect is to push the atoms towards the region where $z = 0$. Based on this principle, this experiment employs a two-dimensional magneto-optical trap (2D-MOT) to focus the atomic beam transversely, thereby achieving better collimation and deflection.

2.2.2.2 Transverse Cooling

At the exit of the radio frequency discharge resonator, the experiment uses two sets of plane mirror arrays with a certain angle between them to perform transverse cooling (TC) on the atomic beam. As shown in Figure 2.5, the mirror dimensions are 200 mm \times 40 mm \times 10 mm, and the distance between each set of mirrors is 90 mm. The mirrors are fixed on aluminum mounting brackets and can be adjusted using a piezoelectric actuator (picomotor). The laser is pre-shaped into a rectangular beam of

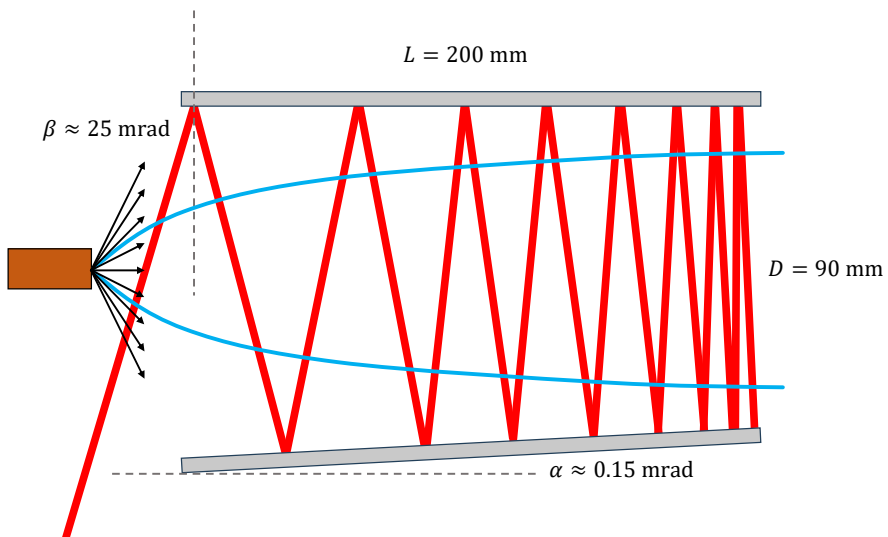


Figure 2.5 Schematic diagram of transverse cooling.

30 mm × 10 mm by a lens system, with an incident angle of 25 mrad, and the mirror angle is 0.15 mrad. After several reflections, the laser beam exits approximately perpendicular to the direction of the atomic beam. This design can capture atoms with an initial transverse velocity of up to 20 m/s. With transverse cooling, the atomic beam is expected to increase by a factor of 50, and after actual adjustment, it is amplified by about 65 times. After transverse cooling, the atomic beam transitions from diverging to nearly parallel motion, facilitating further transverse compression and longitudinal deceleration.

2.2.2.3 Longitudinal Deceleration

In previous experiments conducted by our research group, the first-order Doppler effect was identified as the largest source of system error. Therefore, it is necessary to decelerate the atomic beam. As mentioned earlier, after deceleration, the frequency detuning changes, and the frequency must be adjusted or compensated using a magnetic field to ensure continuous deceleration of the atomic beam. In this experiment, a Zeeman decelerator is used. By varying the number of coil turns at different positions, the atomic beam can be continuously decelerated. In the ideal case, the magnetic field variation can continuously compensate for the change in velocity:

$$\frac{\mu_B B(z)}{\hbar} = \delta + kv \quad (2.7)$$

When the atoms start decelerating from $z = 0$, their velocity can be expressed as:

$$v(z) = \sqrt{v^2(0) - 2az} \quad (2.8)$$

Due to the limitation of light intensity, it is difficult to achieve the maximum acceleration. In this experimental setup, $a = 0.6a_{\max}$ is chosen. The ideal magnetic field variation curve is:

$$B(z) = \frac{\hbar}{\mu_B} \left[k \sqrt{v^2(0) - 2az} + \delta \right] \quad (2.9)$$

In the design, the capture velocity considered is 820 m/s, with a laser detuning of $\delta = -2\pi \times 80$ MHz, and the total length of the decelerator is 115.6 cm. Theoretically, the capture efficiencies for liquid-nitrogen pre-cooled ${}^4\text{He}$ and ${}^3\text{He}$ are 32.8 % and 22.0 %, respectively, which is an improvement of 3.2 and 3.5 times compared to the beam source at room temperature. Specific design details can be found in the doctoral thesis^[229].

In the experiment, the Zeeman decelerator consists of 13 layers of coils. The comparison between the obtained magnetic field and the ideal magnetic field is shown in

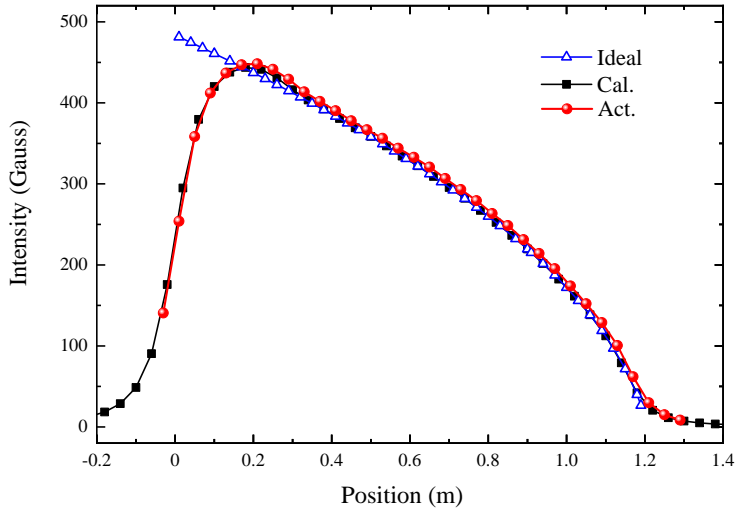


Figure 2.6 Magnetic field variation inside the Zeeman decelerator. The blue hollow triangles represent the ideal magnetic field curve calculated using Equation 2.9, the black squares represent the theoretical magnetic field variation curve calculated during the design of the coils, and the red dots represent the actual measured magnetic field variation.

Figure 2.6. The designed operating current is 2 A, but due to severe heating during operation, the current is typically set to 1.45 A in the experiment, with cooling provided by fans. Therefore, the magnetic field curve is shifted slightly downward compared to the original design, and the deviation is compensated by adjusting the laser power and other parameters. Since the magnetic field of the Zeeman decelerator is relatively strong, it significantly affects the surrounding 2D-MOT and other setups, so the entire decelerator is wrapped with a layer of permalloy to reduce its external influence.

During the deceleration process, the atomic beam will spread transversely. As a result, the deceleration laser is designed as a weakly focused Gaussian beam. When the laser enters from the deflected window, the beam diameter is about 20 mm, and when it exits from the front of the device, the beam diameter is about 10 mm. The laser power is stabilized at 20 mW using a Liquid Crystal Laser Amplitude Stabilizer (NEL04A/M, Thorlabs).

According to Equation 2.9, to change the velocity of the atomic beam, the magnetic field current, laser power, or frequency detuning can be adjusted. In the experiment, changing the frequency detuning can significantly alter the velocity, and the beam velocity and frequency detuning are approximately linearly related, as shown in Figure 2.9(b). Changing the magnetic field current or laser power has little effect on the velocity, only slightly affecting the slope of the linear relationship between velocity and detuning. Adjusting the laser incidence direction and focusing can also slightly adjust the velocity, but to ensure reproducibility, the optical path is typically not adjusted when changing the velocity. Ultimately, the experimental setup can achieve continuous

velocity tuning within the range of 50 to 450 m/s. To obtain sufficiently high signal-to-noise ratio spectra and shorten the measurement time, spectra are measured only within the range of 100 to 400 m/s.

2.2.2.4 Beam Focusing

In order to achieve better deceleration and deflection effects, the atomic beam needs to be focused to a certain degree. Especially after the Zeeman decelerator, since the transverse velocity is not decelerated during the longitudinal deceleration process, the atomic beam expands transversely, and focusing is necessary to avoid the loss of counts caused by this expansion. In the experiment, a two-dimensional magneto-optical trap (2D-MOT) is used to focus the atomic beam. The 2D-MOT consists of two pairs of anti-Helmholtz coils and two pairs of standing wave lasers, with each pair of lasers having left- or right-handed circular polarization for the incident and reflected beams. During the design, the 2D-MOT laser frequency was red-detuned by 1.8Γ . For a beam with a velocity of 100 m/s, it can focus atoms within a ± 1 cm range transversely to a deflection point at 0.55 m. However, due to the strong magnetic field of the Zeeman decelerator, which affects the magnetic field distribution at the location of the 2D-MOT, the actual laser frequency used in the experiment is blue-detuned by 2 MHz. Fortunately, a 100-fold gain in the atomic beam can still be achieved. During the velocity adjustment process, optimizing the optical path of the 2D-MOT after the Zeeman decelerator can significantly enhance the signal. Therefore, in future device improvements, the 2D-MOT section should be redesigned as a priority.

2.2.2.5 Deflection of Metastable Atomic Beams

During the radio-frequency discharge process, in addition to the required 2^3S state atoms for the experiment, large amounts of 2^1S state atoms and high-energy photons are also produced. If a detector is placed directly along the beam direction, a high amplitude background signal will be observed. Therefore, in the experiment, a laser is used to actively deflect the 2^3S state atoms. The designed parameters include a frequency redshift of 1.8Γ , a light intensity of 6 times the saturation intensity, and an angle of 9.8° between the laser and the beam direction. This setup allows for a deflection of the beam by 0.1 rad. In the experiment, the deflection laser shares the same laser as the 2D-MOT. To ensure that the beam is deflected to the same position, different deflection powers are required at different speeds, with higher speeds needing higher deflection power. Compared with the previous setup without a Zeeman decelerator, the current

setup has a lower beam velocity and a larger deflection angle. Additionally, with the inclusion of the Zeeman decelerator, the device is longer, and the background signal is weaker. Without slits, the signal-to-noise ratio is approximately 1000. After adding slits to capture the final beam, the background signal becomes almost zero when no deflection light is present. The high signal-to-noise ratio of the metastable atomic beam lays a solid foundation for high-precision spectral measurements.

2.2.2.6 Beam Slit

The experiment uses the crossed-beam method to reduce the influence of the Doppler effect on the frequency center. This method requires that the probe laser be as perpendicular as possible to the beam, and the divergence angle of the beam should be minimized. In the experiment, the deflected beam still has a broad transverse velocity distribution, so it is necessary to use slits to capture a narrower transverse distribution. In this experiment, a Linear Bellows Drive by Lesker is used to precisely control the position of the slit. The slit is a rectangular opening of 0.3 mm in width and 8 mm in length, cut into a 100 mm \times 22 mm aluminum alloy plate. Due to processing limitations, the actual width has an error of ± 0.1 mm. In this experimental setup, slits can be installed at three positions, two of which are located before the detection laser region, and one is located in front of the detector. For convenience in description, these are labeled Slit 1, 2, and 3, in the direction of the beam's propagation from front to back.

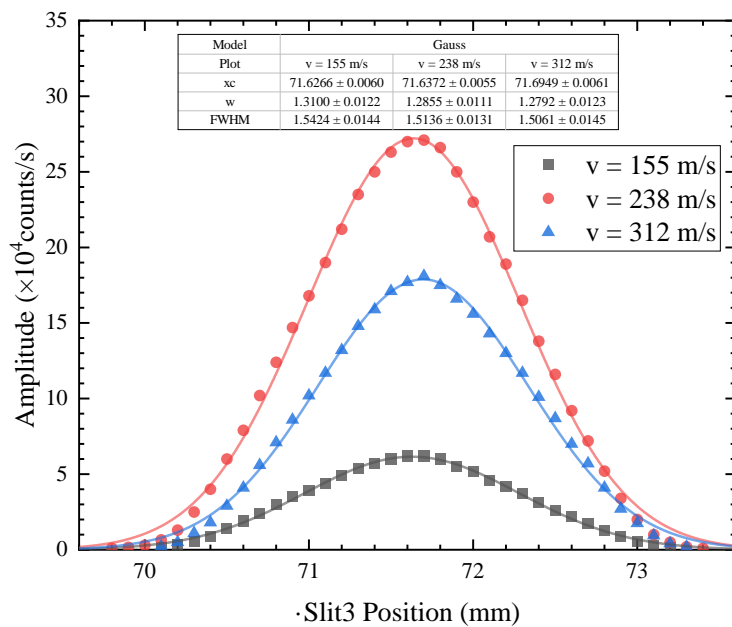


Figure 2.7 Fixed positions of Slit 1 and 2, with Slit 3 moved to measure the beam distribution. The measured beam width is approximately 1.5 mm at different beam velocities.

With Slits 1 and 2 fixed, the final geometric dimensions of the beam have been fully determined. As shown in Figure 2.7, the beam width measured using Slit 3 is 1.5 mm (full width at half maximum), and this width is not affected by the longitudinal speed of the beam. Due to the inherent width of the slit, the measured width is slightly broader than the actual value, but this was not accounted for in the experiment, and all data presented are raw. This width corresponds to a beam divergence angle of approximately 0.1 mrad, which meets the experimental requirements. When the beam velocity is higher, spectra are measured at different powers and Lorentzian fitting is applied. When the power is extrapolated to zero, the linewidth of the spectrum and the natural linewidth are essentially the same, indicating that the current system is no longer significantly affected by Doppler broadening, and the beam divergence angle is sufficiently small.

2.2.3 Beam Performance Evaluation

2.2.3.1 Excitation Source Beam Flux

In the experiment, the fluorescence detection area is set on the six-way chamber adjacent to the source cavity. The laser is injected horizontally, and the detector is located above. The fluorescence collection efficiency can be expressed as:

$$Q = \frac{\eta \kappa \pi r_{\text{PD}}^2}{4\pi L_0^2} \quad (2.10)$$

here, $\eta = 0.25$ A/W is the photon conversion rate of the photodetector (SM1PD2A, Thorlabs), $r_{\text{PD}} = 4.5$ mm is the radius of the detector's photosensitive surface, $\kappa = 0.8$ is the efficiency of the detector's front optical filter, and $L_0 = 17.5$ cm is the distance from the detector to the center of the beam. From this, the collection efficiency can be calculated as $Q \approx 3.3 \times 10^{-5}$. The current contributed by a single atom per second is $q = QRe$, where e is the electron charge, and $R = \frac{\Gamma}{2} \frac{I/I_{\text{sat}}}{1+I/I_{\text{sat}}}$ is the photon scattering rate at resonance. Since the fluorescence signal is weak, the current signal output by the detector is connected to a current amplifier (SR570, SRS) with a gain of $K = 100$ pA/V, and the output voltage signal is connected to a data acquisition card for data collection. In the experiment, a 3.5 mW laser is used for detection, and the measured fluorescence signal peak height is $H \approx 1.8$ V. The beam flux can be expressed as:

$$\text{Flux} = \frac{KH/q}{(D_0/v)(D_0 D_1 / L^2)} \quad (2.11)$$

here, $D_0 = 1$ cm is the beam spot diameter at the detection region, $D_1 = 3$ cm is the diameter of the skimmer between the source cavity and the detection region's six-way

chamber, i.e., the detectable beam diameter, and $L = 45$ cm is the distance from the detection region to the excitation source exit. The beam velocity v is calculated using the most probable velocity of 927 m/s at a working temperature of 138 K. Finally, the calculated metastable helium atomic beam intensity is approximately 4.8×10^{14} atoms/s/sr.

2.2.3.2 Beam Cooling Effect

In the experiment, laser cooling principles were used to collimate, focus, and decelerate the metastable helium atoms that were excited. As shown in Figure 2.8, the beam intensity was first adjusted to its maximum at a speed of 100 m/s, after which all lasers were blocked, and each laser section was gradually turned on to assess the cooling effect. At a velocity within the range of 100 ± 10 m/s, atoms in the initial Maxwell distribution account for only 0.012 %, and the proportion that can be deflected and ultimately collected is even lower. After cooling with different components, the beam intensity gradually increased, with the Zeeman decelerator having a significant effect, enhancing the intensity by over 7000 times. The transverse cooling and 2D-MOT contributed increases of 65 and 100 times, respectively.

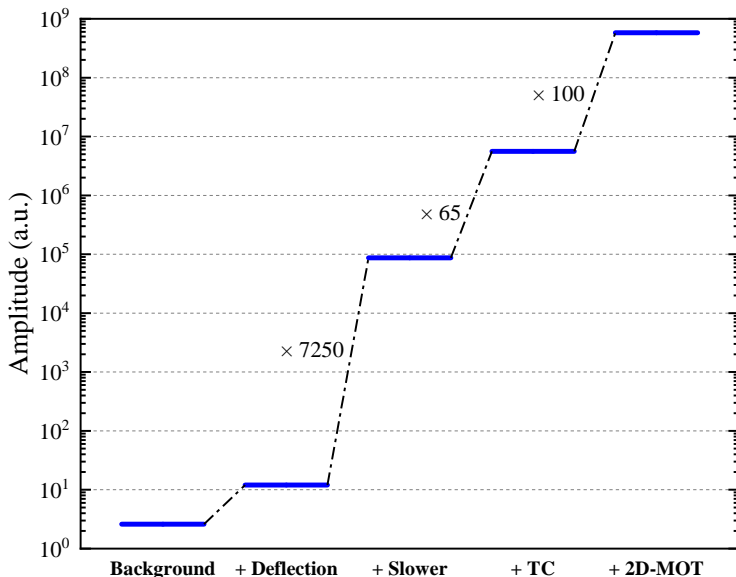


Figure 2.8 Variation in beam intensity as different cooling lasers are progressively turned on at a velocity of 100 m/s.

2.2.3.3 Adjustable Speed Range

To measure the longitudinal velocity of the beam, the experimental setup splits the probe light into two paths, which are directed through windows that are perpendicular to the beam and at a 45° angle relative to the beam. The first-order Doppler effect is

then utilized:

$$\Delta\omega_{\text{Doppler},1\text{st}} = \vec{k} \cdot \vec{v} = kv \cos \theta \quad (2.12)$$

where θ is the angle between the laser and the beam. The peak center shift measured by the two probe lasers is given by:

$$\Delta f = \frac{v}{\lambda}(\cos 45^\circ - \cos 90^\circ) \quad (2.13)$$

Substituting the wavelength and other parameters, the relationship v (m/s) \approx 1.532 Δf (MHz) can be derived. If there is a deviation of $\pm 1^\circ$ in the angle, it will introduce a maximum deviation of $\pm 4.4\%$ in the calculated coefficient, meaning the velocity's accuracy could be affected by $\pm 4.4\%$. However, throughout the experiment, the optical path remains unchanged, and the final result is obtained by extrapolating the velocity results at various speeds. Therefore, the deviation in the optical path angle will affect the slope of the velocity extrapolation but has minimal effect on the intercept of the velocity extrapolation, i.e., the final result.

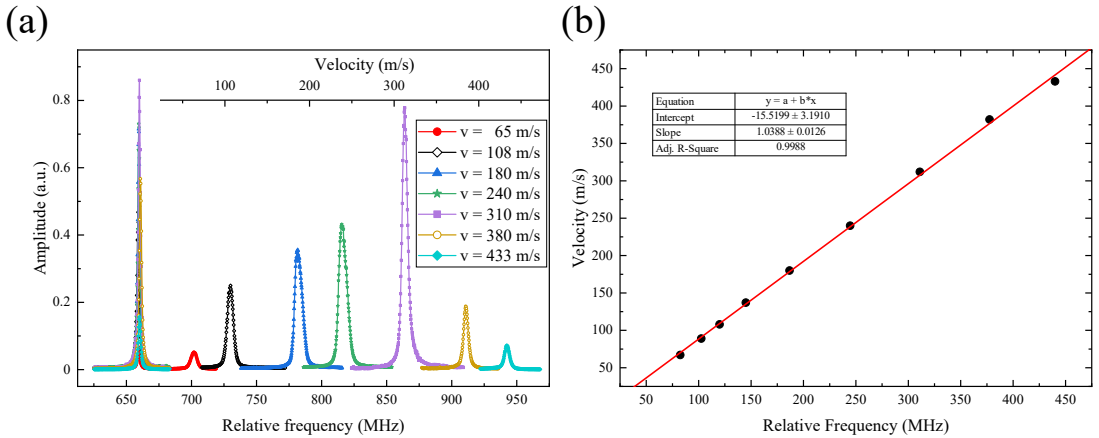


Figure 2.9 (a) Measurement results of the longitudinal velocity of the beam. (b) Relationship between the longitudinal velocity of the beam and the detuning of the Zeeman decelerator.

As shown in Figure 2.9(a), by adjusting the laser frequency detuning of the Zeeman slower, the beam velocity can be tuned within the range of 50 ~ 450 m/s. For the laser perpendicular to the beam, there is almost no Doppler shift, so the peak centers measured at different speeds are nearly identical. For the laser incident at a 45° angle, the full width at half maximum (FWHM) of the peaks is less than 3.2 MHz, which corresponds to a beam velocity distribution within ± 5 m/s.

2.2.3.4 Beam Stability

Since the spectral signal in this experiment depends on the number of atoms, the long-term drift of the beam intensity may affect the frequency center if the probe laser

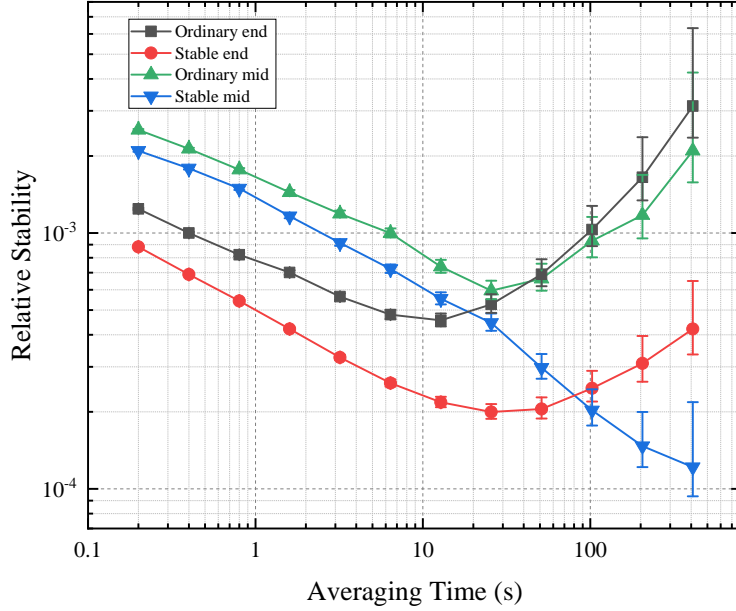


Figure 2.10 Relative Allan deviation plot before and after beam locking.

frequency is scanned in sequence or reverse sequence. In the experiment, before the probe laser interacts with the beam, a 45° stainless steel grid was used to cause some atoms to collide with the grid and produce electrons. Another channel electron multiplier was added in the direction perpendicular to the beam to detect the electrons. The atomic number signal output from this detection was used as a reference, and a digital PID program was used to provide feedback to the transverse cooling (TC) laser frequency to compensate for the long-term drift caused by changes in the beam source temperature or excitation efficiency^[228]. As shown in Figure 2.10, after feedback, the beam fluctuation was reduced by about one order of magnitude, effectively improving the long-term drift issue. However, in practical experiments, the additional grid structure not only reduces the number of atoms but also may alter the beam distribution, which has a significant impact on the experimental results. Considering that the experiment has already adopted the “four-point random scan” frequency setting (see Section 3.1.1), which has effectively immune the beam’s long drift effect, this beam stabilization device was not used in the final setup. In future experiments, if needed, this method can be applied after the beam deflection and before the slit to further improve the beam stability.

2.3 Atomic Single-Quantum State Preparation and Detection

After cooling, collimating, focusing, deflecting, and selecting the metastable atomic beam, the atoms are approximately uniformly distributed across the three mag-

netic sublevels of the 2^3S state. To accurately measure the absolute frequency of the $2^3S - 2^3P$ transition, the atoms need to be prepared in a single quantum state, and the effects of the Zeeman effect and other influences must be eliminated during the measurement. In the experiment, Stern-Gerlach magnets are used to ensure that only atoms in a single quantum state can be detected. Therefore, the atoms can be prepared into a detectable single magnetic sublevel by controlling the laser and magnetic field. Additionally, optical pumping is used to clear background signals, and external magnetic field interference is shielded in the detection region, followed by the application of an additional uniform magnetic field, enabling precise measurement of the $2^3S - 2^3P$ transition.

2.3.1 Optical Pumping

Optical pumping is a method that utilizes a magnetic field to separate the atomic magnetic sublevels and interacts with the atoms through laser light to pump the atoms into dark states. As shown in Figure 2.11(a), taking the $2^3S_1 - 2^3P_2$ transition of ${}^4\text{He}$ as an example, under the influence of a magnetic field, the three magnetic sublevels of the 2^3S_1 state experience a shift in energy levels, and similarly, the five magnetic sublevels of the 2^3P_2 state also undergo energy level shifts. In this case, if a σ^+ polarized laser is applied, transitions such as $2^3S_1(M_J = -1) - 2^3P_2(M_J = 0)$, $2^3S_1(M_J = 0) - 2^3P_2(M_J = +1)$, and $2^3S_1(M_J = +1) - 2^3P_2(M_J = +2)$ will occur. Since the energy differences between these transitions are nearly the same, meaning the frequency detuning is the same, they can be excited by the same laser beam simultaneously. After the laser interacts with the atoms for a sufficient amount of time, the atoms will theoretically be fully pumped into the $2^3S_1(M_J = +1)$ state.

The optical pumping setup used in the experiment is shown in Figure 2.11(b). The direction of the atomic beam is along the z axis, and the laser is injected horizontally

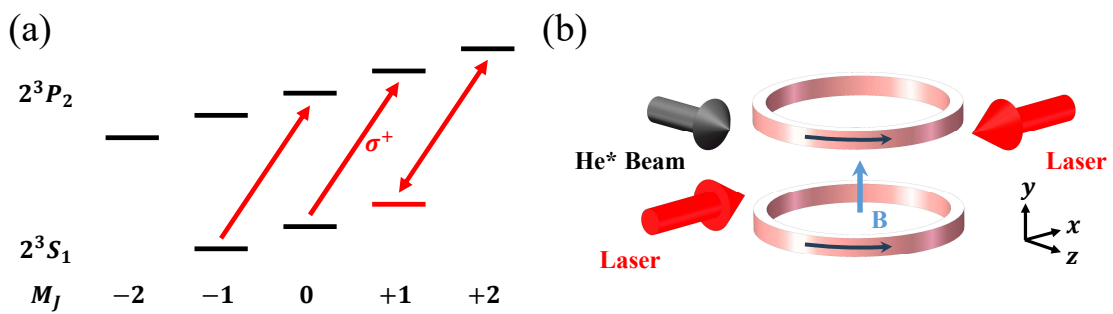


Figure 2.11 (a) Schematic of the optical pumping principle. A σ^+ polarized laser is used for pumping the $2^3S_1 - 2^3P_2$ transition, and all atoms are ultimately pumped to the $2^3S_1(M_J = +1)$ state. (b) Schematic of the optical pumping setup.

along the x direction from both sides. A uniform magnetic field is provided by a pair of Helmholtz coils, with the magnetic field direction along the vertical y direction. For the primary transition measured in the experiment, the $2^3S_1 - 2^3P_0$ transition, the frequency of the pumping laser is also locked around this transition. The pumping laser is purified into horizontally polarized light through a Glan-Taylor prism before being injected, exciting π transitions and pumping the $M_J = 0$ atoms in the 2^3S_1 state completely to the $M_J = \pm 1$ states.

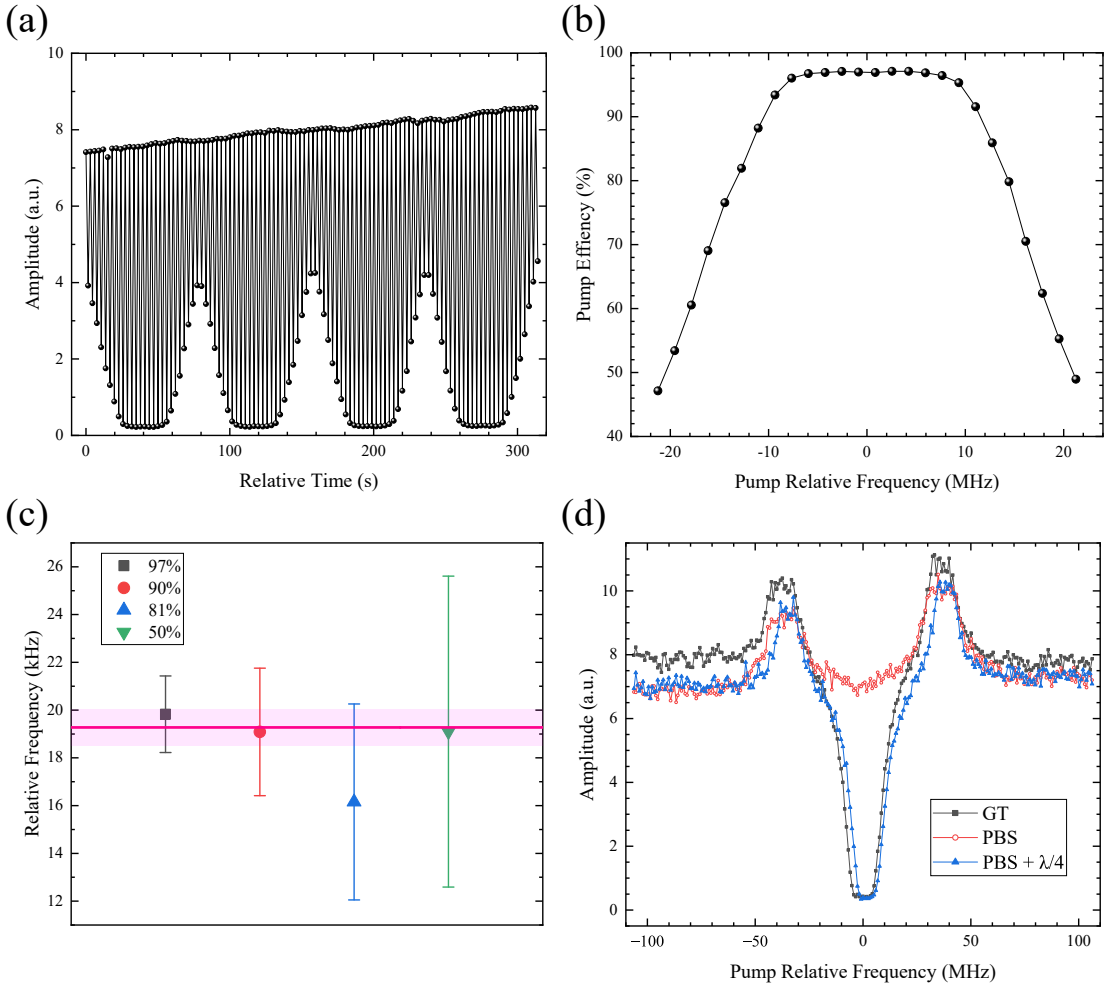


Figure 2.12 Pumping effect of ${}^4\text{He}$. (a) During rapid variations of the atomic beam, a chopper is used to actively switch the pumping laser, and the reference frequency is scanned within a certain range to measure the pumping effect. (b) The corresponding pumping efficiency from the data in (a). It can be seen that the pumping effect is independent of the atomic beam intensity. Since a DFB laser is used to provide the pumping laser, high pumping efficiency can be maintained over a wide frequency range. (c) The frequency center obtained from 40 spectra measurements at different pumping efficiencies. The results show that the lower the pumping efficiency, the larger the frequency center error. (d) After replacing the Glan-Taylor prism (GT prism) with a Polarizing Beam Splitter (PBS), an additional $\lambda/4$ plate is needed to achieve the same pumping effect.

It is worth noting that the pumping effect is independent of the atomic beam intensity variation. As shown in Figure 2.12(a), during the period when the atomic beam has

not stabilized, the chopper is used to switch the pumping laser, and the pumping laser frequency is scanned to measure the pumping effect. Considering the transverse distribution of the atomic beam, a DFB laser with a relatively wide linewidth (about MHz level) is chosen as the pumping light source in order to pump as many atoms as possible. Therefore, in Figure 2.12(b), it can be seen that the pumping efficiency remains above 95 % within a 20 MHz range. As shown in Figure 2.12(c), spectra from 40 measurements are taken and averaged at different pumping efficiencies. The results show that the lower the pumping efficiency, the larger the error in the frequency center. Therefore, the pumping efficiency must be adjusted to the optimal state before measuring the spectrum. In the experiment, the pumping efficiency is maintained above 95 %.

Due to the size limitation of the Glan-Taylor prism, in the experiment, the transmitted light from the PBS can also be used as a substitute. However, the pumping process has a high polarization requirement for the laser. Although the transmitted light from the PBS is approximately horizontally polarized, its extinction ratio is not as good as that of the Glan-Taylor prism. In practical operation, an additional $\lambda/4$ waveplate is required and rotated to a specific angle to achieve the same pumping effect as with the Glan-Taylor prism, as shown in Figure 2.12(d). In the experiment, although increasing the pumping laser power can improve the pumping effect, after the pump-probe process, by comparing the collected spectra, it is found that excessive power actually reduces the spectrum count rate. This suggests that when the pumping power is too high, the laser's force on the atoms becomes dominant, which is not conducive to optical pumping. In the experiment, the pumping power is fixed at around 200 μW , and the beam diameter is 2 cm.

It was found during the experiment that the distribution of the atomic beam has a significant impact on the final results. Due to the presence of the laser force on the atoms during the optical pumping process, it inevitably affects the beam distribution. However, in this experiment, the optical pumping section is located before the beam interception, and the beam distribution interacting with the detection light is entirely determined by the geometry of Slit 1 and 2. Therefore, the optical pumping does not affect the final beam distribution.

2.3.2 Magnetic Shielding and Bias Magnetic Field

In the detection region of the probe light, if the external magnetic field is not shielded, it can affect the frequency center. For example, the Earth's magnetic field, $B_G \approx 0.5$ Gauss, can cause a frequency shift of approximately 1.4 MHz for the

$2^3S_1(M_J = -1) - 2^3P_0(M_J = 0)$ transition. To eliminate the influence of external magnetic fields, this experiment employs a magnetic shielding system consisting of three concentric cylindrical shells made from high permeability iron-nickel alloy, which is annealed to achieve a relative permeability of approximately 15,000^[226]. As shown in Fig.2.13, using a fluxgate magnetometer (CTM-6W, with an uncertainty of 0.05 % \pm 10 nT), measurements show that within the central region of \pm 10 cm, the remanent magnetization in both axial and radial directions is less than 2 nT. Considering the precision of the fluxgate, this can be amplified to 20 nT, which is sufficient for the experimental requirements (see section 3.4.2 for more details)..

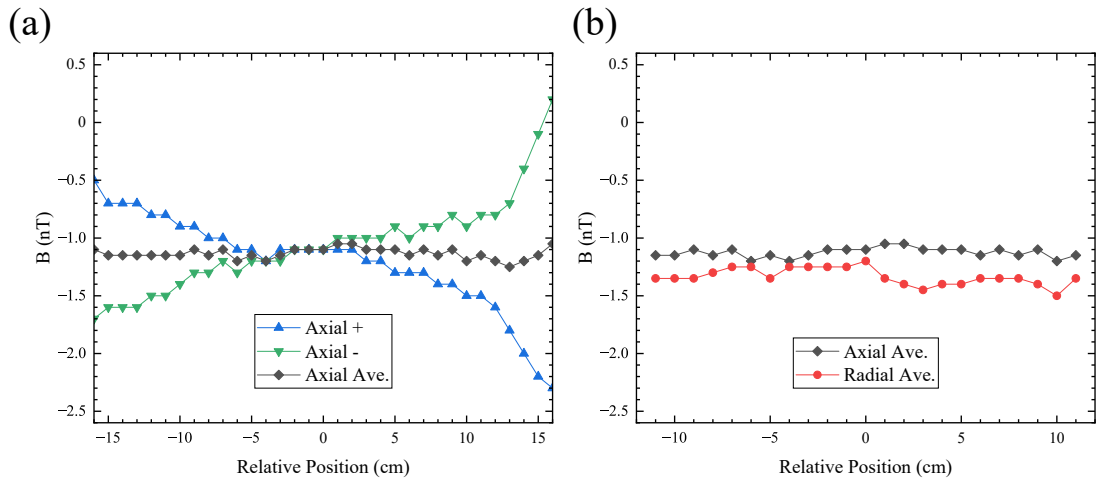


Figure 2.13 Magnetic shielding effect measurement. (a) The final remanent magnetization is obtained by averaging the measurements in both positive and negative directions. (b) In the central region within \pm 10 cm, the remanent magnetization along both axial and radial directions is less than 2 nT. Considering the precision of the fluxgate, it can be amplified to 20 nT.

Inside the magnetic shielding, a cosine coil is used to generate a uniform bias magnetic field. Compared to Helmholtz coils, cosine coils can produce a more uniform magnetic field^[239-240]. The principle behind this is that along the surface of an infinitely long current-carrying cylinder, the current density \mathbf{J} is related to the azimuthal angle ϕ as follows^[240]: $\mathbf{J}(\phi) = (2B_x/\mu_0) \cos \phi \cdot \mathbf{k}$, where \mathbf{k} is the unit vector along the cylinder axis, and μ_0 is the permeability of free space. This relation indicates that the projection of the current on the x direction is evenly distributed. Based on this principle, two sets of coils were designed through finite element simulation^[241-242] to generate uniform magnetic fields along the direction of the probe laser and perpendicular to both the probe laser and beam direction. The coil diameter is 173 mm, with a total of 64 wires, and a total length of 400 mm. Simulation results show that within a 10 mm cubic region at the center of the detection area, the magnetic field uniformity is better than 1 %, meeting the experimental requirements.

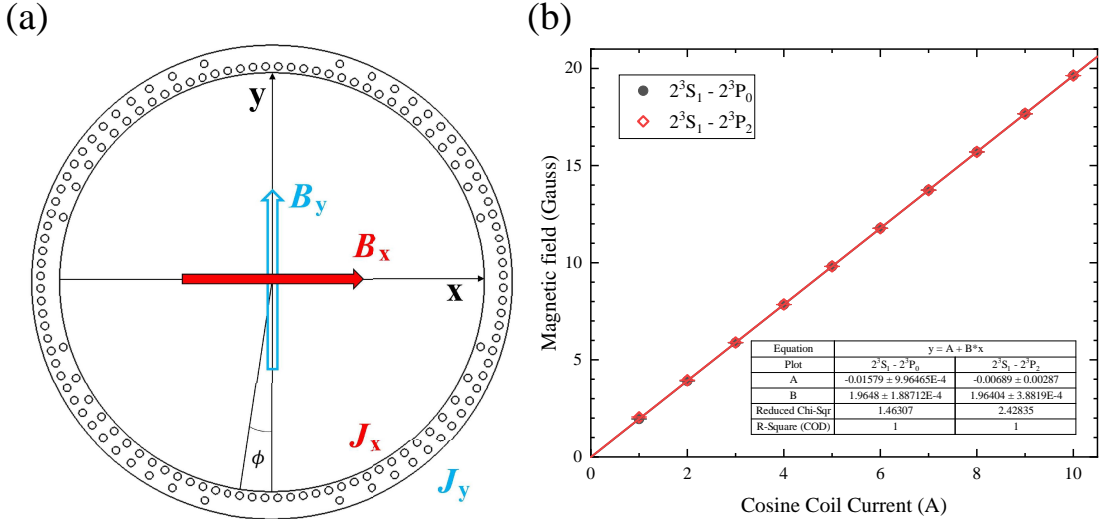


Figure 2.14 (a) Schematic of the cosine coil design. The inner and outer layers generate uniform magnetic fields along the x and y directions, respectively. (b) By varying the current in the cosine coil and measuring the spectrum, the magnetic field strength is determined. The results of both transitions show good linearity.

In the experiment, the effect of the magnetic field (i.e., the Zeeman effect) on the results is investigated by measuring the spectra under different magnetic field strengths. For more details, see section 3.4.

2.3.3 Gradient Magnetic Field Detection of Single Quantum States

In this experiment, a Channeltron Electron Multiplier (CEM) is used to count atoms. Since the internal energy of the metastable helium atoms is about 20 eV, high signal-to-noise ratio counting signals can be generated on the CEM without additional ionization. The model of the CEM used in the experiment is CEM4820COAG (Photonics), and a high-voltage source (PS350, SRS) is used to apply 2600 V and 500 V to its two electrodes, respectively. The signal output by the CEM is amplified by an amplifier, then identified and counted by a photon counter (SR400, SRS).

Two types of amplifiers have been used: a voltage amplifier (SR445A, SRS) and a current amplifier (C6438-01, Hamamatsu). Compared to the voltage amplifier, the current amplifier has a larger amplification factor, so the output signal must be attenuated before being connected to the photon counter. However, it has a better signal-to-noise ratio and is less sensitive to external signal interference. The amplified signal is monitored on an oscilloscope, with stray noise typically maintained at around 20 mV. To ensure accurate counting, the threshold voltage for the photon counter is set to 50 mV.

To avoid stray photons, a deflection electrode with an angle was installed in the previous setup^[223] in front of the CEM, allowing it to detect the atom beam in the vertical direction. However, because the deflection electrode selects the atomic beam

distribution again, it acts like a relatively wide slit, which may affect the results. Considering the current setup is longer and the deflection angle is larger, the influence of stray photons has been greatly reduced. Therefore, the decision was made to remove the deflection electrode and allow the CEM to directly align with the beam for detection. During the experiment, when the RF discharge is turned off or the deflection laser is blocked, the atom count is zero, ensuring the authenticity of the atom counting signal.

Before the detector, there is a gradient magnetic field region with a Stern-Gerlach magnet as the main component. The length of the Stern-Gerlach magnet used in the experiment is 0.3 m, and it is equipped with a vacuum tube that is 0.4 m long and has an inner diameter of 10 mm. The force on the atoms in the gradient magnetic field can be expressed as:

$$F = m_J g_J \mu_B \frac{\partial B}{\partial x} \quad (2.14)$$

here, μ_B is the Bohr magneton, and g_J is the Landé g-factor. The gradient of the Stern-Gerlach magnet designed in the experiment is $\partial B / \partial x \approx 0.6 \text{ T/cm}$. In this region, atoms in the $M_J = \pm 1$ states will be deflected and quenched after colliding with the chamber wall, while only atoms in the $M_J = 0$ state will pass through and be detected by the CEM. However, in subsequent ^3He experiments, it was found that due to the design of this magnet not considering the requirements of ^3He measurements^[241-242], the magnet can no longer support the completion of ^3He experimental measurements, as detailed in section 4.3.

Thus, a detailed introduction to the beamline device has been provided. The beamline device is shown in Figure 2.15. Next, a brief introduction will be given to another major part of the experimental setup: the optical system.

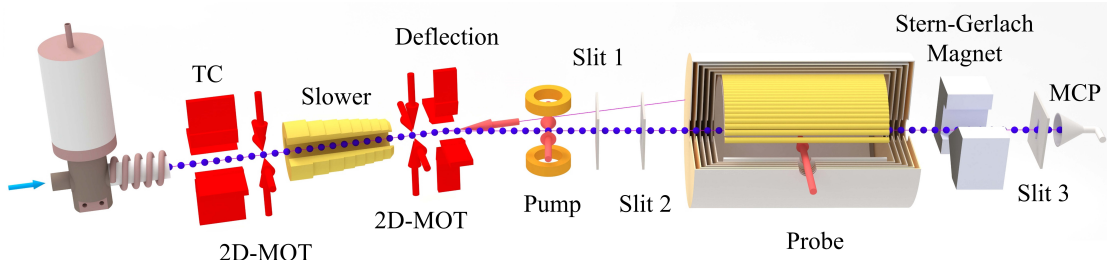


Figure 2.15 Schematic diagram of the beamline device.

2.4 Optical System

Currently, more mature international schemes typically divide a high-power external cavity diode laser (ECDL) into multiple channels, with each channel undergoing frequency modulation through electro-optic modulators (EOMs), acousto-optic modu-

lators (AOMs), etc., to meet different frequency requirements. However, this approach is usually adopted when the experimental setup has already been developed and the laser frequency and power requirements for each component are clearly defined. Compared to previous experimental setups, this experiment introduces a Zeeman decelerator, which necessitates the addition of optical paths such as a 2D-MOT to match the Zeeman decelerator. Additionally, for different beam velocities, it is necessary to adjust the frequency and power of each laser part. Furthermore, when switching to the ^3He measurement, if a single-laser branching method is used, due to the change in frequency detuning, it may be necessary to replace devices such as EOMs and AOMs, making the overall adjustment process quite complex. Therefore, this experiment chooses to independently use lower-power ECDLs for each part, with all lasers locked to a master laser using a Phase-Locked Loop (PLL). The master laser is stabilized using Pound-Drever-Hall (PDH) frequency stabilization technology to lock it to an ultra-stable cavity made from ultra-low expansion (ULE) materials. The frequency of the master laser is determined by beat frequency with an Optical Frequency Comb (OFC), thus achieving locking and precise determination of all laser frequencies. Next, the locking methods for the master laser, cooling laser, pumping laser, and detection laser, as well as the methods for locking laser power and polarization, will be briefly introduced.

2.4.1 Frequency Metrology

2.4.1.1 Master Laser Frequency Locking

The master laser used is a commercial narrow-linewidth laser (Koheras Adjustik Y10, NKT Photonics), with a nominal linewidth of approximately 20 kHz and a piezo-electric ceramic (PZT) modulation range of up to 10 GHz, with a bandwidth of 20 kHz. To suppress frequency drift caused by temperature variations and further narrow the laser linewidth, the master laser is locked to a commercial ultra-stable cavity (VH6010-4, Stable Laser Systems) in the experiment. The cavity length of the ultra-stable cavity is $L = 10$ cm, and its free spectral range is $\text{FSR} = 1.5$ GHz. The custom high-reflectivity mirrors have a reflectivity of $R = 99.999\%$ at 1083.3 nm, with a finesse of approximately 300,000 and a linewidth of about 5 kHz. In the experiment, the ultra-stable cavity is pumped to a pressure below 10^{-6} Torr using a molecular pump, and the internal high-vacuum state is maintained by an ion pump (Titan 5s, Gamma Vacuum). To minimize the effects of external vibrations, the ultra-stable cavity and optical path components are placed on an active vibration isolation platform (AVI 200LP, Herzan).

The optical path diagram for locking the master laser to the ultra-stable cavity is

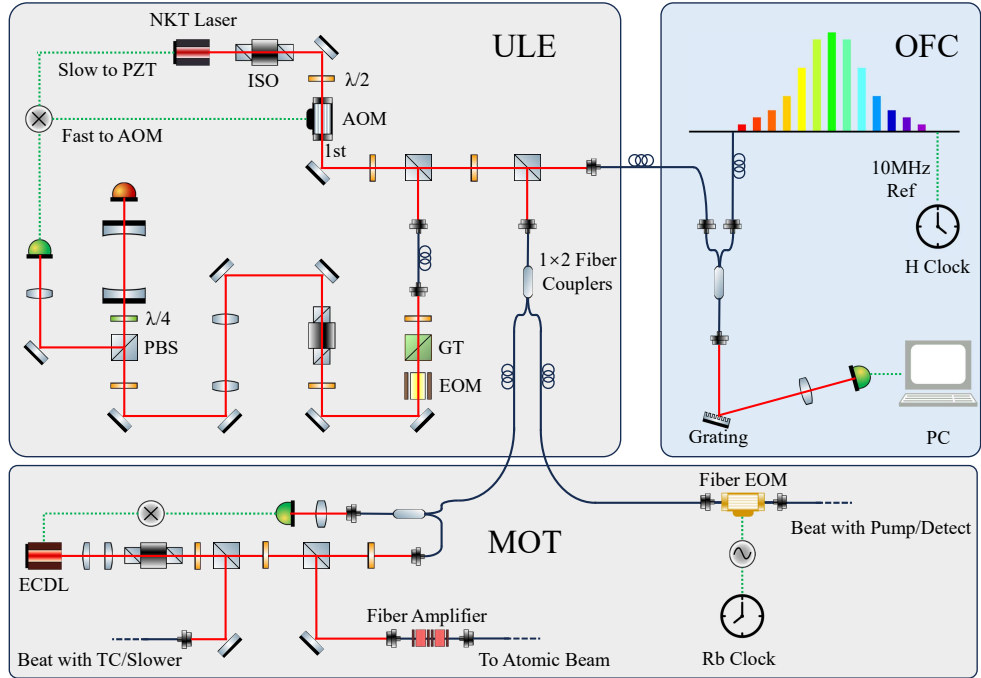


Figure 2.16 Optical path diagram. The master laser is frequency-shifted using an AOM and divided into three channels. One channel enters the ultra-stable cavity via a mode-matching lens, where it undergoes modulation and demodulation, and is frequency-locked using the PDH principle. Another channel is transmitted to another room via optical fiber, where it is beat-frequency measured with an optical frequency comb to determine the master laser's frequency. The third channel is split into two parts, one of which passes through a Fiber EOM to generate sidebands. The three laser beams used for beam cooling have frequencies close to each other. The MOT laser is directly beat-frequency locked to the master laser, while the TC and Slower lasers are locked via beat frequency with the MOT laser. The pumping and detection lasers are locked to the sidebands generated by the Fiber EOM.

shown in Fig. 2.16. Since the laser can only be controlled via PZT feedback, an AOM is added to the optical path to suppress MHz-level noise. After frequency shifting with the AOM, the laser is divided into three channels: one for locking the ultra-stable cavity, another for beat-frequency locking with other lasers, and the third for beat-frequency measurement with the optical frequency comb to determine the frequency.

2.4.1.2 Optical Frequency Comb and Frequency Reference

The optical frequency comb uses the laser mode-locking technique to simultaneously lock the phase shift of the carrier-envelope and the repetition frequency of femtosecond pulsed lasers, enabling the conversion between radio frequency (RF) and optical frequencies. When a laser beam beats with an optical frequency comb, its frequency can be expressed as:

$$f = n f_r \pm f_{ceo} \pm f_{beat} \quad (2.15)$$

where f_r is the repetition frequency of the optical frequency comb, f_{ceo} is the carrier-envelope offset, f_{beat} is the beat frequency value, and n is the closest comb tooth number to the laser frequency.

The optical frequency comb used in this experiment is provided by the team of Jiang Haifeng at the National Time Service Center of the Chinese Academy of Sciences^[243]. After locking, the stability of f_{ceo} is better than $2 \times 10^{-17} / \text{s}$, and the stability of f_r is better than $1 \times 10^{-13} / \text{s}$. The single-mode power at 1083 nm is approximately 200 nW.

To achieve high-precision optical frequency measurements, the optical frequency comb must be combined with a high-precision frequency reference. The best commercially available frequency reference is the cesium atomic clock, but it is complex. Therefore, rubidium clocks, which are simpler in structure, are often used. The previous experimental setup used a GPS-referenced rubidium clock (FS725, SRS) with a stability of $2 \times 10^{-11} / \text{s}$, and the long-term stability, calibrated by GPS, reached 2×10^{-12} after 100 seconds. Therefore, the error introduced by the frequency reference was $\Delta f \approx 2 \times 10^{-12} \times 276.7365 \times 10^{12} \approx 550 \text{ Hz}$.

In this experiment, the frequency reference has been replaced with a hydrogen maser (VCH-1003M Option L, VREMYA—CH), with a frequency accuracy of $\pm 1 \times 10^{-13}$, which significantly reduces the error introduced by the frequency reference by an order of magnitude.

2.4.1.3 Main Laser Performance

In the experiment, the helium atom measurement device and the optical frequency comb are located in two separate rooms. Therefore, single-mode optical fibers are used to guide the main laser to the room where the optical comb is located for beat frequency measurement. During the beat frequency measurement, the two laser beams are combined using a fiber optic coupler and then spatially separated by a grating to isolate other frequencies. The first-order diffracted light from the grating enters an indium gallium arsenide (InGaAs) detector (ET3000A, EOT) to detect the beat frequency. After filtering and amplification, the beat frequency results are read and recorded by a frequency counter (Frequency Counter, B&K 1832A).

As shown in Figure 2.17, the main laser frequency was continuously monitored for 12 days. The frequency variations were primarily caused by fluctuations in the laboratory temperature and stress release in the ultra-stable cavity. Simultaneously, the laboratory temperature was monitored using a thermometer (174T, Testo, resolution

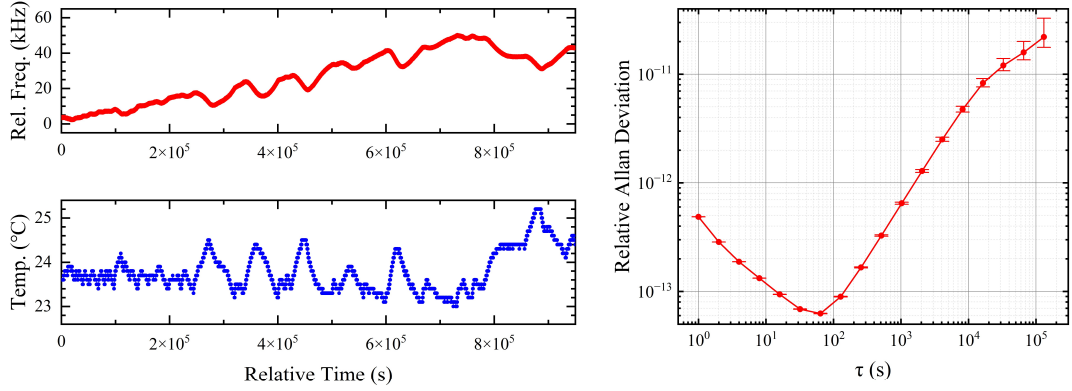


Figure 2.17 Continuous 12-day monitoring of the main laser frequency and laboratory temperature, as well as the Allan deviation of the frequency measurement results.

0.1°C, accuracy $\pm 0.5^\circ\text{C}$) placed near the ultra-stable cavity. By performing a linear fit of the frequency and temperature measurement results and subtracting the long-term drift, it was found that the temperature sensitivity of the ultra-stable cavity is approximately -12.6 kHz/°C, and the drift rate due to stress release is about 0.05 Hz/s. Allan deviation analysis of the frequency measurement results shows a short-term stability of 4.9×10^{-13} , with the best stability reaching 6.3×10^{-14} .

During the experiment, the main laser frequency was continuously monitored and compared over time, allowing corrections to be made to the probe laser frequency. These corrections were then incorporated into the spectral data for fitting. The computers in the two rooms were networked, with the time automatically updated. Several comparisons showed that the deviation was less than 5 seconds, corresponding to a frequency deviation of less than 1 Hz, which can be neglected. This method successfully achieved high-precision measurement of the laser frequency.

2.4.2 Cooling Beam Laser

In this experiment, a 1083 nm wavelength laser diode (EYP-RWE series, Eagleyard) was used, and an ECDL was custom-made with a Littrow configuration. The self-made ECDL was frequency-locked with the main laser through a phase-lock loop to ensure that the phase and linewidth of all lasers were synchronized with the main laser. After locking, the beat signal's full-width at half-maximum was measured to be less than 10 Hz at the spectrum analyzer's limit resolution of 10 Hz^[223].

The cooling optical paths are roughly the same, with the MOT optical path shown in Figure 2.16. For detailed optical paths, refer to the previous doctoral thesis from our group^[229]. After the laser is emitted, it is shaped by a cylindrical lens and split into two paths after passing through an isolator. One path is frequency-locked with the main

laser through beat frequency locking, where the MOT laser is directly locked to the main laser, and the TC and Slower lasers are locked to the MOT laser's beat frequency. The other path is coupled into an optical fiber amplifier. After amplification, the laser is split into several paths and transmitted through optical fibers to the beamline apparatus. At the beamline apparatus, the laser is shaped by lenses to enlarge the beam spot size and then split by a PBS to interact with the beam in both the horizontal and vertical directions.

2.4.3 Pump and Probe Lasers

To pump as many atoms as possible, the linewidth of the pumping laser does not need to be very narrow. Therefore, a distributed feedback (DFB) laser (EYP-DFB series, Eagleyard) with a nominal linewidth of 2 MHz is used. The probe laser uses another narrow linewidth laser (Koheras BoostiK Y10, NKT Photonics). Since the pumping and probe lasers correspond to the $2^3 S_1 - 2^3 P_2$ and $2^3 S_1 - 2^3 P_0$ transitions, respectively, with a frequency difference of approximately 32 GHz, the experiment sets the main laser frequency near the average of these two transition frequencies. Then, a 16.2 GHz sideband is generated using a fiber EOM (Fiber-EOM, PM-0S5-20-PFA-PFA-1083, EOSPACE), and the pumping and probe lasers are frequency-locked to the sidebands using the fiber-EOM. The RF drive for the Fiber-EOM is provided by an RF source, which is referenced to a rubidium clock to ensure frequency accuracy.

2.4.4 Laser Power and Polarization Locking

To ensure the stability of the beam and reduce measurement errors, it is necessary to lock the laser power and polarization. In this experiment, two locking methods are employed. The first method uses a liquid crystal noise attenuator (NEL04A/M, Thorlabs). This device forms a variable attenuator through a liquid crystal waveplate and polarizer, and the internal servo loop is used for feedback control. The liquid crystal noise attenuator requires input linearly polarized light, and a Glan-Taylor prism is added before it to purify the polarization, ensuring the output is also linearly polarized in the same direction. Therefore, after passing through the liquid crystal noise attenuator, both the power and polarization of the laser are locked. The second method uses an acousto-optic modulator (AOM) for locking. As shown in Figure 2.20(a), for the detection optical path, the laser must pass through an AOM before coupling into the optical fiber. At this stage, the zeroth-order light is used, meaning the frequency has not been changed, but the first-order efficiency needs to be adjusted to its maximum to expand

the locking range. After emerging from the optical fiber, the laser is split by a beam splitter (BS) and detected. By locking the signal from the detector and feeding back to the AOM drive voltage, the power fluctuation of the zeroth-order light is compensated. In this process, the AOM drive should be selected for analog control to achieve efficiency adjustment. If a Glan-Taylor prism is added before the BS, it can also lock the polarization. The BS is also temperature-controlled in the experiment to prevent the splitting ratio from being affected by external temperature changes.

Additionally, all optical fibers leading from the optical system to the beam apparatus are polarization-maintaining fibers, which are sensitive to temperature and stress. To ensure polarization stability, a polarization analyzer (SK010PA-NIR) is used for adjustment every 1 to 2 months. Re-adjustment is also necessary after significant temperature changes or when the fiber is moved.

2.5 SCTOP Measurement Method

2.5.1 Background Introduction

2.5.1.1 Suppression of First-Order Doppler Effect

The Doppler effect is typically the most significant systematic error in single-photon spectroscopy measurements. In the spectral experiments of the beam apparatus, to suppress the first-order Doppler effect, the incident direction of the laser is usually optimized such that the laser is as perpendicular as possible to the beam. The first-order Doppler effect can be expressed as:

$$\Delta\omega = \vec{k} \cdot \vec{v} = kv \cos \alpha \quad (2.16)$$

where α is the angle between the laser and the forward direction of the beam. To suppress the Doppler effect, two counter-propagating laser beams are typically used in the experiment to form a standing wave optical field. Since the wave vectors of the two lasers are in opposite directions, the resulting residual first-order Doppler effect is:

$$\begin{aligned} \delta\nu_D &= \frac{1}{2\pi} \frac{\vec{k}_1 \cdot \vec{v} + \vec{k}_2 \cdot \vec{v}}{2} \\ &= \frac{v}{\lambda} \frac{\cos(\alpha + \xi) - \cos(\alpha)}{2} \\ &= v_0 \frac{v \cos(\alpha + \xi) - \cos(\alpha)}{c} \end{aligned} \quad (2.17)$$

where λ is the laser wavelength, and v_0 is the laser frequency. If the two laser beams perfectly overlap and only propagate in opposite directions, the residual Doppler effect

would be zero. However, this is difficult to achieve in practice. The two laser beams usually have a small angle ξ . Since the laser and beam are approximately perpendicular, i.e., $\alpha \sim \pi/2$, the residual first-order Doppler effect can be simplified as:

$$\delta v_D \approx \frac{v}{\lambda} \frac{\xi}{2} = v_0 \frac{v}{c} \frac{\xi}{2} \quad (2.18)$$

Substituting the conditions of this experiment, when the beam velocity is 100 m/s, a 1 μ rad angular deviation corresponds to a residual first-order Doppler effect of 46 Hz.

2.5.1.2 Standing Wave Optical Path Method

In the experiment, it is necessary to design the detection optical path to minimize the angle ξ between the two laser beams, thereby reducing the impact of the residual first-order Doppler effect on the results. In atomic spectroscopy measurements, common methods include prism reflection methods^[143,244-245], interferometer methods^[246-247], cat-eye methods^[145,151,164,177,226-227,248-249], and active fiber-based retroreflector methods^[33,91,250]. Additionally, the introduction of optical cavities is also a common method for obtaining round-trip reflected lasers.

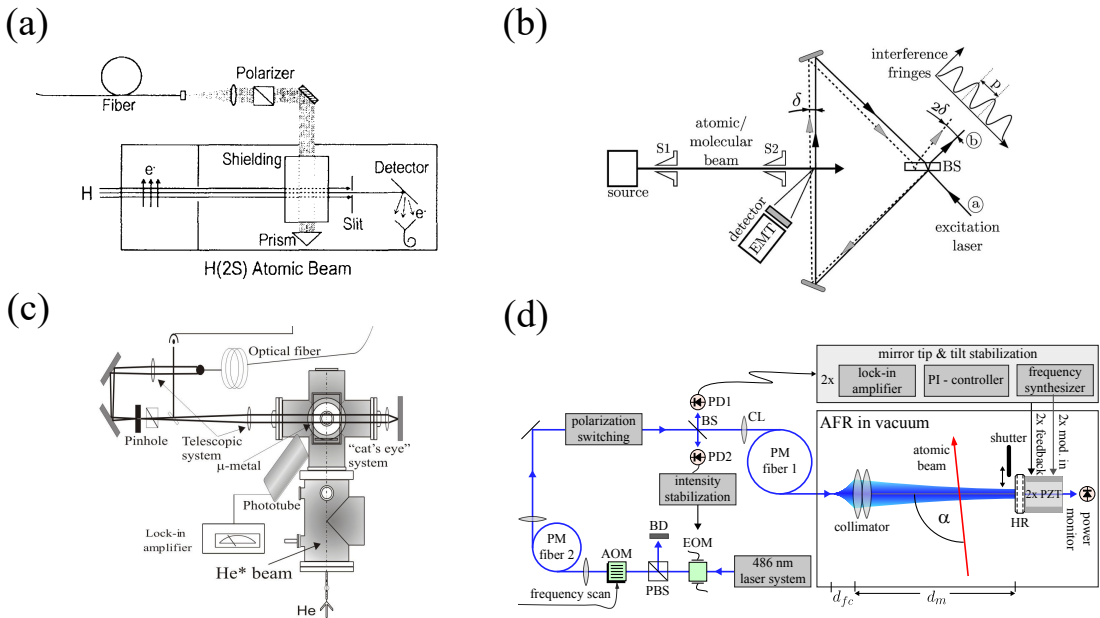


Figure 2.18 Diagram of standing wave optical path methods. (a) Prism reflection method, adapted from Ref.^[244]. (b) Interferometer method, adapted from Ref.^[246]. (c) Cat-eye method, adapted from Ref.^[248]. (d) Active fiber-based retroreflector method, adapted from Ref.^[91].

(1) Prism Reflection Method

As shown in Figure 2.18(a), the prism reflection method uses a corner cube retroreflector. After reflection, the incident light returns along its original direction. During this process, the incident and reflected light have high precision wavefront overlap,

with a combined deviation angle $\xi \sim 3 \mu\text{rad}$. However, the reflected light undergoes a translation, and its polarization rotates. This can lead to atoms being pumped to specific Zeeman sublevels as they pass through the two laser beams sequentially, with the first interaction region pumping the atoms, and the second interaction region probing them with light of a different polarization. This complexity in polarization and pumping causes nonlinear distortions and complicates the analysis of quantum interference^[91].

(2) Interferometer Method

As shown in Figure 2.18(b), the interferometer method uses a Sagnac interferometer to achieve the retro-reflection of the probe laser. The interference fringe spacing is given by $p = \lambda / \sin(2\delta)$, where δ is the deviation angle between the two laser beams. By observing the interference fringes, the two laser beams can be made to counterpropagate and overlap. However, any imbalance between the two laser beams will result in significant residual Doppler effects^[91]. Typically, this method is used in deep ultraviolet wavelength experiments where high-quality optical fibers are not available.

(3) Cat's Eye Method and Active Fiber-based Retroreflector method

The cat's eye method and active fiber-based retroreflector method are two of the most widely used methods in recent years. As the name suggests, the cat's eye method utilizes the principle of a cat's eye, using lenses and mirrors to achieve retro-reflection of the laser. As shown in Figure 2.18(c), earlier versions of the cat's eye method typically required an optical system made of three lenses (usually the “ $f : 2f : f$ ” configuration), where two lenses were located before the incident beam, and one lens and mirror were used to reflect the laser, thereby achieving the retro-reflection of spatially exiting laser from a small aperture^[145,248]. In experiments, the detection region is typically located at the laser waist of this optical system.

With the introduction of high-quality optical fibers, the optical path design of the cat's eye method has been simplified. In experiments, one only needs to observe the effect of re-coupling the laser, after it has been reflected by a lens and mirror, back into the fiber to evaluate the effect of the retro-reflection. After the laser exits, it passes through a collimating lens to be collimated, then interacts with the atomic beam, and on the other side, the laser is reflected by a lens and mirror. Since there are no additional lenses for complex optical designs, the detection region is usually not at the laser waist. However, since the positions of the lens and mirror are adjustable, the laser can still undergo retro-reflection as long as the re-coupling efficiency into the fiber is ensured. In experiments, no influence of the laser waist on the results has been observed so far. Additionally, in the deep ultraviolet wavelength range, where high-quality fibers are still

a limitation, the retro-reflection effect can also be assessed by extending the optical path and observing the reflected laser power at a sufficiently long distance, or by examining the interference fringes of the incident and reflected laser beams^[151,164].

The active fiber-based retroreflector (AFR) method modulates the mirror and observes changes in the re-coupled power intensity into the fiber. The modulated signal is demodulated using a lock-in amplifier and fed back to the mirror mount, ensuring that the re-coupling efficiency remains at its maximum value. The device is shown in Figure 2.18(d). Since only a single mirror is used without lenses for laser reflection, the experiment requires additional design of the collimating lens at the fiber output to ensure that the laser waist is exactly at the position of the mirror. However, this also increases the complexity of the setup. In the latest experimental setups, custom-designed groups of four lenses are used to form the collimating lens group, and extensive optical testing and simulations are conducted to maximize re-coupling efficiency^[250].

While ensuring that the laser beams overlap and are aligned, it is still important to keep the laser as perpendicular as possible to the atomic beam when using the cat's eye and active fiber-based retroreflector methods. In the experiment, the return laser can be blocked to measure the single-sided incident light. By comparing the results of the single-sided light and the retro-reflection, the alignment of the laser and the atomic beam can be verified. However, it should be noted that the power dependence is not the same for the single-sided light and the retro-reflection; typically, the slope of the power extrapolation for retro-reflection is much steeper than for the single-sided light^[226-227,249]. Therefore, the experiment usually requires measuring at several power points for both

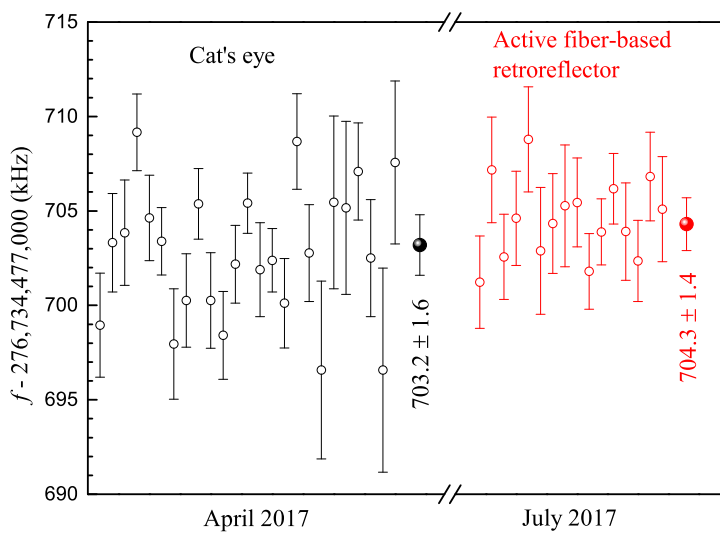


Figure 2.19 Results measured using the cat's eye method and active fiber-based retroreflector method, adapted from Ref.^[177].

single-sided light and retro-reflection, and if the results after power extrapolation are consistent in both cases, it can be concluded that the laser is nearly perpendicular to the atomic beam. In previous experiments in this lab, this range is typically taken as $\pm 20\text{kHz}$ ^[223].

As shown in Figure 2.19, in previous work from our research group, continuous measurements were performed using both the cat's eye method and the active fiber-based retroreflector method . The results indicate that there is no significant deviation between the two methods within the experimental error range^[177].

(4) Cavity Method

Introducing an optical cavity can effectively enhance the laser's retro-reflection and improve wavefront control. However, for atomic spectroscopy experiments, power amplification inside the cavity can lead to power-related systematic errors, such as the ac-Stark effect and saturation effects^[145]. Therefore, it is necessary to limit the input power to the cavity to reduce these errors. In this case, due to the low power of the input light, it is difficult to obtain a high-quality error signal to lock the cavity. Theoretically, another laser, far from the frequency to be measured, can be introduced to stabilize the cavity, but this design would significantly increase the complexity of the system, and when calculating systematic errors such as quantum interference, additional considerations for the locking laser's interference must be made. Additionally, cavity locking often requires the use of a piezoelectric ceramic (PZT) to adjust the cavity length, which may introduce additional magnetic field interference. Therefore, introducing an optical cavity in atomic beam experiments involves complex experimental design to avoid interference from these various factors. In contrast, molecular spectral lines are relatively weak and not sensitive to power, magnetic fields, etc. Cavity-based spectral techniques, such as cavity ring-down spectroscopy (CRDS) and cavity-enhanced absorption spectroscopy (CEAS), have been widely applied in molecular line measurements.

The methods described above all form a standing wave field by using two counter-propagating lasers, with overlapping light paths to cancel the first-order Doppler effect. However, the final spectrum detected in standing wave measurements is the superimposed envelope of the spectra from both sides of the laser interacting with the beam. Since it is difficult to ensure that the laser and beam are strictly perpendicular in the experiment, and the laser experiences power loss when passing through optical elements such as vacuum windows and lenses, the laser power on both sides may not be consistent, resulting in an asymmetric spectral envelope. When fitting the measured spectral envelope with a Lorentzian or Gaussian line shape, the central frequency often shows

a deviation. In previous work from our group, a simulation analysis of this systematic error showed it to be around 0.3 kHz^[177]. If a traveling wave measurement is used instead, with identical probe lasers incident on both sides of the beam, and the spectra on both sides are fitted separately, the final fitting result will not be affected by the power difference between the two lasers. Since the Doppler effects of the two lasers are opposite when the light paths overlap, the frequency shift can be eliminated after averaging. Therefore, using traveling waves for measurements can avoid the frequency shift caused by the difference in peak intensities between the two sides in standing wave measurements. Moreover, in practical measurements using the cat-eye method and active optical feedback method, it was found that the standing wave method has a strong power dependence, with a large slope for power extrapolation, while the slope for power extrapolation is much smaller when the probe laser interacts with the beam on one side. Considering the linear issues present in standing wave measurements and the significant power dependence, using traveling wave measurements can effectively address these two problems. Therefore, designing a precise spectral detection scheme based on traveling waves is expected to overcome the limitations of the standing wave method and improve measurement accuracy and stability.

2.5.2 Experimental Scheme

For traveling wave measurements, the challenge lies in eliminating the Doppler effect. According to formula 2.17, in the traveling wave method, two laser beams still need to be incident from both sides of the beam, and these two beams must overlap precisely. Furthermore, the switching of the laser beams on both sides must alternate to achieve traveling wave detection. Therefore, this experiment proposes using the method of Sequential Counterpropagating Traveling-wave Optical Pulses (SCTOP) for precise spectral detection^[251].

The optical layout of the SCTOP method is shown in Figure 2.20(a). The detection laser is split into two beams (Probe 1 and Probe 2), which are coupled into two 8-meter-long polarization-maintaining fibers. Upon emission, an aspheric lens with a focal length of 8 mm is used to collimate the laser, placing the beam waist near the atomic beam. The waist size was measured to be approximately 1.0 mm using a beam quality analyzer. Before coupling into the fibers, each beam is equipped with an AOM for power locking. After exiting the fiber, the laser's polarization is purified by a GT prism, and then it passes through a BS beam splitter. One beam is directed into a detector for laser power monitoring, and the feedback adjusts the AOM's RF driving signal

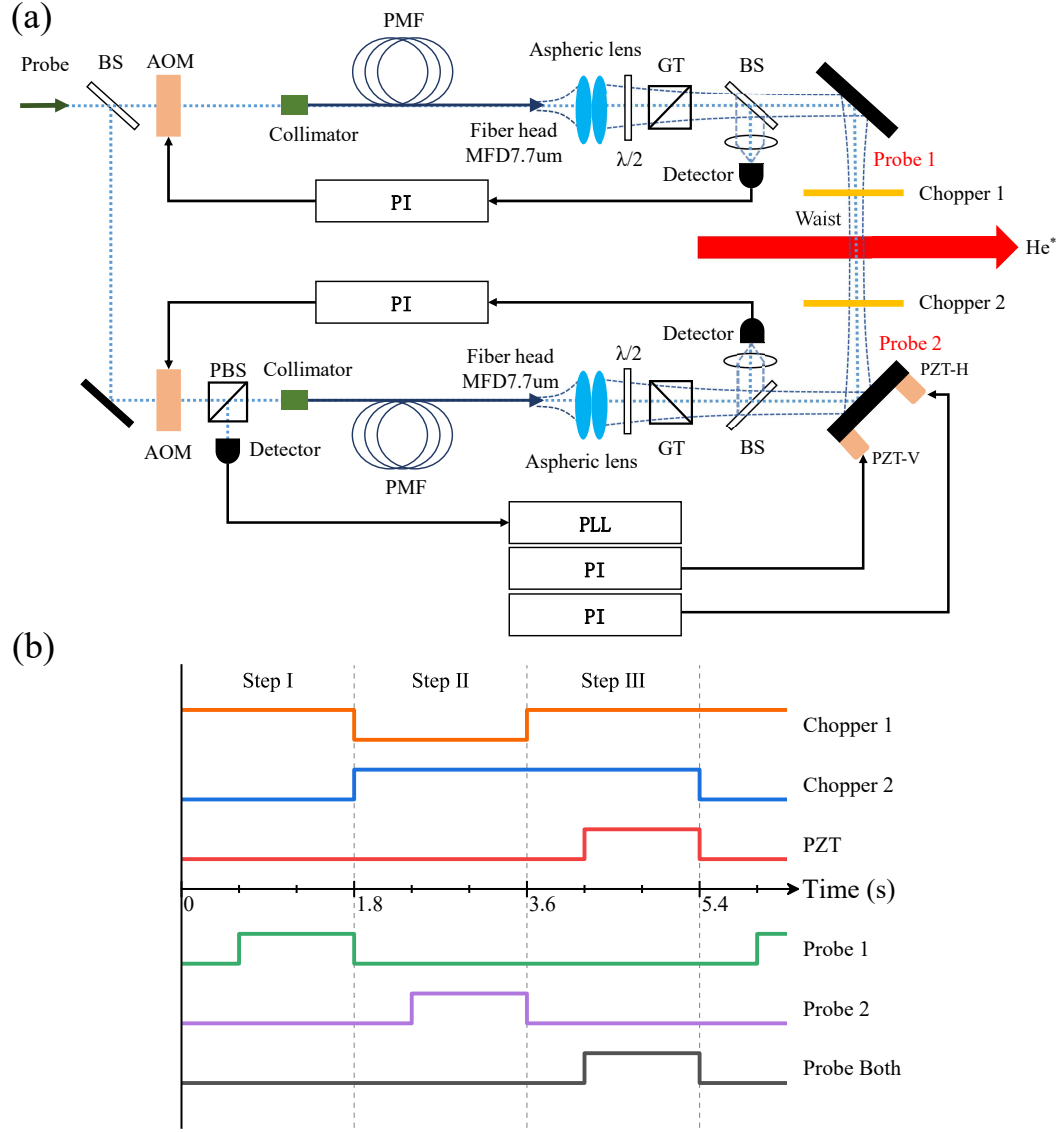


Figure 2.20 Optical layout and timing diagram of the SCTOP method. (a) Optical layout: The detection laser is split into two beams, which interact with the beam after power and polarization locking via AOM. At the same time, a modulation mirror system is used to maximize the coupling efficiency of one-side laser into the other-side fiber to achieve overlap of the optical paths. (b) Timing diagram: high level indicates “on”, low level indicates “off”. The switches of two choppers are controlled to alternately perform traveling wave detection on both sides. The feedback mirror system is activated simultaneously to ensure real-time overlap of the optical path.

strength. This method reduces power drift to less than 0.1 %, with polarization purity better than 1000 : 1. In the experiment, the power is adjusted to the desired value by tuning the half-wave plate ($\lambda/2$) in front of the GT prism and then locked. The overlap of the two laser beams is achieved through fiber re-coupling, with adjustments made to the optical path so that one laser is coupled into the other fiber. Typically, the re-coupling efficiency is greater than 85 %.

For precise control of the laser overlap, the active fiber-based retroreflector method is used. Modulation is applied to two dimensions of a mirror holder in the optical path

(PZT-H and PZT-V in the diagram represent the horizontal and vertical dimensions of the holder, respectively). The re-coupling efficiency of the fiber is monitored, and the voltage signal from the monitoring system is demodulated using a lock-in amplifier (SR830, SRS). The error signal is collected using a data acquisition card (PCI-6259, NI). A digital Proportional-Integral (PI) feedback algorithm locks the error signal to zero and the voltage is fed back to the mirror holder. This method ensures that the fiber re-coupling efficiency is maintained at its maximum value.

As shown in Figure 2.20(b), the experiment uses sequential control of choppers and feedback loops to achieve alternating measurements of the traveling waves from both sides and ensure the overlap of the optical paths. Each measurement cycle is divided into three steps, each lasting approximately 1.8 seconds. Of this, 600 ms is used to change and lock the laser frequency and power, followed by a 200 ms interval to ensure the system has fully stabilized, and finally, 1 second is used to collect the spectral signal. First, Chopper 1 is turned on, and Chopper 2 is turned off, so that only Probe 1 interacts with the atomic beam. Then, Chopper 1 is turned off, and Chopper 2 is turned on, so that only the spectrum of Probe 2 is collected. Finally, both Chopper 1 and Chopper 2 are turned on, and the feedback loop is activated to adjust the PZT voltage on the mirror holder in order to optimize the overlap of the two laser beams. It should be noted that in the first two steps, the voltage on the mirror holder is kept the same as the final voltage value from the previous cycle. The spectrum collected in the final step can be considered as the spectral signal under standing wave conditions.

To avoid interference between the error signals in the horizontal and vertical dimensions of the feedback loop, the modulation signals for the two dimensions are set to 290 Hz, 1.5 V and 310 Hz, 1 V, respectively. These settings are determined by observing the signal-to-noise ratio of the error signals at different frequencies and amplitudes. The output voltage of the feedback loop is kept within ± 1 V to ensure that the PZT always operates within its linear range. During the experiment, it was found that determining the zero point of the feedback loop is very important. Therefore, during the experiment, both choppers are periodically turned off simultaneously, and the signal without laser is collected and averaged to serve as the zero point.

2.5.3 Evaluation of Effectiveness

This experiment evaluates the effectiveness of the SCTOP method in suppressing the Doppler effect by measuring the $2^3S_1 - 2^3P_0$ transition of ${}^4\text{He}$. As shown in Figure 2.21(a), the blue and green triangles represent the spectra measured with the two

traveling waves, with the Lorentzian fitting centers indicated by the corresponding colored vertical lines. The red vertical line represents the average of the two centers. The figure only shows the spectrum for $M_J = +1$, with a similar result for $M_J = -1$. Since the laser is not perpendicular to the atomic beam during the measurement, a noticeable deviation exists between the fitting centers. If a single Lorentzian function is used to fit the overlapping spectra, as in the case of standing wave measurements, the fitted center will significantly differ from the current result. This is the cause of the line-shape distortion due to the asymmetric reflection in the standing wave method^[177].

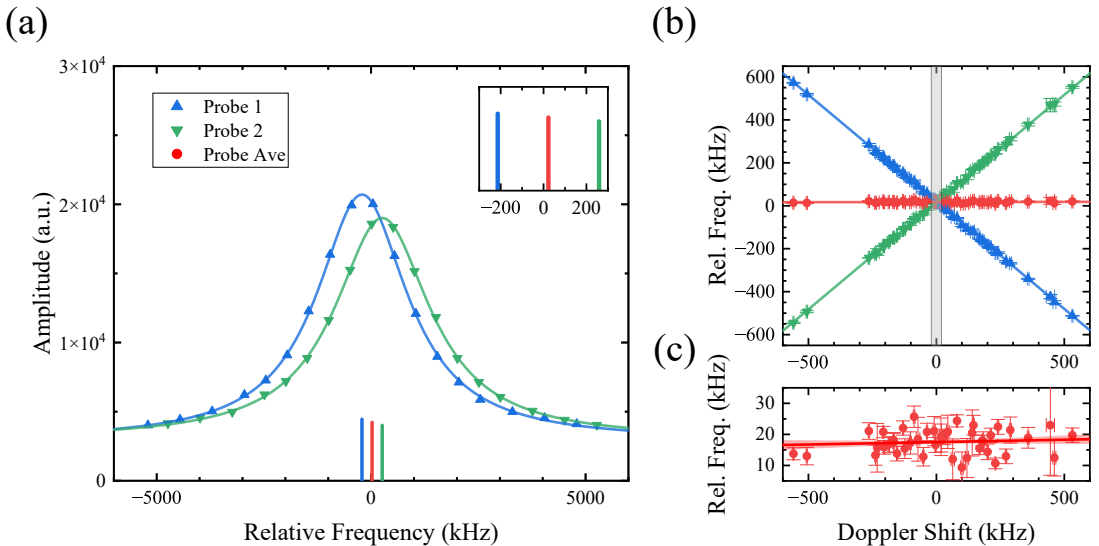


Figure 2.21 (a) Spectra of the two traveling wave measurements and their centers. The red line represents the average of the two spectral centers. (b) Centers of the two traveling wave measurements (green and blue triangles) and their average (red dots) for different incident angles. The horizontal axis represents half of the center difference of the two traveling wave measurements, corresponding to the first-order Doppler effect for the incident angle. The gray region represents the incident angle range from previous experiments using the cat-eye method and active fiber-based retroreflector method. (c) An enlarged view of the average values from panel (b). The red solid line and shaded region represent the linear fit and the 1σ range, respectively. Near zero Doppler, the measurement error is approximately 0.6 kHz.

The SCTOP method allows for measurement over a broader range of incident angles. As shown in Figure 2.21(b), the horizontal axis represents half of the difference between the fitted centers of the spectra measured on both sides, which corresponds to the first-order Doppler effect associated with the incident angle. The blue and green triangles denote the results of the traveling wave measurements from both sides, while the red dots indicate their average, representing the final result of the traveling wave measurement. Figure 2.21(c) provides an enlarged view of the linear fitting results for the traveling wave measurement. Within a Doppler shift range of ± 500 kHz (corresponding to an incident angle deviation of ± 3.5 mrad), the results remain consistent, with an

uncertainty of approximately 0.6 kHz near zero Doppler shift. This demonstrates that the SCTOP method can suppress the Doppler effect by three orders of magnitude. In contrast, the standing wave method requires the laser to be as perpendicular to the atomic beam as possible. In previous experiments, the allowable range of incident angles corresponded to a Doppler shift of approximately ± 20 kHz, as indicated by the gray shaded region in Figure 2.21(b). By adopting the SCTOP method, the strict requirement on the incident angle is significantly relaxed, thereby reducing the experimental difficulty.

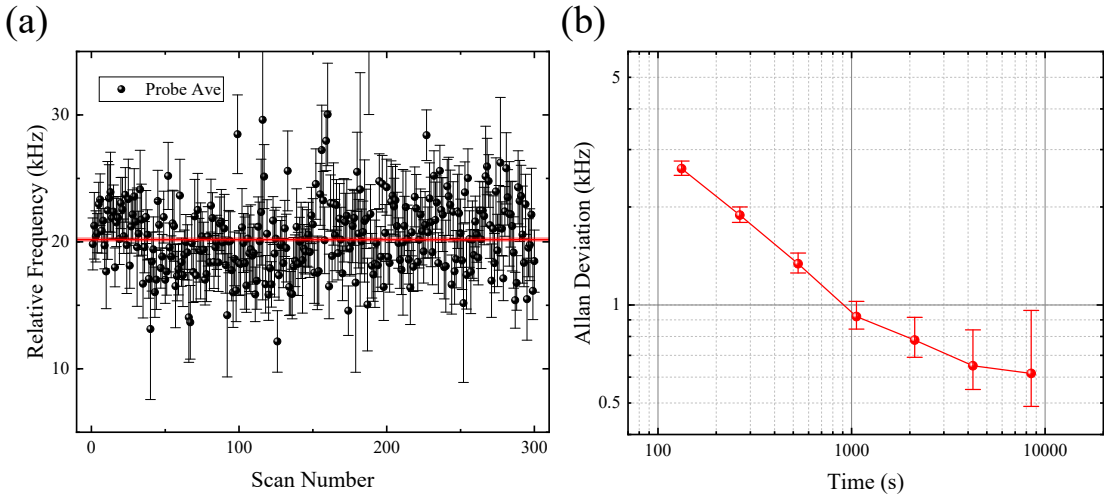


Figure 2.22 (a) Experimental results from continuous measurements over approximately 11 hours. (b) Allan variance analysis of the data in (a).

Under the above experimental conditions, this experiment enables long-term measurements. The results of continuous measurements over approximately 11 hours are shown in Fig.2.22(a), where each data point corresponds to the center of a single spectrum collected within 130 s. The Allan variance is presented in Fig.2.22(b), showing that after 1000 s, the statistical uncertainty can be averaged to below the 1 kHz level.

As mentioned above, the overlap of the two laser beams is ensured through mirror mount feedback. However, the position of the laser beam waist and wavefront properties may also influence the experimental results. As shown in Fig.2.23, to evaluate these effects, a translation stage was used to adjust the position of the collimating lens in one optical path, thereby altering the fiber re-coupling efficiency, followed by spectral measurements. In the figure, the black squares and red circles represent the final averaged results when the lens was moved closer to and farther from the fiber tip, respectively. The red solid line and shaded area indicate the average value and 1σ range for all cases where the re-coupling efficiency exceeded 80 %. When the re-coupling efficiency dropped below 75 %, a noticeable deviation was observed. However, when the efficiency exceeded 80 %, the experimental results remained within the experimen-

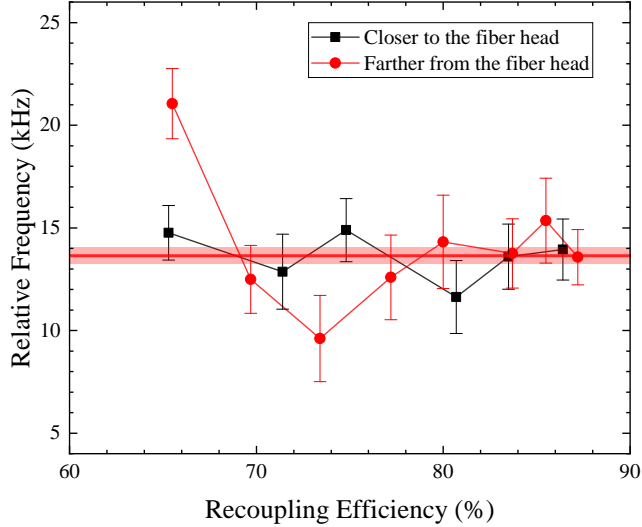


Figure 2.23 Relationship between fiber recoupling efficiency and frequency variations. Black squares and red dots represent measurements when the lens is moved closer to and farther from the fiber tip, respectively. The red solid line and shaded region indicate the average value and 1σ range for all results with recoupling efficiencies above 80 %.

tal uncertainty. During the experiment, the incident angle was adjusted daily, and the re-coupling efficiency was remeasured to ensure that the adjusted efficiency remained above 85 %.

According to Eq.2.18, the residual Doppler effect is proportional to the beam velocity. Therefore, in the experiment, the effectiveness of the SCTOP method in suppressing the Doppler effect can be evaluated by varying the beam velocity. As shown in Fig.2.24, the $2^3S_1 - 2^3P_0$ transition was measured using the SCTOP method within

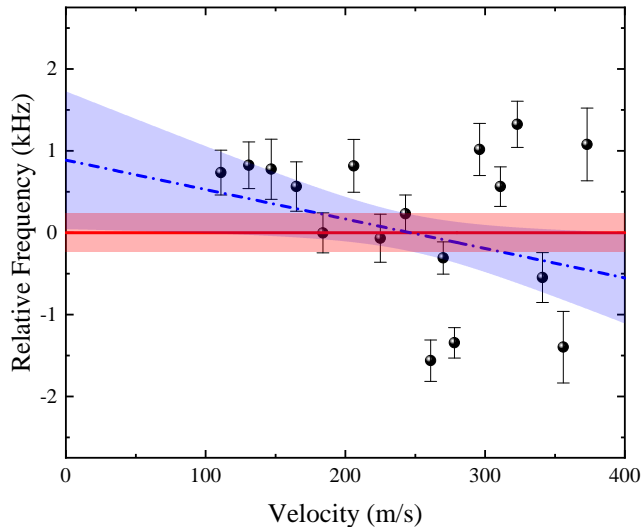


Figure 2.24 Measurement results at different beam velocities. The red solid line and shaded region represent the average value and its uncertainty range, with an error of 0.22 kHz. The blue dashed line and shaded region indicate the linear fit result and its uncertainty, with an intercept of +0.89(82) kHz and a slope of -0.0036(32) kHz m⁻¹ s. For a detailed discussion of the errors, see Section3.2.

a velocity range of 100~400 m/s. By performing both constant and linear fittings on these measurement results, the linear fit yields a slope of $-0.0036(32)$ kHz m $^{-1}$ s, corresponding to a residual angle of $\xi \approx 7.8 \pm 6.9 \mu\text{rad}$, which is consistent with the levels achieved using the cat's-eye method and the active fiber-based retroreflector method. The deviation between the linear fit and the constant fit is $+0.89(82)$ kHz, indicating that the dominant error term in previous work, namely the first-order Doppler effect, has been reduced to the sub-kHz level. This result demonstrates that the SCTOP method effectively aligns the two optical paths and significantly suppresses the influence of the first-order Doppler effect on the measurement results.

In previous experiments, it was found that the $2^3S - 2^3P$ transition in standing-wave measurements exhibits a strong dependence on laser power^[177], necessitating a linear extrapolation of the power to zero. However, the frequency-power relationship is not strictly linear at high power levels, requiring measurements at lower power for accurate extrapolation. As shown in Fig. 2.25(a), measurements were conducted using both traveling-wave and standing-wave configurations at different power levels, yielding slopes of $+9.7$ kHz/ μW and -59 kHz/ μW , respectively. Evidently, the power dependence in the traveling-wave case is significantly weaker than that in the standing-wave case. By repeating the experiment at different beam velocities, it was observed that as the beam velocity decreases, the absolute value of the standing-wave power-extrapolation slope increases, whereas the traveling-wave method remains largely un-

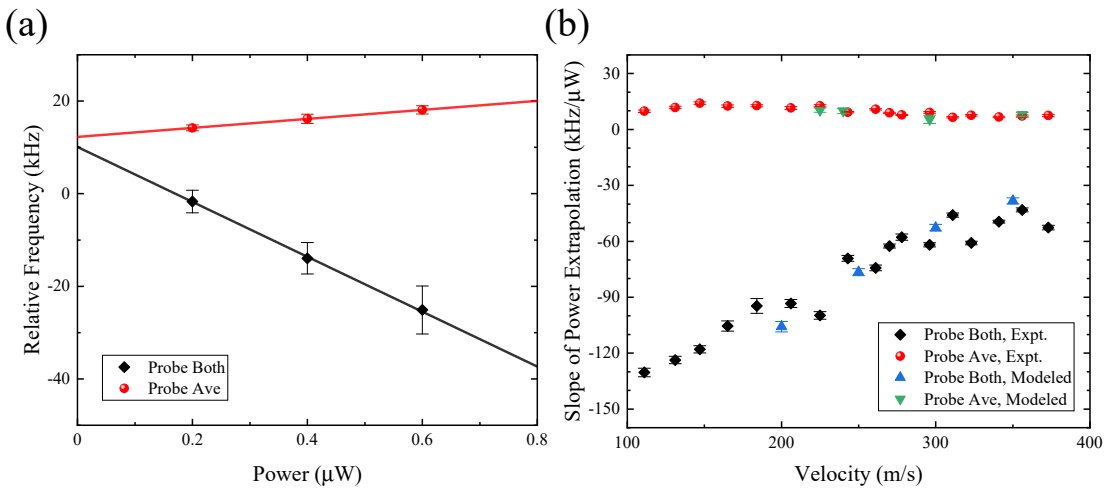


Figure 2.25 (a) Power dependence of the traveling-wave and standing-wave results. The beam velocity is 250 m/s, with red circles and black squares representing the measurements for the traveling-wave and standing-wave cases, respectively. (b) Power dependence of the traveling-wave and standing-wave results at different velocities. Each point represents the slope obtained from a linear fit of frequency versus power at the corresponding velocity. Green and blue triangles indicate the power dependence of the traveling-wave and standing-wave cases, respectively, as obtained from Monte Carlo Wave Function (MCWF) simulations.

changed, as illustrated in Fig. 2.25(b). Furthermore, our group employed the Monte Carlo Wave Function (MCWF) method to simulate both traveling-wave and standing-wave scenarios, with simulation results aligning well with experimental observations. This finding indicates that the SCTOP method effectively reduces systematic errors arising from the probe laser power.

2.6 Summary and Discussion

This chapter introduces the metastable helium atomic beam apparatus, the optical system, and the newly developed detection optical path method. The following summarizes and discusses the improvements in the experimental setup and system in this work.

Compared with previous beam setups, the current apparatus incorporates a Zeeman decelerator to cool the longitudinal velocity of the atomic beam. By adjusting experimental parameters such as laser detuning, the beam velocity can be continuously tuned within the range of 50~450 m/s. Conducting measurements at different velocities and extrapolating the results to zero velocity significantly reduces the influence of the Doppler effect. Additionally, by increasing the pumping speed of the source chamber and optimizing the gas mixture during radio-frequency discharge, the atomic beam intensity at the source chamber has been enhanced to approximately 4.8×10^{14} atoms/s/sr. The high-brightness and stable beam source further improves the signal-to-noise ratio of the measured spectra.

Regarding the optical system, an ultra-stable cavity with a finesse of approximately 300,000 has been employed, with optimizations in temperature control, vibration isolation, and frequency locking, further enhancing frequency stability. Additionally, the reference source for the optical frequency comb has been upgraded to a hydrogen maser, reducing errors associated with the frequency standard.

To address issues such as lineshape distortion and power dependence in standing-wave measurements, this work proposes a new detection optical path method that utilizes a traveling wave instead of a standing wave. Compared with commonly used standing-wave detection methods such as the cat's eye method and active fiber feedback, this approach not only effectively eliminates the Doppler effect but also expands the available measurement angles and significantly reduces the influence of detection laser power on experimental results.

These improvements in the experimental setup and system effectively mitigate the

most significant systematic error in previous work—the Doppler effect—while enhancing overall system stability. Furthermore, the standing-wave measurement issues have been specifically addressed. These advancements and optimizations provide a solid foundation for high-precision spectroscopic measurements.

Chapter 3 ${}^4\text{He}$ Atom $2^3S - 2^3P$ Transition Measurement

This chapter introduces the measurement method, error analysis, and the latest results for the $2^3S - 2^3P$ transition of ${}^4\text{He}$. The chapter also focuses on discussing a newly discovered systematic error effect in the experiment—the post-selection effect. Due to the post-selection effect, the previous measurement results for the $2^3S - 2^3P$ transition in our group required significant corrections. After theoretical simulations and corrections, the adjusted results were found to be consistent with the measurements obtained in this experiment, where the post-selection effect was absent. Furthermore, since the same apparatus was also used for measurements of the 2^3P_J interval, the interval measurements were verified to ensure that the post-selection effect did not significantly affect the previously obtained interval measurement results.

3.1 Measurement Method

Chapter 2 has detailed the experimental setup. After cooling, trapping, and optical pumping, the atoms in the detection region are in the $M_J = \pm 1$ states. After interaction with the probe laser, there is a 1/3 probability that the atoms will return to the $M_J = 0$ state. These atoms are detected and contribute to the signal. Due to the applied bias magnetic field in the detection region, two spectral peaks can be observed when scanning the laser frequency, corresponding to the transitions $2^3S_1(M_J = -1) - 2^3P_0(M_J = 0)$ and $2^3S_1(M_J = +1) - 2^3P_0(M_J = 0)$, respectively. The following section will provide a detailed description of the spectral scan timing and data processing methods.

3.1.1 Spectral Scan Timing

Since the spectrum in this experiment is in the form of “frequency-atom number,” any fluctuation in the beam intensity can affect the spectral center. To mitigate the impact of long-term drift in beam intensity on the frequency center, a “four-point random scan” method is used for spectral scanning. Before the measurement, the centers of the two peaks are roughly set, denoted as f_{c1} and f_{c2} , and a series of deviation values are defined, such as $\delta f = 0.2, 0.5, 0.75, 1, 1.25, 1.75, 2.5, 3.75$ MHz, etc. These deviation values ensure a complete scan of the spectrum. During the scanning process, for each δf value, there are four frequency points corresponding to $f_{c1} - \delta f, f_{c1} + \delta f, f_{c2} - \delta f, f_{c2} + \delta f$, and the order of scanning these four frequencies is

randomly determined. After scanning these four frequency points, the next δf value is selected, and the process is repeated until the entire δf sequence is scanned, thus completing one full spectrum scan. Subsequently, a Lorentzian fit is performed within the acquisition program, and the two center values of the spectrum, fc'_1 and fc'_2 , are iteratively updated to the next spectrum, while the deviation sequence remains unchanged. Through this method, the initial center deviations of the two peaks are iteratively corrected, ensuring that both complete spectral peaks can be consistently scanned. Assuming that the long-term variation of the beam intensity corresponds to a 1 Hz/s change in laser frequency, then in a typical single-direction sequential scan over approximately 100 s for one spectrum, the spectral center would shift by about 100 Hz. In contrast, using the “four-point random scan” method, after acquiring enough spectra, the system error contribution caused by this method will be less than 1 Hz, which is almost negligible.

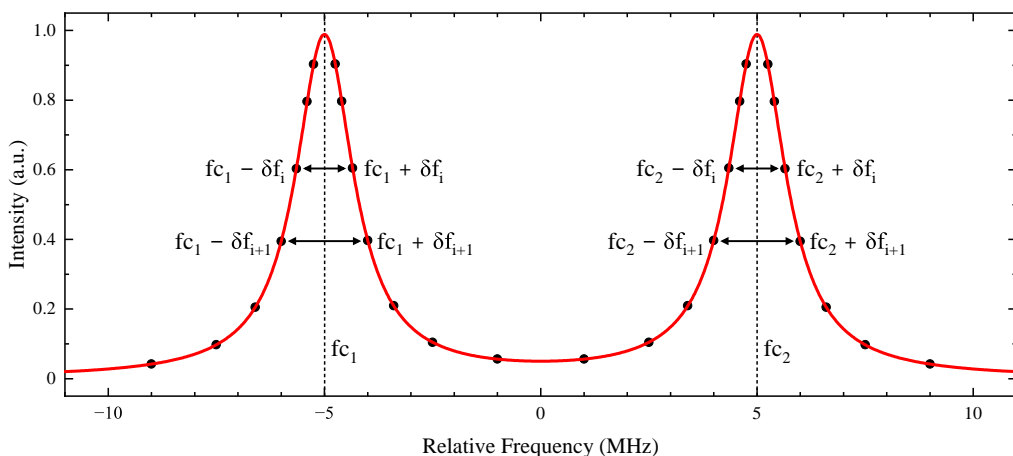


Figure 3.1 Diagram of the four-point random scan method. For each δf value, four frequency points on the two spectral peaks are randomly arranged for scanning. This method effectively avoids the influence of long-term drift in beam intensity.

After using the SCTOP method, three spectra need to be simultaneously acquired, corresponding to the spectra when the two single-side probes and the two-side probe are both applied. Therefore, each δf value corresponds to 12 frequency values. In the experiment, the switching sequence “Probe 1 - Probe 2 - Probe Both” is prioritized, and the four frequency values under each optical path condition are still randomly arranged. For each incident angle and power condition, 9 spectra will be measured. Since the SCTOP method requires some time for feedback locking, the first spectrum data is discarded, and 8 spectra are retained for further processing under each condition. At each optical path angle, three power points are measured, and the measurement sequence of power points is random. When changing the power, the mirror frame voltage does not

need to be reset, but when changing the optical path angle, the mirror frame voltage must first be reset, followed by the change in the optical path angle. In the experiment, the horizontal one-dimensional adjustment of the last mirror frame before the Probe 1 incidence is performed to change the angle between the optical path and the beam. Then, the mirror frame for the Probe 2 optical path is adjusted to achieve the highest re-coupling efficiency. The feedback program is then used to obtain the initial value of the mirror frame voltage, which is substituted into the measurement program for spectral measurement.

3.1.2 Spectral Data Processing

After the experiment, all the data will be grouped and processed. For each frequency point, the frequency will first be calibrated using the optical frequency comb. Then, a Lorentzian fit (detailed derivation in Section 3.4.4) is applied to obtain the peak center. The average of the positive and negative peaks is then taken to determine the spectral center, and the first-order Zeeman effect is eliminated by subtraction to obtain the magnetic field strength. Finally, corrections for second-order Zeeman effects and other systematic errors are applied to obtain the final result.

At each beam velocity, three power points are measured at different optical incidence angles. Therefore, there are two possible data processing methods. One approach is to first perform a power extrapolation for the data at each optical incidence angle, then extrapolate the results to zero power and perform angle extrapolation. The other approach is to first perform angle extrapolation for the data at each power point for all optical incidence angles, and then perform power extrapolation to the zero-Doppler position for the results of angle extrapolation. The final results from both data processing methods are consistent.^① Finally, the results from all velocity points are compiled, and system errors related to velocity, such as second-order Doppler effects and quantum interference effects, are corrected for each velocity point. Then, a velocity extrapolation is performed to obtain the final result. This approach avoids the influence of velocity-related systematic error effects on the evaluation of the SCTOP method's suppression of Doppler effects.

^①In each fitting process, if the Reduced Chi-Sqr (RCS) ≥ 1 , the result is corrected by multiplying by $\sqrt{\text{RCS}}$; if RCS < 1 , no correction is made. In this thesis, all fitting error tables in the figures show the raw fitting results, whereas the fitting results mentioned in the text are the corrected ones.

3.2 Measurement Results

In this experiment, the SCTOP method was used to measure the $2^3S_1 - 2^3P_0$ transition of ${}^4\text{He}$ within a velocity range of $100 \sim 400$ m/s. At each velocity point, measurements were made at three different power points for various laser incidence angles. The laser incidence angle was controlled within the Doppler Shift $< \pm 150$ kHz range. Power points were selected as follows: for the velocity range of $100 \sim 250$ m/s, power values of 0.2, 0.4, and 0.6 μW were chosen, and for the velocity range of $250 \sim 400$ m/s, power values of 0.3, 0.6, and 0.9 μW were selected for measurements. Below, the measurement results at 260 m/s are used as an example for detailed explanation.

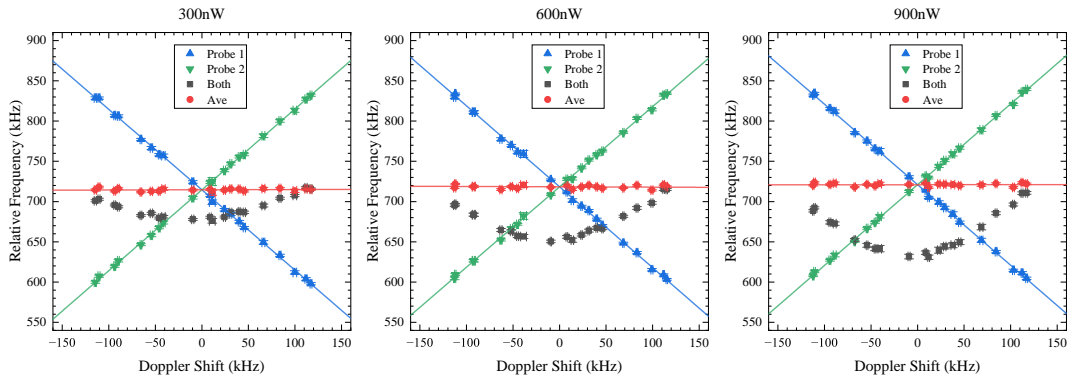


Figure 3.2 Summary of measurement results at three power points for a velocity of 260 m/s. From left to right, the measurement results for power values of 0.3, 0.6, and 0.9 μW are shown.

At this velocity, all the measurement results are summarized in Figure 3.2. Two data processing methods can be applied to these results. One method is to first perform angle extrapolation at each of the three power points, and then proceed with power extrapolation. The resulting data is shown in Figure 3.3(a). The other method is to first perform power extrapolation at each incidence angle, followed by angle extrapolation, as shown in Figure 3.3(b). Comparing these two methods, the results are essentially consistent. Since the standing wave mechanism is quite complex and direct angle extrapolation fitting is not feasible, the first method is applied only to traveling wave results. In the second method, although power extrapolation has been performed for each angle, the power points selected during the experiment were chosen based on traveling wave measurements. The powers of 0.3, 0.6, and 0.9 μW chosen in the experiment likely already fall within the nonlinear range of the standing wave. Therefore, even though the standing wave results at each angle in Figure 3.3(b) are distributed within a small range after power extrapolation, the results of the forced linear fit, which cannot exclude the interference of power, are not meaningful.

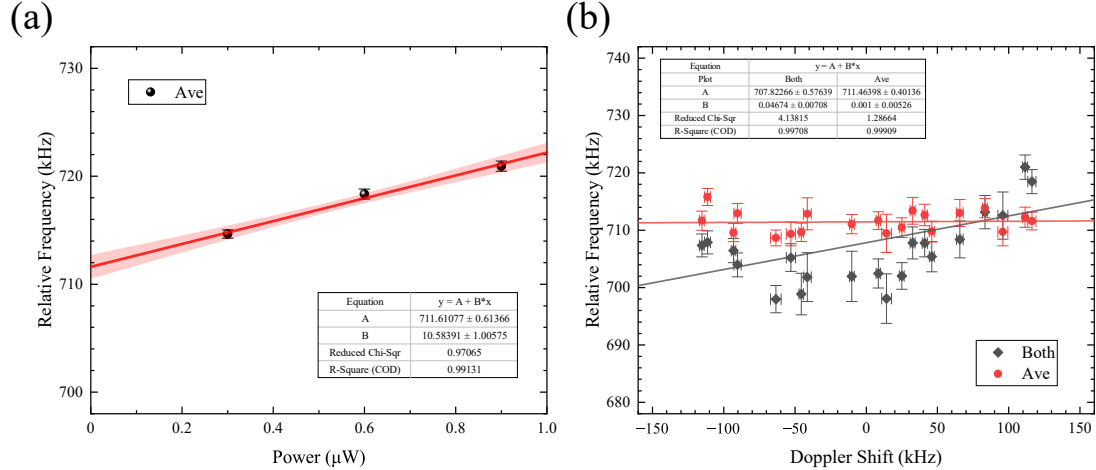


Figure 3.3 (a) Results obtained by first performing angle extrapolation for the three power points at 260 m/s, followed by power extrapolation. (b) The same raw data as in (a), where power extrapolation is performed for each power point at each laser incidence angle, followed by angle extrapolation.

After applying the above processing to the results at all velocities, the final results are summarized in Figure 3.4. A constant fit and a linear fit were performed on these results. The central value of the constant fit is the final result, with an intercept error of 0.22 kHz representing the statistical error, and the intercept error of 0.82 kHz from the linear fit corresponds to the residual first-order Doppler effect. The slope of the linear fit can be converted into a residual first-order angle, which is used to evaluate the effectiveness of the first-order Doppler elimination, as discussed in Section 2.5.

Considering that the Doppler cancellation effect is sufficiently effective in this

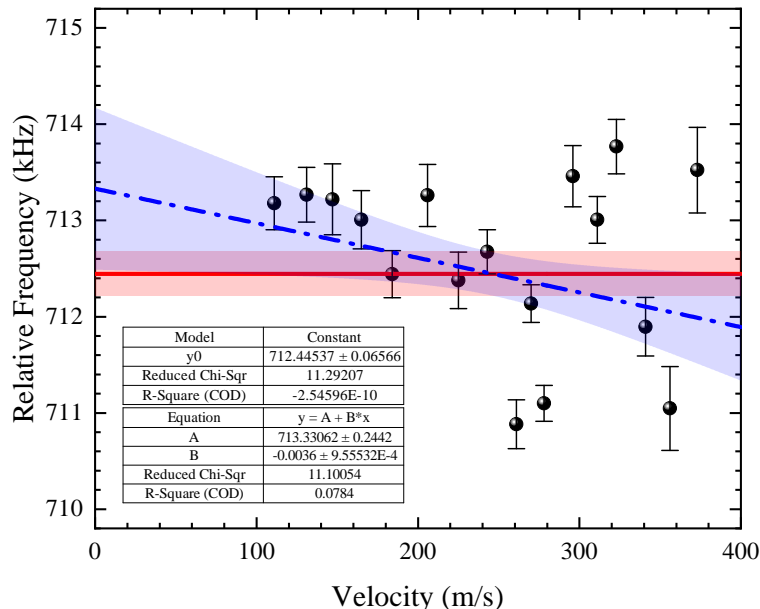


Figure 3.4 Summary of results at all velocities. The red solid line and the blue dashed line represent the results of constant fitting and linear fitting, respectively. The shaded areas corresponding to each color represent the 1σ confidence intervals of the fits.

experiment, the results from all velocities, with power extrapolated for each incident angle, are compiled, totaling 397 data points, as shown in Figure 3.5. After performing angle extrapolation on these results, the obtained results are consistent with the final results mentioned above. Furthermore, a frequency analysis of these results yields a Kolmogorov-Smirnov test result of $P \approx 0.16 > 0.05$, indicating that the data follows a normal distribution and confirming that the experimental data are reliable.

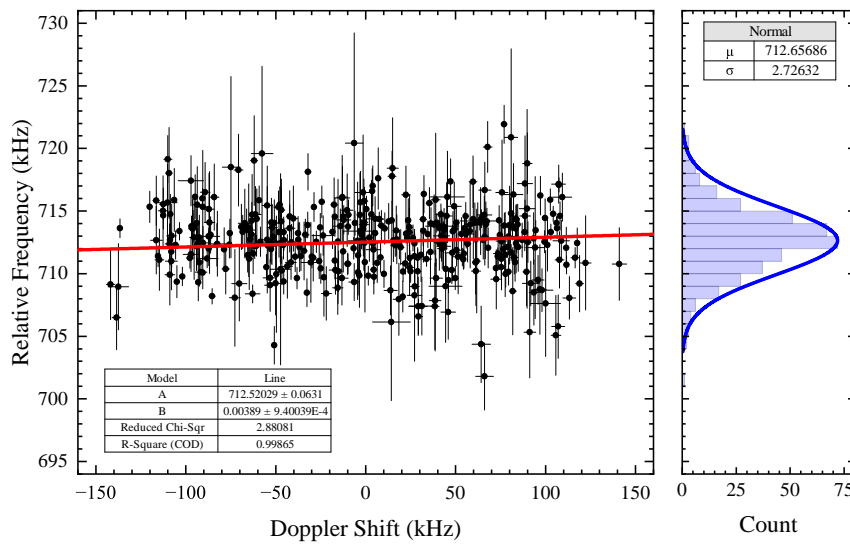


Figure 3.5 Summary of results for all velocities and incident angles after power extrapolation and frequency distribution chart.

Considering that power and incident angle may vary during the experiment, multiple processing methods were used and compared to ensure the reliability of the experimental results. In the experiment, the power at both sides was measured using a power meter, and the power locking level was recorded simultaneously with the spectrum. All power monitoring levels were summarized, and a fitting line for the average variation was derived. This fitting function was then used to correct the power for each experimental point, which was then re-fitted into the original measurement results. The results corrected in this way were consistent with the uncorrected ones. Moreover, due to external interference during the experiment, frequency jumps or instability in the RF discharge mode caused unstable beam signals, leading to jumps in some spectral signals and increasing the fitting error. Based on the fitting frequency errors, linewidths, and residuals, the spectra containing jumps were entirely removed, and the results after this processing were consistent with the results before any spectra were removed. To avoid issues in the fitting or processing programs, different software and programs were tried for fitting. Due to the large amount of data, fitting with multiple Origin files and then summarizing may lead to loss of data precision, so using Mathematica for unified

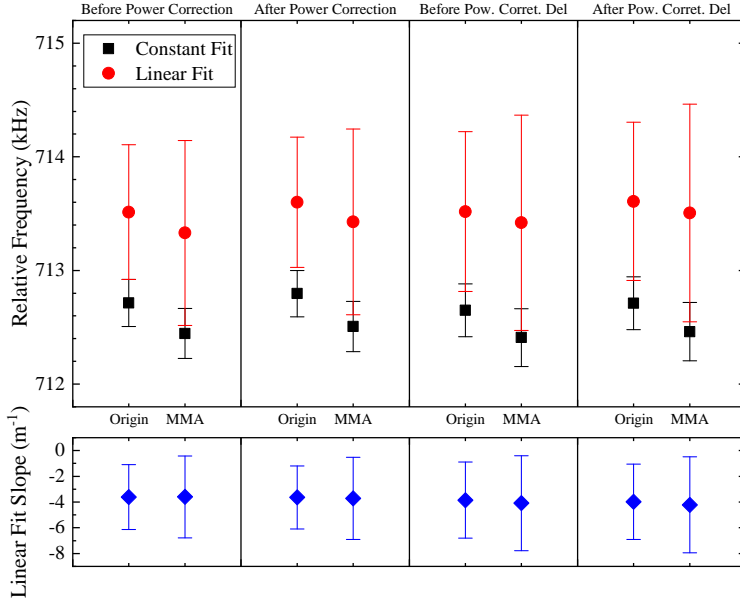


Figure 3.6 Summary of fitting results under different processing methods. From left to right, the four columns represent: raw data, results after power correction, raw data after point removal, and results after point removal and power correction. The data in each column were processed using Origin and Mathematica programs.

processing was found to be more reliable. Additionally, when storing files, sufficient digit precision should be specified to avoid loss of accuracy. After comparison, the final results processed using Origin and Mathematica were generally consistent. The results of the various processing methods are summarized in Figure 3.6. The final results of this experiment were chosen using the Mathematica-processed raw data without power correction or spectrum removal.

3.3 Post-Selection Effect

In precision spectroscopy experiments, the evaluation of systematic errors is crucial. Over many years of development, a relatively complete system for evaluating systematic errors has been established. For common systematic errors, such as the Doppler effect and Zeeman effect, these can be assessed by changing experimental conditions such as beam velocity and magnetic field strength. However, for some unavoidable effects, such as the linearity issues caused by unequal laser powers on both sides in standing wave measurements, they are typically estimated and corrected through methods like simulation calculations. However, as experimental techniques and measurement precision continue to improve, new systematic error effects are also constantly being discovered. In this experiment, by further studying the impact of atomic distribution in the beam on the frequency results, a new systematic error effect was found—“post-

selection effect.” This effect originates from structures such as slits or small holes in front of the detector, leading to the failure to collect all the signals that interacted with the laser or microwave. Since such structures are widely present in precision spectroscopy experiments, many experiments require an evaluation of the potential impact of this effect on the results.

3.3.1 Light-Force-Induced Shift Effect

In previous experiments conducted by our research group, the interaction of the standing wave probe light field with the atomic beam was observed, resulting in a shift in the spectral center, known as the Light-Force-induced Shift (LFS)^[178]. During further investigation of the LFS effect, this experiment discovered a frequency shift induced by the post-selection effect. Therefore, the following will first provide a brief introduction to the LFS effect.

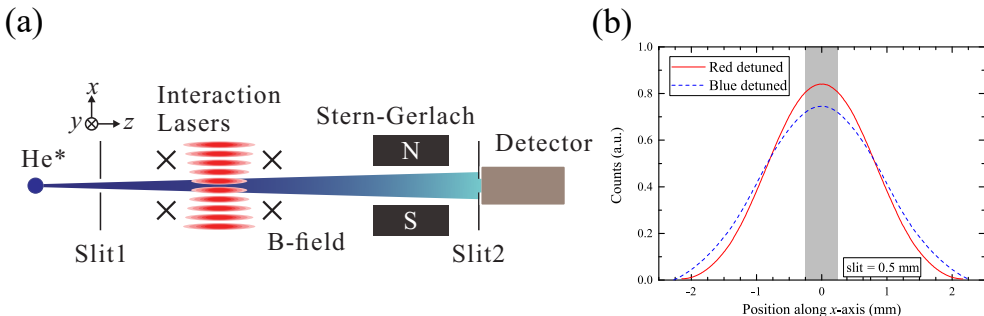


Figure 3.7 (a) Schematic diagram of the apparatus used to investigate the LFS effect. Two slits are located before the probe light interaction region and in front of the detector. The probe light, which is reflected back and forth, forms a standing wave field that interacts with the atomic beam. (b) Simulation of the change in the number of atoms when the probe laser is detuned red or blue. The shaded area represents the atoms that can pass through the 0.5 mm wide slit in front of the detector. Adapted from reference^[178].

As shown in Figure 3.7(a), a pair of 0.5 mm wide slits is used in the experiment to intercept the atomic beam, reducing the Doppler effect. Before passing through the first slit, the atomic beam is pumped to the $M_J = \pm 1$ state. Due to the deflection of the Stern-Gerlach magnet, there is no atomic counting signal at this point. Only when the atomic beam interacts with the probe laser can it be repopulated into the $M_J = 0$ state and detected. The probe light is located between the two slits, and in the experiment, either the cat-eye method or active optical feedback is used to make the probe light reflect back and forth, forming a standing wave field, further reducing the Doppler effect. If only spectral detection were present in the experiment, when scanning the laser frequency, the atomic count should be the same when red or blue detuned to the same frequency. However, it was found in the experiment that the spatial selection effect of the slits in front of the detector could influence the central frequency of the spectrum. According

to Equation 2.4, when the probe laser frequency is red-detuned, the atomic beam will be focused after passing through the probe light standing wave field; whereas, when blue-detuned, the beam will slightly diverge. Since there are slits in front of the detector, the proportion of the focused and divergent beam signals generated is not the same, as shown in Figure 3.7(b).

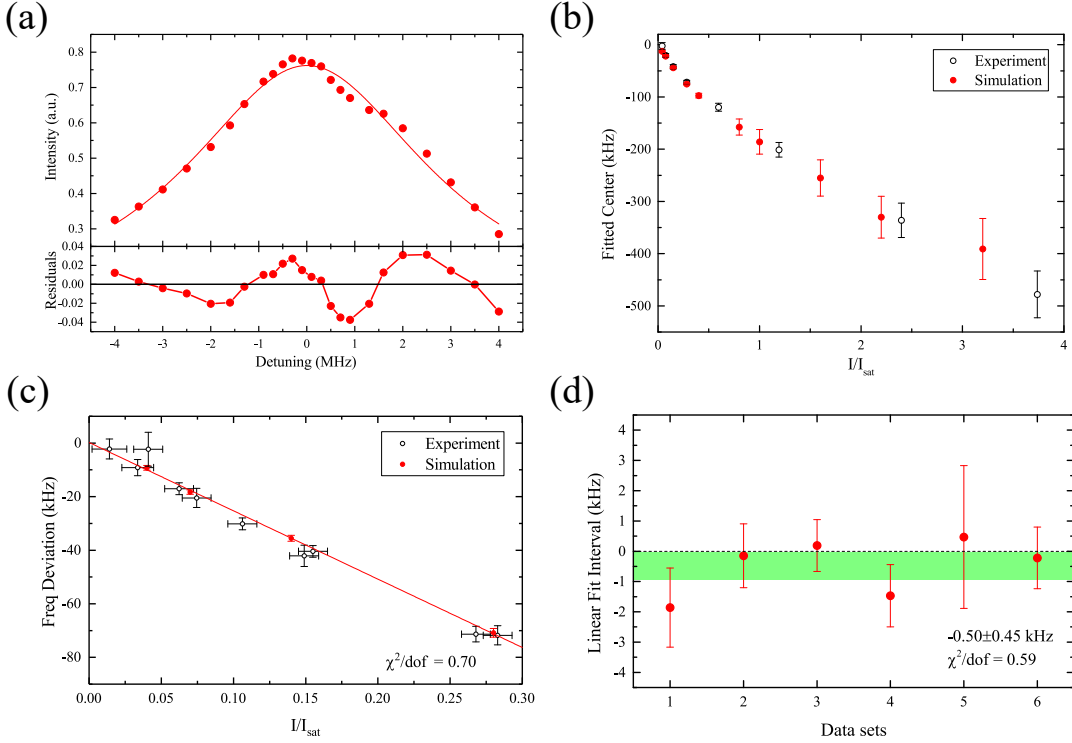


Figure 3.8 (a) Spectral simulation diagram at twice the saturation intensity and its fitting residuals. (b) Shift of the spectral fitting center at different light intensities. (c) Power linear extrapolation result at lower power ($I/I_{\text{sat}} < 0.3$). (d) Effect of the LFS effect averaged from multiple simulations. The black and red dots in the figure represent experimental data and simulation results, respectively. Adapted from Ref.^[178].

Due to this spatial selection effect, the spectrum obtained by scanning the frequency is not symmetric on both sides, as shown in Fig.3.8(a). The higher the power, the more pronounced this asymmetry effect becomes, and the corresponding spectral center shift also becomes larger, as shown in Fig.3.8(b). To avoid saturation effects at high powers, the power conditions selected for measurement during power extrapolation in the experiment are $I/I_{\text{sat}} < 0.3$. As shown in Fig. 3.8(c), all results, within the error range, are mostly located near the fitted line, so it can be concluded that power extrapolation at low power is feasible. After averaging multiple simulations, the deviation caused by the LFS effect is approximately $-0.50 \pm 0.45 \text{ kHz}$.

Considering that the essence of the LFS effect is that the standing wave light field alters the transverse distribution of the atomic beam, and the slit further selects the transverse distribution of the beam, increasing the slit width helps alleviate the LFS effect,

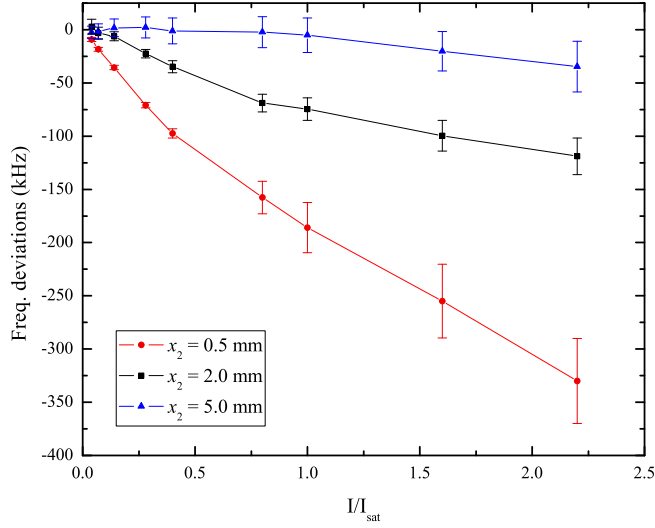


Figure 3.9 Results of simulated spectral center shift for different slit widths in front of the detector. From Ref.^[178].

as shown in Fig. 3.9. Based on the simulation results, it can be reasonably inferred that when there is no slit in front of the detector, the LFS effect will no longer exist. However, since the atomic beam spectral measurement requires the transverse distribution of the atomic beam to be sufficiently narrow, it was not possible to achieve both conditions with the current setup. To address this issue, a new setup was designed with two sufficiently narrow slits in front of the probe light interaction region to obtain a beam with a narrower transverse velocity distribution, while no slits were added in front of the detector to avoid the LFS effect. In subsequent experiments, the spatial effects present in the atomic beam experiment were further investigated by adjusting the positions of the three slits and the laser incidence angle.

3.3.2 Experimental Phenomenon

As shown in Figure 3.10, the new apparatus employs a double-slit structure in the detection light interaction region, with both slits having a width of 0.3 mm. Additionally, there is another slit, 0.5 mm wide, placed in front of the detector to measure the distribution of the atomic beam. These three slits are mounted on a vacuum displacement stage, allowing them to move along the x -direction and be completely retracted from the path of the beam, thus enabling the investigation of experimental phenomena under different beam distributions. For convenience, these slits will be referred to as Slit 1, Slit 2, and Slit 3.

Initially, the atoms are optically pumped to the $M_J = \pm 1$ states. At this stage, no signal is detected by the detector due to the deflection of the atomic beam by the Stern-Gerlach magnet. Only after the atoms interact with the detection laser will they

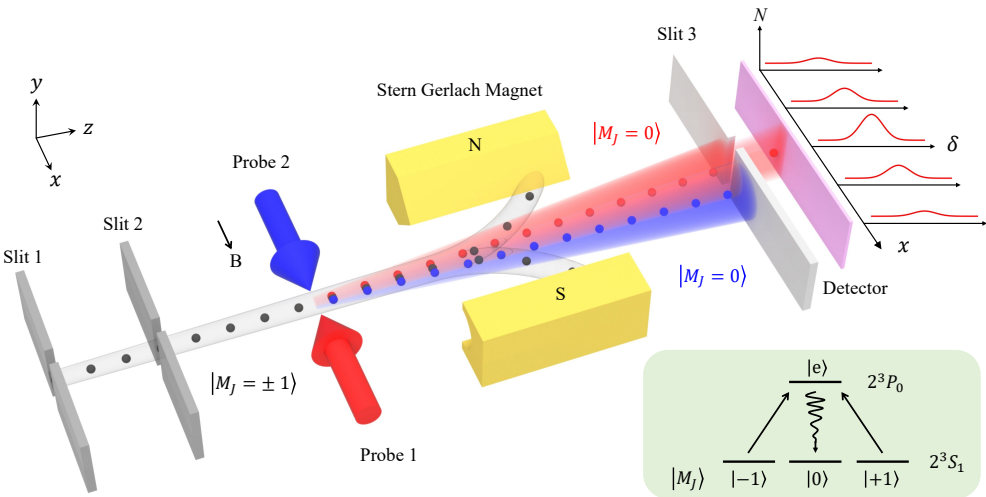


Figure 3.10 Schematic diagram of the experimental setup. Before the beam passes through two 0.3 mm wide slits for collimation, it has been pumped to the $M_J = \pm 1$ state. In the absence of probe light, the beam will be deflected by the Stern-Gerlach magnet. The probe light is split into two beams that are incident from both sides. Atoms interacting with the probe light have a 1/3 probability of populating the $M_J = 0$ state and thus entering the detector to form a signal. After interaction with the two probe light beams, the atomic beam will slightly deviate from its original direction of motion. In front of the detector, there is another slit (Slit 3) with a width of 0.5 mm to detect the beam distribution. By recording the atomic counts at different Slit 3 positions and frequencies, a series of spectra can be obtained.

potentially relax to the $M_J = 0$ state, allowing detection. In combination with the SCTOP method (described in Section 2.5), the detection laser is split into two beams, which are directed from both sides of the atomic beam. By switching the laser beams on and off, interaction between the laser beams and the atomic beam from either side can be controlled. The position of Slit 3, located in front of the detector, can be adjusted to observe changes in the spatial distribution of the beam after interaction with the laser. The frequency of the detection laser is locked near the $2^3S_1 - 2^3P_0$ transition. By scanning the laser frequency and recording the corresponding atomic count at each frequency, the spectrum can be measured. Therefore, by scanning the laser frequency at different slit positions, a series of spectra can be obtained.

When the atomic beam interacts with the detection laser, in the x -direction, the atomic momentum changes from $|mv_x\rangle$ to $|mv_x + \hbar k - \hbar r\rangle$, where $\hbar k$ represents the momentum of a photon absorbed from the detection laser, and $\hbar r$ represents the momentum of a photon emitted randomly during spontaneous emission, projected onto the x -direction. Since the direction of $\hbar k$ aligns with the direction of the detection laser, while $\hbar r$ is emitted randomly, after interacting with a laser beam from one side, the atomic beam will be slightly deflected in the direction of the laser's incidence, as shown

in Figure 3.10.

By organizing the spectral data from all slit positions, a three-dimensional relationship between slit position, laser frequency, and atomic count can be obtained, as shown in Figure 3.11. Two methods can be used to process these data. One method is to fit the spectrum at each slit position and then process the frequency center results from different positions. The other method is to first average the atomic counts at all frequencies, then fit the spectrum.

Figures 3.11(a) and (c) show the measurement results for Probe 1 and Probe 2, respectively. If a specific position is selected, such as the $x = +0.6$ mm position indicated by the black line in Figures 3.11(b) and (d), which correspond to the spectrum signal with slit selection. By fitting the spectrum obtained at each slit position, the results shown by the blue and green triangles in Figure 3.11(e) can be derived. These results exhibit a linear relationship with the slit position, and the fitted slope matches the value of 0.09 MHz/mm calculated using the Doppler effect formula $v_d = v_z \cdot x/L$, where x is the slit position

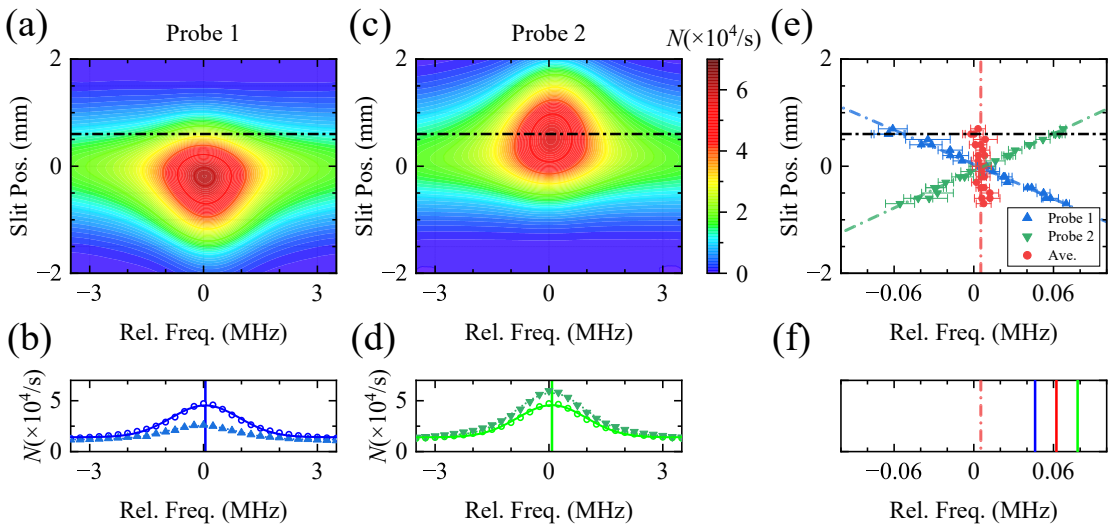


Figure 3.11 (a) Atomic count signals measured by Probe 1 laser at different slit positions. (b) The solid triangle represents the spectrum at $x = +0.6$ mm (the position indicated by the black dashed line in (a)), corresponding to the case with post-selection effect; the hollow circle represents the result obtained by averaging the signal at the corresponding frequency for all slit positions, corresponding to the case without the post-selection effect. The dashed and solid lines correspond to the fitted spectra under the two cases. The blue vertical line indicates the fitted spectrum center when there is no post-selection effect. (c) and (d) show the results measured by Probe 2 laser. (e) The blue and green triangles represent the spectrum centers measured by Probe 1 and Probe 2 at each slit position, and the red circles represent their average values. (f) The blue and green solid lines represent the center frequencies measured by the two lasers without the post-selection effect (corresponding to the vertical lines in (b) and (d)). The red solid line represents their average value, indicating the center frequency without the post-selection effect. The red dashed line indicates the final center frequency with the post-selection effect (corresponding to the red dashed line in (e)).

and L is the distance from the laser interaction region to Slit 3. Averaging the spectrum centers from both lasers effectively eliminates the Doppler effect, as shown by the red dots in Figure 3.11(e). The final result is completely independent of the slit position x , as indicated by the red dashed line in Figures 3.11(e) and (f).

By averaging the atomic count signals obtained at all slit positions for the same frequency, the spectra shown by the hollow circles and solid lines in Figures 3.11(b) and (d) can be obtained. Since the signals from all positions have been averaged, these can be regarded as the signal without slit selection. The averaged signal is then fitted using a Lorentzian curve, and the center frequency is indicated by the vertical lines in Figures 3.11(b) and (d). Upon observing the spectra in Figures 3.11(b) and (d), it is difficult to visually distinguish any difference in the frequency center between the cases with and without slit selection.

A comparison of the results from the two processing methods is shown in Figure 3.11(f). The blue and green solid lines represent the center frequencies obtained from Figure 3.11(b) and (d), respectively. Their average is indicated by the red solid line, which corresponds to the final result without slit selection. The red dashed line represents the center frequency obtained from Figure 3.11(e), which corresponds to the final result with slit selection. A noticeable deviation is observed between the red solid and dashed lines. Ideally, since the same raw data is used, the center frequencies from

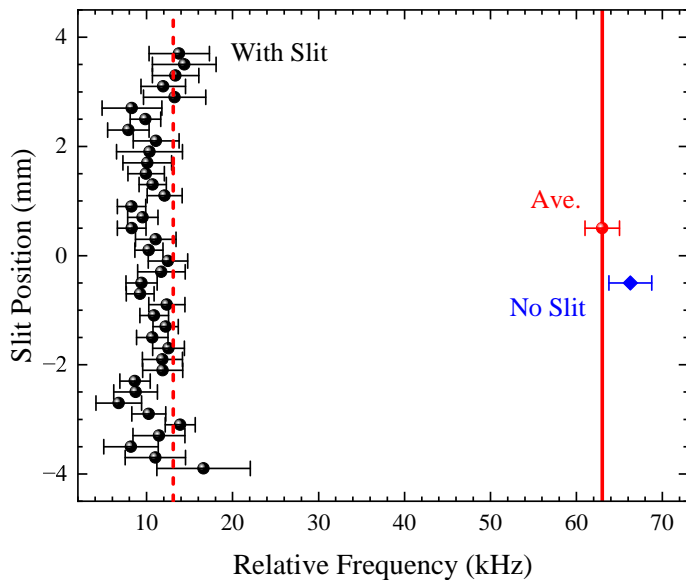


Figure 3.12 Comparison of results with and without slits. The black points represent the spectral center frequencies obtained at each slit position, corresponding to the red circles in Figure 3.11(e). The red points represent the spectral center obtained by averaging the atomic counts measured at all slit positions for the same frequency, corresponding to the red solid line in Figure 3.11(f). The blue diamonds represent the spectral center results obtained after removing Slit 3.

both methods should be identical. However, after applying both methods, the center frequencies not only differ but the deviation is as large as approximately 50 kHz, which exceeds the experimental error margin.

It is important to note that due to the finite width of the slits in the experiment and the limitations imposed by the spectral signal-to-noise ratio, measurements can only be conducted within a limited range of slit positions. Therefore, averaging the atomic counting signals at the same frequency across all slit positions does not fully equate to the case without slits. To further verify this, the experiment was conducted with Slit 3 completely removed, and the resulting spectral center is shown by the blue diamond points in Figure 3.12. The results indicate that the outcome with the slit removed is consistent with the average signal obtained from all slit positions. However, compared to the results with slit selection, there is a deviation of over 50 kHz.

3.3.3 Theoretical Explanation and Numerical Simulation

In this experiment, significant effects of the presence or absence of slits on the measurement results were observed. However, to correct the results from previous experiments conducted by our research group and explore experimental conditions that are unaffected by this effect, theoretical analysis and numerical simulations are required. This work was primarily carried out by Lv Yanan and Tang Jiadong^[252], and the following is a brief introduction.

3.3.3.1 Post-Selection Effect and Theoretical Model

In this experimental system, at different slit positions, not only were the spectra measured separately, but atoms with different transverse velocities were also simultaneously selected. This selection process is directly related to the post-selection effect, which is widely applied in the field of quantum optics.

In the past few decades, quantum mechanics has revolutionized our understanding of the world and introduced many counterintuitive technologies. One such technology is Weak Value Amplification (WVA), a method based on quantum mechanics to enhance measurement precision, which is both controversial and counterintuitive. In Von Neumann's quantum measurement model^[253], measurement is understood as a process where an observable or pointer interacts with the system to extract information. When the interaction is strong, the quantum state of the system collapses to a specific eigenstate, known as a strong measurement (e.g., projection measurement). On the other hand, when the interaction is weak and induces minimal changes in the system, it is

called a weak measurement. Building on weak measurements, if the system's initial state is pre-selected and the detection outcome is post-selected, the weak measurement technique with post-selection, introduced by Y. Aharonov and L. Vaidman in 1988^[254], can be applied. When the pre-selection and post-selection are nearly orthogonal, i.e., they satisfy a specific relationship, measurement results far greater than the system's eigenvalues can be obtained, known as weak value amplification. These amplified results, called weak values, sacrifice part of the detection signal to magnify subtle physical effects and have found widespread applications, with one of the most famous being the discovery of the quantum Hall effect^[255].

In this experimental system, different slit positions correspond to different projections of the atomic momentum. During this process, the post-selection effect amplifies the small momentum changes during the detection light-induced transition and spontaneous radiation, which is ultimately reflected in the transition frequency. In the experimental setup, the two sets of slits before and after the detection light interaction can be viewed as pre-selection or post-selection of the transverse velocity of the atomic beam.

In the experiment, the number of atoms that can ultimately be detected can be expressed as:

$$N(\delta) \propto |\langle \psi_f(p) | U_{SE} \langle e | O(\delta) | \pm 1 \rangle | \psi_i(p) \rangle|^2 \quad (3.1)$$

The initial and final momentum wavefunctions are denoted as $\psi_{i/f}(p)$, respectively. U_{SE} represents the spontaneous emission operator for the excited state $|e\rangle$, and $O(\delta)$ represents a weak interaction that alters the atomic population and exchanges momentum between the photon and the atom, where δ is the detuning of the probe laser. By performing post-selection with a very small probability $|\langle \psi_f(p) | \psi_i(p) \rangle|^2 \ll 1$, the tiny momentum change will be amplified and detectable.

To avoid directly solving the complex operator $O(\delta)$ and to account for the velocity distribution, a simplified model can be used instead of Equation 3.1:

$$N(\delta) \propto \int \int dv_0 dv_1 \frac{P_0(v_0) P_t(v_0, v_1) P_1(v_1)}{(\delta - kv_0)^2 + \gamma^2} \quad (3.2)$$

The probability function $P_t(v_0, v_1) = \frac{1}{2} \sqrt{1 - (v_1 - v_0 - v_R)^2/v_R^2}$ represents the probability of atomic velocity change due to the absorption and spontaneous emission of photons, where $0 \leq |v_1 - v_0| \leq 2v_R$ and $v_R = \hbar k/m$ is the recoil velocity. For atoms that can pass through Slit 3, the transverse (in the x -direction) velocity distribution before interaction with the laser and in front of the detector can be estimated as $P_0(v_0) = e^{-(v_0 - v_{0,b})^2/\sigma_0^2}$ and $P_1(v_1) = e^{-(v_1 - \xi x)^2/\sigma_1^2}$, where $v_{0,b}$ and ξx are the offset

velocities, ξ is the conversion coefficient related to the longitudinal (in the z -direction) velocity, and $\sigma_{0,1}$ represents the Gaussian half-width of the velocity distributions, which is related to the width of the slit. Since $v_R \ll \sigma_{0,1}$ in the experiment, Equation 3.2 can be further simplified to:

$$N(\delta) \propto \int dv_0 \frac{P_0(v_0)P_1(v_0 + v_R)}{(\delta - kv_0)^2 + \gamma^2} \quad (3.3)$$

Therefore, when a slit is present, i.e., $\sigma_1 \ll \sigma_0$, the spectral center is approximately given by $\delta_{PS,+} = k(v_R - \xi x)$. If the detection light is directed from the opposite direction, the result is $\delta_{PS,-} = k(v_R + \xi x)$. These results indicate a linear relationship between the spectral center and the position x , as shown by the blue and green points in Figure 3.11(e), while their average value kv_R is independent of x , as shown by the red points in Figure 3.11(e). If there is no slit in front of the detector, which is equivalent to the case without post-selection, since $\sigma_1 \ll \gamma/k$, $P_1(v_0 + v_R)$ can be considered constant. In this case, the spectral centers obtained from the two lasers are $\delta_{NPS,+} \approx kv_b$ and $\delta_{NPS,-} \approx -kv_b$, with an average result of 0, indicating no deviation from the true result. Comparing these two cases, the deviation caused by the post-selection effect is on the order of kv_R , and it is independent of the slit position x or the Doppler effect.

The post-selection shift (PSS) obtained in Figure 3.11 is approximately $\Omega_{PSS} \approx 2\pi \times 55$ kHz, which is slightly smaller than the predicted value $kv_R \approx 2\pi \times 84$ kHz. This difference is due to the presence of pre-selection in the experiment, which will be briefly discussed in the simplified model, as detailed in Section 3.3.3.

3.3.3.2 Monte-Carlo Wave Function Method

The Monte-Carlo Wave Function (MCWF) method is a technique for solving the evolution of a wave function under an effective Hamiltonian, aimed at replacing the master equation and handling dissipation processes in light-atom interaction systems. This method involves selecting an appropriate iteration step size δt and a sufficient number of averages, so that the results obtained are equivalent to solving the master equation directly. Compared to solving the master equation using a density matrix, the computational complexity of the MCWF method is $O(N)$, whereas the density matrix method is $O(N^2)$. Therefore, when simulating high-degree-of-freedom systems, such as solving atomic motion trajectories in laser cooling processes, the MCWF method has a significant computational advantage. In previous work by our research group, the MCWF method was used to simulate the LFS effect, as detailed in Section 3.3.1.

The general procedure of the MCWF method is as follows. Suppose the system's

wave function at time t is $|\phi(t)\rangle$. To obtain the wave function at time $t + \delta t$, $|\phi(t + \delta t)\rangle$, the first step is to solve the wave function evolution under the total Hamiltonian to get $|\phi^{(1)}(t + \delta t)\rangle$:

$$H = H_0 - \frac{i\hbar}{2} \sum_m C_m^\dagger C_m \quad (3.4)$$

$$|\phi^{(1)}(t + \delta t)\rangle = \left(1 - \frac{iH\delta t}{\hbar}\right) |\phi(t)\rangle$$

where H_0 is Hermitian, representing the atomic system itself and the nondissipative interactions with light, while the second term represents the dissipative part. Therefore, the total Hamiltonian is non-Hermitian, and its modulus squared is:

$$\langle \phi^{(1)}(t + \delta t) | \phi^{(1)}(t + \delta t) \rangle = \langle \phi(t) | \left(1 + \frac{iH^\dagger \delta t}{\hbar}\right) \left(1 - \frac{iH\delta t}{\hbar}\right) |\phi(t)\rangle \quad (3.5)$$

$$= 1 - \delta p + O(\delta t^2)$$

where δp represents the total probability of a quantum jump.

$$\delta p = \delta t \frac{i}{\hbar} \langle \phi(t) | H - H^\dagger | \phi(t) \rangle = \sum_m \delta p_m \quad (3.6)$$

$$\delta p_m = \delta t \langle \phi(t) | C_m^\dagger C_m | \phi(t) \rangle \geq 0$$

In the MCWF method, a random number ϵ between 0 and 1 is generated and compared with δp to determine whether a quantum jump occurs. If $\epsilon > \delta p$, no quantum jump occurs, and the wave function is simply normalized:

$$|\phi(t + \delta t)\rangle = \frac{|\phi^{(1)}(t + \delta t)\rangle}{\sqrt{1 - \delta p}} \quad (3.7)$$

If $\epsilon \leq \delta p$, it indicates that a quantum jump has occurred. In this case, the wave function is affected by the dissipative term as follows:

$$|\phi(t + \delta t)\rangle = \frac{C_m |\phi(t)\rangle}{\sqrt{\delta p_m / \delta t}} \quad (3.8)$$

For each δt time step, the above process is repeated until the evolution reaches the desired time.

For the experimental system, both the atomic energy levels and atomic momentum changes need to be considered. In the system, the dissipation term is only the spontaneous emission term, so the total Hamiltonian can be expressed as:

$$H = \frac{\hat{P}^2}{2m} + \hbar\omega_0 |e\rangle\langle e| - \hat{d} \cdot \hat{E} - \frac{i\hbar}{2}\Gamma |e\rangle\langle e| \quad (3.9)$$

For the traveling wave field and standing wave field, the light field can be expressed as $E_t = E_0 \cos(\omega t - kx)$ and $E_s = E_0 \cos(\omega t - kx) + E_0 \cos(\omega t + kx) =$

$E_0 \cos(kx)(e^{i\omega t} + e^{-i\omega t})$. Substituting these into the total Hamiltonian, they can be expressed as:

$$\begin{aligned} H_t &= \frac{\hat{P}^2}{2m} + \frac{\hbar\Omega}{2} (e^{ikx} S^+ + e^{-ikx} S^-) - \hbar\Delta S^+ S^- - \frac{i\hbar}{2}\Gamma S^+ S^- \\ H_s &= \frac{\hat{P}^2}{2m} + \frac{\hbar\Omega}{2} (e^{ikx} + e^{-ikx}) (S^+ + S^-) - \hbar\Delta S^+ S^- - \frac{i\hbar}{2}\Gamma S^+ S^- \end{aligned} \quad (3.10)$$

where $S^+ = |e\rangle\langle g|$ and $S^- = |g\rangle\langle e|$ are the raising and lowering operators, $\Delta = \omega - \omega_0$ is the detuning, and Ω is the Rabi frequency.

To simultaneously consider the changes in atomic energy levels and momentum, the basis vectors are chosen as $\{|g, p\rangle, |e, p\rangle\}$, and the momentum space is discretized using photon momentum $\hbar k$ as the step size. The normalized wavefunction can be expressed as:

$$|\phi(t)\rangle = \sum_n c_{e,n}(t) |e, n\hbar k\rangle + c_{g,n}(t) |g, n\hbar k\rangle \quad (3.11)$$

Where $c_{e,n}(t)$ and $c_{g,n}(t)$ represent the probability amplitudes at time t for the atom to be in the excited state and ground state, with the momentum projection along the x -direction equal to $n\hbar k$. Since the wavefunction is normalized, the sum of the squared magnitudes at any time t is 1. At time $t + \delta t$, the probability of the atom undergoing spontaneous emission is:

$$\Delta p = 1 - \sum \left[|c_{e,n}^{(1)}(t + \delta t)|^2 + |c_{g,n}^{(1)}(t + \delta t)|^2 \right] \quad (3.12)$$

This corresponds to the probability of a quantum jump occurring in the MCWF method. Since the interaction process changes the atomic momentum, when solving for the probability amplitudes at time $t + \delta t$, the direction of the light field must be taken into account. By substituting into equation 3.10 and solving, we can obtain the iterative relationship for the probability amplitudes. The iterative relation under the traveling-wave field is:

$$\begin{aligned} c_{e,n}^{(1)}(t + \delta t) &= c_{e,n}(t) - \frac{i\delta t}{\hbar} \left[\frac{(n\hbar k + mv_x)^2}{2m} - \hbar\Delta - \frac{i\hbar\Gamma}{2} \right] c_{e,n}(t) \\ &\quad - \frac{i\Omega\delta t}{2} c_{g,n-1}(t) \\ c_{g,n}^{(1)}(t + \delta t) &= c_{g,n}(t) - \frac{i\delta t}{\hbar} \frac{(n\hbar k + mv_x)^2}{2m} c_{g,n}(t) - \frac{i\Omega\delta t}{2} c_{e,n+1}(t) \end{aligned} \quad (3.13)$$

The iterative relationship under the standing-wave field is:

$$\begin{aligned} c_{e,n}^{(1)}(t + \delta t) &= c_{e,n}(t) - \frac{i\delta t}{\hbar} \left[\frac{(n\hbar k + mv_x)^2}{2m} - \hbar\Delta - \frac{i\hbar\Gamma}{2} \right] c_{e,n}(t) \\ &\quad - \frac{i\Omega\delta t}{2} [c_{g,n-1}(t) + c_{g,n+1}(t)] \\ c_{g,n}^{(1)}(t + \delta t) &= c_{g,n}(t) - \frac{i\delta t}{\hbar} \frac{(n\hbar k + mv_x)^2}{2m} c_{g,n}(t) - \frac{i\Omega\delta t}{2} [c_{e,n+1}(t) + c_{e,n-1}(t)] \end{aligned} \quad (3.14)$$

Where $n + 1$ and $n - 1$ represent shifts in momentum space. When an atom absorbs a photon, it transitions from $|g, n\hbar k\rangle$ to $|e, (n + 1)\hbar k\rangle$ or $|e, (n - 1)\hbar k\rangle$; while when emitting a photon, the atom transitions from $|e, n\hbar k\rangle$ to $|g, (n + 1)\hbar k\rangle$ or $|g, (n - 1)\hbar k\rangle$. The sign of each term is determined by whether the absorbed or emitted photon propagates in the positive or negative x -direction.

When a random number ϵ is generated to determine whether spontaneous emission occurs, if $\epsilon > \Delta p$, no quantum jump happens, as mentioned above. In this case, the wave function is simply normalized:

$$\begin{aligned} c_{e,n}(t + \delta t) &= \frac{c_{e,n}^{(1)}(t + \delta t)}{\sqrt{1 - \Delta p}} \\ c_{g,n}(t + \delta t) &= \frac{c_{g,n}^{(1)}(t + \delta t)}{\sqrt{1 - \Delta p}} \end{aligned} \quad (3.15)$$

If $\epsilon \leq \Delta p$, spontaneous emission occurs. At this point, it is necessary to further determine which substate the atom will emit to. For the $2^3S_1 - 2^3P_0$ transition studied in this experiment, the probability of spontaneous emission from the excited state to the three substates of $M_J = +1, 0$, and -1 in the ground state is each $1/3$, as calculated from the C-G coefficients. Since the experiment detects peaks from $M_J = \pm 1$, and the process is symmetric, only one of the peaks needs to be considered. Suppose the ground state $|g\rangle$ corresponds to $M_J = +1$, and the excited state $|e\rangle$ corresponds to the $M_J = 0$ sublevel of the 2^3P_0 state. If the atom falls into the $M_J = -1$ state, due to the large detuning, it will almost no longer interact with the laser. Additionally, due to the deflection by the Stern-Gerlach magnet, it will not be detected, so it is not considered further. The state that can finally be detected is the $M_J = 0$ state, denoted as $|0\rangle$, and atoms that fall into this state will no longer interact with the laser. The probabilities for spontaneous emission to the $|g\rangle$ or $|0\rangle$ states are:

$$\begin{aligned} c_{e,n}(t + \delta t) &= 0, \\ c_{g,n}(t + \delta t) &= \frac{c_{e,n}^{(1)}(t + \delta t)}{\sum |c_{e,n}^{(1)}(t + \delta t)|^2}, \text{ or} \\ c_{0,n}(t + \delta t) &= \frac{c_{e,n}^{(1)}(t + \delta t)}{\sum |c_{e,n}^{(1)}(t + \delta t)|^2} \end{aligned} \quad (3.16)$$

Repeat the above process until the atom leaves the laser field, at which point the final probability of emission can be determined as $|c_{0,n}|^2$.

Similarly, when considering spontaneous emission, the velocity change due to recoil needs to be discretized. Each time the atom spontaneously emits a photon, the

velocity change caused by the recoil momentum is projected along the x direction. At this point, the atom's velocity along the x direction becomes:

$$v_x^{(1)} = v_x - \frac{\hbar k}{m} \sin \theta \cos \varphi \quad (3.17)$$

Where θ and φ are the solid angles of spontaneous emission in the three-dimensional coordinate system. The updated velocity does not need to be normalized and is directly updated as $v_x = v_x^{(1)}$, which is then used in the next cycle of calculations. Finally, when the atom leaves the laser field, the final transverse velocity is $v_{x,n} = v_x + n\hbar k/m$. Combining the longitudinal velocity of the beam and the length of the apparatus, the position of the atom in front of the detector slit can be determined and compared with the slit width to determine whether the atom can pass through the slit and be detected.

3.3.3.3 Numerical Simulation Results and Comparison with Experimental Results

By using the two methods described above, numerical simulations of the results under the post-selection effect can be conducted and compared with the experimental results to validate the accuracy of the model. When two slits are present before the laser interaction region, as shown in Figure 3.13(a), the transverse velocity of the beam is proportional to its longitudinal velocity due to the geometric constraints of the two slits. As the longitudinal velocity of the beam is gradually increased, the difference between the results with and without slits becomes larger and eventually approaches a limiting value. However, when only one slit is present before the laser interaction region, the initial transverse velocity is no longer constrained by geometric conditions and is almost independent of the longitudinal velocity of the beam. The measurement result remains close to the limiting value. The measurements conducted in our previous experiment^[177] were performed under these conditions. Due to structural differences between the previous and current setups, including the varying distance between the laser and the two slits, the limiting value differs. The conditions for the two setups are distinguished by the shaded region in Figure 3.13 (b). Under both conditions, the results from the numerical simulations align with the experimental results, demonstrating that both simulation methods are reliable. Ultimately, by incorporating the experimental conditions from the previous setup into the simulation, a correction of approximately +55 kHz can be applied to the previous measurement results.

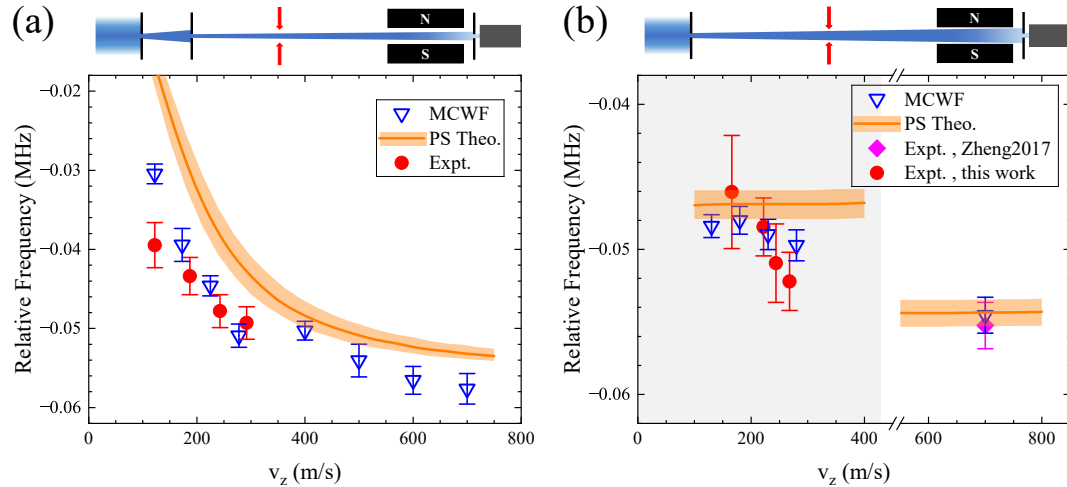


Figure 3.13 Comparison of simulation and experimental results of post-selection effects at different velocities. (a) Simulation and experimental results when there are two slits before the laser interaction region. Due to the geometric constraints provided by the two slits, the transverse velocity distribution before the probe light is proportional to the longitudinal velocity of the beam. (b) Simulation and experimental results when there is only one slit before the laser interaction region. Since there is only one slit before the probe light interaction region, the transverse distribution is almost independent of the longitudinal velocity, so the results remain essentially unchanged when the beam velocity is altered. In panel (b), the regions below 450 m/s and above 600 m/s are distinguished by background shaded areas, representing the results under the conditions of two different experimental setups. Red dots represent experimental results, blue hollow triangles represent the results from MCWF method simulations, and the orange line represents the theoretical results derived from post-selection theory. The orange bands in panel (a) represent the error when the initial transverse velocity distribution σ_0 changes by 10 %, and in panel (b) represent the error when the slit width σ_1 changes by 5 %.

3.3.3.4 Simple Classical Model Estimation of the Limiting Value

The limit value has been mentioned multiple times earlier, and the experimentally observed limit value is typically smaller than the theoretical predicted value $k v_R = 84$ kHz, which is related to the presence of pre-selection in the apparatus. Here, we use a simple classical model to estimate the limit value. As shown in Figure 3.14, the transverse positions of the two slits are at $x = 0$. Assume both slits are sufficiently narrow to allow only one atom to pass through. After the atom interacts with the laser, it absorbs and spontaneously emits photons, and the total velocity in the x -direction changes from v_i to v_f , with the change in velocity v_{photon} represented as:

$$v_{\text{photon}} = v_R \cos \theta = \frac{\hbar k}{m} \cos \theta \quad (3.18)$$

here, $\cos \theta$ represents the projection of the total change in momentum in the x -direction after absorbing and spontaneously emitting a photon. Under the limit condition, when $\cos \theta = 1$, that is, when the total momentum change occurs entirely in the x -direction, $v_{\text{photon}} = v_R = \hbar k / m$. In this case, after the atom interacts with the laser from one side, in order to pass through the slit and be detected, certain geometric conditions need to

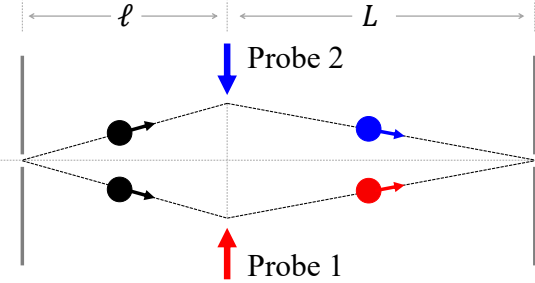


Figure 3.14 Schematic diagram of the simple classical model. The centers of the two slits are aligned along the x direction. In this case, only atoms with a non-zero initial velocity $v_i \approx -v_R \frac{L}{\ell+L}$, after interacting with Probe 1, can pass through the slit in front of the detector and be detected, resulting in a redshift of the spectral center. The same situation applies to Probe 2, and the result will also show a redshift. This deviation cannot be averaged out when eliminating the Doppler effect, so the final result will also show a redshift.

be satisfied:

$$v_i \frac{\ell}{v} + v_f \frac{L}{v} = 0 \quad (3.19)$$

$$v_i + v_R = v_f$$

The atom must have a non-zero initial transverse velocity $v_i = -v_R \cdot L/(\ell + L)$, with the initial velocity direction opposite to the laser direction. For the other side, the same relationship must hold for the atom to pass through the slit after interacting with the laser. Therefore, redshift will appear at both sides of the spectrum center. During the averaging process to eliminate the Doppler effect at both sides, this redshift cannot be canceled out, and thus a deviation arises in the final result. At this point, the additional Doppler effect caused by the atom's initial velocity is the limit value (angular frequency):

$$\begin{aligned} \Delta\omega &= \vec{k} \cdot \vec{v} = kv_i \\ &= -kv_R \frac{L}{\ell + L} \end{aligned} \quad (3.20)$$

or expressed in terms of frequency:

$$\Delta\nu = \frac{\Delta\omega}{2\pi} = -\frac{h}{mc^2} \frac{L}{\ell + L} v_c^2 \quad (3.21)$$

where v_c is the transition frequency to be measured, ℓ and L represent the distances between the laser and the slits on either side. It is easy to see that this limit value is exactly the theoretical predicted value $-kv_R$ multiplied by the distance factor $L/(\ell + L)$. If the front slit is removed, and there are no geometric constraints, the limit value becomes $\Delta\omega = -kv_R$, which is the same as the predicted value.

This simple model can be used to estimate the limit of the post-selection effect in the experimental setup. For example, in the previous setup used by our research group,

with $\ell = 0.55$ m and $L = 1.05$ m, the limit value is approximately $-2\pi \times 55.7$ kHz. This means that the previous result needs to be corrected by about +55.7 kHz, which is consistent with the results obtained using both the post-selection theory and the MCWF method. However, in the actual setup, the slits have some width, the beam has a certain transverse velocity distribution, and factors such as laser power need to be considered. Therefore, the results derived from equation 3.21 can only serve as a reference, and the exact deviation must be determined through detailed simulation calculations.

3.3.4 Post-selection Phenomena under Different Experimental Conditions

In the experiment, by varying the incident direction of the laser and choosing different slit positions, a series of experimental conditions can be combined. The post-selection phenomenon varies under different experimental conditions. Measuring and simulating the post-selection effect under these conditions helps further verify the accuracy of the model and explore experimental conditions that can avoid the influence of the post-selection effect. The following sections describe the post-selection phenomena under different experimental conditions.

For comparison purposes, unless otherwise specified, the horizontal axis of all experimental results has been converted from position to Doppler shift, which is half the frequency difference between the center frequencies of the two traveling waves. The vertical axis represents the frequency shift relative to 276 764 094 MHz. As a reference, without Slit 3, the frequency should be around 717 kHz, while with Slit 3, the frequency should be near 662 kHz. In the simulation results, if there is no post-selection effect, the frequency center is at 0 kHz. The beam velocity in the experiment is 290 m/s, and the laser intensities on both sides are locked at 1 μW . When the laser incident direction is fixed, the light path is made as perpendicular to the beam as possible, so the measured results appear symmetric. Except for the last experimental condition, the position of Slit 1 remains constant. Slit 2 and Slit 3 are positioned at the center of the beam distribution when there is no laser, and these two slits can be completely removed, referred to as “No Slit 2” or “No Slit 3”.

In the distribution measurements, the measurement sequence was carefully designed and alternated between the left and right sides to minimize the impact of beam intensity drift on the results. In the figure, blue upward triangles represent the single-side results for Probe 1, green downward triangles represent the single-side results for Probe 2, black squares represent the results when both sides of the light are applied simultaneously (marked as “Both” in the figure), and red circles represent the average of

the results from Probe 1 and Probe 2 (marked as “Ave” in the figure). The corresponding color lines represent the fitted results.

3.3.4.1 Fixed Laser Incidence Direction and Slit 2 Position, Varying Slit 3 Position

During the initial experiment, when the laser incidence direction and Slit 2 position were fixed, and the Slit 3 position was changed, the relative orientation of the beam and laser was determined. As shown in Figure 3.15(a), due to the influence of the laser force on the atoms, when one side of the laser interacts with the beam, the beam will shift toward the opposite side. Therefore, both laser beams fail to provide sufficient signal-to-noise ratio in the spectrum on one side, leading to a lack of data points at larger Doppler shifts (either positive or negative). When both sides of the laser can fit the spectral center within a certain range (approximately ± 50 kHz on the x-axis), the average result remains largely unchanged, stabilizing at about 55 kHz smaller than the case without Slit 3. The distribution and bias under these experimental conditions have been discussed in detail earlier. Under the standing wave interaction, the beam distribution center remains almost unchanged, so signals can be obtained from both sides. However, throughout the measurement range, the standing wave exhibits significant nonlinear variations. Similar phenomena can also be simulated using the Monte Carlo Wave Function method, as shown in Figure 3.15(b), although the underlying mechanism has not yet been fully explained.

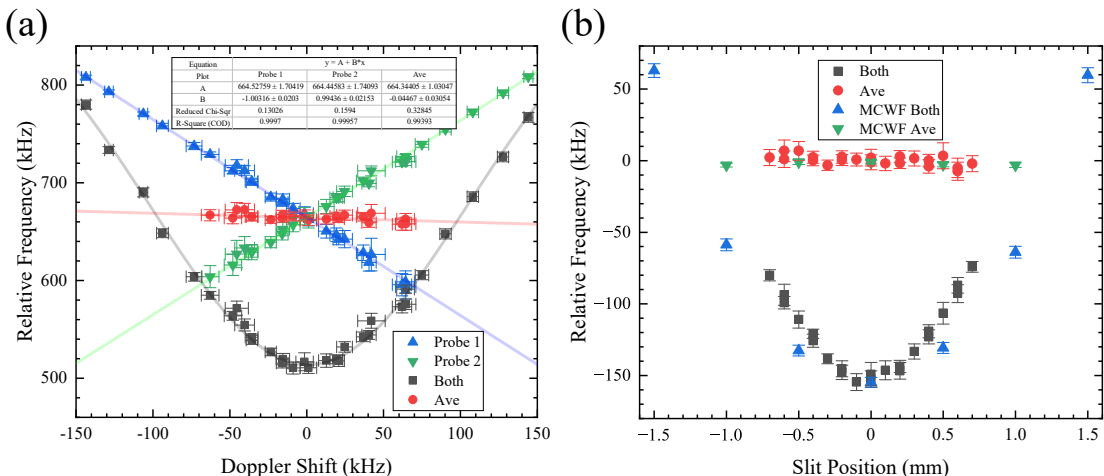


Figure 3.15 (a) Measurement results when the laser incidence direction and Slit 2 position are fixed, while varying the Slit 3 position. (b) Comparison of the Monte Carlo Wave Function (MCWF) simulation results with experimental results.

3.3.4.2 Fixed Laser Incidence Direction, No Slit 2, Varying Slit 3 Position

After removing Slit 2, the same experiment was repeated, i.e., fixing the laser incidence direction and changing the Slit 3 position. The measured distribution and fre-

quency results correspond to those obtained in the previous setup. In the absence of Slit 2, the beam distribution interacting with the probing laser significantly broadens, allowing signals to be observed over a larger range. Comparing the distributions under these two experimental conditions, as shown in Figure 3.16, the beam distribution in the case with Slit 2 is confined within ± 2 mm, while in the absence of Slit 2, the distribution range expands to nearly ± 4 mm.

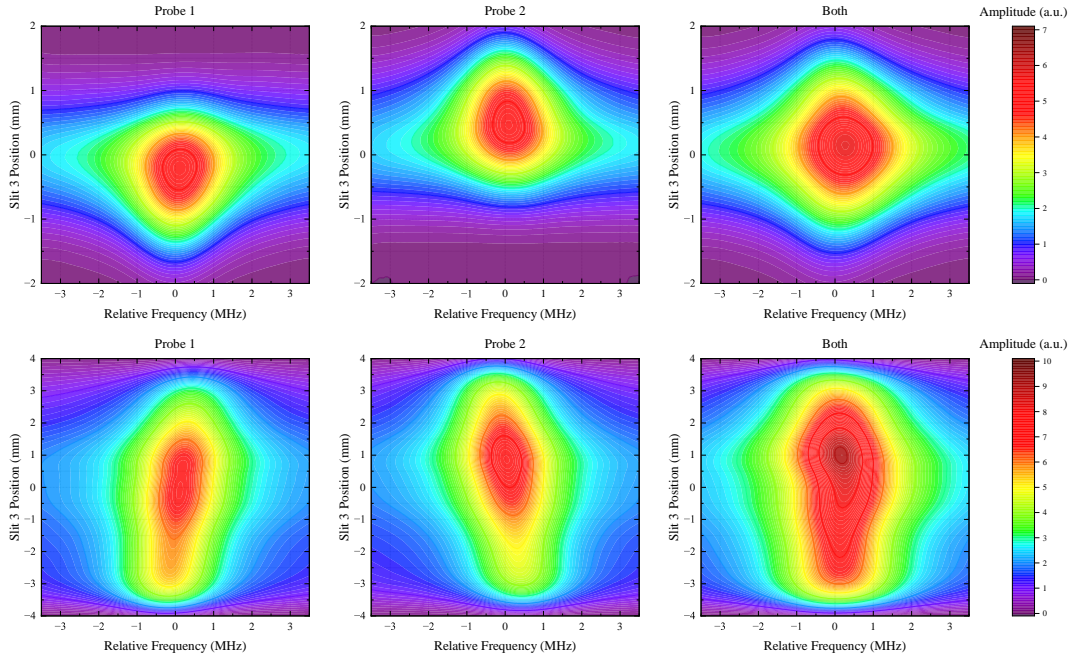


Figure 3.16 Comparison of the beam distribution when the laser incidence direction is fixed and Slit 3 position is varied, with and without Slit 2. The first row shows the results with Slit 2, and the second row shows the results without Slit 2. From left to right, the three columns represent the results from Probe 1, Probe 2, and standing wave interaction, respectively.

At the same time, the measurement range of the spectrum also increased. When Slit 2 was present, the spectrum could only be detected when Slit 3 moved within the central ± 1.6 mm range, and the range for obtaining the average value was limited to ± 0.7 mm. However, in the absence of Slit 2, the spectrum could be measured when Slit 3 moved within the central ± 3.8 mm range, and the average value could be obtained throughout this range. It is worth noting that within such a wide range, the average value remains almost constant, as shown in Figure 3.17. This indicates that in the previous setup, although the position of the detector slit was changed, there was little change in the frequency, so the post-selection effect was not detected at that time. The results from the standing wave show that its mechanism is very complex, and this complexity is clearly detrimental to precision measurements. In contrast, the traveling wave measurement method demonstrates its superiority by providing stable average values over

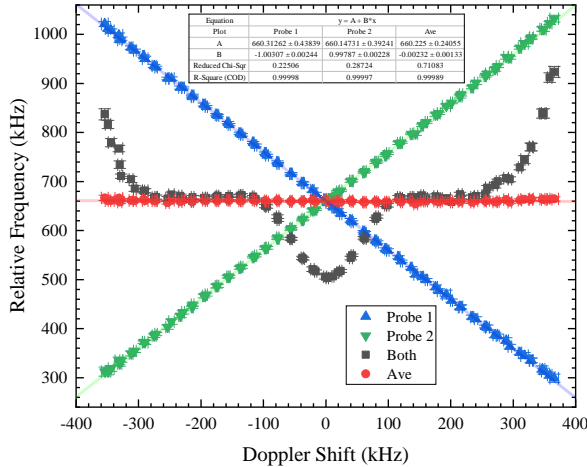


Figure 3.17 Measurement results when the laser incidence direction is fixed, and Slit 3 position is varied, with and without Slit 2.

a larger range.

3.3.4.3 Fixed Laser Incidence Direction, Varying Slit 2 Position, Fixed Slit 3 Position

As shown in Figure 3.18(a), if the initial experiment is modified to fix Slit 3's position and change the position of Slit 2, the initial direction and distribution of the atomic beam are altered under the conditions where post-selection effects exist. The results show that within the range where the signal can be detected, the average value remains almost unchanged, as depicted in Figure 3.18(b). Meanwhile, the standing wave result continues to decrease. This suggests that when there is a very narrow slit in front of the detector for post-selection, even if the initial direction or distribution of the beam is actively altered in the experiment, the results remain stable and it is difficult to observe the impact of post-selection on the outcomes.

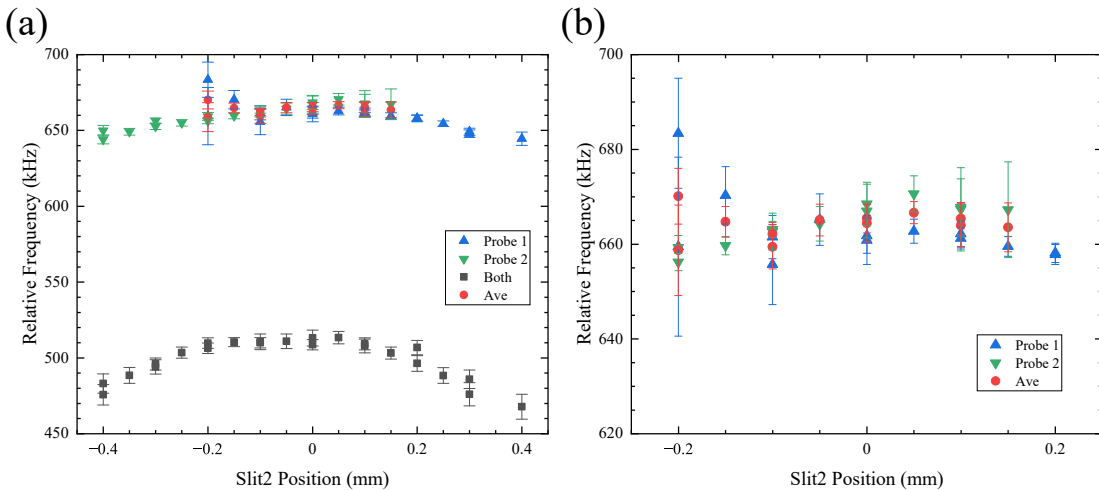


Figure 3.18 Measurement results when the laser incidence direction is fixed, Slit 2 position is varied, and Slit 3 position is fixed.

3.3.4.4 Fixed Laser Incidence Direction, Varying Slit 2 Position, No Slit 3

In the previous three sets of experiments, the phenomena were investigated when a narrow slit (Slit 3) is present in front of the detector, which introduces a strong post-selection effect, and when the positions of Slit 2 or Slit 3 are changed. It is evident that as long as a strong post-selection effect is present, the average value results remain largely stable, making it difficult to observe the impact of the post-selection effect on the results by simply changing the experimental conditions.

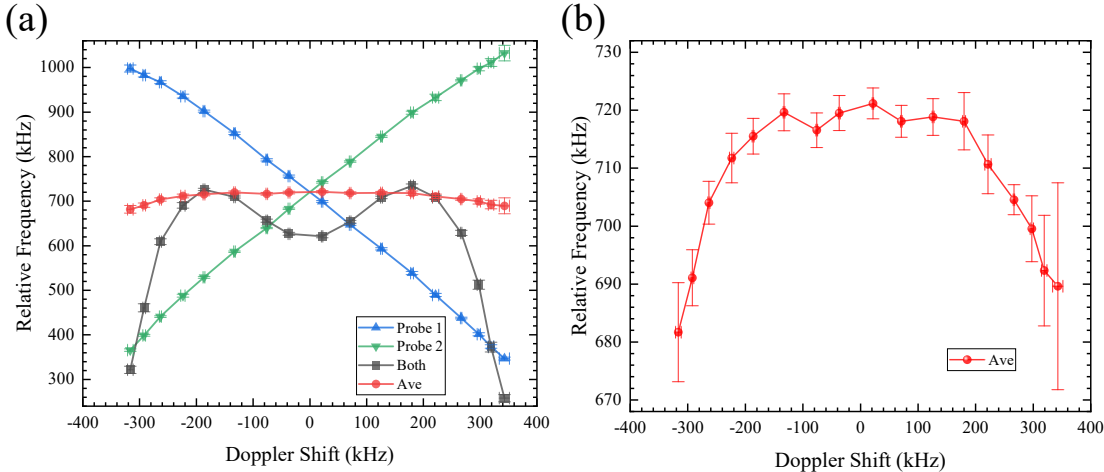


Figure 3.19 Measurement results when the laser incidence direction is fixed, and Slit 2 position is varied, with no Slit 3.

When Slit 3 is removed, the post-selection effect no longer exists, and theoretically, the results should stabilize at those without the post-selection effect. However, in the case of a fixed laser incident direction and the removal of Slit 3, changing the position of Slit 2 revealed a noticeable redshift on both sides, as shown in Fig. 3.19. Notably, this phenomenon was observed not only in the standing wave case but also in the single-sided light case. In comparison with the previous three sets of experimental results, both Probe 1 and Probe 2 exhibited a redshift on the side with the larger measured result. This corresponds to a situation where the incident laser's wave vector forms a sharp angle with the forward direction of the atomic beam, causing the result to shift lower. Based on earlier analysis, it can be inferred that the atomic beam is spatially blocked, leading to a redshift in the measured results.

More specifically, within this experimental setup, there may be a wider slit, creating a weak post-selection effect that only becomes apparent when strong post-selection effects are absent. Upon careful inspection of the experimental design, it was found that the front and rear slits (corresponding to Slit 1 and Slit 3 in this work) had already narrowed the beam distribution significantly to enhance the gradient of the deflection magnetic field. To achieve this, the pipe diameter was set to only 10 mm. Consider-

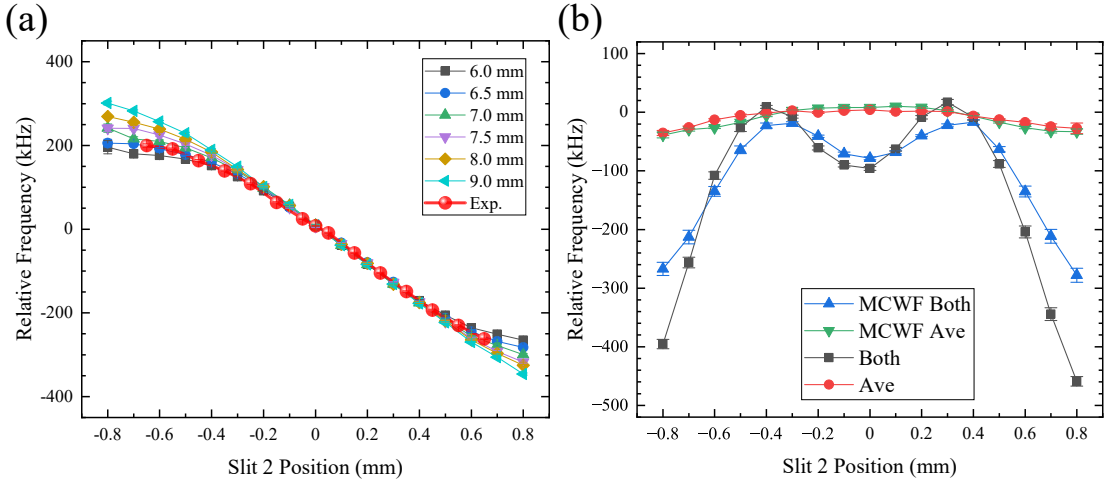


Figure 3.20 Monte Carlo Wave Function (MCWF) simulation of equivalent slit. (a) Changes in the results when the width of the equivalent slit is varied during simulation with one-sided light. By comparing the simulation results with one-sided light in the experiment, the equivalent slit width is determined to be approximately 6.5 mm. (b) Comparison of simulation and experimental results when the equivalent slit is 6.5 mm wide.

ing the difficulties in precisely aligning large components during the assembly process, flexible bellows were used to connect the components before and after the magnetic shielding region. This may have introduced positional deviations, resulting in a wider equivalent slit within the apparatus, ultimately leading to a weak post-selection effect.

By considering this factor in the Monte Carlo wave function (MCWF) simulations, it can be assumed that there exists an equivalent slit approximately 6.5 mm wide at the Stern-Gerlach magnet, as shown in Fig. 3.20. The simulation results obtained using the MCWF method in this study all account for the influence of this equivalent slit. Comparing the distributions measured in the first two experimental setups, as shown in Fig. 3.16, it can be seen that when the positions of Slit 1 and Slit 2 are fixed, the entire beam distribution is fully detectable. However, when Slit 2 is removed, a noticeable truncation occurs at both sides of the beam distribution, further confirming the presence of this equivalent slit. In the final experiment, since both Slit 1 and Slit 2 were used, the beam's distribution at the edge of the Stern-Gerlach magnet remained within ± 2 mm. Moreover, the probe power was always less than $1 \mu\text{W}$. Therefore, in the final measurement, the influence of this equivalent slit does not need to be considered.

3.3.4.5 Changing Laser Incidence Direction, Fixed Slit 2 Position, With and Without Slit 3

The previous experiments focused on investigating the post-selection effects within the system by changing the slit positions while keeping the laser incidence direction fixed. Here, we will study the case where the slit positions are fixed, but the laser

incidence direction is varied.

In the experiment, with Slit 1 and Slit 2 positions fixed, we conducted measurements in two cases: one with Slit 3 fixed at the beam center and the other without Slit 3. The laser incidence direction was varied for each case. The experimental results are shown in Fig. 3.21, where darker colors represent the results without Slit 3, and lighter colors represent the results with Slit 3. From the frequency results, we observe that under the traveling-wave measurement condition, the results with and without Slit 3 are consistently offset by approximately 50 kHz. This is consistent with our previous conclusion that when a strong post-selection effect is present, the results remain stable despite changes in various experimental conditions. Furthermore, when compared to the results from the earlier experiments, where the laser incidence angle was fixed and the slit positions were varied, the phenomena in both cases align. In essence, both setups involve selecting the momentum of the detected atoms. Additionally, since the results are very stable within the Doppler range of ± 300 kHz, we can confirm that the final experiment will not be affected by the equivalent slit.

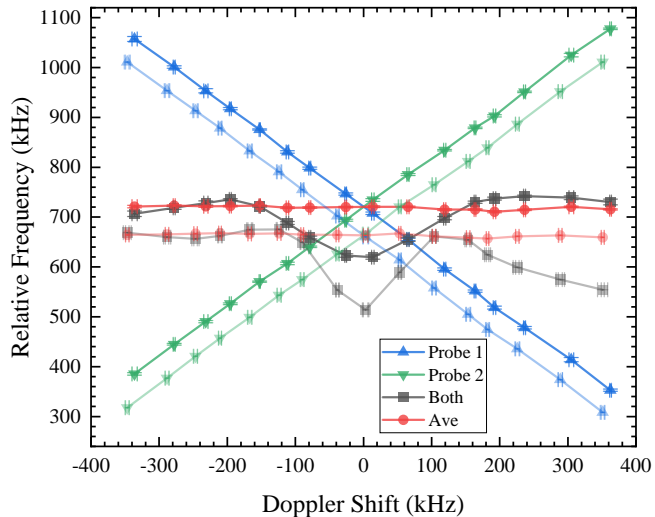


Figure 3.21 Measurement results when the laser incidence direction is changed, and Slit 2 position is fixed, with and without Slit 3. The darker colors represent the results without Slit 3, while the lighter colors correspond to the results with Slit 3.

In the experiment, the beam distribution was also measured when the laser incidence angle corresponded to a Doppler shift of $+350$ kHz, as shown in Fig. 3.22. When compared to the initial experiment, where the laser was nearly perpendicular to the beam, a noticeable shift in the distribution to both sides is observed. However, the distribution is not obstructed. In the final experiment, the laser incidence angle was controlled within a ± 150 kHz Doppler range. Therefore, it can be concluded that the equivalent slit will not affect the results in the final experiment.

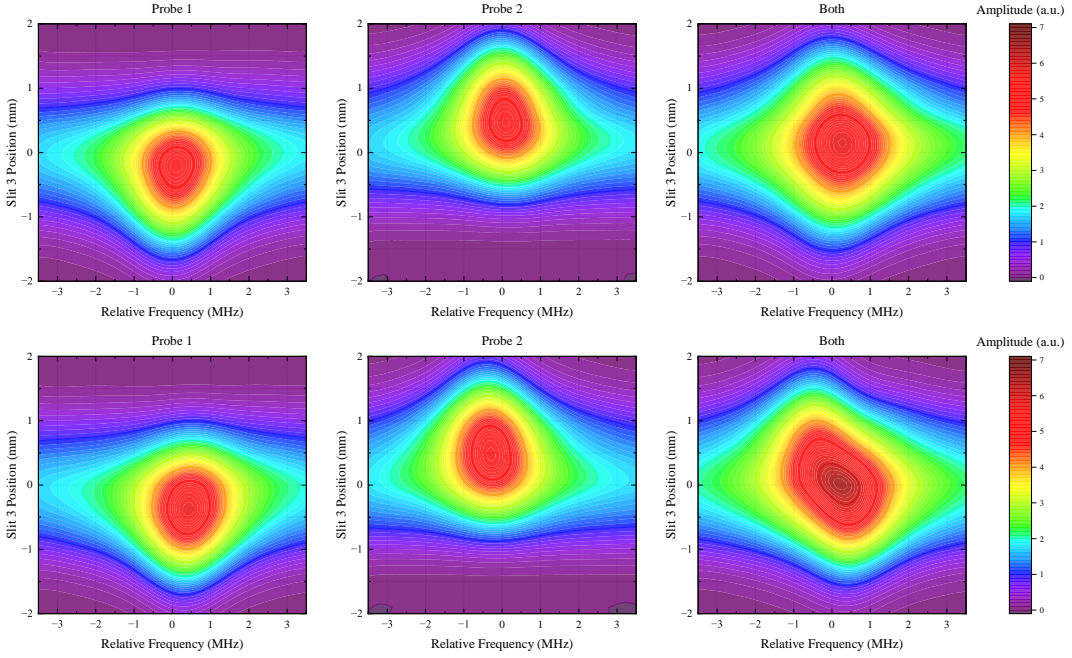


Figure 3.22 Comparison of the beam distribution when the laser incidence angle corresponds to Doppler shifts of nearly 0 and about +350 kHz. The first row shows the distribution when the laser is nearly perpendicular to the beam, and the second row shows the distribution when the laser incidence direction makes an angle with the perpendicular to the beam, corresponding to Doppler shifts of approximately +350 kHz. From left to right, the three columns represent results from Probe 1, Probe 2, and standing wave interaction.

3.3.4.6 Fixed Laser Incidence Direction, Varying Slit 3 Position at Each Slit 2 Location

The previous experiments focused on investigating the effect of post-selection on the experimental results. However, in the theoretical derivation, we have already seen that pre-selection can also influence post-selection effects. In the experiment, we can study the relationship between pre-selection and post-selection by changing the position of Slit 3 while fixing the laser incident direction and varying the position of Slit 2.

After the beam passes through Slit 1, it presents as a broad Gaussian distribution. Therefore, changing the position of Slit 2 is equivalent to slicing different parts of a wide Gaussian distribution, which differs from the initial distribution of the beam interacting with the laser, effectively changing the pre-selection. As shown in Fig. 3.23(a), by integrating the results from all positions, we observe that the traveling-wave results remain very stable, while the standing-wave results depend on the positions of the two slits. This further proves the superiority of the traveling-wave measurement.

When summarizing the standing-wave results for each position of Slit 2, as shown in Fig. 3.23(c), and plotting these results in a 3D graph, smoothing and projection yield the final result shown in Fig. 3.23(d). Compared to the distribution in Fig. 3.23(b) with-

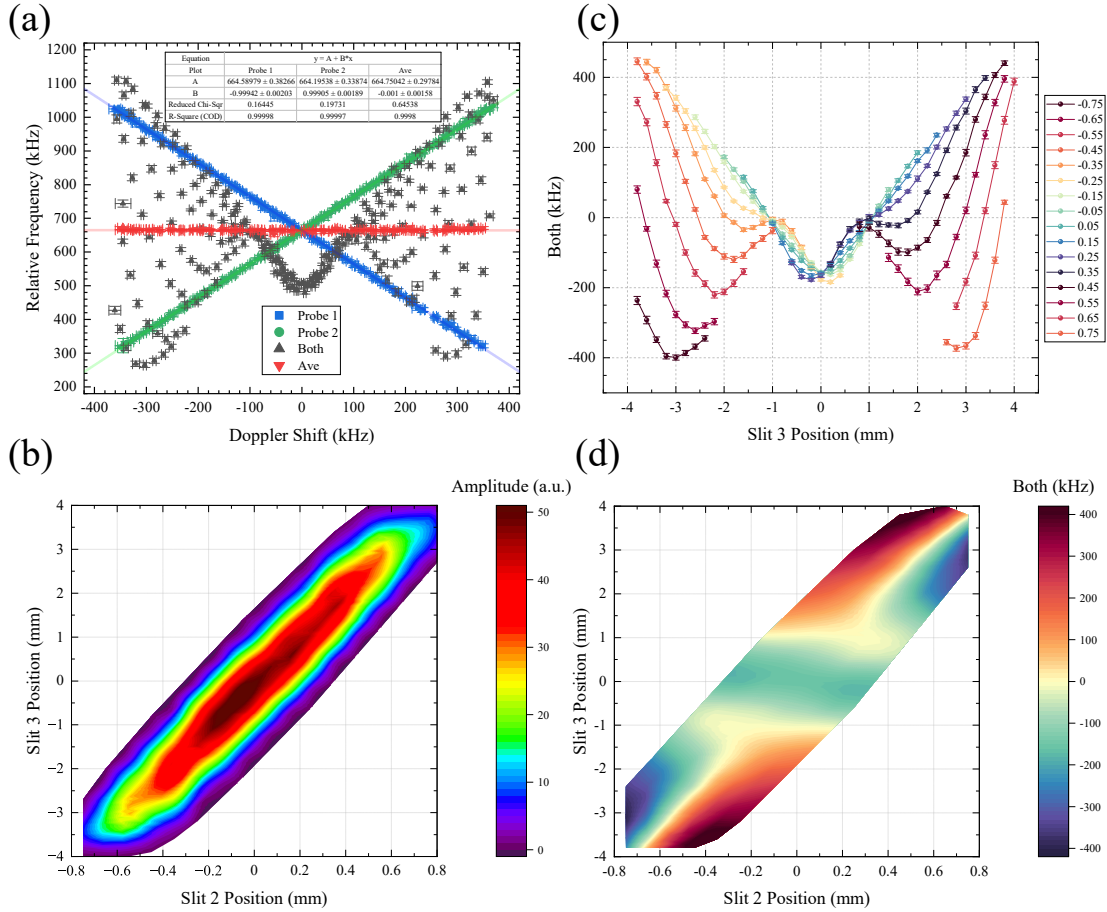


Figure 3.23 Experimental results when varying the Slit 3 position at each Slit 2 location with a fixed laser incidence direction. (a) All results combined, with the average value remaining stable. (b) Results of beam distribution measurements when varying Slit 3 position at each Slit 2 location without any laser. (c) Results of standing wave measurements at each Slit 2 position, with varying Slit 3 positions, where different colors represent different Slit 2 positions. (d) Three-dimensional plot of the results in (c), smoothed and projected, revealing clear interference patterns.

out the laser, a noticeable interference pattern appears in the standing-wave results. This suggests that there may be an interference-like mechanism under the influence of the standing wave. This phenomenon may indicate the modulation effect of pre-selection on post-selection. The specific mechanism and physical significance of this need further investigation.

3.3.4.7 Detector Efficiency Bias at Different Positions

If the detection efficiency at different positions of the detector varies, it could lead to different contributions from atoms at different positions in the beam, potentially introducing post-selection effects. Given the significant danger posed by the electron multiplier tube connected to high-voltage channels in a vacuum, the experiment chooses to explore this issue by simultaneously adjusting the positions of Slit 1 and Slit 2 to translate the beam. This method allows for the investigation of the impact of varying

detection efficiencies across different beam positions without the need for repositioning the detector itself.

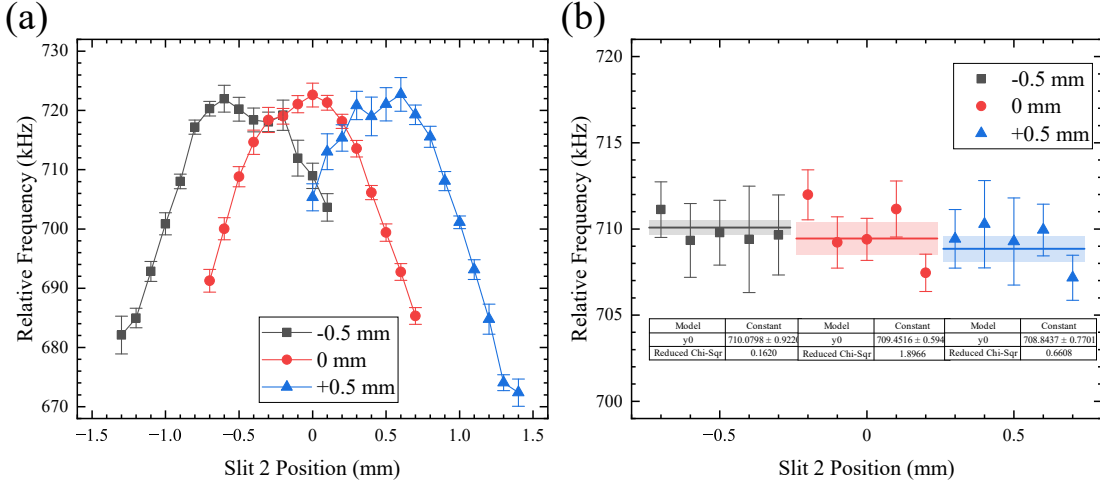


Figure 3.24 Exploring the results at different detector positions by laterally shifting both Slit 1 and Slit 2, and changing the beam orientation. (a) Changes in the results when the Slit 2 position is varied with a fixed Slit 1 position at $1 \mu\text{W}$ power. (b) After power extrapolation, the results at the three beam positions are nearly identical.

As shown in Figure 3.24(a), in the experiment, simultaneously shifting the positions of Slit 1 and Slit 2 by ± 0.5 mm results in the beam ultimately hitting the detector with a shift of ± 0.5 mm. When the position of Slit 1 is fixed and the position of Slit 2 is changed, the post-selection effect from the equivalent slit at the Stern-Gerlach magnet can be observed for all three beam orientations. In the flat region unaffected by post-selection effects, power extrapolation is performed, as shown in Figure 3.24(b), and the results for all three orientations are nearly identical. This suggests that when the detector position is changed by ± 0.5 mm, the results remain consistent, indicating that the position shift does not significantly affect the measurements.

3.3.5 Summary and Discussion

Based on the various experimental phenomena discussed above, it is evident that when there is a strong post-selection effect in front of the detector, it is difficult to observe the impact of the post-selection effect by changing different experimental parameters. This also explains why this systematic error was not detected in previous experiments. Additionally, by observing the measurement results of the beam distribution under various experimental conditions, it is clear that when the laser direction is fixed and perpendicular to the beam, the distribution results in standing wave measurements are mostly symmetric, whereas in traveling wave measurements, the results are significantly asymmetric. This work began with the asymmetric distribution phenomenon and ultimately led to the discovery of the post-selection effect. In other words, using trav-

eling waves instead of standing waves for measurement facilitated the discovery and investigation of the post-selection effect.

It is noteworthy that in precision spectroscopy experiments with helium atoms, although previous studies have mentioned that slits in front of the detector could influence the experimental results, the research on this phenomenon has not been in-depth. Some studies simply attributed it to light-force-induced frequency shifts^[248], or even considered it part of the recoil effect, intentionally aligning the detector laser and the slits to avoid its influence^[256]. When this effect is viewed as part of the light-force-induced frequency shift or recoil effect, the correction is usually only a few kHz and has minimal impact on the experimental results. However, this experiment shows that the post-selection effect leads to significant frequency shifts. It must be pointed out that the mechanism of this effect is entirely different from that of the recoil effect and should not be confused. Although similar to light-force-induced frequency shifts, the post-selection effect also involves changes in atomic momentum due to interaction with the laser, its resulting deviation is much larger than the impact of light-force-induced frequency shifts. For example, in our group's work on light-force-induced frequency shifts^[178], this effect can be seen as a special case under strong post-selection.

Moreover, this effect is not only present in helium atom precision spectroscopy experiments, but also widely exists in historical experiments across various systems, such as helium Rydberg state microwave spectroscopy^[160], helium ion spectroscopy^[257], and hydrogen atom spectroscopy^[244]. Analyzing the experimental setup diagrams of these experiments, it is clear that small holes or slits were used in front of the detectors to obtain narrow beams and improve the signal-to-noise ratio. The results of these experiments are crucial for determining physical constants and deriving physical laws, and therefore, it is necessary to study and correct the post-selection effects based on each setup's conditions. For example, in the “proton radius puzzle,” the CODATA2018 still considers the 1995 hydrogen atom Lamb shift measurement by Berkland et al.^[244], but this experiment required correction for the post-selection effect, which directly impacted the determination of the proton radius.

In comparison to previous experimental setups, to avoid the impact of the post-selection effect, in the final transition frequency measurement experiment, the position of the second slit was moved from in front of the detector to before the detection light, and no slits were set in front of the detector. Since beam spectroscopy experiments require the beam's transverse distribution to be as narrow as possible, and due to the limitations of the apparatus length, the distance between the first two slits before the

detection light could no longer be extended. Therefore, in the experiment, the slit aperture was narrowed to 0.3 mm. As a result, the obtained beam divergence angle was approximately 0.1 mrad, which is consistent with the divergence level from previous experiments. However, this adjustment also led to a reduction in atomic signal strength and a decrease in the spectral signal-to-noise ratio, limiting further improvement in spectral statistical errors.

3.4 $2^3S - 2^3P$ Transition Frequency Measurement Error Analysis

After completing the improvements to the beamline setup and detection optics methods described earlier, and identifying the impact of the newly recognized post-selection effect on our previous experimental results, this experiment measured the absolute transition frequency of the $2^3S_1 - 2^3P_0$ transition of ${}^4\text{He}$ under conditions where the post-selection effect was ensured to have no influence. The measurement method, results, and data analysis process for the spectrum in this experiment have been detailed in Sections 3.1 and 3.2. Next, a detailed discussion of the systematic errors in the experiment will be provided.

3.4.1 Doppler Effect

When probing the spectrum in the beamline setup, the first-order Doppler effect is usually the largest source of systematic error. In this experiment, the SCTOP method was used, employing a traveling wave for detection, which achieves the same Doppler cancellation effect as the cat-eye method, active fiber feedback method, and other standing wave methods, as detailed in Section 2.5. The experiment was conducted over a velocity range of $100 \sim 400$ m/s, with random measurement sequences, and the final results are shown in Figure 2.24. The results at each velocity point have been corrected for systematic errors such as the Zeeman effect, second-order Doppler effect, and quantum interference. A constant fit to the data gives a statistical error of 0.22 kHz; a linear fit yields a slope of $-0.0036(32)$ kHz m⁻¹s, with the intercept deviating by $+0.89(82)$ kHz from the constant fit results. In this experiment, the error of 0.82 kHz in the intercept from the linear fit is taken as the residual first-order Doppler effect.

Due to relativistic effects, the second-order Doppler effect (SOD) causes a redshift in the frequency center, which can be expressed as:

$$\Delta\nu_{\text{SOD}} = -\frac{v^2}{2c^2}\nu_0 \quad (3.22)$$

Due to the variation in the second-order Doppler effect at different velocities, cor-

rections were made at each velocity point, with the maximum correction being less than ± 0.25 kHz. Considering that the longitudinal velocity spread is approximately ± 5 m/s, there is also an error when correcting for the second-order Doppler effect, and the resulting error is less than 10 Hz.

3.4.2 Zeeman Effect

3.4.2.1 Calculation of Zeeman Shift Coefficient

To assess the impact of the magnetic field on the experimental results, it is necessary to calculate the Zeeman shift coefficient. Theoretically, the Landé g -factor is typically calculated. Therefore, we referred to the method of S. A. Lewis et al.^[135,258] for the calculation of the Zeeman shift coefficient. Given that the theoretical method for calculating the Landé g -factor has been updated, this experiment used the results calculated by Z. C. Yan et al. in 1994^[188], which were also verified in 2012 by M. Puchalski et al. using a different calculation method^[259]. Both theoretical methods for calculating the g -factor have taken relativistic corrections into account and extended the calculations to the α^2 order.

By comparing the theoretical calculation results from the two references^[188,259], the g -factor value finally adopted in this work is:

$$\begin{aligned} g'_L &= 0.99873657 \\ g'_S &= 2.00224150 \\ g_x &= -5.3855 \times 10^{-6} \\ g_{Q1} &= 22.88613573 \\ g_{Q2} &= -14.057066130 \end{aligned} \quad (3.23)$$

Here, g'_L and g'_S represent the relativistically corrected orbital and spin Landé factors, respectively, and their relationships with the electron's Landé factors are given by:

$$\begin{aligned} g'_L &= \sqrt{\frac{(2L+1)L(L+1)}{6}}g_L + \delta g_L \\ g'_S &= \sqrt{\frac{(2S+1)S(S+1)}{6}}g_S + \delta g_S \end{aligned} \quad (3.24)$$

The deviations δg_S and δg_L are provided by the theoretical calculations. g_S and g_L represent the electron's spin and orbital Landé factors, respectively:

$$\begin{aligned} g_S &= 2 \left[1 + \frac{\alpha}{2\pi} - 0.328478965 \left(\frac{\alpha}{2\pi} \right)^2 \right] \\ g_L &= 1 - \frac{m}{M} \end{aligned} \quad (3.25)$$

where m/M is the mass ratio between the electron and the atomic nucleus. For the 2^3P state, since $L = 1$ and $S = 1$, we have $g'_L = g_L + \delta g_L$ and $g'_S = g_S + \delta g_S$.

According to standard angular momentum theory^[260], the Zeeman Hamiltonian can be expanded as^[188]:

$$\begin{aligned} & \langle LSJ'M_J | \hat{H}_{\text{zeeman}} | LSJM_J \rangle = \\ & (\mu_B H) \sqrt{6} (-1)^{1-M_J} \sqrt{(2J+1)(2J'+1)} \begin{pmatrix} J' & 1 & J \\ -M_J & 0 & M_J \end{pmatrix} \\ & \left[\left\{ \begin{array}{ccc} L & J' & S \\ J & L & 1 \end{array} \right\} (-1)^{J+J'+L+S} g'_L + \left\{ \begin{array}{ccc} J & J' & 1 \\ S & S & L \end{array} \right\} (-1)^{L+S} g'_S \right. \\ & + (-1)^{J'} \left. \left\{ \begin{array}{ccc} L & L & 2 \\ S & S & 1 \\ J' & J & 1 \end{array} \right\} g_x \right] \quad (3.26) \\ & + \frac{(\mu_B H)^2}{R_\infty} \frac{2}{3} (-1)^{J+J'-M_J} \sqrt{(2J+1)(2J'+1)} \\ & \left[\left(\begin{array}{ccc} J' & 0 & J \\ -M_J & 0 & M_J \end{array} \right) \left\{ \begin{array}{ccc} L & J' & S \\ J & L & 0 \end{array} \right\} (-1)^{L+S} g_{Q1} \right. \\ & \left. - \left(\begin{array}{ccc} J' & 2 & J \\ -M_J & 0 & M_J \end{array} \right) \left\{ \begin{array}{ccc} L & J' & S \\ J & L & 2 \end{array} \right\} (-1)^{L+S} g_{Q2} \right] \end{aligned}$$

Here, H represents the external magnetic field strength, $\mu_B = 1.399625$ MHz/Gauss is the Bohr magneton, and $R_\infty = 109737.315709$ cm⁻¹ is the Rydberg constant. It is important to note that, in comparison with another reference^[261], it can be observed that the term $(\mu_B B)^2$ in the original reference^[188] was not divided by the factor R_∞ .

The total Hamiltonian is $\hat{H} = \hat{H}_0 + \hat{H}_{\text{zeeman}}$, where \hat{H}_0 corresponds to the original energy levels E_J . In the calculation, $E_2 = 0$ can be set, and the fine structure interval results are used to determine E_1 and E_2 . These interval results are obtained from previous measurements in our group^[227], where $E_1 = 2291.17635$ MHz and $E_0 = 31908.13090$ MHz. For $M_J = \pm 2$, due to the absence of angular momentum coupling, solving yields:

$$\left[E_2 + \frac{1}{2} \mu_B B M_J \left(g'_L + g'_S + \frac{1}{15} g_x \right) + \frac{2}{3\sqrt{3}} \left(g_{Q1} - \frac{g_{Q2}}{\sqrt{10}} \right) \left(\frac{\mu_B B}{R_\infty} \right)^2 \right] \quad (3.27)$$

For $M_J = \pm 1$, the coupling between 2^3P_1 and 2^3P_2 must be considered:

$$\left[\begin{array}{cc} E_1 + \frac{1}{2} \mu_B B M_J \left(g'_L + g'_S - \frac{1}{3} g_x \right) + \frac{2}{3\sqrt{3}} \left(g_{Q1} + \frac{g_{Q2}}{2\sqrt{10}} \right) \left(\frac{\mu_B B}{R_\infty} \right)^2 & \frac{1}{2} \mu_B B \left(g'_L - g'_S + \frac{2}{15} g_x \right) - \frac{g_{Q2}}{\sqrt{30}} \left(\frac{\mu_B B}{R_\infty} \right)^2 \\ \frac{1}{2} \mu_B B \left(g'_L - g'_S + \frac{2}{15} g_x \right) - \frac{g_{Q2}}{\sqrt{30}} \left(\frac{\mu_B B}{R_\infty} \right)^2 & E_2 + \frac{1}{2} \mu_B B M_J \left(g'_L + g'_S + \frac{1}{15} g_x \right) + \frac{2}{3\sqrt{3}} \left(g_{Q1} + \frac{g_{Q2}}{2\sqrt{10}} \right) \left(\frac{\mu_B B}{R_\infty} \right)^2 \end{array} \right] \quad (3.28)$$

For $M_J = 0$, the coupling between the three substates must be considered:

$$\begin{bmatrix} E_0 + \frac{2}{3\sqrt{3}}g_{Q1}\left(\frac{\mu_B B}{R_\infty}\right)^2 & \sqrt{\frac{2}{3}}\mu_B B\left(g'_L - g'_S - \frac{1}{6}g_x\right) & -\frac{2}{3\sqrt{15}}g_{Q2}\left(\frac{\mu_B B}{R_\infty}\right)^2 \\ \sqrt{\frac{2}{3}}\mu_B B\left(g'_L - g'_S - \frac{1}{6}g_x\right) & E_1 + \frac{2}{3\sqrt{3}}\left(g_{Q1} - \frac{g_{Q2}}{\sqrt{10}}\right)\left(\frac{\mu_B B}{R_\infty}\right)^2 & \sqrt{\frac{1}{3}}\mu_B B\left(g'_L - g'_S + \frac{2}{15}g_x\right) \\ -\frac{2}{3\sqrt{15}}g_{Q2}\left(\frac{\mu_B B}{R_\infty}\right)^2 & \sqrt{\frac{1}{3}}\mu_B B\left(g'_L - g'_S + \frac{2}{15}g_x\right) & E_2 + \frac{2}{3\sqrt{3}}\left(g_{Q1} + \frac{g_{Q2}}{\sqrt{10}}\right)\left(\frac{\mu_B B}{R_\infty}\right)^2 \end{bmatrix} \quad (3.29)$$

Since the magnetic field strength B in the experiment is between 10 Gauss and 20 Gauss, and the magnetic field is relatively small, these matrices can be diagonalized. After obtaining the eigenvalues, a Taylor expansion can be performed under small magnetic field conditions to obtain the Zeeman shift coefficients required for the experiment. The frequency shift $\delta\nu_{\text{Zeeman}}(J, M_J)$ for each substate is (to 8 significant digits):

$$\begin{aligned} \delta\nu_{\text{Zeeman}}(0, 0) &= (+ 0.044309476 \text{ kHz/G}^2) B^2 \\ \delta\nu_{\text{Zeeman}}(1, 0) &= (+ 0.24205289 \text{ kHz/G}^2) B^2 \\ \delta\nu_{\text{Zeeman}}(1, \pm 1) &= (\pm 2.1009190 \text{ MHz/G}) B + (0.21476788 \text{ kHz/G}^2) B^2 \\ \delta\nu_{\text{Zeeman}}(2, 0) &= (- 0.28634663 \text{ kHz/G}^2) B^2 \\ \delta\nu_{\text{Zeeman}}(2, \pm 1) &= (\pm 2.1009175 \text{ MHz/G}) B - (0.21475841 \text{ kHz/G}^2) B^2 \\ \delta\nu_{\text{Zeeman}}(2, \pm 2) &= (\pm 4.2018349 \text{ MHz/G}) B + (6.2640882 \text{ mHz/G}^2) B^2 \end{aligned} \quad (3.30)$$

For the 2^3S_1 state, the result expanded to the α^3 order can be directly used. From the calculation in reference^[262], $g_S(2^3S_1) = -g_J(2^3S_1) = 2.0022373778 \text{ MHz/G}$, we obtain:

$$\delta\nu_{\text{Zeeman}}(2^3S_1, M_J = \pm 1) = \mu_B M_J g_S(2^3S_1) B = (\pm 2.8023815 \text{ MHz/G}) B \quad (3.31)$$

These results are consistent with the calculations of T. Zelevinsky in his PhD thesis^[263] and also match our group's previous calculations^[223,229].

For the $2^3S_1 - 2^3P_0$ transition measured in this experiment, the first-order coefficient only considers the 2^3S_1 state, and the second-order coefficient only considers the 2^3P_0 state. The first-order coefficient is $\alpha = 2.8023815 \text{ MHz/G}$, and the second-order coefficient is $\beta = 0.044309476 \text{ kHz/G}^2$.

3.4.2.2 Verification of Zeeman Shift Coefficients

After calculating the Zeeman shift coefficients, experimental verification is required. As shown in Figure 2.14(b), by adjusting the current in the cosine coils, magnetic fields within the range of 0 to 20 Gauss can be achieved. Prior to interacting with the probe light, the atoms have been pumped into the $M_J = \pm 1$ states. Therefore, by

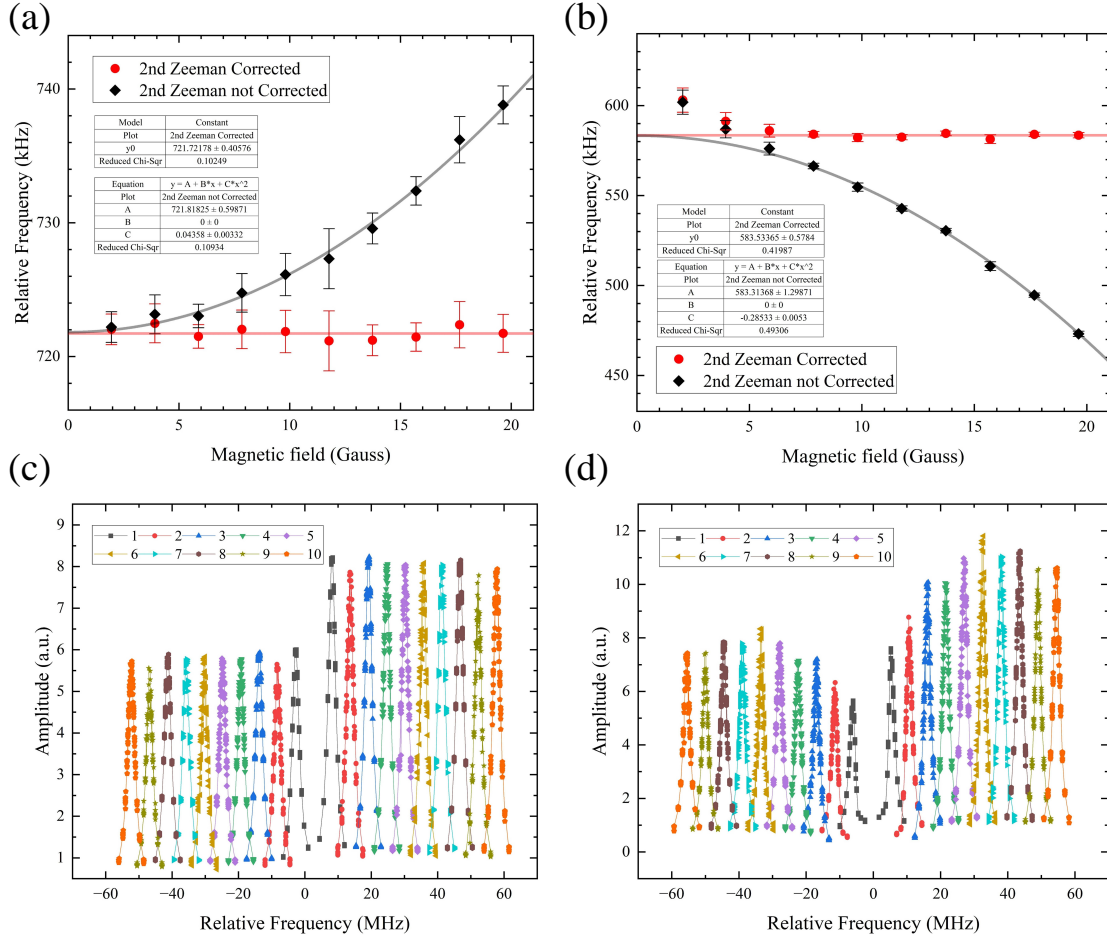


Figure 3.25 (a) and (b) show the results of the $2^3S_1 - 2^3P_0$ and $2^3S_1 - 2^3P_2$ transitions at different magnetic field strengths, comparing results with and without second-order Zeeman effect correction. Since the 2^3P_1 and 2^3P_2 states interfere below 7 Gauss, only results above 7 Gauss are selected for fitting in panel (b). The second-order fitting results in (a) and (b) agree with the calculated coefficients. Due to experimental precision limitations, verification is only possible at the 0.001 kHz/G² level. (c) and (d) show the scans of single spectra at different magnetic field strengths. Different colors and numbers in the figure represent the current of the cosine coils. For both transitions, the coil current and resulting magnetic field are in excellent linear correlation, with a coefficient of 1.964 Gauss/A. At low currents below 3 A, i.e., when the magnetic field is less than 7 Gauss, the peak area of the $2^3S_1 - 2^3P_0$ transition shows no significant change, while the peak area of the $2^3S_1 - 2^3P_2$ transition is significantly smaller at higher magnetic fields.

scanning the frequency, two peaks corresponding to the positive and negative shifts can be observed. The center frequencies of these two peaks can be expressed as:

$$\begin{aligned} f_+ &= f_c + \alpha B + \beta B^2 \\ f_- &= f_c - \alpha B + \beta B^2 \end{aligned} \tag{3.32}$$

where f_c is the center frequency without the Zeeman effect, and α and β are the first and second-order Zeeman coefficients, respectively. By averaging and subtracting the

center frequencies of the two peaks, we obtain:

$$\begin{aligned} f_0 &= \frac{f_+ + f_-}{2} = f_c + \beta B^2 \\ f_B &= \frac{f_+ - f_-}{2} = \alpha B \end{aligned} \quad (3.33)$$

Therefore, the magnetic field strength can be obtained from the measured positive and negative peak frequencies in the experiment, and the Zeeman shift coefficients can be verified. For the $2^3S_1 - 2^3P_0$ transition, as shown in Figure 3.25(a), the horizontal axis represents the magnetic field strength calculated from the frequency difference and the first-order Zeeman coefficient, while the vertical axis represents the average center frequency, which corresponds to the result after the first-order Zeeman effect has been removed. The second-order coefficient obtained from the fitting agrees with the calculated value. After correcting for the second-order Zeeman effect, the results at all magnetic field strengths are essentially consistent.

For the $2^3S_1 - 2^3P_2$ transition, as shown in Figure 3.25(b), due to the small energy gap between the 2^3P_1 and 2^3P_2 states at low magnetic fields, interference occurs between them. Therefore, noticeable deviations appear below 7 Gauss, while the results above 7 Gauss are consistent with the calculated values. Observing the peak areas of the two measured peaks in the experiment, as shown in Figures 3.25(c) and (d), it is clear that the peak area significantly decreases below 7 Gauss, while no noticeable changes are observed when measuring the $2^3S_1 - 2^3P_0$ transition. This indicates that there is indeed interference between the 2^3P_1 and 2^3P_2 states. Therefore, when performing 2^3P_J interval measurements, it is essential to ensure that the magnetic field strength is greater than 7 Gauss.

3.4.2.3 Zeeman Effect on the Results

In the experiment, the first-order Zeeman effect is eliminated by averaging the positive and negative peaks, and the second-order Zeeman effect is corrected using the resulting magnetic field. From equation 3.33, we obtain:

$$\begin{aligned} f_c &= f_0 - \beta B^2 \\ &= \frac{f_+ + f_-}{2} - \beta \left(\frac{f_+ - f_-}{2\alpha} \right)^2 \end{aligned} \quad (3.34)$$

The calculation error of the coefficients mainly arises from the g -factor. By comparing the results calculated using different theoretical g -factors and considering whether to include the $(\mu_B B)^2$ term, the deviation is also at the Hz level.

In the experiment, the current for the cosine coils is supplied by a low-noise DC power supply (E3633A, Keysight), with a current stability better than 2 mA. For absolute frequency measurements, the current is set to 8 A, and the error caused by current fluctuations is:

$$\frac{\Delta f}{f} = \frac{\Delta(\beta B^2)}{\beta B^2} = 2 \frac{\delta B}{B} = 2 \frac{\delta I}{I} = \frac{2 \times 2 \times 10^{-3}}{8} = 5 \times 10^{-4} \quad (3.35)$$

For a current of 8 A, the corresponding magnetic field is approximately 15.7 Gauss, and the second-order Zeeman correction is about 10.9 kHz. Therefore, the error caused by current fluctuations is approximately 5.5 Hz.

Assuming that the residual magnetism after magnetic shielding is B_0 , the absolute frequency shift δf_{B_0} caused by the residual magnetism can be derived as ($B \gg B_0$):

$$\begin{aligned} f_+ &= f_c + \alpha(B + B_0) + \beta(B + B_0)^2 \\ f_- &= f_c - \alpha(B + B_0) + \beta(B + B_0)^2 \\ f_c &= \frac{f_+ + f_-}{2} - \beta B^2 - 2\beta B_0 B - B_0^2 \\ \delta f_{B_0} &= -2\beta B_0 B - B_0^2 \approx -2\beta B_0 B \end{aligned} \quad (3.36)$$

In the experiment, the residual magnetism in the central area of the magnetic shielding is measured to be less than 20 nT (i.e., 2×10^{-4} Gauss), corresponding to a frequency shift of less than 1 Hz. In summary, the systematic error caused by the Zeeman effect is less than 10 Hz.

3.4.3 Laser Power

In previous work from our research group, the frequency of the $2^3S - 2^3P$ transition showed a strong correlation with laser power. When the power approached or exceeded the saturation intensity, nonlinear effects became very significant. Typically, measurements were made in the low-power linear region, such as in previous studies where the power was kept below 1/4 of the saturation intensity, in order to eliminate the impact of power on the results. This power-dependent effect has also been observed in the work of other research groups, but since the ac-Stark effect for this transition is almost negligible^[143], the physical mechanism behind the power dependence has not been clearly explained.

In this work, the detection optical path utilizes the SCTOP method, where traveling waves replace standing waves, thus significantly reducing the power dependence effect. As shown in Figure 2.25, measurements were performed at different speeds in the experiment. Each point in the figure represents the result after extrapolating the angle

for the traveling wave and standing wave results at the corresponding velocity, i.e., the slope of the power extrapolation for vertical incidence. Without angle extrapolation, the traveling wave results remain almost unchanged, while for standing waves, the power extrapolation slope varies significantly at different incident angles. The slope is largest near the perpendicular incidence (within the Doppler ± 100 kHz range). As the velocity decreases, the standing wave power extrapolation slope increases significantly, with the maximum exceeding 100 kHz/ μW , while the traveling wave slope remains relatively stable, around 10 kHz/ μW .

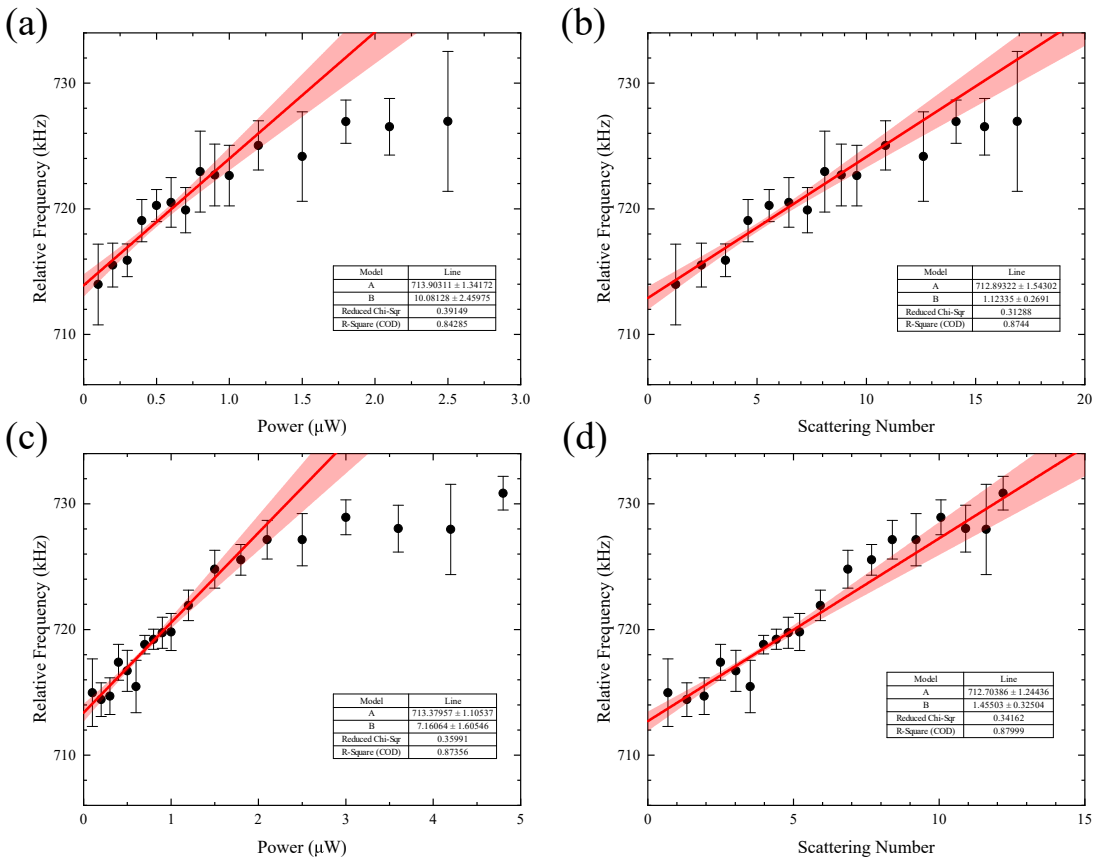


Figure 3.26 Detailed power extrapolation results at 147 m/s and 270 m/s, and the corresponding results after converting power to scattering rates. In the figure, only data with power less than 1 μW are considered for fitting, and the red shaded area represents the 1σ confidence band. Panels (a) and (b) show the results at 147 m/s, while panels (c) and (d) show the results at 270 m/s.

Detailed power extrapolation results at 147 m/s and 270 m/s are shown in Figure 3.26(a) and (c). Even with the traveling wave method, nonlinear effects are still evident when the power exceeds a certain value. As in the previous method, when using results below 1 μW , a nearly perfect linear relationship between power and frequency is observed, and the results after power extrapolation at both speeds are consistent. During the previous simulations of standing wave experiments, it was found that even at

high power, the scattering number and frequency results maintained a good linear relationship. Therefore, a similar treatment was applied to the traveling wave data in this work, as shown in Figures 3.26(b) and (d). Comparing the results with respect to power and scattering numbers, the results from both treatments are consistent. Hence, controlling the laser power below 1 μW ensures the reliability of the power extrapolation method. When the beam speed is low, lower power values were used to ensure linearity. However, excessively low detection power severely reduces the signal-to-noise ratio, so appropriate power values are chosen for measurements. In the final measurements, power values of 0.2, 0.4, and 0.6 μW were used for the $100 \sim 250$ m/s range, while for the $250 \sim 400$ m/s range, power values of 0.3, 0.6, and 0.9 μW were used.

For power values below 1 μW , the stability and linearity of the power measurements must be tightly controlled. To avoid interference from external stray light, four optical filters were placed in front of the power meter probe (S120C, Thorlabs). Before measuring the laser intensity, when the laser is actively blocked, the power meter reading is almost zero. It was also found that variations in probe position affected power measurements. Therefore, a cage structure was used, ensuring that the probe was placed in the same position each time. The power measurements remained consistent within each group of spectra, with measurements taken 30 minutes apart. Additionally, the power meter body (PM200D, Thorlabs) needs to remain stationary and preferably always connected to the power supply to maintain stable power measurements.

The power and polarization locking methods used in this experiment are detailed in Section 2.4.4. The detector used for power locking is placed in a dark box to avoid interference from external stray light. The current signal from the detector is amplified by a current amplifier (SR570, SRS) and split into two channels: one is fed into the locking loop, and the other is sent to a data acquisition card. Thus, in the experiment, in addition to the power meter readings, the voltage values read by the data acquisition card are also monitored. Long-term averaging is required in the experiment, and power meter or detector absolute values inevitably fluctuate with room temperature variations. Furthermore, each power locking measurement has some deviation, so every 8 spectra form a group (actually 9 spectra, with the first one discarded due to SCTOP feedback time, totaling about 30 minutes). After completing one group, the power point is changed, and measurements are continued. In the data processing, both the power meter readings and the averaged voltage values from the acquisition card are used as power values, and the results from both methods are consistent, as detailed in Section 3.2.

Asymmetry in power measurements can also cause certain deviations. By fixing

one side's power and changing the power on the other side, it was found that the resulting slope is half of the normal power extrapolation slope. In the data processing, all power levels are normalized and then returned to the original data for fitting. The final result falls within the error range, as shown in Figure 3.6, so no additional corrections were made.

The previous discussion explains that performing linear power extrapolation below $1 \mu\text{W}$ and addressing power locking and asymmetry during measurements does not introduce significant additional deviations. Therefore, the error due to power is primarily associated with the linearity of the power and measurement deviations. The linearity of the power meter used in the experiment is 0.5 %, corresponding to a maximum error of 5 nW. The fluctuations and zero-point offset of the power measurement are also ± 5 nW, so the total power deviation is less than 10 nW. Since the traveling wave power extrapolation slope is below $20 \text{ kHz}/\mu\text{W}$, the error due to power is less than 200 Hz.

3.4.4 Quantum Interference Effect

In a multi-level system, there exists interference between adjacent resonant energy levels. However, because the energy gaps between adjacent levels in atomic systems are usually much larger than the natural linewidth, this interference effect has often been neglected in previous experiments. Starting in 2012, Professor E. A. Hessel's research group began examining the results of the 2^3P_J level interval measurements in helium atoms. They found that as the measurement precision improved, this interference effect became significant and could no longer be ignored. They proposed a corresponding theoretical calculation method to correct the interval measurement results^[218-219,264]. This method has also been applied in precision spectroscopic experiments for other systems, such as hydrogen^[33].

This interference effect can be estimated using an empirical formula:

$$\delta\nu_{\text{QI}} = \frac{\Gamma^2}{2\pi \times \Delta_{\text{int}}} \quad (3.37)$$

For example, in the measurement of the $2^3P_1 - 2^3P_2$ interval, the natural linewidth $\Gamma \approx 2\pi \times 1.62 \text{ MHz}$ and the energy gap $\Delta_{\text{int}} \approx 2\pi \times 2.29 \text{ GHz}$ between the adjacent 2^3P_1 state, resulting in a quantum interference effect of approximately $\delta\nu_{\text{QI}} \approx 1.14 \text{ kHz}$. In our group's previous work, we calculated the quantum interference effects for the three measurable transitions^[177,223]. Under the experimental conditions at that time, the quantum interference values for the $2^3S_1 - 2^3P_{0,1,2}$ transitions were $\delta\nu_{\text{QI}}(0, 1, 2) = +0.08(3) \text{ kHz}$, $+0.60(10) \text{ kHz}$, and $-0.60(10) \text{ kHz}$, respectively. Since the energy gap

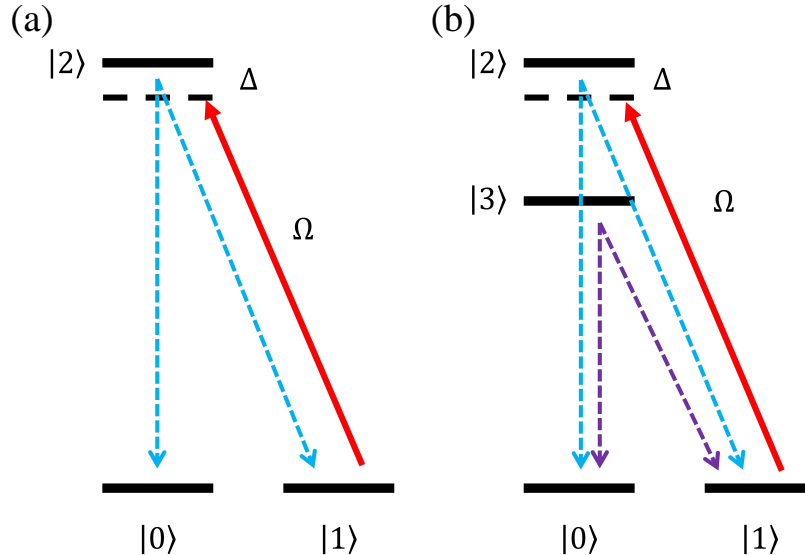


Figure 3.27 Schematic diagram of the energy level structure for the line shape simulation. (a) Without quantum interference effects. (b) With quantum interference effects.

between the 2^3P_1 and 2^3P_2 states is relatively small, these two states are more strongly affected by quantum interference. Therefore, in this experiment, the $2^3S_1 - 2^3P_0$ transition, which is least affected by quantum interference, was selected for measurement. Next, we will apply the theoretical calculation method proposed by Hessel's group and compare the line shapes with and without considering quantum interference. This will allow us to perform a correction for the quantum interference effect in our experimental results.

First, the line shape without considering quantum interference effects is derived. As shown in Fig. 3.27(a), the state $|0\rangle$ represents the final state $2^3S_1(M_J = 0)$, $|1\rangle$ represents the ground state $2^3S_1(M_J = +1)$, and $|2\rangle$ represents the excited state $2^3P_0(M_J = 0)$. Since the positive and negative branches of the effect are the same, only the $M_J = +1$ branch is calculated here. The density matrix is solved as:

$$\begin{aligned}\dot{\rho}_{11} &= \frac{i}{2}\Omega_{12}^*\rho_{12} - \frac{i}{2}\Omega_{12}\rho_{21} + \gamma_2\rho_{22} \\ \dot{\rho}_{12} &= -\left(\frac{\gamma_2}{2} + i\Delta_2\right)\rho_{12} - \frac{i}{2}\Omega_{12}(\rho_{22} - \rho_{11}) \\ \dot{\rho}_{22} &= -\frac{i}{2}\Omega_{12}^*\rho_{12} + \frac{i}{2}\Omega_{12}\rho_{21} - \gamma_2\rho_{22},\end{aligned}\quad (3.38)$$

Initially, $\rho_{11} = 1$, $\rho_{12} = \rho_{22} = \rho_{00} = 0$, and the final population in the final state is obtained by solving $\rho_{00} = 1 - \rho_{11} - \rho_{22}$. During the solution process, the distribution of the laser field and the configuration of the apparatus must be considered, as these factors lead to changes in the evolution time. For example, in our previous experimental setup, the Gaussian waist diameter of the laser was $L = 2.8$ mm, and the beam velocity was $v = 700$ m/s, so the evolution time $T_L = L/v$. The laser intensity changes according

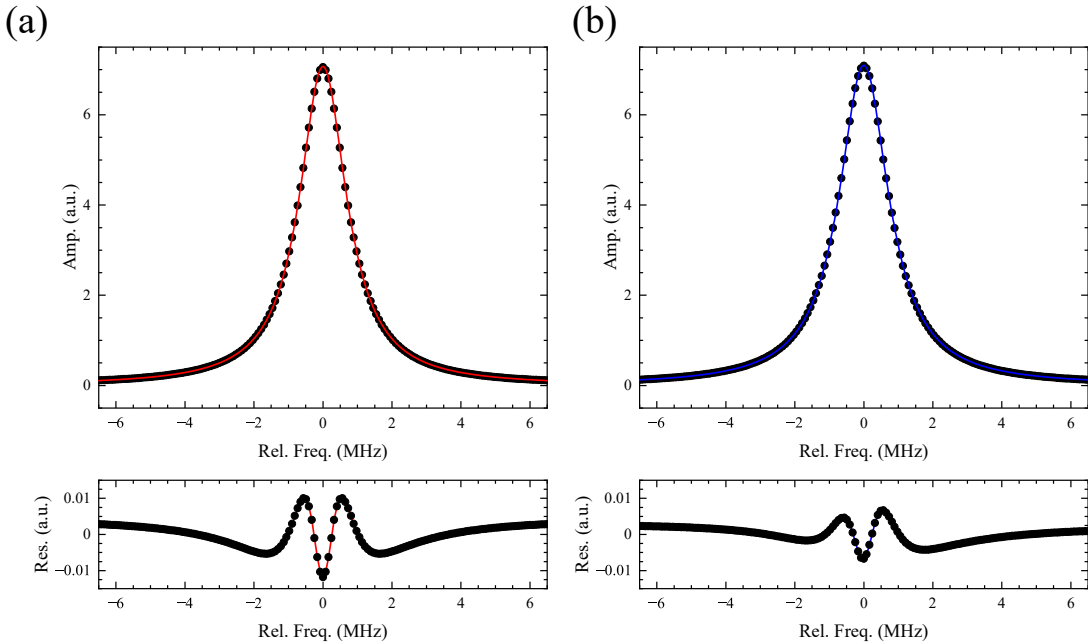


Figure 3.28 (a) Line shape and Lorentzian fitting residuals when quantum interference effects are not considered. (b) Line shape and Lorentzian fitting residuals when quantum interference effects are considered. Considering that the $2^3S_1 - 2^3P_0$ transition is minimally affected by quantum interference, no obvious difference in the fitting residuals can be observed. Therefore, the more sensitive $2^3S_1 - 2^3P_1$ transition is chosen for illustration. The fitting parameters are beam velocity $v = 700 \text{ m/s}$, laser power $P = 0.1 \mu\text{W}$, and beam diameter $L = 2.8 \text{ mm}$.

to the Gaussian distribution. Since the detector is far from the interaction region, only the steady-state solution after a sufficient evolution time is required in the simulation. A Lorentzian line shape is used to fit the results, and the fitting results and residuals are shown in Fig. 3.28(a). It can be seen that the spectral line shape and the residuals are symmetric, and the result fitted with a Lorentzian line shape does not require further corrections.

However, if quantum interference effects are considered, as shown in Fig. 3.27(b), because the electric dipole transition between $2^3S_1(M_J = 0)$ and $2^3P_1(M_J = 0)$ is forbidden, only the interference from the $2^3P_2(M_J = 0)$ state (denoted as $|3\rangle$) needs to

be considered. At this point, the density matrix becomes:

$$\begin{aligned}
 \dot{\rho_{11}} &= i\frac{\Omega_2}{2}\rho_{12} - i\frac{\Omega_2^*}{2}\rho_{21} + \gamma_{2\rightarrow 1}\rho_{22} + i\frac{\Omega_3}{2}\rho_{13} - i\frac{\Omega_3^*}{2}\rho_{31} \\
 &\quad + \gamma_{23\rightarrow 1}(\rho_{23} + \rho_{32}) + \gamma_{3\rightarrow 1}\rho_{33} \\
 \dot{\rho_{12}} &= i\frac{\Omega_2^*}{2}(\rho_{11} - \rho_{22}) - \left(\frac{\gamma_2}{2} + i\Delta\right)\rho_{12} - \frac{\gamma_{23}}{2}\rho_{13} - i\frac{\Omega_3^*}{2}\rho_{32}, \\
 \dot{\rho_{22}} &= i\frac{\Omega_2^*}{2}\rho_{21} - i\frac{\Omega_2}{2}\rho_{12} - \gamma_2\rho_{22} - \frac{\gamma_{23}}{2}(\rho_{23} + \rho_{32}) \\
 \dot{\rho_{13}} &= i\frac{\Omega_3^*}{2}(\rho_{11} - \rho_{33}) - \frac{\gamma_{23}}{2}\rho_{12} - i\frac{\Omega_2^*}{2}\rho_{23} - \left(\frac{\gamma_3}{2} + i(\Delta + \omega_{23})\right)\rho_{13} \\
 \dot{\rho_{23}} &= i\frac{\Omega_3}{2}\rho_{21} - \frac{\gamma_{23}}{2}(\rho_{22} + \rho_{33}) - i\frac{\Omega_2}{2}\rho_{13} - \left(\frac{\gamma_2 + \gamma_3}{2} + i\omega_{23}\right)\rho_{23} \\
 \dot{\rho_{33}} &= i\frac{\Omega_3^*}{2}\rho_{31} - i\frac{\Omega_3}{2}\rho_{13} - \gamma_3\rho_{33} - \frac{\gamma_{23}}{2}(\rho_{23} + \rho_{32})
 \end{aligned} \tag{3.39}$$

Here, the term $\gamma_{23\rightarrow 1}$ represents the interference effect between the two states. Similar to the previous method, the final ρ_{00} is fitted using a Lorentzian, and as shown in Fig. 3.28(b), a shift in the center can be observed.

This system of equations applies to experimental conditions with varying beam velocities, laser powers, and beam sizes. The equations and the parameters used in the fittings are based on the related work by the Hessel group^[218-219,264] and the doctoral thesis^[220]. In the previous work of this research group, this method was used to simulate quantum interference effects in detail^[177]. Given the significant changes in the current experimental setup, a new simulation is required. Since a traveling wave is used

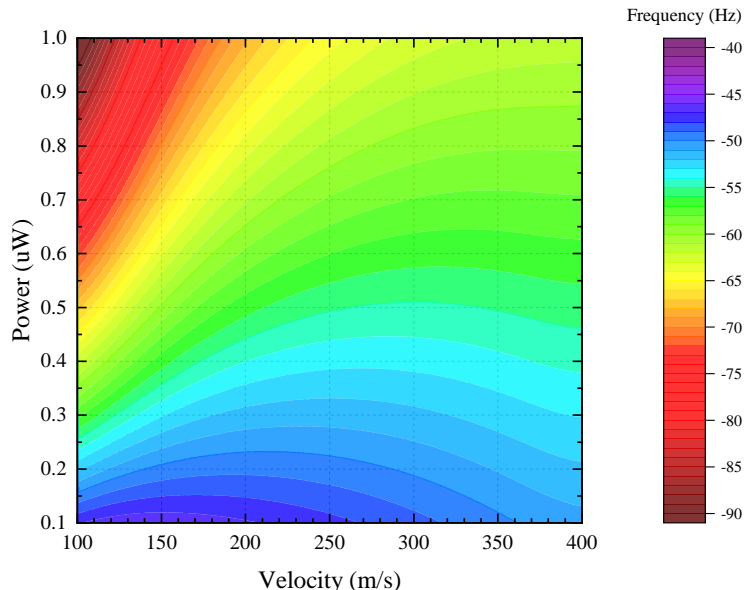


Figure 3.29 Results of simulating quantum interference effects under different power and velocity conditions.

in place of the standing wave for detection, in addition to adjusting experimental parameters like the apparatus length, the light intensity also needs to be processed separately. Otherwise, the linewidth obtained from the simulation will be significantly broader than the experimental detection results.

In the experiment, a linearly polarized laser is used for detection. Since the magnetic field direction is the same as the laser incidence direction, the linearly polarized light can only be decomposed into left- or right-handed circular polarization, exciting σ^\pm transitions. Therefore, in the quantum interference calculation, regardless of whether a traveling wave or standing wave is used for detection, the light intensity must be halved. Furthermore, since a traveling wave is used for detection in the current experiment, when calculating the Rabi frequency, the light intensity must be halved again. For example, when the beam velocity is 111 m/s and the power is 0.6 μW , if the light intensity is not processed as described above, the fitted linewidth will be 4.6 MHz. If only the laser polarization is halved, the fitted linewidth is 3.1 MHz, which matches the results of the standing wave detection in the experiment. After halving the light intensity again, the fitted linewidth is 2.4 MHz, which is consistent with the traveling wave experiment results. Multiple verifications have been performed under different velocity and light intensity conditions, and the results show that after the above processing, the simulation results match the experimental values.

Finally, substituting the current experimental conditions, i.e., beam velocity $v = 100 \sim 400$ m/s and beam diameter $L = 1.1$ mm, simulations of quantum interference effects under different power and velocity conditions are shown in Fig.3.29. Based on the experimental conditions, the final quantum interference correction is + 0.05(2) kHz.

3.4.5 Recoil Effect

The $2^3S - 2^3P$ transition measured in this experiment is a single-photon transition. When an atom interacts with the laser, by conservation of momentum and energy, we have:

$$\begin{aligned} m\Delta v &= \hbar k \\ \frac{1}{2}m(\Delta v)^2 &= h\Delta v = h(v - v_0) \\ k &= \frac{2\pi}{\lambda} = \frac{2\pi c}{v_0} \end{aligned} \tag{3.40}$$

Thus, the correction due to the recoil effect is:

$$f_{\text{Recoil,correction}} = -\Delta v = -\frac{hc^2}{2mv_0^2} \tag{3.41}$$

Substituting numerical values, the correction is found to be -42.48 kHz, where the mass of the helium atom m is taken from the latest CODATA2018^[95], and ν_0 is the frequency of the measured transition. Additionally, the frequencies of the other two branches of the $2^3S - 2^3P_J$ transitions and the spin-averaged centroid frequency are also substituted for the calculation, with the resulting deviation being less than 10 Hz.

3.4.6 Frequency Standard

In the experiment, the frequency reference for the optical comb is the hydrogen atomic clock (VCH-1003M Option L, VREMYA—CH), with a frequency accuracy of $\pm 1 \times 10^{-13}$. Therefore, the error caused by the frequency reference is $\Delta f \approx 2 \times 10^{-13} \times 276.7365 \times 10^{12} \approx 55$ Hz.

3.4.7 Other Systematic Errors

In the previous standing wave experiment, due to the asymmetry in the reflection of the laser beams on both sides, there was a central offset when fitting with a single Lorentzian line shape^[177]. This effect arises because the two laser beams in the standing wave setup in the experiment did not completely overlap, and there was a certain power mismatch. Therefore, the actual spectrum was the result of the superposition of the Lorentzian line shapes of the two laser beams. When fitting the spectrum with a single Lorentzian function, a central shift was observed. However, in the current experiment, since a traveling wave detection method is used, only one laser interacts with the atoms, and this phenomenon no longer occurs.

Additionally, since the pressure in the detection chamber is less than 10^{-7} Torr, and at room temperature, the pressure shift coefficient for the $2^3S - 2^3P$ transition is approximately -1.9 MHz/Torr^[265], the pressure-induced frequency shift is less than 0.2 Hz, which is negligible at the current experimental precision.

3.4.8 Total Error Table

Based on the discussion of the various systematic errors and corrections mentioned above, the total error for the $2^3S_1 - 2^3P_0$ transition measurement in this experiment is summarized in Table 3.1. The second-order Doppler effect has been corrected at each velocity, and therefore its correction is not included in the table.

The total error for the final result is 0.86 kHz, marking the first time the absolute frequency measurement precision for the $2^3S - 2^3P$ transition of helium atoms has been improved to below 1 kHz.

Table 3.1 $2^3S_1 - 2^3P_0$ Transition Frequency Measurement Error Table (Unit: kHz)

Source	Corrections	$\Delta f(1\sigma)$
Statistics		0.22
First-order Doppler		0.82
Second-order Doppler		0.01
Frequency calibration		0.06
Quantum interference	+0.06	0.02
Laser power		0.20
Zeeman effect		0.01
Recoil shift	-42.48	0.01
Total	276 764 094 712.45	0.86

3.5 $2^3S - 2^3P$ Transition Frequency and Nuclear Charge Radius

By combining the high-precision (< 200 Hz precision) measurements of the 2^3P_J intervals, the spin-averaged center frequency (Centroid Frequency) f_c for ${}^4\text{He}$ can be derived:

$$\begin{aligned} f_c &= \frac{\sum_J (2J+1)f_J}{\sum_J (2J+1)} = \frac{f_0 + 3f_1 + 5f_2}{9} \\ &= f_0 - \frac{3\nu_{01} + 5\nu_{02}}{9} = f_0 - \frac{8\nu_{01} + 5\nu_{12}}{9} = f_0 - \frac{8\nu_{02} - 3\nu_{12}}{9} \end{aligned} \quad (3.42)$$

Here, ν_{01} , ν_{12} , and ν_{02} represent the fine structure interval measurements. Substituting the interval results measured by our group, $\nu_{02} = 31\ 908\ 180.98$ (0.13) kHz and $\nu_{12} = 2\ 291\ 177.56$ (0.19) kHz^[227], the final result for the center frequency of the $2^3S - 2^3P$ transition is $f_c = 276\ 736\ 495\ 655.21$ (0.87) kHz.

Table 3.2 Comparison of the ${}^4\text{He}$ $2^3S - 2^3P$ Transition Center Frequency f_c (Unit: kHz)

$f_c - 276\ 736\ 495\ 000$	$\Delta f(1\sigma)$
Shiner <i>et al.</i> ^[143]	580
Cancio Pastor <i>et al.</i> ^[145-146]	649.5
Zheng <i>et al.</i> ^[177]	600.0
Zheng <i>et al.</i> + Correction	654.5
Patkóš <i>et al.</i> ^[37]	620
This work	655.21
	0.87

Table 3.2 and Figure 3.30 show the comparison of the experimental results from this study with other experimental results and theoretical values, including the corrections to our group's previous results^[177]. After the correction for the post-selection effect, the measurement results from the previous experiment are consistent with the

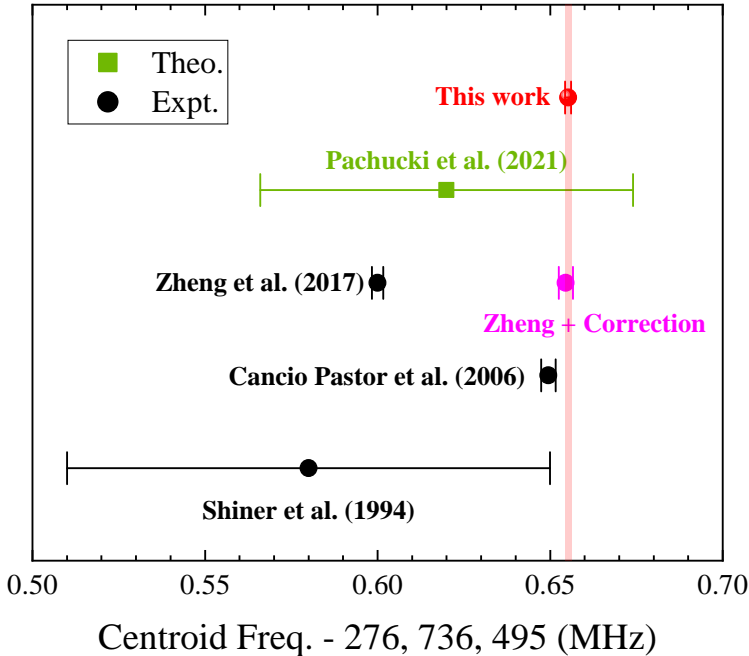


Figure 3.30 ${}^4\text{He}$'s $2^3S - 2^3P$ transition center frequency comparison. The pink points represent the results from our research group's 2017 measurements, with corrections for the post-selection effect, which are consistent with the results re-measured in this experiment under conditions without the post-selection effect.

results obtained in this study under conditions without the post-selection effect. The results from this experiment are consistent with the measurements made by Cancio Pastor et al. using the saturated fluorescence spectroscopy method within 2 standard deviations^[145-146]. The theoretical calculation results have a precision of only 54 kHz, which is consistent with all the experimental results shown in the figure.

It should be noted that the method of calculating the center frequency from a single transition frequency depends on the accuracy of the interval results. Therefore, using different interval results may lead to deviations in the center frequency. If the interval results from the Hessels group, $\nu_{12} = 2\ 291\ 176.590$ (0.025) kHz^[163] and $\nu_{01} = 29\ 616\ 955.018$ (0.060) kHz^[266], are substituted, the spin-averaged center frequency result becomes $f'_c = 276\ 736\ 495\ 654.33$ (0.86) kHz. The deviation between the center frequencies obtained from the two sets of intervals is $f_c - f'_c = 0.88$ (1.22) kHz, which is within the standard deviation range, indicating that the two sets of results are in agreement.

By combining the results of ${}^3\text{He}$ measured by Cancio Pastor et al.^[147], the isotope shift results can be calculated, as shown in Table 3.3. Compared with the results of the $2^3S - 2^1S$ transition and μHe^+ , as shown in Figure 3.31, the results of this experiment are basically consistent with those of the $2^3S - 2^1S$ transition, but there is a deviation of about 2.6 times the standard deviation when compared with the μHe^+ results. This

result seems to suggest that a similar phenomenon, observed in the H- μ H system with a different nuclear radius, also appears in the He- μ He system. However, since the ${}^3\text{He}$ results in this experiment still rely on the experimental results obtained by Cancio Pastor et al. using the saturated fluorescence method, their reliability needs further verification. Therefore, it cannot be concluded that the nuclear radius puzzle also exists in the He- μ He system. Additionally, since the experimental setup of the Shiner group is similar to that of this experiment, their experimental results also require correction for the post-selection effect. In future work, our group will measure the $2^3S - 2^3P$ transition in ${}^3\text{He}$, obtain independent isotope shift results in the atomic beam, and compare them with other systems. If subsequent experiments confirm a deviation between the results for helium and muonic helium, and similar deviations are observed in systems with few-electron atoms like hydrogen, lithium, and beryllium, this would indicate that the electromagnetic interaction between the muon and the electron is not symmetric, and the universality of lepton interactions might no longer hold, suggesting new physics beyond the Standard Model.

3.6 Impact of Post-Selection Effect on the 2^3P_J Interval

In previous experiments conducted by our group, the measurement of the 2^3P_J interval was an important research direction, as the measurement results could be used to determine the fine structure constant α ^[226-227]. Therefore, when the post-selection effect was found to be a significant systematic error affecting the results during the absolute frequency measurement of the $2^3S - 2^3P$ transition in this experiment, we also considered whether it would affect the interval measurement results. Below, we will evaluate the impact of the post-selection effect on interval measurement results, using the $2^3P_0 - 2^3P_2$ interval as an example.

Table 3.3 Comparison of isotope shift results from different systems

$v({}^3\text{He}, 2^3S - 2^3P)$ (centroid)	276 702 827 204.8 (2.4) kHz	Exp. ^[147]
$-\delta E_{\text{iso}}$ (point nucleus)	+33 667 149.3 (0.9) kHz	Theo. ^[199]
$-v({}^4\text{He}, 2^3S - 2^3P)$ (centroid)	-276 736 495 655.21 (87) kHz	this work
$\delta\nu_{\text{FNS}}$	-1 245.9 (2.9) kHz	
$C(2^3S - 2^3P)$	-1 212.2 (1) kHz/fm ²	Theo. ^[199]
δr^2	1.0733 (21) fm ²	
$2^3S - 2^1S$	1.0757 (15) fm ²	Exp. ^[172]
$\mu\text{He}^+(2S - 2P)$	1.0636 (31) fm ²	Exp. ^[217]

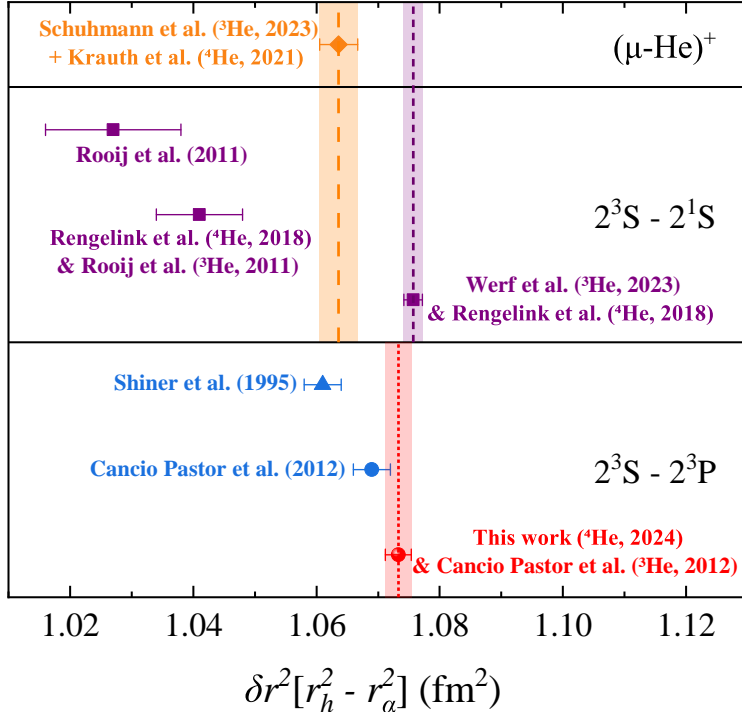


Figure 3.31 The difference in nuclear charge radii between ${}^3\text{He}$ and ${}^4\text{He}$. The results are divided into three groups, each corresponding to a different system or transition. The orange circles represent the measurements of muonic helium ions, the purple square points represent the measurements of the $2^3S - 2^1S$ transition, and the red points represent the results from the $2^3S - 2^3P$ transition measured in this experiment. The latest measurement results and their uncertainties for these three systems or transitions are represented by dashed lines and shaded bands in the corresponding colors. The blue points for the $2^3S - 2^3P$ transition represent previous experimental results, with triangle points indicating that the corresponding experimental results need to account for the post-selection effect.

3.6.1 Experimental Scheme

Referring to the interval measurement scheme in our previous work^[226-227], this experiment alternately measures the frequencies of the $2^3S_1 - 2^3P_0$ and $2^3S_1 - 2^3P_2$ transitions, and the interval result is obtained by subtracting the two frequencies. Since the frequency interval between these two transitions is approximately 32 GHz, using a single laser for hopping scans would place high demands on the laser and frequency locking systems, which cannot be achieved under the current experimental conditions. To address this, two lasers were used in the experiment, and a mechanical chopper was controlled by a program to ensure that only one laser interacted with the atoms. These two lasers were locked to the first-order sidebands of the Fiber-EOM, and frequency scans within the spectral measurement range (about 20 MHz) were performed. This method avoided systematic errors such as power instability that could occur when using the Fiber-EOM scan. As this was only for verification purposes, the experiment scanned the positive peaks of the two transitions under a single velocity and magnetic

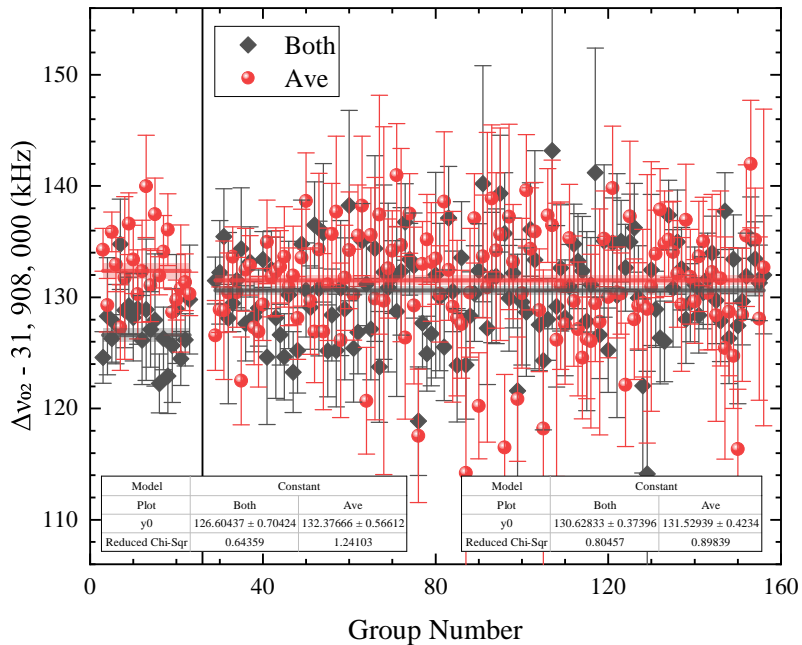


Figure 3.32 Measurement results of the ν_{02} interval. The first part of the figure shows the measurement results under higher powers ($0.3, 0.6, 0.9 \mu\text{W}$). Due to the nonlinear effects of power extrapolation during standing wave measurements, the results for standing waves and traveling waves are inconsistent. The second part of the figure shows the measurement results under lower powers ($0.1, 0.2, 0.3 \mu\text{W}$), where the results for traveling waves and standing waves are generally consistent.

field condition. The scanning method was the same as when measuring the absolute frequency, with the only difference being that only the frequencies of the two positive peaks were scanned instead of both positive and negative peaks.

3.6.2 Measurement Results and Discussion

As shown in Figure 3.32, the $2^3P_0 - 2^3P_2$ interval was measured in this experiment when the beam velocity was 295 m/s and the magnetic field current was 8 A. Due to the lower beam velocity in the experiment, the nonlinear effects during power extrapolation become more sensitive at lower velocities, causing a significant deviation between the traveling wave and standing wave results under higher powers ($0.3, 0.6, 0.9 \mu\text{W}$). Afterward, measurements were taken at lower powers ($0.1, 0.2, 0.3 \mu\text{W}$), where the traveling wave and standing wave results were consistent within the error range. Since no detailed power extrapolation tests were performed, the standing wave results may still be influenced by some power nonlinear effects, whereas the traveling wave results remain stable under both high and low power conditions. Therefore, the traveling wave measurement results were chosen as the final result. The final interval measurement result is $\nu_{02} = 31\ 908\ 131.53(0.43)$ kHz. The error in the result is statistical only, and

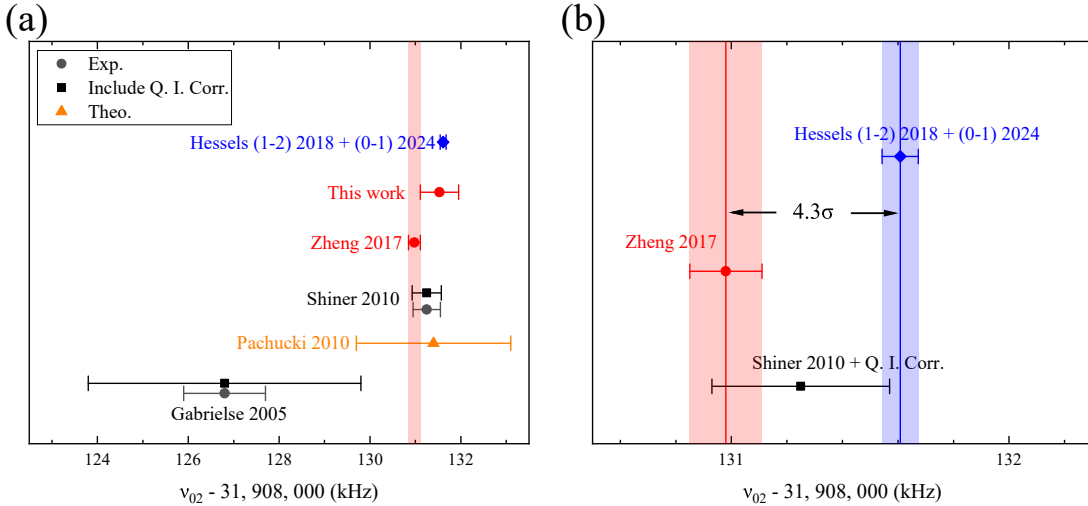


Figure 3.33 v_{02} interval measurement result comparison. (a) Summary of measurement results over the past 20 years. (b) Comparison of the latest measurement results. Results from experiments conducted in 2010 and earlier require quantum interference corrections, and the corrected results are shown as squares.

other potential systematic errors, such as laser power, magnetic field strength, and laser polarization, were not thoroughly evaluated. As shown in Figure 3.33(a), this result is consistent with the measurement result from our group in 2017^[227], indicating that the post-selection effect did not significantly impact the interval measurement.

During the interval measurement, it was observed that as the beam velocity decreased, the nonlinear effects of power increased significantly. To ensure the reliability of power extrapolation, the experimental power had to be reduced, leading to a significant decrease in the spectral signal-to-noise ratio. This indicates that, unlike absolute frequency measurements, lower speeds are not ideal for interval measurements. To meet the experimental needs of absolute frequency measurements, the beam velocity was reduced, and a Zeeman decelerator was added to the existing setup, but this inevitably resulted in the loss of many atoms. During the interval measurement, two transitions were measured alternately, which naturally immune to the Doppler effect, so there is no strict requirement for beam velocity. Additionally, at higher velocities, there are more atoms, and the signal-to-noise ratio is better.

Currently, the bottleneck for interval measurements in the beam lies in quantum interference effects, which can only be addressed by solving the density matrix. The reliability of this method still requires experimental validation. Based on Hessels' group's research^[163], if ionization detection methods are used in future experiments to directly measure the number of atoms in the 2^3P state, the effects of quantum interference can be avoided. A detailed discussion of this experimental plan can be found in Section 5.2.2.

Theoretically, using a simple model, the deviation caused by the post-selection

effect in interval measurements can also be estimated (for details, see Section 3.3.3):

$$\delta\nu_{\text{PSS}} = -\frac{\hbar}{mc^2} \frac{L}{\ell + L} (\nu_0^2 - \nu_2^2) \quad (3.43)$$

Here, ν_0 and ν_2 represent the center frequencies of the two transitions, and ℓ and L represent the distances between the laser and the front and rear slits, respectively. Substituting the experimental parameters from previous measurements, the resulting deviation is -13 Hz, indicating that the post-selection effect does not significantly affect the measurement results.

Both theoretical and experimental findings in this study conclude that the post-selection effect does not influence the interval result, which is consistent with the measurement results from our group in 2017^[227]. However, it is worth noting that in microwave direct interval measurement methods, Hessels' group improved the separated resonance cavity method and achieved higher precision results. In 2018, their measurement precision for the $2^3P_1 - 2^3P_2$ interval reached an impressive 25 Hz^[163], but this result deviated from our group's 2017 measurement by nearly five standard deviations. In 2024, their precision for the $2^3P_0 - 2^3P_1$ interval reached 60 Hz^[266]. As shown in Figure 3.33(b), when all results are converted to the interval ν_{02} , which is least affected by quantum interference effects, i.e., the $2^3P_0 - 2^3P_2$ interval, Hessels' group's results are about 630 Hz larger than our group's results, corresponding to 4.3 standard deviations. For this interval, the effect of quantum interference is less than 100 Hz, and this deviation is clearly much larger than the effect of quantum interference. Therefore, future interval measurement work needs to focus on examining various systematic errors.

3.7 Summary and Discussion

This chapter focuses on the discussion of a newly discovered systematic error in this work—the post-selection effect. Thanks to improvements in the experimental setup and detection optical path method, this work was able to detect the spectrum and beam distribution under various conditions such as different slit combinations and beam velocities, ultimately revealing this new systematic error effect. When a small slit exists in front of the detector, i.e., a stronger post-selection effect, changing experimental conditions such as the slit position, beam distribution, and laser incidence angle still keeps the results stable. This is the main reason why this systematic error was not identified in previous work. Due to the numerous variable parameters in the experiment, spectral and distribution measurements were carried out under different slit combinations and

optical path angles, further revealing a potentially wide spatial limitation in the current setup, leading to a weak post-selection effect, which was avoided in the final measurements. Moreover, by comparing experimental results under different conditions, the theoretical model and numerical simulations were validated and optimized, allowing for more precise corrections to the previous experimental results. Since structures such as slits and apertures are commonly found in precision spectroscopy setups, many important experimental results require detailed discussion and simulated corrections of the post-selection effect according to specific experimental conditions. Some key physical laws and conclusions may thus need to be revised.

After the setup modifications and the elimination of the post-selection effect, this experiment measured the ${}^4\text{He}$ atom $2^3S - 2^3P$ transition, improving the experimental precision of this transition to the sub-kHz level for the first time. However, there is still room for further improvement in the precision of this transition. In the current experiment, to avoid the influence of the post-selection effect, both slits used to capture the beam are positioned before the detection light. To obtain a sufficiently small divergence angle for the beam, the aperture of the two slits was restricted to 0.3 mm, which resulted in the final atomic beam intensity being 1 to 2 orders of magnitude weaker than expected, limiting further improvement in statistical precision. Although the current beam setup successfully slowed down the atoms, the lowest velocity achieved was only about 100 m/s, making measurements at lower velocities impossible. This leads to larger extrapolation errors in velocity and difficulties in reducing the errors induced by the Doppler effect. In the future, if cold atom technology is utilized to trap atoms in an optical molasses trap and then release them, it is expected that atoms with lower velocities can be obtained, further reducing the impact of the Doppler effect. Quantum interference effects are an unavoidable systematic error when measuring lower states. If methods such as ionization detection are used to directly probe the upper states, the quantum interference effect can be eliminated. Additionally, laser power and magnetic fields can be further minimized by optimizing the device design and improving control accuracy. If these improvements are realized, the measurement precision of this transition is expected to reach the level of hundreds of Hz.

Considering the significant discrepancies in isotope shift results for several systems, and given that the measurement precision for the ${}^4\text{He}$ atom $2^3S - 2^3P$ transition is already high and consistent across different methods, directly using the ${}^4\text{He}$ transition results to calculate the nuclear radius and compare it with the muonic helium ion results would provide a more straightforward and reliable comparison. However, the

current theoretical calculation precision is only 54 kHz, which is insufficient to obtain a sufficiently accurate nuclear radius result. If the calculations can be expanded to $m\alpha^8$ or higher orders, the theoretical precision of this transition will increase by several tens of times, and the nuclear radius result will match the precision of the muonic helium ion system, thus meeting the requirements for direct comparison.

Chapter 4 ${}^3\text{He}$ Atom $2^3S - 2^3P$ Transition Preliminary Measurement

4.1 Experimental Scheme

4.1.1 Transition Selection

The ${}^3\text{He}$ atomic nucleus has a spin of $I = 1/2$, resulting in hyperfine structure. The energy level structure of the 2^3S and 2^3P states is shown in Fig. 2.3. According to the Wigner-Eckart theorem, the coupling matrix for electric dipole transitions can be expressed as the product of the reduced matrix element and Clebsch-Gordan coefficients:

$$\begin{aligned}\langle Fm_F | e\mathbf{r}_q | F'm'_F \rangle &= \langle F \| e\mathbf{r} \| F' \rangle \langle Fm_F | F' 1m'_F q \rangle \\ &= \langle F \| e\mathbf{r} \| F' \rangle (-1)^{F'-1+m_F} \sqrt{2F+1} \left(\begin{array}{ccc} F' & 1 & F \\ m'_F & q & -m_F \end{array} \right) \quad (4.1)\end{aligned}$$

Here, $q = \pm 1$ and 0 correspond to σ^\pm and π transitions, respectively, and F' and F represent the upper and lower states, with the parentheses denoting Wigner $3-j$ symbols. The reduced matrix element can be further simplified into expressions involving the quantum numbers L , S , and J :

$$\langle F \| e\mathbf{r} \| F' \rangle = \langle J \| \mathbf{r} \| J' \rangle (-1)^{F'+J+1+I} \sqrt{(2F'+1)(2J+1)} \left\{ \begin{array}{ccc} J & J' & 1 \\ F' & F & I \end{array} \right\} \quad (4.2)$$

Where the curly brackets represent the Wigner $6-j$ symbols. Although the reduced matrix element $\langle J \| \mathbf{r} \| J' \rangle$ can be simplified further, this level of expansion is sufficient for the present experiment. Using the expression from equation 4.2, the probability ratio of an atom being in one of the 2^3P sublevels and transitioning to the two sublevels of 2^3S can be calculated. The result is shown in Table 4.1.

Table 4.1 Probability ratio for the transition from 2^3P sublevels to sublevels of 2^3S

2^3S	2^3P	$J = 2$ $F = 5/2$	$J = 1$ $F = 3/2$	$J = 1$ $F = 1/2$	$J = 2$ $F = 3/2$	$J = 0$ $F = 1/2$
$F = 1/2$		0	1/6	2/3	5/6	1/3
$F = 3/2$		1	5/6	1/3	1/6	2/3

Therefore, the $2^3S_1(F = 3/2) - 2^3P_2(F = 5/2)$ transition is suitable for cooling light. By selecting this transition and using a σ^+ polarized laser, all the atoms can be pumped to the dark state $M_F = +5/2$. If another transition were chosen, additional

repump light would be required. Hence, the lasers for MOT, TC, and Slower can simply replace the reference transition from ${}^4\text{He}$'s $2^3S_1 - 2^3P_2$ to ${}^3\text{He}$'s $2^3S_1(F = 3/2) - 2^3P_2(F = 5/2)$ without changing the frequency spacing between TC, Slower, and MOT.

Similar to ${}^4\text{He}$, if transitions to the 2^3P_1 or 2^3P_2 states are measured, the small energy gap between these levels will cause quantum interference effects to have a significant impact on the results. Currently, this effect can only be evaluated theoretically and cannot be eliminated experimentally. Furthermore, high-precision theoretical calculations of the hyperfine splitting in ${}^3\text{He}$ have already been performed^[267-268], so it is only necessary to measure one of the transitions. Therefore, the transition with minimal quantum interference effects, $2^3S_1(F = 3/2) - 2^3P_0(F = 1/2)$, is chosen for detection. For the optical pumping region, in order to ensure that as many atoms as possible are in the $2^3S_1(F = 3/2)$ state, the $2^3S_1(F = 3/2) - 2^3P_2(F = 5/2)$ transition is similarly chosen.

4.1.2 Calculation of the Zeeman Shift Coefficient

Following the same method as in Section 3.4.2 for ${}^4\text{He}$, the Zeeman shift coefficient for ${}^3\text{He}$ is calculated using the theoretical g -factor. Referring to the work of^[261], the Zeeman Hamiltonian under the standard angular momentum theory can be divided into four terms:

$$\langle LSJ'IF'M'_F | \hat{H}_{\text{Zeeman}} | LSJIFM_F \rangle = H_Z(1) + H_Z(2) + H_Z(3) + H_Z(4) \quad (4.3)$$

These four terms are:

$$H_Z(1) = (-1)^{F'+F+I-M_F+J'} \sqrt{6(2F'+1)(2F+1)(2J'+1)(2J+1)} \\ \times \left[(-1)^{J+L+S} g'_L \begin{Bmatrix} L & J' & S \\ J & L & 1 \end{Bmatrix} + (-1)^{L+S-J'} g'_S \begin{Bmatrix} J & J' & 1 \\ S & S & L \end{Bmatrix} \right] \\ + g_x \left[\begin{Bmatrix} L & L & 2 \\ S' & S & 1 \\ J' & J & 1 \end{Bmatrix} \right] \left(\begin{matrix} F' & 1 & F \\ -M_F & 0 & M_F \end{matrix} \right) \left\{ \begin{Bmatrix} J' & F' & I \\ F & J & 1 \end{Bmatrix} \right\} \delta_{M'_F, M_F}(\mu_0 B) \quad (4.4)$$

$$H_Z(2) = (-1)^{2F+I-M_F+2J+L+S} (2F+1)(2J+1) \left(\begin{matrix} F & 0 & F \\ -M_F & 0 & M_F \end{matrix} \right) \\ \times \left\{ \begin{Bmatrix} J & F & I \\ F & J & 0 \end{Bmatrix} \right\} \left\{ \begin{Bmatrix} L & J & S \\ J & L & 0 \end{Bmatrix} \right\} \delta_{F', F} \delta_{M'_F, M_F} \delta_{J', J} \frac{(\mu_0 B)^2 g_{Q_1}}{3 R_\infty} \quad (4.5)$$

$$H_Z(3) = (-1)^{F'+F+I-M_F+J+J'+L+S+1} \times \sqrt{(2F'+1)(2F+1)(2J'+1)(2J+1)} \begin{pmatrix} F' & 2 & F \\ -M_F & 0 & M_F \end{pmatrix} \quad (4.6)$$

$$\times \begin{Bmatrix} J' & F' & I \\ F & J & 2 \end{Bmatrix} \begin{Bmatrix} L & J' & S \\ J & L & 2 \end{Bmatrix} \delta_{M'_F, M_F} \frac{(\mu_0 B)^2}{3} \frac{g_{Q_2}}{R_\infty} \\ H_Z(4) = (-1)^{2F'-M_F+I+J} \sqrt{(2F'+1)(2F+1)(2I+1)(I+1)I} \times \begin{pmatrix} F' & 1 & F \\ -M_F & 0 & M_F \end{pmatrix} \begin{Bmatrix} I & F' & J \\ F & I & 1 \end{Bmatrix} \delta_{M_{F'}, M_F} \delta_{J', J} (\mu_0 B) g_I \quad (4.7)$$

Where the $H_Z(1)$ term includes the lowest-order Zeeman effect (the g_L and g_S terms), the correction due to the center-of-mass motion (the m/M term), and relativistic corrections (α^2 term). The $H_Z(2)$ and $H_Z(3)$ terms are the second-order effects of the magnetic field, and the $H_Z(4)$ term represents the interaction between nuclear spin and the magnetic field. For $M_F = \pm 5/2$, there is no angular momentum coupling:

$$\left[E_5 + \mu_B B \left(g'_L + g'_S + \frac{1}{15} g_x - \frac{1}{2} g_I \right) \right] \quad (4.8)$$

For $M_F = \pm 3/2$, it is necessary to consider the coupling between the three energy levels: $2^3P_2(F = 3/2)$, $2^3P_1(F = 3/2)$, and $2^3P_2(F = 5/2)$:

$$\begin{bmatrix} E_2 + H_{11} & H_{12} & H_{13} \\ H_{21} & E_4 + H_{22} & H_{23} \\ H_{31} & H_{32} & E_5 + H_{33} \end{bmatrix} \quad (4.9)$$

The expressions for the terms H_{ij} are:

$$\begin{aligned} H_{11} &= \mu_B B \left(\frac{9}{10} g'_L + \frac{9}{10} g'_S + \frac{3}{50} g_x + \frac{3}{10} g_I \right) + \frac{(\mu_B B)^2}{3\sqrt{3}R_\infty} \left(g_{Q1} - \frac{7}{10\sqrt{10}} g_{Q2} \right) \\ H_{12} &= -\frac{\mu_B B}{2\sqrt{5}} \left(g'_L - g'_S + \frac{2}{15} g_x \right) + \frac{(\mu_B B)^2}{10\sqrt{6}R_\infty} g_{Q2} \\ H_{13} &= \mu_B B \left(\frac{1}{5} g'_L + \frac{1}{5} g'_S + \frac{1}{75} g_x + \frac{2}{5} g_I \right) - \frac{(\mu_B B)^2}{5\sqrt{30}R_\infty} g_{Q2} \\ H_{22} &= \mu_B B \left(\frac{1}{2} g'_L + \frac{1}{2} g'_S - \frac{1}{6} g_x - \frac{1}{2} g_I \right) + \frac{(\mu_B B)^2}{3\sqrt{3}R_\infty} g_{Q1} + \frac{(\mu_B B)^2}{6\sqrt{30}R_\infty} g_{Q2} \\ H_{23} &= \frac{\mu_B B}{\sqrt{5}} \left(g'_L - g'_S + \frac{1}{45} g_x \right) - \frac{(\mu_B B)^2}{5\sqrt{6}R_\infty} g_{Q2} \\ H_{33} &= \mu_B B \left(\frac{3}{5} g'_L + \frac{3}{5} g'_S + \frac{1}{25} g_x - \frac{3}{10} g_I \right) + \frac{(\mu_B B)^2}{3\sqrt{3}R_\infty} g_{Q1} + \frac{(\mu_B B)^2}{15\sqrt{30}R_\infty} g_{Q2} \end{aligned} \quad (4.10)$$

$$H_{21} = H_{12}, \quad H_{31} = H_{13}, \quad H_{32} = H_{23}$$

For $M_F = \pm 1/2$, the coupling between five energy levels must be considered:

$$\begin{bmatrix} E_1 + H_{11} & H_{12} & H_{13} & H_{14} & H_{15} \\ H_{21} & E_2 + H_{22} & H_{23} & H_{24} & H_{25} \\ H_{31} & H_{32} & E_3 + H_{33} & H_{34} & H_{35} \\ H_{41} & H_{42} & H_{43} & E_4 + H_{44} & H_{45} \\ H_{51} & H_{52} & H_{53} & H_{54} & E_5 + H_{55} \end{bmatrix} \quad (4.11)$$

The expressions for these terms are:

$$\begin{aligned} H_{11} &= -\frac{\mu_B B}{2} g_I + \frac{(\mu_B B)^2}{3\sqrt{3}R_\infty} g_{Q1}, \quad H_{12} = \frac{\sqrt{2}(\mu_B B)^2}{15\sqrt{3}R_\infty} g_{Q2} \\ H_{13} &= -\frac{\sqrt{2}\mu_B B}{3} \left(g'_L - g'_S - \frac{1}{6}g_x \right), \quad H_{14} = \frac{2\mu_B B}{3} \left(g'_L - g'_S - \frac{1}{6}g_x \right) \\ H_{15} &= \frac{(\mu_B B)^2}{15R_\infty} g_{Q2} \\ H_{22} &= \mu_B B \left(\frac{3}{10}g'_L + \frac{3}{10}g'_S + \frac{1}{50}g_x + \frac{1}{10}g_I \right) + \frac{(\mu_B B)^2}{3\sqrt{3}R_\infty} g_{Q1} + \frac{7(\mu_B B)^2}{30\sqrt{30}R_\infty} g_{Q2} \\ H_{23} &= \frac{\sqrt{10}\mu_B B}{6} \left(g'_L - g'_S + \frac{2}{15}g_x \right) - \frac{(\mu_B B)^2}{10\sqrt{3}R_\infty} g_{Q2} \\ H_{24} &= \frac{\mu_B B}{6\sqrt{5}} \left(g'_L - g'_S + \frac{2}{15}g_x \right) - \frac{(\mu_B B)^2}{10\sqrt{6}R_\infty} g_{Q2} \\ H_{25} &= \frac{\sqrt{6}\mu_B B}{5} \left(\frac{1}{2}g'_L + \frac{1}{2}g'_S + \frac{1}{15}g_x + g_I \right) - \frac{(\mu_B B)^2}{30\sqrt{5}R_\infty} g_{Q1} + \frac{7(\mu_B B)^2}{15\sqrt{2}R_\infty} g_{Q2} \quad (4.12) \\ H_{33} &= \frac{\mu_B B}{3} \left(g'_L + g'_S - \frac{1}{3}g_x + \frac{1}{2}g_I \right) - \frac{(\mu_B B)^2}{3\sqrt{3}R_\infty} g_{Q1} \\ H_{34} &= \frac{\sqrt{2}\mu_B B}{3} \left(\frac{1}{2}g'_L + \frac{1}{2}g'_S - \frac{1}{6}g_x + g_I \right) + \frac{(\mu_B B)^2}{6\sqrt{15}R_\infty} g_{Q2}, \quad H_{35} = -\frac{(\mu_B B)^2}{15\sqrt{2}R_\infty} g_{Q2} \\ H_{44} &= \frac{\mu_B B}{6} \left(g'_L + g'_S - \frac{1}{3}g_x - g_I \right) + \frac{(\mu_B B)^2}{3\sqrt{3}R_\infty} g_{Q1} - \frac{(\mu_B B)^2}{6\sqrt{30}R_\infty} g_{Q2} \\ H_{45} &= \sqrt{\frac{3}{10}}\mu_B B \left(g'_L - g'_S + \frac{2}{15}g_x \right) - \frac{(\mu_B B)^2}{30R_\infty} g_{Q2} \\ H_{55} &= \frac{\mu_B B}{5} \left(g'_L + g'_S + \frac{1}{15}g_x + \frac{1}{2}g_I \right) + \frac{(\mu_B B)^2}{3\sqrt{3}R_\infty} g_{Q1} + \frac{2\sqrt{2}(\mu_B B)^2}{15\sqrt{15}R_\infty} g_{Q2} \\ H_{21} &= H_{12}, \quad H_{31} = H_{13}, \quad H_{32} = H_{23}, \quad H_{41} = H_{14}, \quad H_{42} = H_{24} \\ H_{43} &= H_{34}, \quad H_{51} = H_{15}, \quad H_{52} = H_{25}, \quad H_{53} = H_{35}, \quad H_{54} = H_{45} \end{aligned}$$

The energy levels are treated in the same way as for ${}^4\text{He}$, where the lowest energy level is set to zero, and the energies of the other levels are derived from the hyperfine splittings of the 2^3P state. In the calculation, the hyperfine splitting is based on the

results from K. Pachucki et al.^[267]. Taking $E_5 = 0$, the energy levels from the lowest to the highest are denoted as E_5 to E_1 , with the unit in MHz:

$$\begin{aligned} E_5 &= 0 \\ E_4 &= E_5 + 1780.8115 \\ E_3 &= E_4 + 4512.2141 \\ E_2 &= E_3 + 668.0095 \\ E_1 &= E_2 + 27424.8464 \end{aligned} \quad (4.13)$$

And the g -factor used in the calculation is:

$$\begin{aligned} g'_L &= 0.99983454458567 \\ g'_S &= 2.002238875776 \\ g_x &= -5.39177042 \times 10^{-6} \\ g_I &= 2.3174824 \times 10^{-3} \\ g_{Q1} &= 22.88702897921 \\ g_{Q2} &= -14.05758960346 \end{aligned} \quad (4.14)$$

By diagonalizing the above matrices and obtaining the eigenvalues, a Taylor expansion is performed under the condition of a small magnetic field, yielding the Zeeman shift coefficient required for the experiment. Finally, the frequency shifts for each sub-level $\delta\nu_{\text{Zeeman}}(J, F, M_J)$ are obtained (to 8 significant digits):

$$\begin{aligned} \delta\nu_{\text{Zeeman}}(0, 1/2, \pm 1/2) &= (\mp 0.0016218032 \text{ MHz/G}) B + (0.042404278 \text{ kHz/G}^2) B^2 \\ \delta\nu_{\text{Zeeman}}(2, 3/2, \pm 1/2) &= (\pm 1.2608573 \text{ MHz/G}) B + (0.97326993 \text{ kHz/G}^2) B^2 \\ \delta\nu_{\text{Zeeman}}(2, 3/2, \pm 3/2) &= (\pm 3.7825719 \text{ MHz/G}) B + (0.12076551 \text{ kHz/G}^2) B^2 \\ \delta\nu_{\text{Zeeman}}(1, 1/2, \pm 1/2) &= (\pm 1.4011338 \text{ MHz/G}) B - (0.61603510 \text{ kHz/G}^2) B^2 \\ \delta\nu_{\text{Zeeman}}(1, 3/2, \pm 1/2) &= (\pm 0.69975599 \text{ MHz/G}) B + (0.084615515 \text{ kHz/G}^2) B^2 \\ \delta\nu_{\text{Zeeman}}(1, 3/2, \pm 3/2) &= (\pm 2.0992680 \text{ MHz/G}) B + (0.20206932 \text{ kHz/G}^2) B^2 \\ \delta\nu_{\text{Zeeman}}(2, 5/2, \pm 1/2) &= (\pm 0.84003094 \text{ MHz/G}) B - (0.48424202 \text{ kHz/G}^2) B^2 \\ \delta\nu_{\text{Zeeman}}(2, 5/2, \pm 3/2) &= (\pm 2.5200928 \text{ MHz/G}) B - (0.32282697 \text{ kHz/G}^2) B^2 \\ \delta\nu_{\text{Zeeman}}(2, 5/2, \pm 5/2) &= (\pm 4.2001547 \text{ MHz/G}) B + (3.1321655 \text{ mHz/G}^2) B^2 \end{aligned} \quad (4.15)$$

For the 2^3S state, the energy levels^[267] and two g -factor values^[188,262] are as

follows:

$$\begin{aligned} E_{S_2} &= 0 \\ E_{S_1} &= 6739.69993 \\ g_S &= 2.0022373827 \\ g_{Q1} &= 11.467588230724521 \end{aligned} \quad (4.16)$$

For $M_F = \pm 3/2$, without angular momentum coupling:

$$\left[E_{S_2} + \mu_B B \left(g_S - \frac{1}{2} g_I \right) + \frac{(\mu_B B)^2}{3R_\infty} g_{Q1} \right] \quad (4.17)$$

For $M_F = \pm 1/2$, the coupling between two energy levels needs to be considered:

$$\begin{bmatrix} E_{S_1} + \frac{2\mu_B B}{3} \left(g_S + \frac{1}{4} g_I \right) + \frac{(\mu_B B)^2}{3R_\infty} g_{Q1} & \frac{\sqrt{2}\mu_B B}{3} (g_S + g_I) \\ \frac{\sqrt{2}\mu_B B}{3} (g_S + g_I) & E_{S_2} + \frac{\mu_B B}{3} \left(g_S - \frac{1}{2} g_I \right) + \frac{(\mu_B B)^2}{3R_\infty} g_{Q1} \end{bmatrix} \quad (4.18)$$

Finally, the frequency shifts for each sublevel $\delta\nu_{\text{Zeeman}}(J, F, M_J)$ are as follows:

$$\begin{aligned} \delta\nu_{\text{Zeeman}}(1, 1/2, \pm 1/2) &= (\pm 1.8687949 \text{ MHz/G}) B + (0.25954341 \text{ kHz/G}^2) B^2 \\ \delta\nu_{\text{Zeeman}}(1, 3/2, \pm 1/2) &= (\pm 0.93358656 \text{ MHz/G}) B - (0.25953886 \text{ kHz/G}^2) B^2 \\ \delta\nu_{\text{Zeeman}}(1, 3/2, \pm 3/2) &= (\pm 2.8007597 \text{ MHz/G}) B + (2.2761411 \text{ mHz/G}^2) B^2 \end{aligned} \quad (4.19)$$

4.2 Experimental Setup Improvements

To meet the requirements for the ${}^3\text{He}$ experiment, improvements are needed to the original setup. Given that ${}^3\text{He}$ gas samples are precious, the gas flow design must first be optimized to minimize the consumption of ${}^3\text{He}$. Additionally, the optical pumping scheme needs to be adjusted. By switching frequencies, the atoms should be populated as much as possible into the required positive and negative sublevels to obtain spectral data with sufficient signal-to-noise ratio. Since ${}^3\text{He}$ has nuclear spin, it will undergo deflection in the Stern-Gerlach magnet. Therefore, the direction of the beam needs to be altered to ensure that the beam is fully detected, minimizing the impact of the post-selection effect. The following sections provide a detailed introduction to these setup modifications.

4.2.1 Gas Flow Path Improvements

Since the natural abundance of ${}^3\text{He}$ is only 1.37 ppm and high-purity samples are very valuable, it is necessary to improve the gas flow path to minimize its usage. The modified inlet structure is shown in Figure 4.1(a). Compared to the ${}^4\text{He}$ experiment, a

small gas tank and pressure gauge were added. In previous experiments, it was found that the pressure regulator often exhibited noticeable gas leakage, so two ball valves were chosen. Each valve is opened only once and then immediately closed, using only the gas in the approximately 3cm-long pipeline (6 mm compression stainless steel pipe, with an inner diameter of about 4 mm) between the gas cylinder and the ball valves. This gas is then introduced into a small gas tank of about 300 mL volume via multiple ball valves. Before venting, the pipeline is evacuated for a long time using the molecular pump in the source chamber, and before opening any ball valve, the previous one must be closed to ensure the purity of the gas entering the gas tank. During the experiment, the gas is released from the small gas tank and introduced into the source chamber through a microleak valve. The gas tank is equipped with a calibrated pressure gauge to monitor real-time pressure changes in the gas line. The modified gas path is leak-tested with helium to ensure there are no leakage points. Krypton gas remains in the same state as in the ${}^4\text{He}$ measurements, introduced into the source chamber after passing through a pressure regulator and microleak valve.

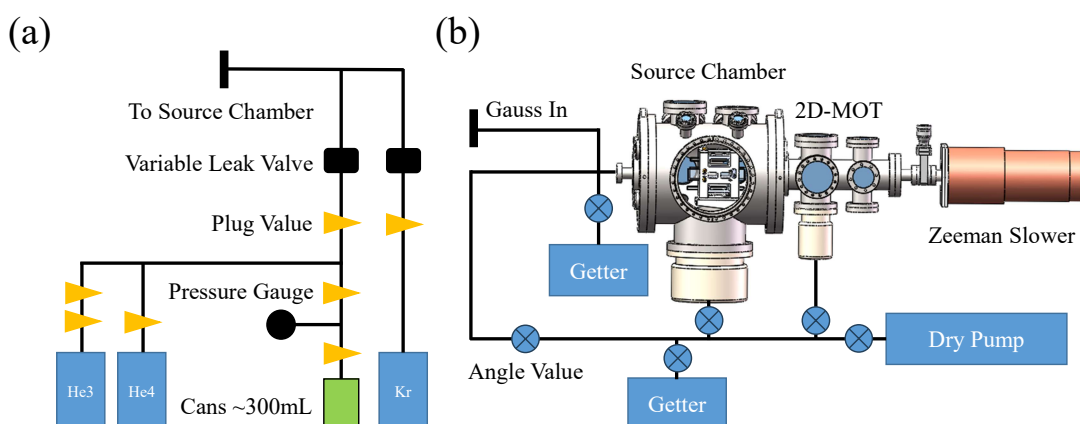


Figure 4.1 (a) Schematic of the inlet section. ${}^3\text{He}$ is first placed into a small gas tank and then introduced into the source chamber through a microleak valve. (b) Schematic of the outlet section. By controlling the angle valves, the gas in the molecular pump stages after the source chamber and 2D-MOT chamber is removed by a getter pump, and nitrogen and other gases are pumped out before being returned to the source chamber.

Since the pressure inside the system decreases step by step, the pressure in the source chamber is approximately 6×10^{-6} Torr, the pressure in the 2D-MOT chamber is one order of magnitude lower, and the pressure after the Slower section is on the order of 10^{-8} Torr. The majority of the gas consumption occurs in the source chamber and 2D-MOT chamber. Therefore, only the molecular pumps before the Slower section require a return gas treatment. The gas flow path in part of the setup is shown in Figure 4.1(b). The angle valves control whether the gas should be returned after the molecular pump stages in the source chamber and 2D-MOT chamber. During the re-

turn process, the gas from both molecular pump stages is purified by the getter pump to remove nitrogen and other gases, and then returned directly to the source chamber. Previous conductance calculations indicate that the gas consumption during the return process is approximately $0.005 \text{ Pa}\cdot\text{L}/\text{s}$ ^[229]. In the experiment, using ${}^4\text{He}$ in a closed-loop system, the measured pressure variation in the gas tank was approximately 0.01 Pa/s , corresponding to a consumption rate of $0.003 \text{ Pa}\cdot\text{L}/\text{s}$, which is in good agreement with the conductance calculation. In the actual ${}^3\text{He}$ measurements, the consumption was also monitored, and the gas consumption was at a similar level.

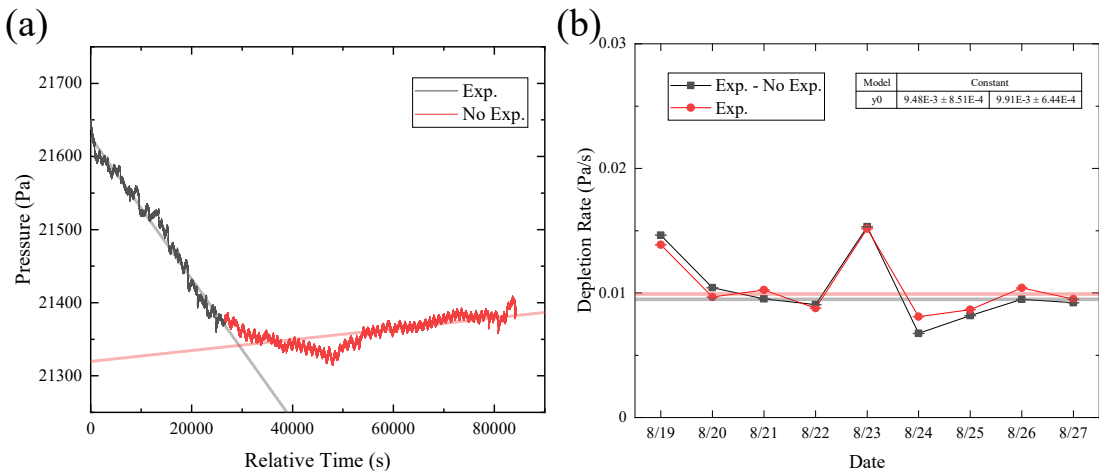


Figure 4.2 Measurement results of helium consumption during the closed-loop process. Considering the impact of temperature changes on the pressure gauge, monitoring was conducted both during and outside of experiments. (a) Monitoring results of gas tank pressure over one day, with black indicating pressure changes during helium release during experiments, and red indicating pressure changes when no experiment was conducted. Linear fitting of these two datasets provides an estimate of the helium consumption rate. (b) Monitoring results of helium consumption over the course of one week. The physical consumption rate, whether adjusted for pressure changes outside the experiment or not, was approximately 0.01 Pa/s . The actual consumption fluctuated between 0.005 and 0.015 Pa/s .

4.2.2 Determining the Detected Substate

In the ${}^4\text{He}$ experiment, the combination of the Stern-Gerlach magnet allowed for the detection of single quantum states. However, since the initial design of the Stern-Gerlach magnet did not consider the specific needs for ${}^3\text{He}$ measurements, it is necessary to first determine which 2^3S_1 substates can be observed on the detector. Based on this, an appropriate experimental plan is designed for detecting the different substates.

First, a Monte Carlo simulation was used to predict the distribution of the atomic beam after passing through the Stern-Gerlach magnet. Theoretically, two substates should be observable on the detector: the $F = 1/2$ and $M_F = -1/2$ state, and the $F = 3/2$ and $M_F = +1/2$ state, both of which have almost identical deflection dis-

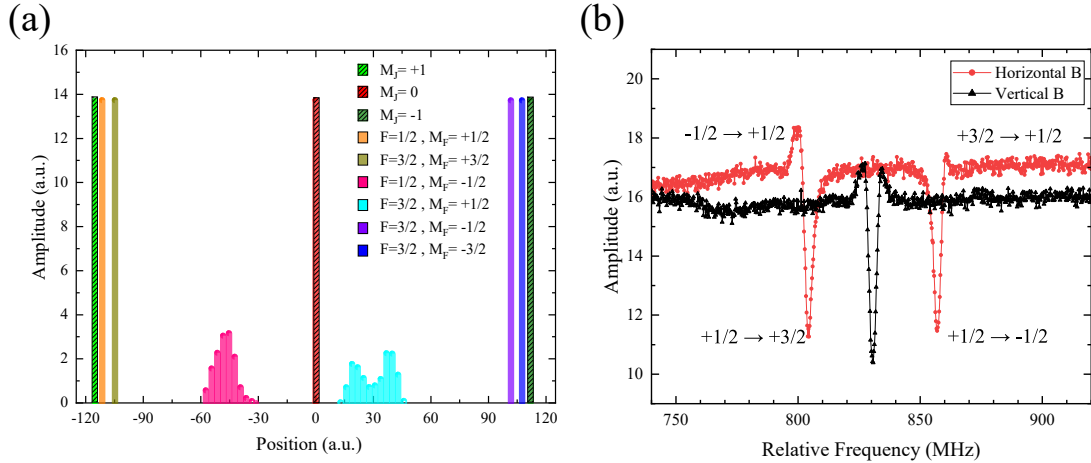


Figure 4.3 (a) During the design of the Stern-Gerlach magnet, Monte Carlo simulations predicted the positions of atoms in various substates after being deflected. According to the simulation results, two substates can be observed within the detector's range. However, in the experiment, by adjusting Slit 3, only a single cloud of atoms was observed. (b) In the experiment, without the repump light, the detection laser directly scanned the $2^3S_1(F=3/2) - 2^3P_2(F=5/2)$ transition. The red line represents a horizontal magnetic field, corresponding to the σ^\pm transitions, while the black line represents a vertical magnetic field, corresponding to the π transition. Fitting the peak centers gives the Zeeman frequency shift coefficients, which, when compared to calculated results, confirm that the observed atoms are in the $F=3/2$ and $M_F=+1/2$ state.

tances, as shown in Figure 4.3(a). However, in the experiment, by adjusting Slit 3, only a single cloud of atoms was observed. Considering that the magnetic field gradient in the simulation is uniform, but the design only considered the gradient uniformity in the central region of the magnetic field, it is plausible that only one cloud of atoms is observed.

To confirm the specific substate observed on the detector, a direct scan of the detection laser was performed to measure the spectrum without using the repump process, as shown in Figure 4.3(b). Since the direction and magnitude of the bias magnetic field were already determined in the ${}^4\text{He}$ measurements, after multi-peak fitting, the frequency shift of each spectral peak was used to obtain the Zeeman frequency shift coefficient. By comparing this with the theoretical calculation (see Section 4.1.2), the detected substate could be identified. Using this method, it was confirmed that the observed substate is the $F=3/2$ and $M_F=+1/2$ state.

4.2.3 Optical Pumping Modification

Considering that the $2^3S_1(F=3/2)$ state of ${}^3\text{He}$ has four substates, while the current setup can only detect the $M_F=+1/2$ state, and that in the experiment, it is necessary to probe transitions to the $M_F=\pm 3/2$ states to eliminate the Zeeman effect, the use of π transitions for pumping is ineffective. Therefore, we changed to using σ^\pm

transitions for optical pumping, aiming to pump as many atoms as possible into the $M_F = \pm 3/2$ states.

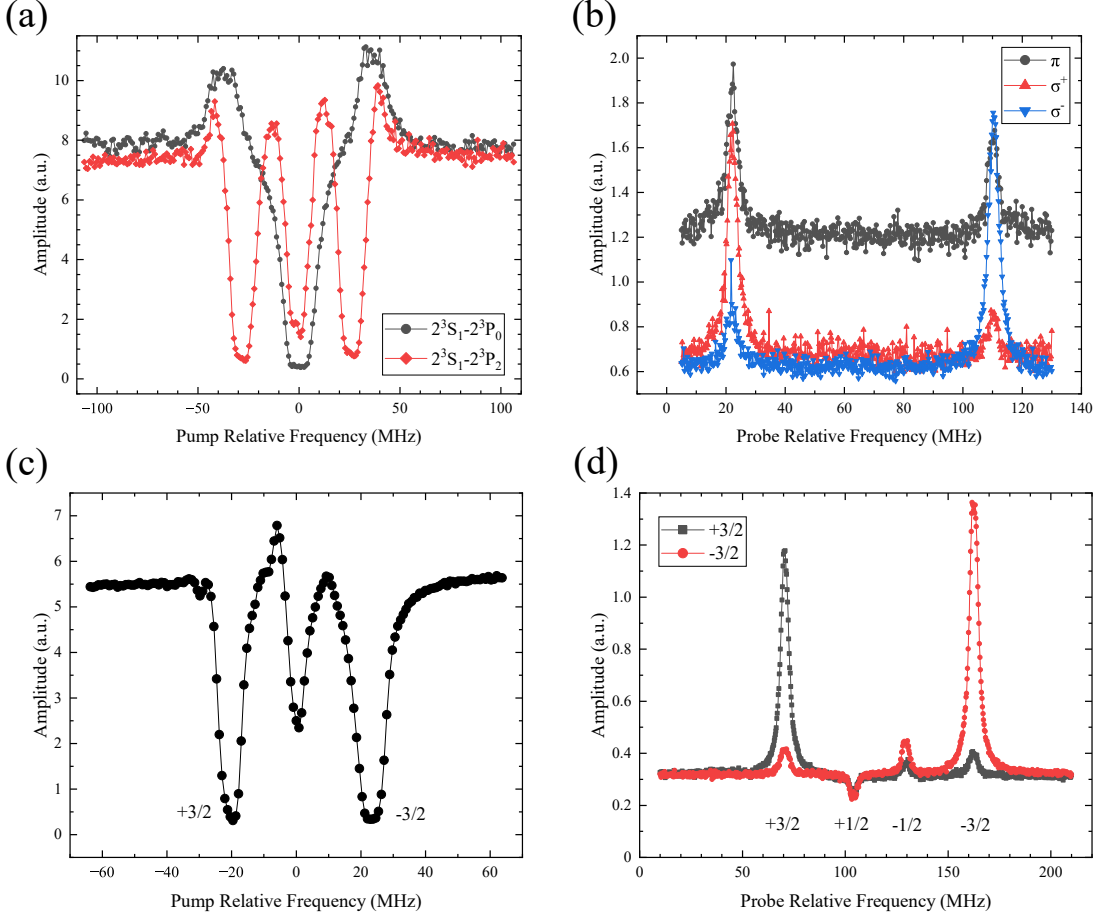


Figure 4.4 (a) In the ${}^4\text{He}$ experiment, the effect of pumping using two different transitions. (b) In the ${}^4\text{He}$ experiment, the pumping of the $2^3S_1 - 2^3P_2$ transition is shown, with the pumping frequency locked at three different peak positions as shown in Figure (a), and the effect of scanning the probe laser. The three colors correspond to pumping with π or σ^\pm transitions. It can be seen that when the pumping occurs with σ^\pm transitions, the corresponding lower-state atoms are more populated. (c) Pumping effect in the ${}^3\text{He}$ experiment. The two larger downward peaks represent atoms being pumped to the $M_F = +3/2$ or $M_F = -3/2$ states. (d) The effect of scanning the probe laser after pumping in the ${}^3\text{He}$ experiment. The transition for the probe laser is $2^3S_1(F = 3/2) - 2^3P_0(F = 1/2)$. The two colors correspond to the pumping frequencies locked to the two peaks in Figure (c), and the four peaks detected are marked with the corresponding ground-state M_F values.

In order to implement the change in the pumping method, there is no need to modify the optical pumping device. Instead, the polarization of the incident laser or the direction of the magnetic field can be adjusted to achieve π or σ^\pm transitions for pumping. To verify this method, experiments need to be conducted first in ${}^4\text{He}$. In the previous ${}^4\text{He}$ measurements, the $2^3S_1 - 2^3P_0$ transition was selected as the pumping light frequency, with the magnetic field in the vertical direction (y-direction) and the laser incident in the horizontal direction (x-direction) with horizontal polarization for pumping. In this setup, theoretically, both π and σ^\pm transitions could occur. However, because the upper

state 2^3P_0 has only one substate, the final result is that the $M_J = 0$ state is emptied. To simulate the pumping situation for ${}^3\text{He}$, the pumping transition in the ${}^4\text{He}$ experiment was switched to $2^3S_1 - 2^3P_2$, and the pumping effect is shown in Figure 4.4(a). Since linearly polarized light can be decomposed into left- and right-circularly polarized light, the pumping effect can be observed at all three frequencies. By performing the pumping at these three frequencies and scanning the probe light, as shown in Figure 4.4(b), it can be seen that when the pumping process occurs via σ^\pm transitions, atoms on the $M_J = \pm 1$ states are more populated.

Similarly, in the ${}^3\text{He}$ experiment, the $2^3S_1(F = 3/2) - 2^3P_2(F = 5/2)$ transition was selected, and the corresponding frequencies for σ^\pm transitions were used for pumping. To maximize the pumping effect, a larger beam spot is needed. However, since the GT prism size is limited, a two-inch PBS and $\lambda/4$ waveplate setup was chosen to replace the GT prism. These two schemes are equivalent, as detailed in Section 2.3.1. The final pumping effect is shown in Figure 4.4(c). At this point, by scanning the probe light, the detected spectrum is shown in Figure 4.4(d). In the experiment, by switching between the two pumping frequencies and scanning the corresponding probe peaks, sufficiently high signal-to-noise ratios for the positive and negative peaks can be obtained, specifically $2^3S_1(M_F = +3/2) - 2^3P_0(M_F = +1/2)$ and $2^3S_1(M_F = -3/2) - 2^3P_0(M_F = -1/2)$. This allows, just like in the ${}^4\text{He}$ case, the average frequency and magnetic field to be obtained from the center frequencies of the positive and negative peaks, and the average frequency to undergo second-order Zeeman correction. It is important to note that since the pumping efficiency differs when switching the pumping frequencies, the baselines of the positive and negative peaks must not be shared in the spectral fitting and should be fitted separately.

4.2.4 Beam Incidence Direction

Since the nuclear spin of ${}^3\text{He}$ atoms is $I = 1/2$, the six magnetic sublevels of its 2^3S_1 state will experience deflection in a gradient magnetic field. In this experiment, the only substate that can be detected by the detector is the $F = 3/2$ state with $M_F = +1/2$. During the deflection process in the Stern-Gerlach magnet, part of the atomic beam may collide with the cavity wall and be quenched. Due to the post-selection effect, when part of the beam is blocked, the measured result will show a redshift. Therefore, the direction of the atomic beam's incidence needs to be adjusted to ensure that the atomic beam can fully pass through the Stern-Gerlach magnet.

In the ${}^4\text{He}$ measurements, to determine the beam orientation in the vertical direc-

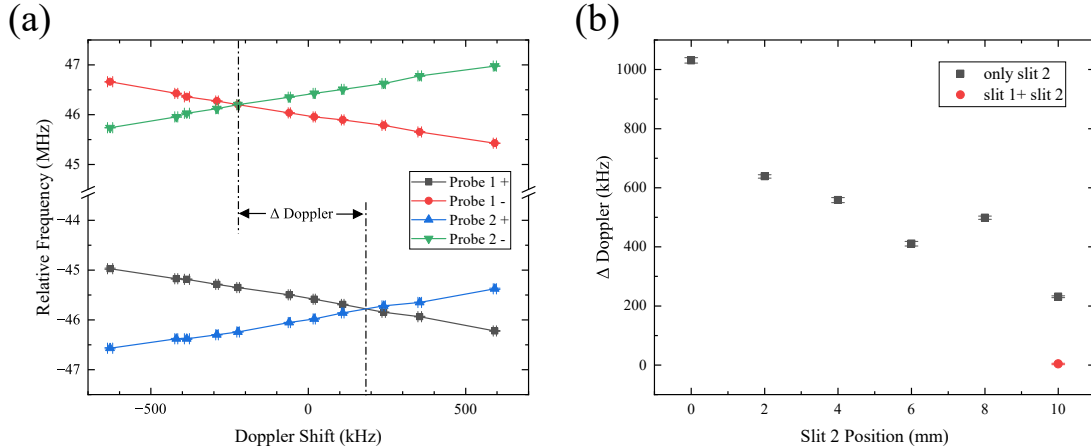


Figure 4.5 Frequency variation when roughly searching for the beam incidence direction for ${}^3\text{He}$. (a) With only Slit 2, the beam is wide, and the final result is affected by the post-selection effect. Since the additional atomic momentum corresponding to the positive and negative peaks differs, a certain Doppler shift, $\Delta\text{Doppler}$, appears along the same optical path. (b) The change in $\Delta\text{Doppler}$ value as Slit 2 moves to different positions. As the beam moves closer to a position where it can fully pass through, the additional atomic momentum corresponding to the positive and negative peaks becomes more similar. At this point, Slit 1 is introduced to narrow the beam, and $\Delta\text{Doppler}$ almost disappears, indicating that the narrow beam can be completely detected.

tion, Slit 1 moves along the y direction, which is perpendicular to both the probe light (x direction) and the beam direction (z direction). Thus, direct adjustments in the horizontal direction are not possible. Therefore, in the preliminary adjustment of the ${}^3\text{He}$ experiment, Slit 1 was removed, and only Slit 2 was used to roughly find the incidence angle of the ${}^3\text{He}$ beam. At this point, since there was only one slit before interacting with the probe light, the beam was wide. After interacting with the probe light, some atoms that would not normally enter the detector were detected. These atoms had a greater momentum in the x direction compared to the atoms that could normally enter the detector, causing a significant Doppler effect, which in turn led to a shift in the results. Moreover, since the lower states corresponding to the positive and negative peaks are different, they experience different deflections in the Stern-Gerlach magnet. As a result, the additional initial momentum of the atoms detected for the positive and negative peaks differs, causing different shifts between the positive and negative peaks. In the experiment, this phenomenon manifests as inconsistent results for the positive and negative peaks when the Doppler shift is the same (same optical path angle), meaning the zero Doppler position of the positive and negative peaks corresponds to different optical path directions, as shown in Fig.4.5(a). This effect only exists when the initial beam distribution is very wide. Therefore, when moving Slit 2, if this effect decreases, it indicates that the initial momentum of the additional atoms that can be detected is closer, and the beam is closer to completely passing through the Stern-Gerlach region.

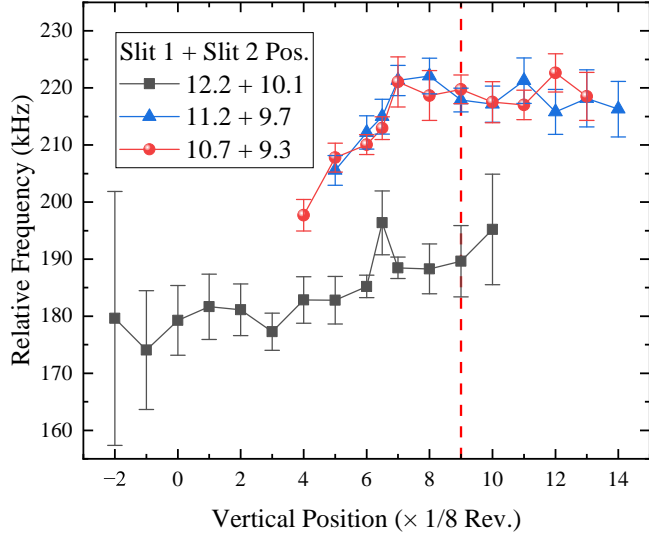


Figure 4.6 Adjusting the vertical dimension of the probe light incident mirror frame at different positions of Slit 1 and Slit 2. By detecting the beam in different vertical directions for various horizontal incidence angles, the beam orientation in both the horizontal and vertical directions can be determined. The figure lists three sets of data closest to the final orientation. The numbers in the legend indicate the position shifts of Slit 1 and Slit 2 (relative to their positions during ${}^4\text{He}$ experiments, in mm). Finally, two slits are chosen to be approximately 10.7 mm and 9.3 mm offset from their positions during ${}^4\text{He}$ experiments, and the vertical incidence angle corresponds to the position indicated by the red dashed line in the figure.

As shown in Fig. 4.5(b), after the preliminary adjustment to minimize this effect, Slit 1 was introduced to narrow the beam. At this point, the beam can be fully detected, and the bias caused by the detection of additional atoms no longer exists.

After finding the general direction, more detailed adjustments were needed. As shown in Fig. 4.6, Slit 1 and Slit 2 were adjusted continuously in the x direction, and eventually, the two slits were offset by approximately 10.7 mm and 9.3 mm from their positions during the ${}^4\text{He}$ measurements, corresponding to a beam incidence direction deviation of about 3 mrad. Meanwhile, due to the geometrical constraints of the vacuum chamber, several changes were made to the slits, which also caused variations in the vertical beam orientation. Therefore, the vertical probe light incidence angle needed to be readjusted to avoid the post-selection effect in the vertical direction. After these adjustments, it was concluded that the beam and probe light angles in both the horizontal and vertical dimensions had been successfully adjusted, effectively minimizing the post-selection effect, and absolute frequency measurements could now be conducted.

4.3 Preliminary Measurement Results

After replacing the pumping scheme and adjusting the beam and laser angle in

both the horizontal and vertical directions to ensure no significant post-selection effects, preliminary measurements were conducted on the ${}^3\text{He}$ $2^3S_1(F = 3/2) - 2^3P_0(F = 1/2)$ transition. However, despite efforts to ensure the beam passed completely through the Stern-Gerlach magnet region before the experiment, the preliminary results were still affected by post-selection effects. Further improvements to the apparatus are necessary to complete the ${}^3\text{He}$ measurements.

4.3.1 Experimental Results

To ensure the signal-to-noise ratio, the beam velocity was chosen to be 445 m/s, at which the beam intensity was maximized. The measurements were taken at power levels of 0.3, 0.6, and 0.9 μW . The results for the three power points are shown in Fig. 4.7. Compared to the ${}^4\text{He}$ experimental results, the average values for the traveling wave remain stable, while the standing wave results show a noticeable slope. This further suggests that the standing wave measurement results are influenced by the beam distribution, and the mechanism is more complex than for the traveling wave.

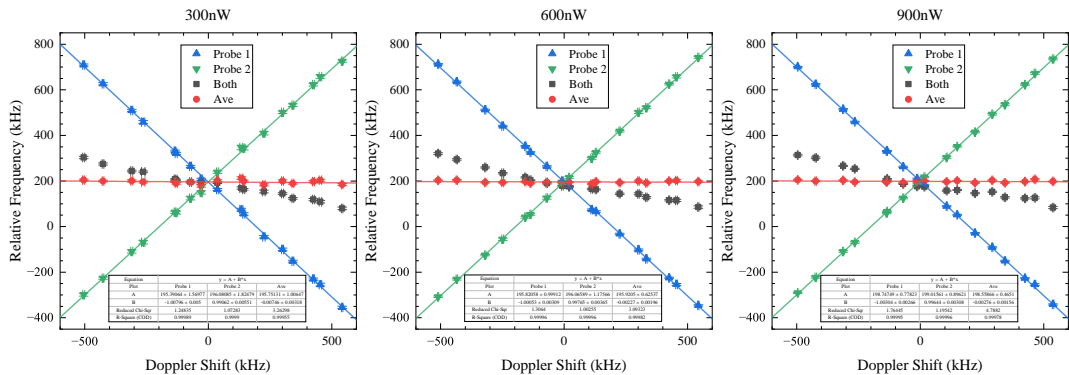


Figure 4.7 At a beam velocity of 445 m/s, preliminary results for the ${}^3\text{He}$ $2^3S_1(F = 3/2) - 2^3P_0(F = 1/2)$ transition were measured at three different power points. From left to right, the results correspond to power levels of 0.3, 0.6, and 0.9 μW .

For the final required traveling wave measurement results, the same processing method used for ${}^4\text{He}$ was applied. Results for each power point can first be extrapolated in angle, then extrapolated in power; alternatively, results for each angle can first be extrapolated in power, and then extrapolated in angle. As shown in Fig. 4.8, both methods yield consistent results.

Considering that common systematic errors, such as the Doppler effect, have been rigorously evaluated in the ${}^4\text{He}$ experiment, the largest Doppler effect can be assessed during formal measurements by measuring at different beam velocities. Other systematic errors have effects below 0.3 kHz. Therefore, the influence of these systematic errors was not considered in the preliminary results. The statistical accuracy of this ex-

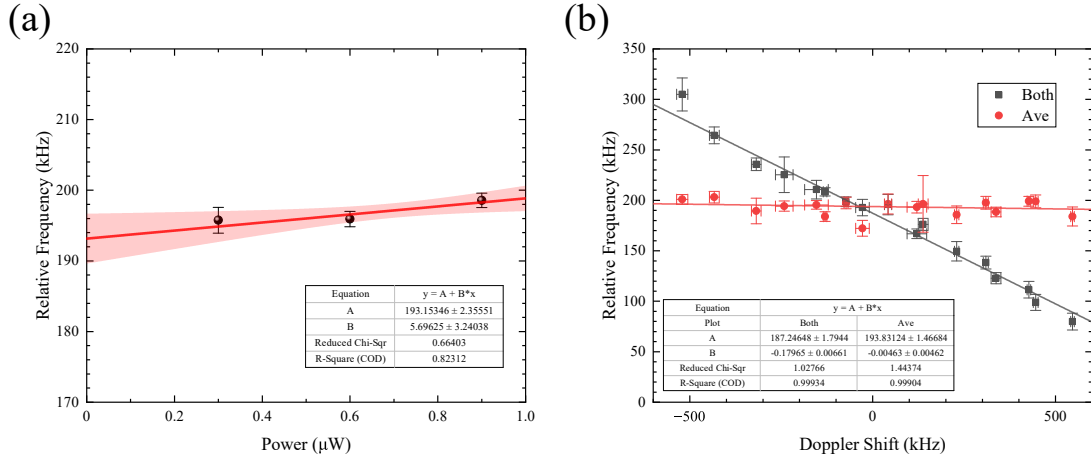


Figure 4.8 Preliminary measurement results for ${}^3\text{He}$. (a) Extrapolation results after power extrapolation for each power point and then angle extrapolation. (b) Extrapolation results after power extrapolation for each optical path angle and then angle extrapolation. The results from both methods are essentially the same.

periment is approximately 2.5 kHz, primarily because the ${}^3\text{He}$ beam signal is weaker by about two orders of magnitude compared to ${}^4\text{He}$, and a frequency-switching pumping method was used, which is less efficient than the single-frequency pumping used for ${}^4\text{He}$, typically around 90 %, leading to a decrease in spectral signal-to-noise ratio. However, since there is a significant deviation in the isotope shift results for the current isotopes, a precision of about 2 kHz for the ${}^3\text{He}$ results is sufficient to distinguish the isotope shift deviation. In subsequent experiments, if the beam intensity can be further optimized and the experimental scheme updated to address the low pumping efficiency, higher-precision results can be obtained.

4.3.2 Post-selection Effect in the ${}^3\text{He}$ Experiment

Due to the nuclear spin of ${}^3\text{He}$, its sublevels experience deflection in the Stern-Gerlach magnet. Under the same experimental conditions, ${}^3\text{He}$ is more susceptible to the post-selection effect. Therefore, further experimental design is required to verify whether the experimental results are influenced by this effect. Although, prior to the formal experiment, adjustments were made to the positions of Slit 1 and Slit 2, as well as to the vertical mirror frame, to find the orientation of the beam and the laser. As shown in Figure 4.6, a stable measurement range was eventually observed, and it was concluded that the beam and laser alignment was correct, allowing the formal experiment to commence. However, since the beam was intercepted using two slits with dimensions of $0.3\text{mm} \times 8\text{mm}$, the beam had a relatively large width in the vertical direction (y -direction), making the existence of a stable measurement range reasonable.

However, in the transverse (x -direction), because the beam is currently incident

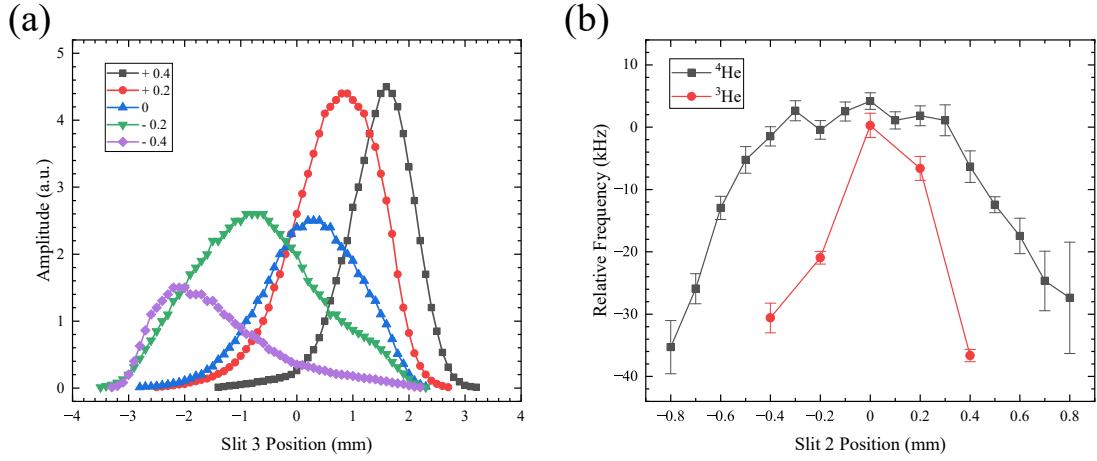


Figure 4.9 (a) Changes in the ${}^3\text{He}$ beam distribution when the position of Slit 2 is adjusted. Different colors represent different positions of Slit 2 (in mm). (b) Changes in the measurement results when Slit 2 is adjusted. For ${}^4\text{He}$, the results remain stable within ± 0.3 mm, whereas no stable measurement range is observed for ${}^3\text{He}$. For comparison, the baseline results for each condition have been subtracted.

at an angle, it will experience deflection when passing through the Stern-Gerlach magnet. As a result, its transverse distribution is much wider than for ${}^4\text{He}$. As shown in Figure 4.9(a), when the position of Slit 2 is changed, both the width and position of the beam change, and the distribution no longer shows the Gaussian shape seen in the ${}^4\text{He}$ experiment but instead shows some asymmetry. Considering that an equivalent slit of approximately 6.5 mm was found in the Stern-Gerlach magnet for the ${}^4\text{He}$ experiment, this part is the most likely to be affected by the post-selection effect in the current experiment. To further verify this, the ${}^4\text{He}$ experiment was repeated without Slit 3, keeping Slit 1 fixed and adjusting the position of Slit 2, thus changing the initial incident direction of the beam. Due to the presence of the equivalent slit, when the beam's incident angle is large, a red shift is expected in the measurement results. The measurements show that within a very narrow range, a clear red shift occurs, unlike the ${}^4\text{He}$ experiment, where a stable measurement range exists. This is shown in Figure 4.9(b), indicating that the current experiment's results are likely still affected by the post-selection effect.

After confirming that the preliminary experiment might be affected by the post-selection effect, it is necessary to determine whether the conclusion of a red shift caused by the post-selection effect remains valid under the beam's oblique incidence. Specifically, we need to establish whether the measured results are higher or lower than the true values. To test this, a 0.5 mm-wide Slit 3 was added to introduce a stronger post-selection effect. As shown in Figure 4.10(a), after adding Slit 3, the measurement results shifted downward by approximately 50 kHz, which aligns with the expected post-

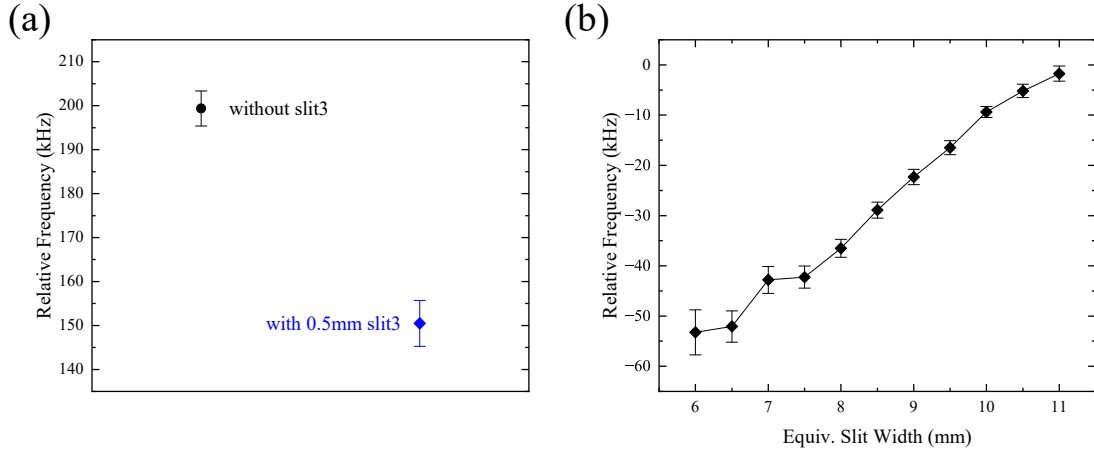


Figure 4.10 (a) After adding a 0.5 mm-wide Slit 3, the measurement results shift by about 50 kHz, consistent with the expected post-selection effect. (b) Monte Carlo wave function simulation showing the effect of changing the width of the equivalent slit in the ${}^3\text{He}$ beam direction. Since the transition parameters used in the simulation are still based on ${}^4\text{He}$ conditions, the specific values of the deviation are not directly meaningful, but the trend in the results is valuable for comparison.

selection effect. Furthermore, in the Monte Carlo wave function simulation, the incident direction of the ${}^3\text{He}$ beam was set to its current angle, and the width of the equivalent slit in the Stern-Gerlach region was varied. As shown in Figure 4.10(b), the simulation results show that as the equivalent slit width increases, the red shift caused by the post-selection effect decreases. It should be noted that the transition parameters in the simulation are based on ${}^4\text{He}$ conditions, and thus the specific numerical deviations are not directly applicable. However, the trend in the simulation results is useful for comparison. Both experimental and simulation results indicate that under the oblique incidence of the beam, the post-selection effect still leads to a red shift in the final results. If subsequent experiments can be conducted under conditions free from the post-selection effect, it is expected that the measurement results will be larger than those obtained in the current experiment.

4.3.3 Results Comparison

The preliminary measurement result for ${}^3\text{He}$ in this experiment is 276 732 997 193.2 (2.5) kHz. This result is approximately 23 kHz larger than the measurement obtained using the saturated fluorescence method at the University of Florence^[147]. Combining high-precision hyperfine structure calculation results^[267-268] and the ${}^4\text{He}$ result from this experiment^[252], and performing the calculation based on Table 3.3, the isotope shift is found to be 1.055(2) fm². This isotope shift result is about 2.4 standard deviations smaller than the result for muonic helium ions^[216-217], and about 8.3 standard deviations smaller than the result for the $2^3S - 2^1S$ transi-

tion^[171-172]. However, considering that the post-selection effect still exists in the current setup, the true frequency value should be larger, resulting in a larger deviation from the Florence University measurement. Accordingly, the isotope shift result would be smaller, and the deviation between this result and the muonic helium and $2^3S - 2^1S$ transition results would also increase.

Given that the apparatus used by the Shiner group is similar to the one used in this experiment, the post-selection effect is likely to also influence their results^[143-144]. Based on the description of their experimental setup in the doctoral thesis^[221], a simple formula for post-selection (Equation 3.21) was used to estimate the correction. The corrected isotope shift result would be $1.053(3)$ fm 2 , with the original error carried over. The corrected result would shift slightly lower and would deviate by approximately 2.5 standard deviations from the muonic helium result but would be consistent with the result of this experiment. It should be noted that this is a rough estimate of the correction to their results, and the specific correction still needs to be validated through simulations and experiments conducted with their original setup.

It is noteworthy that after the latest results for muonic helium ions and the $2^3S - 2^1S$ transition were published, some theoretical studies have discussed the deviation in isotope shift results between these two experiments. From a nuclear theory perspective^[269], the result for muonic helium is expected to be smaller, and the deviation between the two results will increase to about 4 standard deviations. After correcting the hyperfine structure of ${}^3\text{He}$ ^[270-271], the result for the $2^3S - 2^1S$ transition will decrease, and the deviation between the two results will shrink to within two standard deviations. Currently, no consensus has been reached on the isotope shift of helium. We will complete the absolute frequency measurement of ${}^3\text{He}$ as soon as possible to obtain an independent isotope shift result.

4.4 Summary and Discussion

This experiment faced two main challenges in measuring ${}^3\text{He}$. First, due to the low beam intensity and poor pumping efficiency, the signal-to-noise ratio of the spectrum was low, limiting the measurement accuracy. Second, the ${}^3\text{He}$ beam could not fully pass through the Stern-Gerlach magnet region, leading to the post-selection effect affecting the measurement results. The different sublevels of ${}^3\text{He}$ experience deflection within the Stern-Gerlach magnet, causing the beam distribution to broaden. Moreover, the distribution of the beam is related to the incident angle and longitudinal velocity.

This suggests that the current Stern-Gerlach magnet setup may not be suitable for ${}^3\text{He}$ measurements, and a new detection scheme should be designed. Discussions of several detection schemes can be found in Section 5.2.1.

Currently, there are significant discrepancies in the isotope shift results for different systems. For the ${}^3\text{He}$ $2^3S - 2^3P$ transition measurements, an accuracy of just 2 kHz is required to resolve any discrepancies between the results. If the precision similar to that achieved in this work for ${}^4\text{He}$ can be attained, it will be possible to obtain an isotope shift result with an accuracy exceeding one thousandth of a femtometer. Additionally, if future experiments can eliminate quantum interference effects through ionization detection, high-precision probing of ${}^3\text{He}$'s hyperfine structure will be achievable. This structure is closely related to the Zemach radius and will aid in further exploration of atomic nucleus structure.

Chapter 5 Summary and Outlook

5.1 Summary

Helium atoms, being the simplest multi-electron atomic system, hold significant physical importance and serve as an ideal system for testing quantum electrodynamics and fundamental physical constants. Compared to hydrogen atoms, helium atoms have a larger nuclear radius, and the interaction between the muon and the nucleus is stronger. If the discrepancies between hydrogen and muonic hydrogen are caused by nucleus-related effects, these effects will be more pronounced in the helium and muonic helium systems. Therefore, precisely measuring the helium atomic nuclear radius and comparing the results with those from the muonic helium system can test the Standard Model and help resolve the “proton radius puzzle.” Based on previous research within the group, this work, through improvements to the experimental setup and detection methods, achieved the first sub-kHz measurement of the ${}^4\text{He}$ atom $2^3S - 2^3P$ transition frequency and completed the preliminary measurement of the same transition frequency for ${}^3\text{He}$. Furthermore, a new systematic error term, post-selection effects, was discovered during the experiment, which significantly impacts high-precision spectroscopic measurements. The key contributions and results of this thesis are summarized as follows:

1. The beamline apparatus was enhanced by using a Zeeman decelerator to reduce the longitudinal velocity of the atomic beam. By adjusting laser frequency detuning and other methods, the beam velocity was continuously adjustable within the range of 50 to 450 m/s. Spectral measurements were conducted at different velocities, and the results were extrapolated to eliminate the Doppler effect, thus improving the measurement accuracy.
2. A new detection optical path was proposed, replacing standing waves with traveling waves for detection. Compared to common standing-wave detection methods, such as the cat-eye and active fiber feedback methods, the traveling-wave approach not only effectively eliminates the Doppler effect but also expands the angular range for spectral measurements, reducing the influence of detection laser power on the results.
3. A new systematic error, the post-selection effect, was identified and thoroughly studied. By conducting spectral and beam distribution measurements under various experimental conditions and combining theoretical analysis with simulation calculations,

the significant impact of the post-selection effect on frequency measurements was revealed. Since many precision spectroscopic experiments use structures like slits or small apertures in front of the detectors, important results often require in-depth investigation and correction of the post-selection effect in line with experimental conditions.

4. With the improvements to the beamline and detection methods, this work achieved the first sub-kHz level measurement of the $2^3S - 2^3P$ transition frequency for ^4He atoms, unaffected by post-selection effects. The measurement results were consistent with those obtained using the saturation fluorescence method. Combined with existing ^3He measurement results, the isotope shift was determined to be $1.0773(21) \text{ fm}^2$, which agrees with the result for the $2^3S - 2^1S$ transition but differs by 2.6 standard deviations from the muonic helium ion results. If subsequent experiments confirm the discrepancy between the helium and muonic helium results, it would suggest unequal electromagnetic interactions between muons and electrons, potentially pointing to new physics beyond the Standard Model.

5. Through further improvements to the apparatus, the preliminary measurement of the ^3He atom $2^3S - 2^3P$ transition frequency was completed. However, due to the nuclear spin of ^3He atoms, deflection within the Stern-Gerlach magnet caused the preliminary results to be influenced by the post-selection effect. As a result, the current setup is not capable of completing the final measurement and obtaining independent ^3He results. Further improvements to the detection scheme are necessary to ensure the accuracy of the final measurement results.

5.2 Outlook

5.2.1 Elimination of Post-Selection Effects

In previous work within our research group, due to the presence of slits in front of the detector, the atomic beam interacting with the detection laser could not be fully detected, leading to a significant redshift in the frequency. In the preliminary measurement of ^3He in this study, due to the deflection of various sublevels within the Stern-Gerlach magnet, the beam could not fully pass through the magnet region, resulting in a redshift of the final frequency. These experimental results indicate that when the atomic beam, after interacting with the laser, is not fully detected, post-selection effects occur. Therefore, eliminating the post-selection effect corresponds to achieving complete detection of all atomic beams.

In the current experimental setup, the Stern-Gerlach magnet provides a gradient

magnetic field that deflects atoms from different sublevels, with only specific sublevels being detected. If the post-selection effect is to be avoided by simply increasing the diameter of the tube within the Stern-Gerlach magnet, the gradient of the magnetic field would decrease as the tube diameter increases. This would lead to an inability to effectively separate the atoms of different sublevels, causing them to enter the detector simultaneously and preventing effective spectral detection. In this case, a possible solution is to use an imaged MCP system to observe the spatial distribution and position changes of different sublevels and count them separately to achieve spectral measurement. Another option is to extend the beamline and detect specific sublevels at corresponding positions. However, this would require adjusting the position of the detector according to changes in the atomic beam's velocity, complicating the setup.

Considering that the experiment has successfully utilized laser-induced deflection of metastable helium atoms, a potential approach is to use the laser's force on the atoms to separate the sublevels by adopting an optical deflection scheme. To achieve this, a strong uniform magnetic field would be required, along with a low-power laser to deflect atoms from a specific sublevel. For other sublevels, because they are far detuned in the strong magnetic field, they experience very weak laser scattering forces (according to equation 2.2) and are almost not deflected. Therefore, the atoms from one sublevel can be deflected out of the detection range, while atoms from other sublevels can still be detected. By matching with the pumping laser, it is possible to clear a specific sublevel and thus complete the spectral measurement. Since the other sublevels are not deflected, the optical deflection scheme can avoid interference from the deflections of all sublevels in the gradient magnetic field. However, scattering forces are probabilistic, and optical deflection may not always completely deflect a specific sublevel. Additionally, when detecting multiple sublevels simultaneously, quantum interference effects become more complex. These issues need to be carefully considered and validated in subsequent experiments and simulations.

Moreover, if the 2^3P state can be ionized using laser and electric fields and directly detected while interacting with the detection light, it would eliminate the need to track spatial position changes. By designing a sufficiently large beam spot and precise electric field control, it would be possible to fully detect the atomic beam, thus avoiding the impact of post-selection effects. This scheme would also avoid quantum interference effects, which will be discussed further in the next section. Regardless of the chosen scheme, given the changes in the detection method, it is necessary to re-conduct measurements in ${}^4\text{He}$ to assess various systematic errors before performing measurements

in ${}^3\text{He}$.

5.2.2 FEL Excitation and Ionization Detection

To further improve the precision of helium atomic spectroscopy measurements, it is necessary to develop a higher brightness atomic beam source for single-quantum state metastable helium atoms and redesign the detection system to address issues such as unavoidable quantum interference effects in the current setup. Therefore, our research group has partnered with the Institute of Advanced Science Facilities and the Advanced Light Source Science Center at Southern University of Science and Technology to replace RF discharge excitation of metastable helium atoms with free-electron lasers (FEL). Following the ionization detection scheme by Hessels et al.^[163], we plan to use two lasers to excite 2^3P state atoms to high-lying Rydberg states and then detect them through ionization. Simulation results indicate that both excitation efficiency and ionization detection efficiency are about 0.1 %. The S³FEL project, with a high repetition rate, was launched in 2023. The helium atomic precision spectrometer will be designed and constructed by Dr. Du Xiaojiao and Dr. Wei Long at the Institute of Advanced Science Facilities (IASF) in Shenzhen^[272].

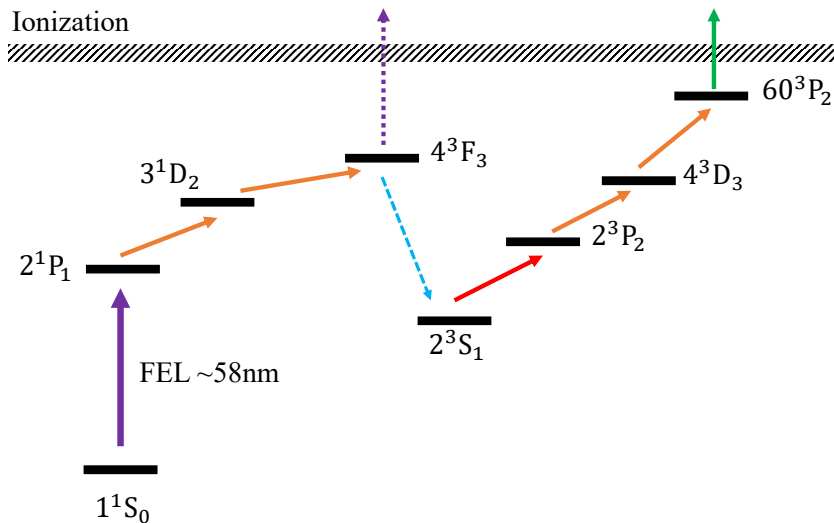


Figure 5.1 Energy level diagram of FEL excitation and ionization detection.

Since the $1^1S_0 - 2^3S_1$ transition is electric dipole forbidden, even using a free-electron laser, helium atoms cannot be directly excited to the 2^3S_1 state. Therefore, we first use the free-electron laser to excite atoms to the 2^1P_1 state, followed by excitation to the 3^1D_2 and 4^3F_3 states using 668 nm and 1870 nm lasers, respectively. Finally, the atom returns to the 2^3S_1 metastable state. Since the free-electron laser and the 668 nm and 1870 nm lasers act simultaneously, the high power density of the free-electron laser

ionizes the 2^1P_1 , 3^1D_2 , and 4^3F_3 states to varying degrees. We simulate the entire excitation process using a density matrix, considering ionization only from the 4^3F_3 state. Assuming the photon flux of the free-electron laser is 10^{-12} photons/cm $^{-1}$, with a repetition rate of 100 kHz and a pulse width of 100 fs, and the 668 nm and 1870 nm lasers have a power of 1 W with a beam spot size of 10 mm \times 10 mm, the simulation results show the changes in population distributions of various energy levels after one laser pulse, as shown in Fig. 5.2(a). After 40 ns evolution, the population in the 2^3S_1 state stabilizes at about 0.1 %. This method achieves at least an order of magnitude improvement in efficiency compared to the discharge method.

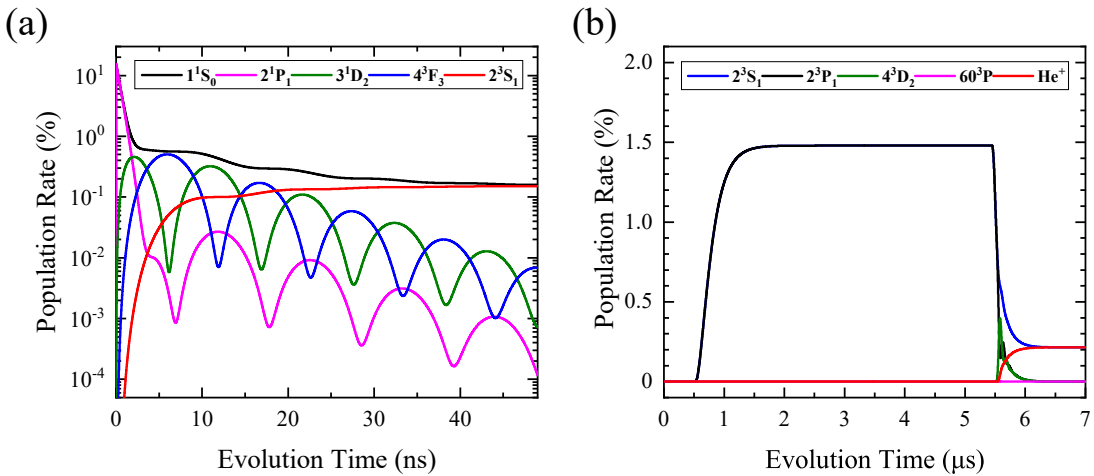


Figure 5.2 (a) Simulation result of FEL excitation efficiency. (b) Simulation result of photoionization detection efficiency.

The original scheme detected atoms transitioning from the 2^3P state back to the 2^3S state. During interaction with the detection laser, despite being far detuned, atoms may transition to other sublevels of the 2^3P state and eventually return to the 2^3S state. Since it is impossible to distinguish which sublevel the atom originated from, quantum interference effects are introduced. To address this issue, Hessels et al. used a laser to excite 2^3P state atoms to high-lying Rydberg states and employed ionization detection to avoid the effects of multiple spontaneous emission channels, thus eliminating quantum interference. Following their experimental scheme^[163,266], we have also simulated the ionization detection process. Using the 2^3P_1 state as an example, we first use 447 nm and 1473 nm lasers to excite the 2^3P_1 state atoms to the 4^3D_2 state and the 60^3P state. The $n = 60$ Rydberg state has a lifetime of about 220 μ s, providing enough time for ionization. Simulation results indicate that approximately 0.1 % of the atoms are ionized to He^+ , as shown in Fig. 5.2(b).

However, since this scheme requires adding two additional high-power lasers and an ionization electric field under the existing 1083 nm laser and magnetic field condi-

tions, Stark effects may be introduced. Therefore, it is necessary to use time-sequenced switching of the lasers and electric fields to avoid interference with the $2^3S - 2^3P$ transition measurements. Additionally, the ionization detection system will disrupt the existing magnetic shielding and bias magnetic fields, requiring a redesign of the shielding and uniform magnetic field devices. In subsequent experiments, we will need to reassess the Stark effects, Zeeman effects, and other factors in the detection region.

5.2.3 Ramsey Spectroscopy Attempt

5.2.3.1 Background

The accuracy of measuring the spectral center is closely related to the linewidth of the spectrum. Under the same signal-to-noise ratio, the narrower the linewidth, the higher the accuracy of the central frequency. However, in experiments, various factors such as velocity distribution and probe gas pressure can lead to effects such as Doppler broadening and pressure broadening. In certain experimental methods, such as the atomic beam method used in this experiment, these broadening effects can be significantly reduced, allowing the detected spectral linewidth to approach the natural linewidth. If the natural linewidth limit can be surpassed, higher precision in measuring the central frequency could be achieved. In 1949, Ramsey, building on the Rabi method, developed the Separated Oscillatory Field Molecular Beam Resonance Method (SOF), successfully breaking through the natural linewidth limit by dividing the microwave field into two parts and inserting a gap between them^[273]. However, because the wavelength of light is much smaller than the interaction scale between atoms and light, Ramsey fringes are averaged out. This presents a challenge in extending the SOF method from microwaves to optical frequencies. In 1976, Baklanov et al. proposed using three spatially separated standing wave fields to achieve optical Ramsey interference^[274], and in the following year, three research groups—J. L. Hall, C. Cohen-Tannoudji, and T. W. Hänsch—successfully observed optical Ramsey interference^[275-277]. In 1984, Ch. J. Bordé et al. also observed Ramsey fringes in a four-wave light field^[278]. Today, the Ramsey method is widely applied in precision spectroscopy, interferometry, and time-frequency standards.

In helium atomic precision spectroscopy research, E. A. Hessel's group employed the Ramsey method in measuring the 2^3P_J intervals, achieving a series of high-precision results^[279]. Recently, they developed the Frequency-Offset Separated Oscillatory Fields (FOSOF) method^[280], which involves actively offsetting the frequencies of the two microwave fields to create a simple linear relationship between phase and fre-

quency, significantly improving measurement accuracy. The higher signal-to-noise ratio also makes the investigation of various systematic errors more convenient. This method has been successfully applied in measurements of the Lamb shift in hydrogen^[93] and the 2^3P_J intervals in helium^[163,266], achieving an astonishing precision of 25 Hz in the helium atomic interval measurement. In 2023, the Institute of Precision Measurement Science and Technology Innovation, Chinese Academy of Sciences, achieved the first optical Ramsey measurement of an ion beam system in the ${}^6\text{Li}^+$ system^[120]. These research achievements inspire us to attempt Ramsey spectroscopy in the measurement of the $2^3S - 2^3P$ transition, breaking the natural linewidth limit and further improving measurement precision.

5.2.3.2 Derivation of Ramsey Spectral Line Shape

To fit the obtained spectral center, the spectral line shape of the Ramsey spectrum needs to be derived first. Assuming that the microwave or optical field is instantaneously turned on and off with perfect amplitude and phase curves, and that there is a continuously changing phase between the two pulses, an analytical expression for the spectral line shape can be derived. In 1971, Fabjan and Pipkin provided a general expression using the time-dependent Schrödinger equation^[281]. Later, in the microwave spectroscopy measurement of the 2^3P_J interval of helium atoms, Borbély et al. also provided a detailed derivation^[279]. Based on these works, we can theoretically derive the Ramsey spectral line shape for the beam apparatus.

(1) Semi-Classical Equation to Solve for the Line Shape

The interaction between the atom and the optical or microwave field can be described by the following Hamiltonian:

$$\hat{H} = \hat{H}_0 + \hat{H}_D - \vec{\mu}_E \cdot \vec{E}_0 \cos(\omega t + \phi) \quad (5.1)$$

Here, \hat{H}_0 is the Hermitian operator that describes the two-level system, \hat{H}_D is the non-Hermitian operator that describes the dissipation process, and $\vec{\mu}_E$ is the electric dipole operator. $\vec{E}_0 \cos(\omega t + \phi)$ represents the optical or microwave field interacting with the atom.

For a simple two-level system, the wave function can be expressed as $|\Psi\rangle = c_1(t)|1\rangle + c_2(t)|2\rangle$. By solving the time-dependent Schrödinger equation $i\hbar \frac{\partial |\Psi\rangle}{\partial t}$, we obtain:

$$\begin{aligned} i\dot{c}_1 &= \omega_1 c_1 - i\frac{1}{2}\gamma_1 c_1 + 2V c_2 \cos(\omega t + \phi) \\ i\dot{c}_2 &= \omega_2 c_2 - i\frac{1}{2}\gamma_2 c_2 + 2V c_1 \cos(\omega t + \phi) \end{aligned} \quad (5.2)$$

where $V = -\frac{1}{2\hbar} \langle 1 | \mu_E E_0 | 2 \rangle$. In the rotating wave approximation, the equation simplifies to:

$$\begin{aligned} i\dot{c}_1 &= \omega_1 c_1 - i\frac{1}{2}\gamma_1 c_1 + V c_2 e^{-i(\omega t+\phi)} \\ i\dot{c}_2 &= \omega_2 c_2 - i\frac{1}{2}\gamma_2 c_2 + V c_1 e^{i(\omega t+\phi)} \end{aligned} \quad (5.3)$$

Considering the initial conditions, $c_1(0) = c_1(0)$ and $c_2(0) = c_2(0)$ at $t = 0$, we solve for:

$$\begin{aligned} c_1(t) &= \exp \left[-\frac{\gamma_1 + \gamma_2}{4}t - i\frac{\omega_1 + \omega_2}{2}t - i\frac{\omega}{2}t \right] \\ &\quad \times \left[c_1(0) \left(\cos \frac{at}{2} + i \cos \theta \sin \frac{at}{2} \right) - c_2(0) e^{-i\phi} \left(i \sin \theta \sin \frac{at}{2} \right) \right] \\ c_2(t) &= \exp \left[-\frac{\gamma_1 + \gamma_2}{4}t - i\frac{\omega_1 + \omega_2}{2}t + i\frac{\omega}{2}t \right] \\ &\quad \times \left[c_2(0) \left(\cos \frac{at}{2} - i \cos \theta \sin \frac{at}{2} \right) - c_1(0) e^{i\phi} \left(i \sin \theta \sin \frac{at}{2} \right) \right] \end{aligned} \quad (5.4)$$

where $a = [4V^2 + (\Delta + iQ)^2]^{1/2}$, $\omega_0 = \omega_1 - \omega_2$, $\Delta = \omega - \omega_0$, and $Q = \frac{1}{2}(\gamma_1 - \gamma_2)$, with $\sin \theta = 2V/a$ and $\cos \theta = (\Delta + iQ)/a$.

Next, we derive the population change of the atom under the Ramsey method. In the experiment, the atom starts in the ground state, i.e., $c_1(0) = 1$, $c_2(0) = 0$. After a duration of D in the first interaction region, the atom's population is:

$$\begin{aligned} c_1(D) &= \exp \left[-\frac{\gamma_1 + \gamma_2}{4}D - i\frac{\omega + \omega_1 + \omega_2}{2}D \right] \times \left(\cos \frac{aD}{2} + i \cos \theta \sin \frac{aD}{2} \right) \\ c_2(D) &= \exp \left[-\frac{\gamma_1 + \gamma_2}{4}D + i\frac{\omega - (\omega_1 + \omega_2)}{2}D \right] \times \left(-ie^{i\phi} \sin \theta \sin \frac{aD}{2} \right) \end{aligned} \quad (5.5)$$

The atom then enters a period of no external field, lasting T , during which the atom freely evolves, with the dissipation term \hat{H}_D contributing only to spontaneous emission. The equation becomes:

$$\begin{aligned} i\dot{c}_1' &= \omega_1 c_1' - i\frac{1}{2}\gamma_1 c_1' \\ i\dot{c}_2' &= \omega_2 c_2' - i\frac{1}{2}\gamma_2 c_2' \end{aligned} \quad (5.6)$$

Substituting the initial conditions $c_1'(0) = c_1(D)$ and $c_2'(0) = c_2(D)$, we solve for:

$$\begin{aligned} c_1(D+T) &= \left(\cos \frac{aD}{2} + i \cos \theta \sin \frac{aD}{2} \right) \\ &\quad \times \exp \left[-\frac{\gamma_1 + \gamma_2}{4}D - i\frac{\omega + \omega_1 + \omega_2}{2}D - \left(\frac{\gamma_1}{2} + i\omega_1 \right)T \right] \\ c_2(D+T) &= -ie^{i\phi} \sin \theta \sin \frac{aD}{2} \\ &\quad \times \exp \left[-\frac{\gamma_1 + \gamma_2}{4}D - i\frac{\omega - (\omega_1 + \omega_2)}{2}D - \left(\frac{\gamma_2}{2} + i\omega_2 \right)T \right] \end{aligned} \quad (5.7)$$

After passing through the second identical optical or radiofrequency field, the final solution becomes:

$$c_1(D + T + D) = \left\{ \left(\cos \frac{aD}{2} + i \cos \theta \sin \frac{aD}{2} \right)^2 - \sin^2 \theta \sin^2 \frac{aD}{2} \exp[QT - i(T\Delta + \phi)] \right\} \times \exp \left[-\frac{\gamma_1 + \gamma_2}{2} D - i(\omega + \omega_1 + \omega_2)D - \left(\frac{\gamma_1}{2} + i\omega_1 \right) T \right] \quad (5.8)$$

$$c_2(D + T + D) = \left(-i \sin \theta \sin \frac{aD}{2} \right) \times \left\{ \left(\cos \frac{aD}{2} - i \cos \theta \sin \frac{aD}{2} \right) + \left(\cos \frac{aD}{2} + i \cos \theta \sin \frac{aD}{2} \right) \exp[-QT + i(T\Delta + \phi)] \right\} \times \exp \left[-\frac{\gamma_1 + \gamma_2}{2} D + i(\omega - (\omega_1 + \omega_2))D - \left(\frac{\gamma_2}{2} + i\omega_2 \right) T \right]$$

In the separated resonance method, the final detected population is that of the atom in state $|2\rangle$. By subtracting the probabilities at $\phi = 0$ and $\phi = 180^\circ$, the SOF line shape is obtained:

$$P_{\text{SOF}} = |c_2(D + T + D)|_{\phi=0^\circ}^2 - |c_2(D + T + D)|_{\phi=180^\circ}^2 = 2 \cos(T\Delta - \Gamma) \times \exp \left[-\frac{\gamma_1 + \gamma_2}{2} (2D + T) \right] \times |\cos \frac{aD}{2} + i \cos \theta \sin \frac{aD}{2}|^2 \times |\sin \theta \sin \frac{aD}{2}|^2 \quad (5.9)$$

where $\Gamma = \arg \frac{\sin \frac{aD}{2}}{\cos \frac{aD}{2} + i \cos \theta \sin \frac{aD}{2}}$, and arg represents the principal value of the complex argument. Γ is an odd function of detuning Δ , and it is zero exactly at resonance, where the signal amplitude is maximized.

For the $2^3S - 2^3P$ transition in the ${}^4\text{He}$ atom to be measured in this experiment, since the lifetime of the 2^3S metastable state is much longer than the upper state 2^3P , i.e., $\gamma_1 \ll \gamma_2$, the influence of γ_1 can be neglected. Thus, $Q = -\frac{\gamma_2}{2}$, and $\cos \theta = \frac{(\Delta - i\gamma_2/2)}{a}$. Additionally, the high-frequency terms in the exponential can also be neglected. Therefore, the expression for $c_2(D + T + D)$ can be simplified to:

$$c_2(D + T + D) = \left\{ \left(\cos \frac{aD}{2} - i \cos \theta \sin \frac{aD}{2} \right) + \left(\cos \frac{aD}{2} + i \cos \theta \sin \frac{aD}{2} \right) \exp \left[\frac{\gamma_2}{2} T + i(T\Delta + \phi) \right] \right\} \times \left(-i \sin \theta \sin \frac{aD}{2} \right) \exp \left[-\frac{\gamma_2}{2} (T + D) \right] \quad (5.10)$$

In the experiment, the atoms initially reside in the 2^3S_1 state with $M_J = \pm 1$, and upon interaction with the probe light, they transition to the 2^3P_0 state, after which they return to the 2^3S_1 sublevels with equal probability. Due to the deflection of the

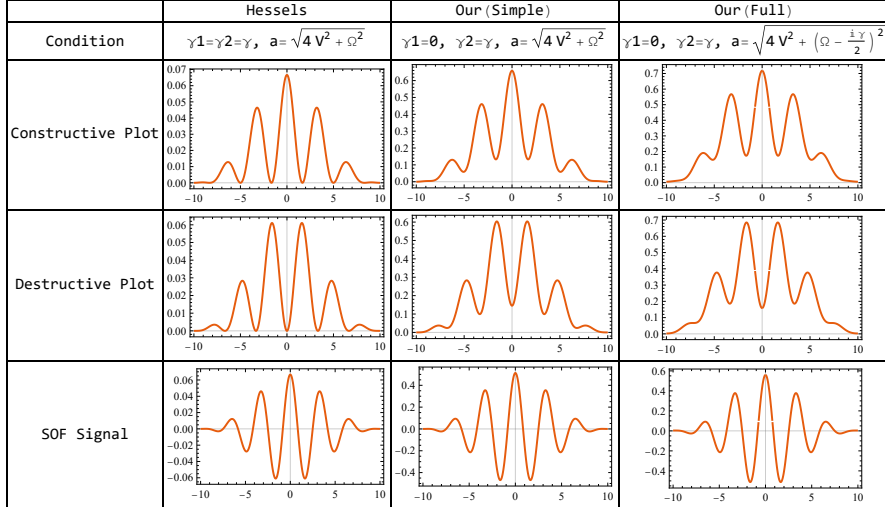


Figure 5.3 Theoretical Line Shape Comparison. Constructive and Destructive represent the line shapes when the phase $\phi = 0$ and $\phi = 180^\circ$, respectively, with the final SOF signal being the difference between the two. The calculation parameters are $V = 1$, $T = 200$ ns, and $D = 100$ ns.

Stern-Gerlach magnet, only atoms in the $M_J = 0$ state can be detected. Therefore, the actual signal is the probability of the atom being in the $|2\rangle$ state, i.e., $|c_2(D + T + D)|^2$. Since the laser frequency is much greater than the microwave frequency, it is not possible to precisely control the phase of the laser in the experiment. Thus, the laser phase term can be neglected in the line shape function, and the imaginary term can be omitted. To verify this, we numerically solve and compare the results, as shown in Figure 5.3. It can be seen that the simplified line shape obtained by removing the imaginary term is essentially identical to the result from the full calculation, with only a slight reduction in amplitude. In the figure, Constructive and Destructive represent the line shapes for the relative phase at $\phi = 0$ and $\phi = 180^\circ$, corresponding to coherent addition and coherent cancellation, respectively. The final SOF signal is the difference between the two. Since the laser phase cannot be controlled in the experiment, only signals similar to Constructive can be obtained, and the SOF signal cannot be acquired. Compared to Hessel's group's measurement of the $2^3 P_J$ intervals^[163], where both the upper and lower states are $2^3 P$ states, i.e., $\gamma_1 = \gamma_2$, each minimum in the Constructive and Destructive fringes reaches zero, leading to deeper fringes after cancellation. This also explains why the difference in the decay rates of the two states is represented by the quality factor Q .

(2) Density Matrix Solution for Lineshape

In the previous solution of the lineshape using the semiclassical method, there was not much discussion about the parameter V . However, in actual experiments, the corresponding parameters such as light intensity are crucial. Therefore, using the density

matrix method for the solution will better match the experimental conditions.

Similar to the lineshape of the three-level transition in the Rabi method, the density matrix equation can be expressed as:

$$\begin{aligned}\dot{\rho_{11}} &= \frac{i}{2} \left(\Omega_{12}^* \rho_{12} - \Omega_{12} \rho_{12}^\dagger \right) + \gamma_{21} \rho_{22} \\ \dot{\rho_{12}} &= - \left(\frac{\gamma_2}{2} + i\Delta_2 \right) \rho_{12} - \frac{i\Omega_{12}}{2} (\rho_{22} - \rho_{11}) \\ \dot{\rho_{22}} &= - \frac{i}{2} \left(\Omega_{12}^* \rho_{12} - \Omega_{12} \rho_{12}^\dagger \right) - \gamma_2 \rho_{22}\end{aligned}\quad (5.11)$$

It should be noted that when solving the density matrix equation, the Rabi frequency Ω is obtained from the experimental parameters in the two interaction regions, while in the free evolution period, it is set to $\Omega = 0$.

5.2.3.3 Experimental Setup and Phenomenon

In the three-wave or four-wave experimental schemes, special optical path designs are needed to achieve segmented actions and delays^[120,274,278,278]. These two schemes can observe the SOF signal through careful design, but it is difficult to precisely adjust the action time D and the interval time T . Considering the complexity of the optical path requirements in these two schemes, the experiment attempts to control the AOM switch via a delay generator, replacing the spatial separation with temporal intervals, thus greatly simplifying the experimental setup. At the same time, since the temporal interval can be directly adjusted by the delay generator, the action time and the interval time can be easily changed.

The experimental setup is shown in Figure 5.4. A spatial AOM is added in the detection optical path to use the first-order light for detection. In the preliminary experiment, only single-sided laser detection is used. The digital driver for the AOM is controlled by a delay generator (DG535, SRS). The delay generator can customize waveforms and adjust the action time D and interval time T . On the other side of the beam, a detector (PDA10, Thorlabs) is used to monitor the laser switching. To ensure that the beam only interacts with two laser pulses, a delay of 10 μ s is added after each pair of pulses. However, the AOM switch has a certain delay, which depends on the laser beam waist position. In the experiment, by adjusting the lens position, the beam waist is set about 2 mm after the AOM, reducing the switching delay to below 100 ns. The beam velocity is 110 m/s, and the laser power is locked at 75 μ W.

For reference, the delay generator is first adjusted to apply a 200 ns laser pulse every 10 μ s. The measured spectrum is shown in Figure 5.5(a). A Lorentzian fit with a shared linewidth gives a linewidth of about 4.7 MHz. Then, the system is adjusted

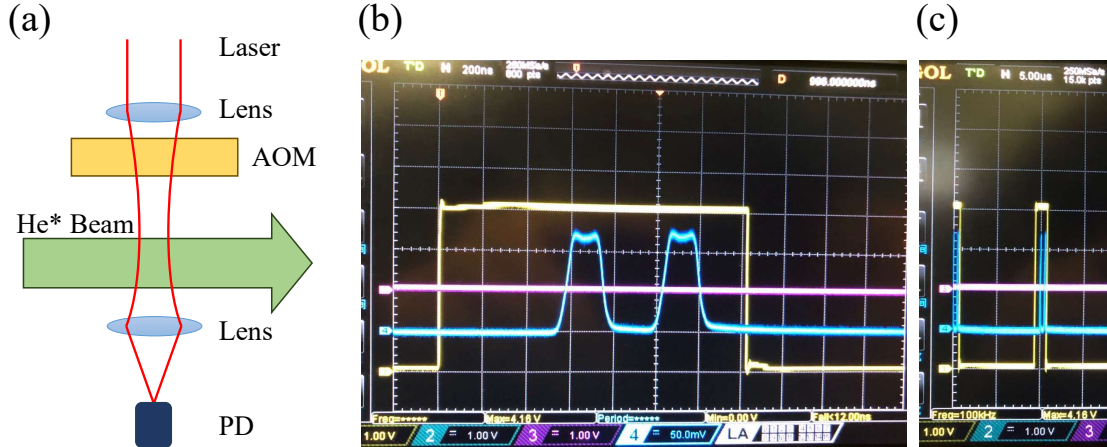


Figure 5.4 (a) Schematic of the Ramsey spectroscopy experimental setup. (b) and (c) are the detector monitoring signals. The AOM is driven by the delay generator to control the switching of the light, and the detector on the other side of the beam monitors the switching of the laser. In the experiment, the action time $D = 100$ ns and the free evolution time $T = 300$ ns are set. In figures (b) and (c), the blue signal is the light pulse signal monitored by the detector. Due to the delay in the AOM switching, the monitoring signal shows about 100 ns rise and fall times. The yellow signal represents the pulse delay, with two pulses generated every 10 μ s to ensure the atom interacts with only two pulses.

to a dual-pulse mode, where two laser pulses with an action time of $D = 100$ ns and an interval of $T = 300$ ns are applied every 10 μ s. The measured spectrum is shown in Figure 5.5(b). Since there is no suitable fitting function for the lineshape, each distinguishable small peak is fitted using a Lorentzian function with a shared linewidth, giving a linewidth of about 2.4 MHz. This experimental result is in good agreement with the simulated lineshape, as shown in Figure 5.5(c). Theoretically, the linewidth of each small peak should be $1/2T \approx 1.67$ MHz. However, in the experiment, to minimize the AOM switching delay, the beam waist is adjusted to be very small, with a waist radius of less than 0.2 mm at the interaction point with the beam. Additionally,

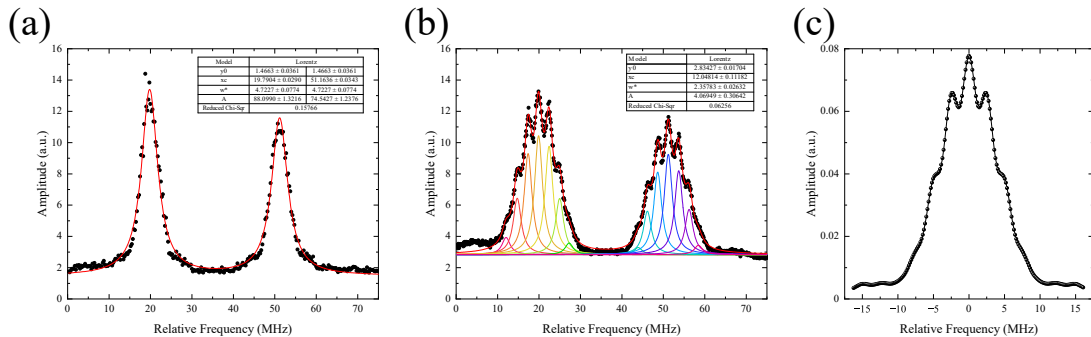


Figure 5.5 (a) A 200 ns laser pulse is applied with a 10 μ s interval, and the measured spectrum. A Lorentzian fit with a shared linewidth gives a linewidth of about 4.7 MHz. (b) Two laser pulses with an interval of 10 μ s, an action time of $D = 100$ ns, and an interval of $T = 300$ ns, and the measured spectrum. A Lorentzian fit with a shared linewidth is applied to each distinguishable small peak, and the linewidth is about 2.4 MHz. The fit table in the figure only shows the result for the first peak. (c) Simulation of the lineshape using the density matrix for $D = 100$ ns and $T = 300$ ns.

the experimental power is $75 \mu\text{W}$, which is much larger than the saturation intensity. This leads to both power broadening and saturation broadening, making the observed linewidth much larger than the theoretical linewidth. To obtain a narrower linewidth, increasing the interval time T may be considered. However, simulations show that when the interval time is increased, the oscillations become less prominent. In the experiment, a measurement was performed at $D = 100 \text{ ns}$ and $T = 500 \text{ ns}$, and the result confirmed that under the current experimental conditions, a clearly defined fringe pattern and a linewidth smaller than the natural linewidth cannot be obtained.

This experiment uses a delay generator to drive the AOM to control the switching of the light, and the Ramsey lineshape was observed using only one laser. The experimental results are in good agreement with the simulated lineshape. However, due to the large difference in the lifetimes of the ground and excited states, a significant background appeared in the Ramsey spectrum, making the fringes unclear. To obtain a narrower linewidth, the time interval between the two pulses needs to be increased, but this also increases the background. Therefore, the Ramsey method is not suitable for measuring the frequency of the $2^3S - 2^3P$ transition. In future spectral measurements of other transitions or systems, further exploration and refinement of the Ramsey method will help overcome the limitation of the natural linewidth, leading to higher precision results.

Bibliography

- [1] ÅNGSTRÖM A J. Optische Untersuchungen[J]. Annalen der Physik, 1855, 170(1): 141-165.
- [2] RYDBERG J R. XXXIV. On the structure of the line-spectra of the chemical elements [J]. The London, Edinburgh, and Dublin Philosophical Magazine and Journal of Science, 1890, 29(179): 331-337.
- [3] BOHR N. I. On the constitution of atoms and molecules [J]. The London, Edinburgh, and Dublin Philosophical Magazine and Journal of Science, 1913, 26(151): 1-25.
- [4] SOMMERFELD A. Zur Quantentheorie der Spektrallinien[J]. Annalen der Physik, 1916, 356(17): 1-94.
- [5] DE BROGLIE L. Recherches sur la théorie des quanta[D]. Migration-université en cours d'affectation, 1924.
- [6] SCHRÖDINGER E. Quantisierung als Eigenwertproblem[J]. Annalen der Physik, 1926, 384 (4): 361-376.
- [7] DIRAC P A M, BOHR N H D. The quantum theory of the emission and absorption of radiation[J]. Proceedings of the Royal Society of London. Series A, Containing Papers of a Mathematical and Physical Character, 1927, 114(767): 243-265.
- [8] DIRAC P A M, FOWLER R H. The quantum theory of the electron[J]. Proceedings of the Royal Society of London. Series A, Containing Papers of a Mathematical and Physical Character, 1928, 117(778): 610-624.
- [9] FERMI E. Quantum Theory of Radiation[J]. Reviews of Modern Physics, 1932, 4: 87-132.
- [10] OPPENHEIMER J R. Note on the Theory of the Interaction of Field and Matter[J]. Physical Review, 1930, 35: 461-477.
- [11] LAMB W E, RETHERFORD R C. Fine Structure of the Hydrogen Atom by a Microwave Method[J]. Physical Review, 1947, 72: 241-243.
- [12] BETHE H A. The Electromagnetic Shift of Energy Levels[J]. Physical Review, 1947, 72: 339-341.
- [13] TOMONAGA S. On a Relativistically Invariant Formulation of the Quantum Theory of Wave Fields[J]. Progress of Theoretical Physics, 1946, 1(2): 27-42.
- [14] SCHWINGER J. On Quantum-Electrodynamics and the Magnetic Moment of the Electron [J]. Physical Review, 1948, 73: 416-417.
- [15] SCHWINGER J. Quantum Electrodynamics. I. A Covariant Formulation[J]. Physical Review, 1948, 74: 1439-1461.
- [16] FEYNMAN R P. Space-Time Approach to Quantum Electrodynamics[J]. Physical Review,

- 1949, 76: 769-789.
- [17] FEYNMAN R P. Mathematical Formulation of the Quantum Theory of Electromagnetic Interaction[J]. Physical Review, 1950, 80: 440-457.
- [18] DYSON F J. The Radiation Theories of Tomonaga, Schwinger, and Feynman[J]. Physical Review, 1949, 75: 486-502.
- [19] DYSON F J. The S Matrix in Quantum Electrodynamics[J]. Physical Review, 1949, 75: 1736-1755.
- [20] FAN X, MYERS T G, SUKRA B A D, et al. Measurement of the Electron Magnetic Moment [J]. Physical Review Letters, 2023, 130: 071801.
- [21] YANG C N, MILLS R L. Conservation of Isotopic Spin and Isotopic Gauge Invariance[J]. Physical Review, 1954, 96: 191-195.
- [22] HOOFT G. Renormalization of massless Yang-Mills fields[J]. Nuclear Physics B, 1971, 33 (1): 173-199.
- [23] HOOFT G. Renormalizable Lagrangians for massive Yang-Mills fields[J]. Nuclear Physics B, 1971, 35(1): 167-188.
- [24] HIGGS P W. Broken Symmetries and the Masses of Gauge Bosons[J]. Physical Review Letters, 1964, 13: 508-509.
- [25] WEINBERG S. A Model of Leptons[J]. Physical Review Letters, 1967, 19: 1264-1266.
- [26] GLASHOW S L, ILIOPOULOS J, MAIANI L. Weak Interactions with Lepton-Hadron Symmetry[J]. Physical Review D, 1970, 2: 1285-1292.
- [27] FRITZSCH H, GELL-MANN M, LEUTWYLER H. Advantages of the color octet gluon picture[J]. Physics Letters B, 1973, 47(4): 365-368.
- [28] AAD G, ABAJYAN T, ABBOTT B, et al. Observation of a new particle in the search for the Standard Model Higgs boson with the ATLAS detector at the LHC[J]. Physics Letters B, 2012, 716(1): 1-29.
- [29] CHATRCHYAN S, KHACHATRYAN V, SIRUNYAN A, et al. Observation of a new boson at a mass of 125 GeV with the CMS experiment at the LHC[J]. Physics Letters B, 2012, 716 (1): 30-61.
- [30] SUSHKOV A O, KIM W J, DALVIT D A R, et al. New Experimental Limits on Non-Newtonian Forces in the Micrometer Range[J]. Physical Review Letters, 2011, 107: 171101.
- [31] CLOWE D, BRADAč M, GONZALEZ A H, et al. A Direct Empirical Proof of the Existence of Dark Matter[J]. The Astrophysical Journal, 2006, 648(2): L109.
- [32] FUKUDA Y, HAYAKAWA T, ICHIHARA E, et al. Measurements of the Solar Neutrino Flux from Super-Kamiokande's First 300 Days[J]. Physical Review Letters, 1998, 81: 1158-1162.
- [33] BEYER A, MAISENBACHER L, MATVEEV A, et al. The Rydberg constant and proton

Bibliography

- size from atomic hydrogen[J]. Science, 2017, 358(6359): 79-85.
- [34] GRININ A, MATVEEV A, YOST D C, et al. Two-photon frequency comb spectroscopy of atomic hydrogen[J]. Science, 2020, 370(6520): 1061-1066.
- [35] KARSHENBOIM S G. Precision physics of simple atoms: QED tests, nuclear structure and fundamental constants[J]. Physics Reports, 2005, 422(1): 1-63.
- [36] PATKÓŠ V, YEROKHIN V A, PACHUCKI K. Complete quantum electrodynamic $\alpha^6 m$ correction to energy levels of light atoms[J]. Physical Review A, 2019, 100: 042510.
- [37] PATKÓŠ V, YEROKHIN V A, PACHUCKI K. Complete $\alpha^7 m$ Lamb shift of helium triplet states[J]. Physical Review A, 2021, 103: 042809.
- [38] PACHUCKI K, PATKÓŠ V, YEROKHIN V A. Hyperfine splitting in $^{6,7}\text{Li}^+$ [J]. Physical Review A, 2023, 108: 052802.
- [39] MITROY J, TANG L Y. Tune-out wavelengths for metastable helium[J]. Physical Review A, 2013, 88: 052515.
- [40] HENSON B M, ROSS J A, THOMAS K F, et al. Measurement of a helium tune-out frequency: an independent test of quantum electrodynamics[J]. Science, 2022, 376(6589): 199-203.
- [41] RUTHERFORD E. LXXIX. The scattering of α and β particles by matter and the structure of the atom [J]. The London, Edinburgh, and Dublin Philosophical Magazine and Journal of Science, 1911, 21(125): 669-688.
- [42] RUTHERFORD E. LIV. Collision of α particles with light atoms. IV. An anomalous effect in nitrogen [J]. The London, Edinburgh, and Dublin Philosophical Magazine and Journal of Science, 1919, 37(222): 581-587.
- [43] RUTHERFORD E. Bakerian Lecture: Nuclear constitution of atoms[J]. Proceedings of the Royal Society of London. Series A, Containing Papers of a Mathematical and Physical Character, 1920, 97(686): 374-400.
- [44] RUTHERFORD E. Studies of Atomic Nuclei[J]. Science, 1925, 62(1601): 209-211.
- [45] FRISCH R, STERN O. Über die magnetische Ablenkung von Wasserstoffmolekülen und das magnetische Moment des Protons. I[J]. Zeitschrift für Physik, 1933, 85(1): 4-16.
- [46] HOFSTADTER R, MCALLISTER R W. Electron Scattering from the Proton[J]. Physical Review, 1955, 98: 217-218.
- [47] GELL-MANN M. A schematic model of baryons and mesons[J]. Physics Letters, 1964, 8 (3): 214-215.
- [48] ZWEIG G. An SU_3 model for strong interaction symmetry and its breaking; Version 2[M]// Developments in the Quark Theory of Hadrons. 1964.
- [49] BREIDENBACH M, FRIEDMAN J I, KENDALL H W, et al. Observed Behavior of Highly

Bibliography

- Inelastic Electron-Proton Scattering[J]. Physical Review Letters, 1969, 23: 935-939.
- [50] FEYNMAN R P. Behavior of hadron collisions at extreme energies.[J]. pp 237-58 of High Energy Collisions. New York Gordon and Breach, Science Publishers, Inc., 1969.
- [51] FEYNMAN R P. The Behavior of Hadron Collisions at Extreme Energies[M]//NOZ M E, KIM Y S. Special Relativity and Quantum Theory: A Collection of Papers on the Poincaré Group. Springer Netherlands, 1988: 289-304.
- [52] GROSS D J, WILCZEK F. Ultraviolet Behavior of Non-Abelian Gauge Theories[J]. Physical Review Letters, 1973, 30: 1343-1346.
- [53] POLITZER H D. Reliable Perturbative Results for Strong Interactions?[J]. Physical Review Letters, 1973, 30: 1346-1349.
- [54] POHL R, NEZ F, FERNANDES L M P, et al. Laser spectroscopy of muonic deuterium[J]. Science, 2016, 353(6300): 669-673.
- [55] EDITORIAL. Proton puzzles[J]. Nature Reviews Physics, 2021, 3(1): 1-1.
- [56] MOHR P J, TAYLOR B N, NEWELL D B. CODATA recommended values of the fundamental physical constants: 2006[J]. Reviews of Modern Physics, 2008, 80: 633-730.
- [57] POHL R, ANTOGNINI A, NEZ F, et al. The size of the proton[J]. Nature, 2010, 466(7303): 213-216.
- [58] BERNAUER J C, ACHENBACH P, AYERBE GAYOSO C, et al. High-Precision Determination of the Electric and Magnetic Form Factors of the Proton[J]. Physical Review Letters, 2010, 105: 242001.
- [59] MOHR P J, TAYLOR B N, NEWELL D B. CODATA recommended values of the fundamental physical constants: 2010[J]. Reviews of Modern Physics, 2012, 84: 1527-1605.
- [60] MOHR P J, NEWELL D B, TAYLOR B N. CODATA recommended values of the fundamental physical constants: 2014[J]. Reviews of Modern Physics, 2016, 88: 035009.
- [61] ANTOGNINI A, NEZ F, SCHUHMANN K, et al. Proton Structure from the Measurement of 2S–2P Transition Frequencies of Muonic Hydrogen[J]. Science, 2013, 339(6118): 417-420.
- [62] POHL R. Laser Spectroscopy of Muonic Hydrogen and the Puzzling Proton[J]. Journal of the Physical Society of Japan, 2016, 85(9): 091003.
- [63] KARR J P, MARCHAND D, VOUTIER E. The proton size[J]. Nature Reviews Physics, 2020, 2(11): 601-614.
- [64] CHAMBERS E E, HOFSTADTER R. Structure of the Proton[J]. Physical Review, 1956, 103: 1454-1463.
- [65] LEHMANN P, TAYLOR R, WILSON R. Electron-Proton Scattering at Low Momentum Transfers[J]. Physical Review, 1962, 126: 1183-1188.
- [66] DUDELZAK B, SAUVAGE G, LEHMANN P. Measurements of the form factors of the

Bibliography

- proton at momentum transfers $q^2 \leq 2 \text{ fermi}^{-2}$ [J]. *Il Nuovo Cimento*, 1963, 28(1): 18-24.
- [67] FRÈREJACQUE D, BENAKSAS D, DRICKEY D. Proton Form Factors from Observation of Recoil Protons[J]. *Physical Review*, 1966, 141: 1308-1312.
- [68] AKIMOV Y K, ANDERT K, KAZARINOV Y M, et al. Electron scattering by protons at small angles[J]. *Journal of Experimental and Theoretical Physics*, 1972, 35(4).
- [69] BORKOWSKI F, PEUSER P, SIMON G, et al. Electromagnetic form factors of the proton at low four-momentum transfer[J]. *Nuclear Physics A*, 1974, 222(2): 269-275.
- [70] MURPHY J J, SHIN Y M, SKOPIK D M. Proton form factor from 0.15 to 0.79 fm^{-2} [J]. *Physical Review C*, 1974, 9: 2125-2129.
- [71] BORKOWSKI F, SIMON G, WALTHER V, et al. Electromagnetic form factors of the proton at low four-momentum transfer (II)[J]. *Nuclear Physics B*, 1975, 93(3): 461-478.
- [72] SIMON G, SCHMITT C, BORKOWSKI F, et al. Absolute electron-proton cross sections at low momentum transfer measured with a high pressure gas target system[J]. *Nuclear Physics A*, 1980, 333(3): 381-391.
- [73] MCCORD M, CRANNELL H, FAGG L, et al. Preliminary results of a new determination of the rms charge radius of the proton[J]. *Nuclear Instruments and Methods in Physics Research Section B: Beam Interactions with Materials and Atoms*, 1991, 56-57: 496-499.
- [74] ESCHRICH I, KRÜGER H, SIMON J, et al. Measurement of the Σ^- charge radius by Σ^- -electron elastic scattering[J]. *Physics Letters B*, 2001, 522(3): 233-239.
- [75] HAND L N, MILLER D G, WILSON R. Electric and Magnetic Form Factors of the Nucleon [J]. *Reviews of Modern Physics*, 1963, 35: 335-349.
- [76] HöHLER G, PIETARINEN E, SABBA-STEFANESCU I, et al. Analysis of electromagnetic nucleon form factors[J]. *Nuclear Physics B*, 1976, 114(3): 505-534.
- [77] MERGELL P, MEIßNER U G, DRECHSEL D. Dispersion-theoretical analysis of the nucleon electromagnetic form factors[J]. *Nuclear Physics A*, 1996, 596(3): 367-396.
- [78] ROSENFELDER R. Coulomb corrections to elastic electron-proton scattering and the proton charge radius[J]. *Physics Letters B*, 2000, 479(4): 381-386.
- [79] SICK I. On the rms-radius of the proton[J]. *Physics Letters B*, 2003, 576(1): 62-67.
- [80] BLUNDEN P G, SICK I. Proton radii and two-photon exchange[J]. *Physical Review C*, 2005, 72: 057601.
- [81] BELUSHKIN M A, HAMMER H W, MEIßNER U G. Dispersion analysis of the nucleon form factors including meson continua[J]. *Physical Review C*, 2007, 75: 035202.
- [82] BORISYUK D. Proton charge and magnetic rms radii from the elastic ep scattering data[J]. *Nuclear Physics A*, 2010, 843(1): 59-67.
- [83] HILL R J, PAZ G. Model-independent extraction of the proton charge radius from electron

Bibliography

- scattering[J]. Physical Review D, 2010, 82: 113005.
- [84] XIONG W, GASPARIAN A, GAO H, et al. A small proton charge radius from an electron-proton scattering experiment[J]. Nature, 2019, 575(7781): 147-150.
- [85] PARTHEY C G, MATVEEV A, ALNIS J, et al. Improved Measurement of the Hydrogen 1S–2S Transition Frequency[J]. Physical Review Letters, 2011, 107: 203001.
- [86] MATVEEV A, PARTHEY C G, PREDEHL K, et al. Precision Measurement of the Hydrogen 1S–2S Frequency via a 920-km Fiber Link[J]. Physical Review Letters, 2013, 110: 230801.
- [87] ANTOGNINI A. Muonic atoms and the nuclear structure[A]. 2016. arXiv: 1512.01765.
- [88] HAGLEY E W, PIPKIN F M. Separated oscillatory field measurement of hydrogen $2S_{1/2} - 2P_{3/2}$ fine structure interval[J]. Physical Review Letters, 1994, 72: 1172-1175.
- [89] DE BEAUVOIR B, NEZ F, JULIEN L, et al. Absolute Frequency Measurement of the 2S–8S/D Transitions in Hydrogen and Deuterium: New Determination of the Rydberg Constant[J]. Physical Review Letters, 1997, 78: 440-443.
- [90] ARNOULT O, NEZ F, JULIEN L, et al. Optical frequency measurement of the 1S–3S two-photon transition in hydrogen[J]. The European Physical Journal D, 2010, 60(2): 243-256.
- [91] BEYER A, MAISENBACHER L, MATVEEV A, et al. Active fiber-based retroreflector providing phase-retracing anti-parallel laser beams for precision spectroscopy[J]. Optics Express, 2016, 24(15): 17470-17485.
- [92] FLEURBAEY H, GALTIER S, THOMAS S, et al. New Measurement of the 1S–3S Transition Frequency of Hydrogen: Contribution to the Proton Charge Radius Puzzle[J]. Physical Review Letters, 2018, 120: 183001.
- [93] BEZGINOV N, VALDEZ T, HORBATSCH M, et al. A measurement of the atomic hydrogen Lamb shift and the proton charge radius[J]. Science, 2019, 365(6457): 1007-1012.
- [94] BRANDT A D, COOPER S F, RASOR C, et al. Measurement of the $2S_{1/2} - 8D_{5/2}$ Transition in Hydrogen[J]. Physical Review Letters, 2022, 128: 023001.
- [95] TIESINGA E, MOHR P J, NEWELL D B, et al. CODATA recommended values of the fundamental physical constants: 2018[J]. Reviews of Modern Physics, 2021, 93: 025010.
- [96] PACHUCKI K, LENSKY V, HAGELSTEIN F, et al. Comprehensive theory of the Lamb shift in light muonic atoms[J]. Reviews of Modern Physics, 2024, 96: 015001.
- [97] COOKE D A, CRIVELLI P, ALNIS J, et al. Observation of positronium annihilation in the 2S state: towards a new measurement of the 1S–2S transition frequency[J]. Hyperfine Interactions, 2015, 233(1): 67-73.
- [98] MILLS A. Advances in atomic, molecular, and optical physics: 65, chapter five. Experiments with Dense Low-Energy Positrons and Positronium[M]. Academic Press, 2016: 265-290.

Bibliography

- [99] CASSIDY D B. Experimental progress in positronium laser physics[J]. The European Physical Journal D, 2018, 72(3): 53.
- [100] GURUNG L, BABIJ T J, PÉREZ-RÍOS J, et al. Observation of asymmetric line shapes in precision microwave spectroscopy of the positronium $2^3S_1 \rightarrow 2^3P_J$ ($J=1,2$) fine-structure intervals[J]. Physical Review A, 2021, 103: 042805.
- [101] ADKINS G, CASSIDY D, PéREZ-RíOS J. Precision spectroscopy of positronium: Testing bound-state QED theory and the search for physics beyond the Standard Model[J]. Physics Reports, 2022, 975: 1-61.
- [102] SHELDON R E, BABIJ T J, REEDER S H, et al. Microwave spectroscopy of positronium atoms in free space[J]. Physical Review A, 2023, 107: 042810.
- [103] SHELDON R E, BABIJ T J, REEDER S H, et al. Precision Microwave Spectroscopy of the Positronium $2^3S_1 \rightarrow 2^3P_2$ Interval[J]. Physical Review Letters, 2023, 131: 043001.
- [104] ADKINS G S, KIM M, PARSONS C, et al. Three-Photon-Annihilation Contributions to Positronium Energies at Order $m\alpha^7$ [J]. Physical Review Letters, 2015, 115: 233401.
- [105] OHAYON B, JANKA G, CORTINOVIS I, et al. Precision Measurement of the Lamb Shift in Muonium[J]. Physical Review Letters, 2022, 128: 011802.
- [106] JANKA G, OHAYON B, CORTINOVIS I, et al. Measurement of the transition frequency from $2S_{1/2}$, $F = 0$ to $2P_{1/2}$, $F = 1$ states in Muonium[J]. Nature Communications, 2022, 13(1): 7273.
- [107] PUCHALSKI M, KOMASA J, CZACHOROWSKI P, et al. Complete α^6m Corrections to the Ground State of H_2 [J]. Physical Review Letters, 2016, 117: 263002.
- [108] KARR J P, HILICO L, KOELEMEIJ J C J, et al. Hydrogen molecular ions for improved determination of fundamental constants[J]. Physical Review A, 2016, 94: 050501.
- [109] ALIGHANBARI S, GIRI G S, CONSTANTIN F L, et al. Precise test of quantum electrodynamics and determination of fundamental constants with HD^+ ions[J]. Nature, 2020, 581 (7807): 152-158.
- [110] PATRA S, GERMANN M, KARR J P, et al. Proton-electron mass ratio from laser spectroscopy of HD^+ at the part-per-trillion level[J]. Science, 2020, 369(6508): 1238-1241.
- [111] KOROBOV V I, HILICO L, KARR J P. Fundamental Transitions and Ionization Energies of the Hydrogen Molecular Ions with Few ppt Uncertainty[J]. Physical Review Letters, 2017, 118: 233001.
- [112] TAO L G, LIU A W, PACHUCKI K, et al. Toward a Determination of the Proton-Electron Mass Ratio from the Lamb-Dip Measurement of HD [J]. Physical Review Letters, 2018, 120: 153001.
- [113] COIZIN F M J, DUPRÉ P, SALUMBIDES E J, et al. Sub-Doppler Frequency Metrology in

Bibliography

- HD for Tests of Fundamental Physics[J]. Physical Review Letters, 2018, 120: 153002.
- [114] HÖLSCH N, BEYER M, SALUMBIDES E J, et al. Benchmarking Theory with an Improved Measurement of the Ionization and Dissociation Energies of H₂[J]. Physical Review Letters, 2019, 122: 103002.
- [115] PUCHALSKI M, KOMASA J, CZACHOROWSKI P, et al. Nonadiabatic QED Correction to the Dissociation Energy of the Hydrogen Molecule[J]. Physical Review Letters, 2019, 122: 103003.
- [116] DREISSEN L S, ROTH C, GRÜNDEMAN E L, et al. Ramsey-comb precision spectroscopy in xenon at vacuum ultraviolet wavelengths produced with high-order harmonic generation [J]. Physical Review A, 2020, 101: 052509.
- [117] KARSHENBOIM S G, OZAWA A, SHELYUTO V A, et al. The Lamb shift of the 1s state in hydrogen: Two-loop and three-loop contributions[J]. Physics Letters B, 2019, 795: 432-437.
- [118] JENTSCHURA U D, MOHR P J, TAN J N, et al. Fundamental constants and tests of theory in Rydberg states of hydrogenlike ions[J]. Canadian Journal of Physics, 2009, 87(7): 757-762.
- [119] RAMOS A, MOORE K, RAITHEL G. Measuring the Rydberg constant using circular Rydberg atoms in an intensity-modulated optical lattice[J]. Physical Review A, 2017, 96: 032513.
- [120] SUN W, ZHANG P P, ZHOU P P, et al. Measurement of Hyperfine Structure and the Zemach Radius in ⁶Li⁺ Using Optical Ramsey Technique[J]. Physical Review Letters, 2023, 131: 103002.
- [121] SCHMIDT S, WILLIG M, HAACK J, et al. The next generation of laser spectroscopy experiments using light muonic atoms[J]. Journal of Physics: Conference Series, 2018, 1138 (1): 012010.
- [122] EDITORIAL. Pierre Jules César Janssen[J]. Monthly Notices of the Royal Astronomical Society, 1908, 68(4): 245-249.
- [123] Merrill P W. Wave-Lengths of the Stronger Lines in the Helium Spectrum[J]. The Astrophysical Journal, 1917, 46: 357.
- [124] MARTIN W C. Improved ⁴i 1snl ionization energy, energy levels, and Lamb shifts for 1sns and 1snp terms[J]. Physical Review A, 1987, 36: 3575-3589.
- [125] MEGGERS W F. Infrared spectra of noble gases (10500 to 13000 Å)[J]. Journal of research of the National Bureau of Standards, 1935, 14: 487.
- [126] HERZBERG G. Ionization potentials and Lamb shifts of the ground states of ⁴He and ³He[J]. Proceedings of the Royal Society of London. Series A. Mathematical and Physical Sciences, 1958, 248(1254): 309-332.
- [127] PEKERIS C L. 1¹S and 2³S States of Helium[J]. Physical Review, 1959, 115: 1216-1221.
- [128] PEKERIS C L. 1¹S, 2¹S, and 2³S States of H⁻ and of He[J]. Physical Review, 1962, 126:

- 1470-1476.
- [129] EIKEMA K S E, UBACHS W, VASSEN W, et al. First laser excitation of the ${}^4\text{He}$ $1^1\text{S}-2^1\text{P}$ resonance line at 58 nm[J]. Physical Review Letters, 1993, 71: 1690-1692.
- [130] EIKEMA K S E, UBACHS W, VASSEN W, et al. Precision Measurements in Helium at 58 nm: Ground State Lamb Shift and the $1^1\text{S}-2^1\text{P}$ Transition Isotope Shift[J]. Physical Review Letters, 1996, 76: 1216-1219.
- [131] EIKEMA K S E, UBACHS W, VASSEN W, et al. Lamb shift measurement in the $1t^1\text{S}$ ground state of helium[J]. Physical Review A, 1997, 55: 1866-1884.
- [132] BERGESON S D, BALAKRISHNAN A, BALDWIN K G H, et al. Measurement of the He Ground State Lamb Shift via the Two-Photon $1^1\text{S}-2^1\text{S}$ Transition[J]. Physical Review Letters, 1998, 80: 3475-3478.
- [133] BERGESON S D, BALDWIN K G H, LUCATORTO T B, et al. Doppler-free two-photon spectroscopy in the vacuum ultraviolet: helium $1^1\text{S}-2^1\text{S}$ transition[J]. Journal of the Optical Society of America B: Optical Physics, 2000, 17(9): 1599-1606.
- [134] PICHANICK F M J, SWIFT R D, JOHNSON C E, et al. Experiments on the 2^3P State of Helium. I. A Measurement of the $2^3\text{P}_1 - 2^3\text{P}_2$ Fine Structure[J]. Physical Review, 1968, 169: 55-78.
- [135] LEWIS S A, PICHANICK F M J, HUGHES V W. Experiments on the 2^3P State of Helium. II. Measurements of the Zeeman Effect[J]. Physical Review A, 1970, 2: 86-101.
- [136] KPONOU A, HUGHES V W, JOHNSON C E, et al. Experiments on the 2^3P state of helium. III. Measurement of the $2^3\text{P}_0 - 2^3\text{P}_1$ fine-structure interval[J]. Physical Review A, 1981, 24: 264-278.
- [137] FRIEZE W, HINDS E A, HUGHES V W, et al. Experiments on the 2^3P state of helium. IV. Measurement of the $2^3\text{P}_0 - 2^3\text{P}_2$ fine-structure interval[J]. Physical Review A, 1981, 24: 279-287.
- [138] GIACOBINO E, BIRABEN F. Energy level measurements and Lamb shift in helium[J]. Journal of Physics B: Atomic and Molecular Physics, 1982, 15(11): L385.
- [139] HLOUSEK L, LEE S A, FAIRBANK W M. Precision Wavelength Measurements and New Experimental Lamb Shifts in Helium[J]. Physical Review Letters, 1983, 50: 328-331.
- [140] BLOCH D, TRENEC G, LEDUC M. Isotope shift of the $2^3\text{S}_1 - 2^3\text{P}$ transition in helium[J]. Journal of Physics B: Atomic and Molecular Physics, 1985, 18(6): 1093.
- [141] ZHAO P, LAWALL J R, KAM A W, et al. Direct laser measurement of the Lamb shift of $2^3\text{S}-2^3\text{P}$ transitions in helium[J]. Physical Review Letters, 1989, 63: 1593-1596.
- [142] ZHAO P, LAWALL J R, PIPKIN F M. High-precision isotope-shift measurement of $2^3\text{S}-2^3\text{P}$ transition in helium[J]. Physical Review Letters, 1991, 66: 592-595.

Bibliography

- [143] SHINER D, DIXSON R, ZHAO P. Precise measurement of the Lamb shift and fine structure of the 2S–2P transition in triplet helium[J]. Physical Review Letters, 1994, 72: 1802-1805.
- [144] SHINER D, DIXSON R, VEDANTHAM V. Three-Nucleon Charge Radius: A Precise Laser Determination Using ${}^3\text{He}$ [J]. Physical Review Letters, 1995, 74: 3553-3556.
- [145] PASTOR P C, GIUSFREDI G, NATALE P D, et al. Absolute Frequency Measurements of the ${}^2\text{S}_1 \rightarrow {}^2\text{P}_{0,1,2}$ Atomic Helium Transitions around 1083 nm[J]. Physical Review Letters, 2004, 92: 023001.
- [146] PASTOR P C, GIUSFREDI G, DE NATALE P, et al. Erratum: Absolute Frequency Measurements of the ${}^2\text{S}_1 \rightarrow {}^2\text{P}_{0,1,2}$ Atomic Helium Transitions around 1083 nm [Physical Review Letters 92, 023001 (2004)][J]. Physical Review Letters, 2006, 97: 139903.
- [147] CANCIO PASTOR P, CONSOLINO L, GIUSFREDI G, et al. Frequency Metrology of Helium around 1083 nm and Determination of the Nuclear Charge Radius[J]. Physical Review Letters, 2012, 108: 143001.
- [148] PAVONE F S, MARIN F, DE NATALE P, et al. First Pure Frequency Measurement of an Optical Transition in Helium: Lamb Shift of the ${}^2\text{S}_1$ Metastable Level[J]. Physical Review Letters, 1994, 73: 42-45.
- [149] MARIN F, MINARDI F, PAVONE F S, et al. Hyperfine structure of the ${}^3\text{P}$ state of ${}^3\text{He}$ and isotope shift for the ${}^2\text{S}–{}^3\text{P}_0$ transition[J]. Zeitschrift für Physik D Atoms, Molecules and Clusters, 1995, 32(4): 285-293.
- [150] DORRER C, NEZ F, DE BEAUVOIR B, et al. Accurate Measurement of the ${}^2\text{S}_1 – {}^3\text{D}_1$ Two-Photon Transition Frequency in Helium: New Determination of the ${}^2\text{S}_1$ Lamb Shift[J]. Physical Review Letters, 1997, 78: 3658-3661.
- [151] MUELLER P, WANG L B, DRAKE G W F, et al. Fine Structure of the 1s3p ${}^3\text{P}_j$ Level in Atomic ${}^4\text{He}$: Theory and Experiment[J]. Physical Review Letters, 2005, 94: 133001.
- [152] SULAI I A, WU Q, BISHOF M, et al. Hyperfine Suppression of ${}^2\text{S}_1 – {}^3\text{P}_j$ Transitions in ${}^3\text{He}$ [J]. Physical Review Letters, 2008, 101: 173001.
- [153] LUO P L, PENG J L, HU J, et al. Precision frequency measurements of ${}^{3,4}\text{He}$ ${}^2\text{P} \rightarrow {}^3\text{D}$ transitions at 588 nm[J]. Physical Review A, 2016, 94: 062507.
- [154] LUO P L, PENG J L, SHY J T, et al. Precision Frequency Metrology of Helium ${}^2\text{S}_0 \rightarrow {}^2\text{P}_1$ Transition[J]. Physical Review Letters, 2013, 111: 013002.
- [155] LUO P L, GUAN Y C, PENG J L, et al. Measurement of the ${}^2\text{P}_1 \rightarrow {}^3\text{D}_2$ transition frequency in ${}^4\text{He}$ [J]. Physical Review A, 2013, 88: 054501.
- [156] LUO P L, HU J, FENG Y, et al. Doppler-free intermodulated fluorescence spectroscopy of ${}^4\text{He}$ ${}^2\text{P}–{}^3\text{D}$ transitions at 588 nm with a 1-W compact laser system[J]. Applied Physics B, 2015, 120(2): 279-284.

Bibliography

- [157] HUANG Y J, GUAN Y C, HUANG Y C, et al. Frequency measurement of the $2^1S_0 - 3^1D_2$ two-photon transition in atomic ^4He [J]. Physical Review A, 2018, 97: 032516.
- [158] HUANG Y J, GUAN Y C, PENG J L, et al. Precision laser spectroscopy of the $2^1S_0 - 3^1D_2$ two-photon transition in ^3He [J]. Physical Review A, 2020, 101: 062507.
- [159] PRESTAGE J D, HINDS E A, PICHANICK F M J. Precise Measurements of Hyperfine Structure in the 2^3P State of ^3He [J]. Physical Review Letters, 1983, 50: 828-832.
- [160] HESSELS E A, ARCUNI P W, DECK F J, et al. Microwave spectroscopy of high-L, n=10 Rydberg states of helium[J]. Physical Review A, 1992, 46: 2622-2641.
- [161] GEORGE M C, LOMBARDI L D, HESSELS E A. Precision Microwave Measurement of the $2^3P_1 - 2^3P_0$ Interval in Atomic Helium: A Determination of the Fine-Structure Constant [J]. Physical Review Letters, 2001, 87: 173002.
- [162] DELLER A, HOGAN S D. Microwave spectroscopy of the 1snp 3P_J fine structure of high Rydberg states in ^4He [J]. Physical Review A, 2018, 97: 012505.
- [163] KATO K, SKINNER T D G, HESSELS E A. Ultrahigh-Precision Measurement of the n=2 Triplet P Fine Structure of Atomic Helium Using Frequency-Offset Separated Oscillatory Fields[J]. Physical Review Letters, 2018, 121: 143002.
- [164] CLAUSEN G, JANSEN P, SCHEIDEGGER S, et al. Ionization Energy of the Metastable 2^1S_0 State of ^4He from Rydberg-Series Extrapolation[J]. Physical Review Letters, 2021, 127: 093001.
- [165] CLAUSEN G, SCHEIDEGGER S, AGNER J A, et al. Imaging-Assisted Single-Photon Doppler-Free Laser Spectroscopy and the Ionization Energy of Metastable Triplet Helium [J]. Physical Review Letters, 2023, 131: 103001.
- [166] ROBERT A, SIRJEAN O, BROWAEYS A, et al. A Bose-Einstein Condensate of Metastable Atoms[J]. Science, 2001, 292(5516): 461-464.
- [167] WANG L B, MUELLER P, BAILEY K, et al. Laser Spectroscopic Determination of the ^6He Nuclear Charge Radius[J]. Physical Review Letters, 2004, 93: 142501.
- [168] MUELLER P, SULAI I A, VILLARI A C C, et al. Nuclear Charge Radius of ^8He [J]. Physical Review Letters, 2007, 99: 252501.
- [169] HODGMAN S S, DALL R G, BYRON L J, et al. Metastable Helium: A New Determination of the Longest Atomic Excited-State Lifetime[J]. Physical Review Letters, 2009, 103: 053002.
- [170] VAN ROOIJ R, BORBELY J S, SIMONET J, et al. Frequency Metrology in Quantum Degenerate Helium: Direct Measurement of the $2^3S_1 \rightarrow 2^1S_0$ Transition[J]. Science, 2011, 333 (6039): 196-198.
- [171] RENGELINK R J, VAN DER WERF Y, NOTERMANS R P M J W, et al. Precision spec-

Bibliography

- troscopy of helium in a magic wavelength optical dipole trap[J]. *Nature Physics*, 2018, 14(11): 1132-1137.
- [172] VAN DER WERF Y, STEINEBACH K, JANNIN R, et al. The alpha and helion particle charge radius difference from spectroscopy of quantum-degenerate helium[A]. 2023. arXiv: 2306.02333.
- [173] NOTERMANS R P M J W, VASSEN W. High-Precision Spectroscopy of the Forbidden $2^3S_1 \rightarrow 2^1P_1$ Transition in Quantum Degenerate Metastable Helium[J]. *Physical Review Letters*, 2014, 112: 253002.
- [174] THOMAS K F, ROSS J A, HENSON B M, et al. Direct Measurement of the Forbidden $2^3S_1 \rightarrow 3^3S_1$ Atomic Transition in Helium[J]. *Physical Review Letters*, 2020, 125: 013002.
- [175] ROSS J A, THOMAS K F, HENSON B M, et al. Frequency measurements of transitions from the 2^3P_2 state to the 5^1D_2 , 5^3S_1 , and 5^3D states in ultracold helium[J]. *Physical Review A*, 2020, 102: 042804.
- [176] JUNCAR P, BERRY H G, DAMASCHINI R, et al. Energies of some triplet levels in ${}^4\text{He}$ I [J]. *Journal of Physics B: Atomic and Molecular Physics*, 1983, 16(3): 381.
- [177] ZHENG X, SUN Y R, CHEN J J, et al. Measurement of the Frequency of the 2^3S-2^3P Transition of ${}^4\text{He}$ [J]. *Physical Review Letters*, 2017, 119: 263002.
- [178] ZHENG X, SUN Y R, CHEN J J, et al. Light-force-induced shift in laser spectroscopy of atomic helium[J]. *Physical Review A*, 2019, 99: 032506.
- [179] BREIT G. The Effect of Retardation on the Interaction of Two Electrons[J]. *Physical Review*, 1929, 34: 553-573.
- [180] BREIT G. The Fine Structure of He as a Test of the Spin Interactions of Two Electrons[J]. *Physical Review*, 1930, 36: 383-397.
- [181] BREIT G. Dirac's Equation and the Spin-Spin Interactions of Two Electrons[J]. *Physical Review*, 1932, 39: 616-624.
- [182] BETHE H A, SALPETER E E. *Quantum Mechanics of One- and Two-Electron Systems*[M]. Springer Berlin Heidelberg, 1957: 88-436.
- [183] SCHIFF B, LIFSON H, PEKERIS C L, et al. $2^{1,3}P$, $3^{1,3}P$, and $4^{1,3}P$ States of He and the 2^1P State of Li^+ [J]. *Physical Review*, 1965, 140: A1104-A1121.
- [184] ACCAD Y, PEKERIS C L, SCHIFF B. S and P States of the Helium Isoelectronic Sequence up to $Z=10$ [J]. *Physical Review A*, 1971, 4: 516-536.
- [185] DRAKE G W F. New variational techniques for the 1snd states of helium[J]. *Physical Review Letters*, 1987, 59: 1549-1552.
- [186] DRAKE G W F. Variational eigenvalues for the Rydberg states of helium: Comparison with experiment and with asymptotic expansions[J]. *Physical Review Letters*, 1990, 65: 2769-

2772.

- [187] DRAKE G W F. Asymptotic expansion for δ -function matrix elements of helium[J]. Physical Review A, 1992, 45: 70-80.
- [188] YAN Z C, DRAKE G W F. High-precision calculations of the Zeeman effect in the 2^3P_J , 2^1P_1 , 2^3S_1 , and 3^3P_J states of helium[J]. Physical Review A, 1994, 50: R1980-R1983.
- [189] YAN Z C, DRAKE G W F. High Precision Calculation of Fine Structure Splittings in Helium and He-Like Ions[J]. Physical Review Letters, 1995, 74: 4791-4794.
- [190] ZHANG T, YAN Z C, DRAKE G W F. QED Corrections of $O(mc^2\alpha^7\ln\alpha)$ to the Fine Structure Splittings of Helium and He-like Ions[J]. Physical Review Letters, 1996, 77: 1715-1718.
- [191] FREUND D E, HUXTABLE B D, MORGAN J D. Variational calculations on the helium isoelectronic sequence[J]. Physical Review A, 1984, 29: 980-982.
- [192] PACHUCKI K. Quantum electrodynamics effects on singlet S-states of helium of order[J]. Journal of Physics B: Atomic, Molecular and Optical Physics, 1998, 31(16): 3547.
- [193] PACHUCKI K, SAPIRSTEIN J. Relativistic and QED corrections to the polarizability of helium[J]. Physical Review A, 2000, 63: 012504.
- [194] PACHUCKI K. Improved Result for Helium 2^3S_1 Ionization Energy[J]. Physical Review Letters, 2000, 84: 4561-4564.
- [195] PACHUCKI K. Improved Theory of Helium Fine Structure[J]. Physical Review Letters, 2006, 97: 013002.
- [196] PACHUCKI K. Helium energy levels including $m\alpha^6$ corrections[J]. Physical Review A, 2006, 74: 062510.
- [197] PACHUCKI K, YEROKHIN V A. Reexamination of the helium fine structure[J]. Physical Review A, 2009, 79: 062516.
- [198] PATKÓŠ V, YEROKHIN V A, PACHUCKI K. Higher-order recoil corrections for triplet states of the helium atom[J]. Physical Review A, 2016, 94: 052508.
- [199] PACHUCKI K, PATKÓŠ V, YEROKHIN V A. Testing fundamental interactions on the helium atom[J]. Physical Review A, 2017, 95: 062510.
- [200] PATKÓŠ V, YEROKHIN V A, PACHUCKI K. Higher-order recoil corrections for singlet states of the helium atom[J]. Physical Review A, 2017, 95: 012508.
- [201] YEROKHIN V A, PATKÓŠ V, PACHUCKI K. Relativistic corrections to the Bethe logarithm for the 2^3S and 2^3P states of He[J]. Physical Review A, 2018, 98: 032503.
- [202] WIENCZEK A, PACHUCKI K, PUCHALSKI M, et al. Quantum-electrodynamic corrections to the 1s3d states of the helium atom[J]. Physical Review A, 2019, 99: 052505.
- [203] PATKÓŠ V, YEROKHIN V A, PACHUCKI K. Nonradiative α^7m QED effects in the Lamb shift of helium triplet states[J]. Physical Review A, 2020, 101: 062516.

Bibliography

- [204] YEROKHIN V A, PATKÓŠ V, PUCHALSKI M, et al. QED calculation of ionization energies of 1snd states in helium[J]. Physical Review A, 2020, 102: 012807.
- [205] PATKÓŠ V, YEROKHIN V A, PACHUCKI K. Radiative α^7m QED contribution to the helium Lamb shift[J]. Physical Review A, 2021, 103: 012803.
- [206] GUAN H, CHEN S, QI X Q, et al. Probing atomic and nuclear properties with precision spectroscopy of fine and hyperfine structures in the ${}^7\text{Li}^+$ ion[J]. Physical Review A, 2020, 102: 030801.
- [207] QI X Q, ZHANG P P, YAN Z C, et al. Precision Calculation of Hyperfine Structure and the Zemach Radii of ${}^{6,7}\text{Li}^+$ Ions[J]. Physical Review Letters, 2020, 125: 183002.
- [208] ZHANG Y H, TANG L Y, ZHANG X Z, et al. Dynamic dipole polarizabilities for the low-lying triplet states of helium[J]. Physical Review A, 2015, 92: 012515.
- [209] ZHANG Y H, TANG L Y, ZHANG X Z, et al. Tune-out wavelength around 413 nm for the helium ${}^2\text{S}_1$ state including relativistic and finite-nuclear-mass corrections[J]. Physical Review A, 2016, 93: 052516.
- [210] YANG S J, MEI X S, SHI T Y, et al. Application of the Hylleraas-B-spline basis set: Static dipole polarizabilities of helium[J]. Physical Review A, 2017, 95: 062505.
- [211] YANG S J, TANG Y B, ZHAO Y H, et al. Application of the Hylleraas-B-spline basis set: Nonrelativistic Bethe logarithm of helium[J]. Physical Review A, 2019, 100: 042509.
- [212] ZHANG Y H, TANG L Y, ZHANG J Y, et al. Magic wavelengths for the helium ${}^2\text{S}_1 \rightarrow {}^2\text{P}_1$ forbidden transition[J]. Physical Review A, 2021, 103: 032810.
- [213] SICK I. Zemach moments of ${}^3\text{He}$ and ${}^4\text{He}$ [J]. Physical Review C, 2014, 90: 064002.
- [214] SICK I. Form Factors and Radii of Light Nuclei[J]. Journal of Physical and Chemical Reference Data, 2015, 44(3): 031213.
- [215] MORTON D C, WU Q, DRAKE G W. Energy levels for the stable isotopes of atomic helium(${}^4\text{He}$ I and ${}^3\text{He}$ I)[J]. Canadian Journal of Physics, 2006, 84(2): 83-105.
- [216] KRAUTH J J, SCHUHMANN K, AHMED M A, et al. Measuring the α -particle charge radius with muonic helium-4 ions[J]. Nature, 2021, 589(7843): 527-531.
- [217] SCHUHMANN K, FERNANDES L M P, NEZ F, et al. The helion charge radius from laser spectroscopy of muonic helium-3 ions[A]. 2023. arXiv: 2305.11679.
- [218] MARSMAN A, HORBATSCH M, HESSELS E A. Shifts due to distant neighboring resonances for laser measurements of ${}^2\text{S}_1$ to ${}^2\text{P}_J$ transitions of helium[J]. Physical Review A, 2012, 86: 040501.
- [219] MARSMAN A, HESSELS E A, HORBATSCH M. Shifts due to quantum-mechanical interference from distant neighboring resonances for saturated fluorescence spectroscopy of the ${}^2\text{S}$ to ${}^2\text{P}$ intervals of helium[J]. Physical Review A, 2014, 89: 043403.

- [220] MARSMAN A. Quantum interference effects in precision spectroscopy of helium fine structure[D]. York University Toronto, 2016.
- [221] DIXSON R G. Precision laser spectroscopic measurement of helium-4 ($1s2s\ ^3S$ to $1s2p\ ^3P$) lamb shift and fine structure[D]. Yale University, 1994: 251.
- [222] CANCIO P, GIUSFREDI G, DE MAURO C, et al. Precision spectroscopy of Helium[J]. AIP Conference Proceedings, 2005, 770(1): 79-90.
- [223] 郑昕. 氦原子 2^3S - 2^3P 跃迁精密光谱研究[D]. 中国科学技术大学, 2018.
- [224] HU S M, LU Z T, YAN Z C. Precision spectroscopy of the helium atom[J]. Frontiers of Physics in China, 2009, 4(2): 165-169.
- [225] YU S, GAO-PING F, CUN-FENG C, et al. Precision spectroscopy of helium using a laser-cooled atomic beam[J]. Acta Physica Sinica, 2012, 61(17): 170601.
- [226] FENG G P, ZHENG X, SUN Y R, et al. Laser-spectroscopy measurement of the fine-structure splitting $2^3P_1 - 2^3P_2$ of 4He [J]. Physical Review A, 2015, 91: 030502.
- [227] ZHENG X, SUN Y R, CHEN J J, et al. Laser Spectroscopy of the Fine-Structure Splitting in the 2^3P_J Levels of 4He [J]. Physical Review Letters, 2017, 118: 063001.
- [228] CHEN J J, SUN Y R, WEN J L, et al. Speed-adjustable atomic beam of metastable helium for precision measurement[J]. Physical Review A, 2020, 101(5): 053824.
- [229] 陈娇娇. 速度调控氦原子束精密谱研究[D]. 中国科学技术大学, 2021.
- [230] FREUND R S. High Current Low Voltage Electron Bombarde for Excitation of a Molecular Beam[J]. Review of Scientific Instruments, 1970, 41(8): 1213-1218.
- [231] RUNDEL R D, DUNNING F B, STEBBINGS R F. Velocity distributions in metastable atom beams produced by coaxial electron impact[J]. Review of Scientific Instruments, 1974, 45 (1): 116-119.
- [232] BRUTSCHY B, HABERLAND H. A high-intensity beam of metastable helium atoms with good velocity resolution[J]. Journal of Physics E: Scientific Instruments, 1977, 10(1): 90.
- [233] FAHEY D W, PARKS W F, SCHEARER L D. High flux beam source of thermal rare-gas metastable atoms[J]. Journal of Physics E: Scientific Instruments, 1980, 13(4): 381.
- [234] VERHEIJEN M J, BEIJERINCK H C W, VAN MOLL L H A M, et al. A discharge excited supersonic source of metastable rare gas atoms[J]. Journal of Physics E: Scientific Instruments, 1984, 17(10): 904.
- [235] ROTHE E W, NEYNABER R H, TRUJILLO S M. Velocity Dependence of the Total Cross Section for the Scattering of Metastable $He({}^3S_1)$ by Helium, Argon, and Krypton[J]. The Journal of Chemical Physics, 1965, 42(9): 3310-3314.
- [236] CHEN C Y, BAILEY K, LI Y M, et al. Beam of metastable krypton atoms extracted from a rf-driven discharge[J]. Review of Scientific Instruments, 2001, 72(1): 271-272.

Bibliography

- [237] CHENG C F, JIANG W, YANG G M, et al. An efficient magneto-optical trap of metastable krypton atoms[J]. Review of Scientific Instruments, 2010, 81(12): 123106.
- [238] HAROLD J. METCALF P S. Graduate texts in contemporary physics: Laser Cooling and Trapping[M]. Springer New York, 1999.
- [239] BREUER H. Small NMR Probe for Use in Inhomogeneous Fields[J]. Review of Scientific Instruments, 1995, 36(11): 1666-1667.
- [240] BOLINGER L, PRAMMER M G, LEIGH J S. A multiple-frequency coil with a highly uniform B_1 field[J]. Journal of Magnetic Resonance (1969), 1989, 81(1): 162-166.
- [241] 冯高平. 氦原子 $2^3P_1 - 2^3P_2$ 精细结构的精密光谱[D]. 中国科学技术大学, 2014.
- [242] FENG G P, YU S, XIN Z, et al. Design and measurement of a magnetic field for precision spectroscopy of helium[J]. Acta Physica Sinica, 2014, 63(12): 123201.
- [243] 张颜艳. 掺铒光纤飞秒光梳及其在光频测量中的应用[D]. 中国科学院大学 (中国科学院国家授时中心), 2019.
- [244] BERKELAND D J, HINDS E A, BOSIER M G. Precise Optical Measurement of Lamb Shifts in Atomic Hydrogen[J]. Physical Review Letters, 1995, 75: 2470-2473.
- [245] BROWN R C, WU S, PORTO J V, et al. Quantum interference and light polarization effects in unresolvable atomic lines: Application to a precise measurement of the $^{6,7}\text{Li}$ D_2 lines[J]. Physical Review A, 2013, 87: 032504.
- [246] HANNEMANN S, SALUMBIDES E J, UBACHS W. Reducing the first-order Doppler shift in a Sagnac interferometer[J]. Optics Letters, 2007, 32(11): 1381-1383.
- [247] ALTMANN R K, GALTIER S, DREISSEN L S, et al. High-Precision Ramsey-Comb Spectroscopy at Deep Ultraviolet Wavelengths[J]. Physical Review Letters, 2016, 117: 173201.
- [248] MINARDI F, ARTONI M, CANCIO P, et al. Frequency shift in saturation spectroscopy induced by mechanical effects of light[J]. Physical Review A, 1999, 60: 4164-4167.
- [249] SMICIKLAS M, SHINER D. Determination of the Fine Structure Constant Using Helium Fine Structure[J]. Physical Review Letters, 2010, 105: 123001.
- [250] WIRTHL V, MAISENBACHER L, WEITENBERG J, et al. Improved active fiber-based retroreflector with intensity stabilization and a polarization monitor for the near UV[J]. Optics Express, 2021, 29(5): 7024-7048.
- [251] WEN J L, TANG J D, DONG J F, et al. Doppler-free spectroscopy of an atomic beam probed in traveling-wave fields[J]. Physical Review A, 2023, 107: 042811.
- [252] WEN J L, TANG J D, LV Y N, et al. Postselection shifts the transition frequency of helium in an atomic beam[J]. Science Advances, 2025, 11(9): eadu9796.
- [253] NEUMANN J V. Mathematische Grundlagen der Quantenmechanik: Vol. 38[M]. Springer-Verlag, 2013.

Bibliography

- [254] AHARONOV Y, ALBERT D Z, VAIDMAN L. How the result of a measurement of a component of the spin of a spin-1/2 particle can turn out to be 100[J]. Physical Review Letters, 1988, 60: 1351-1354.
- [255] HOSTEN O, KWIAT P. Observation of the Spin Hall Effect of Light via Weak Measurements [J]. Science, 2008, 319(5864): 787-790.
- [256] REZAEIAN N H. A precise few-nucleon size difference by isotope shift measurements of helium[D]. University of North Texas, 2015.
- [257] VAN WIJNGAARDEN A, HOLUJ F, DRAKE G W F. Lamb shift in He^+ : Resolution of a discrepancy between theory and experiment[J]. Physical Review A, 2000, 63: 012505.
- [258] LEWIS M L, HUGHES V W. Higher-Order Relativistic Contributions to the Zeeman Effect in Helium[J]. Physical Review A, 1973, 8: 2845-2856.
- [259] PUCHALSKI M, JENTSCHURA U D. Quantum electrodynamic corrections to the g factor of helium P states[J]. Physical Review A, 2012, 86: 022508.
- [260] EDMONDS A R. Angular Momentum in Quantum Mechanics[M]. Princeton University Press, 1957.
- [261] WU Q, DRAKE G W F. Hyperfine structure of the 2^3P state of ${}^3\text{He}$ with and without an external magnetic field[J]. Journal of Physics B: Atomic, Molecular and Optical Physics, 2007, 40(2): 393.
- [262] WU Q. Precision calculation of electronic g_J factors for $n^3\text{S}_1$ states of ${}^4\text{He}$ and ${}^7\text{Li}^+$ ion[J]. Journal of Physics B: Atomic, Molecular and Optical Physics, 2006, 39(20): 4213.
- [263] ZELEVINSKY T. Helium 2^3P fine structure measurement in a discharge cell[D]. Harvard University, 2004.
- [264] MARSMAN A, HORBATSCHEK M, HESSELS E A. The Effect of Quantum-Mechanical Interference on Precise Measurements of the $n = 2$ Triplet P Fine Structure of Helium[J]. Journal of Physical and Chemical Reference Data, 2015, 44(3): 031207.
- [265] VRINCEANU D, KOTOCHIGOVA S, SADEGHPOUR H R. Pressure broadening and shift of $\text{He}(2^3\text{P}_{0,1,2})-\text{He}(2^3\text{S})$ lines[J]. Physical Review A, 2004, 69: 022714.
- [266] HEYDARIZADMOTLAGH F, SKINNER T D G, KATO K, et al. Precision Measurement of the $n=2$ Triplet P $J=1$ to $J=0$ Fine Structure of Atomic Helium Using Frequency-Offset Separated Oscillatory Fields[J]. Physical Review Letters, 2024, 132: 163001.
- [267] PACHUCKI K, YEROKHIN V A, CANCIO PASTOR P. Quantum electrodynamic calculation of the hyperfine structure of ${}^3\text{He}$ [J]. Physical Review A, 2012, 85: 042517.
- [268] PATKÓŠ V, YEROKHIN V A, PACHUCKI K. Higher-Order QED Corrections to the Hyperfine Splitting in ${}^3\text{He}$ [J]. Physical Review Letters, 2023, 131: 183001.
- [269] MULI S S L, RICHARDSON T R, BACCA S. Revisiting the helium isotope-shift puzzle

Bibliography

- with improved uncertainties from nuclear structure corrections[A]. 2024. arXiv: 2401.13424.
- [270] QI X Q, ZHANG P P, YAN Z C, et al. Revised ${}^3\text{He}$ nuclear charge radius due to electronic hyperfine mixing[A]. 2024. arXiv: 2409.09279.
- [271] PACHUCKI K, PATKÓŠ V, YEROKHIN V A. Second-order hyperfine correction to H, D, and ${}^3\text{He}$ energy levels[J]. Physical Review A, 2024, 110: 062806.
- [272] DU X J, WEI L, SUN Y, et al. Free electron laser prepared high-intensity metastable helium and helium-like ions[J]. Acta Physica Sinica, 2024, 73(15): 150201.
- [273] RAMSEY N F. A New Molecular Beam Resonance Method[J]. Physical Review, 1949, 76: 996-996.
- [274] BAKLANOV Y V, DUBETSKY B Y, CHEBOTAYEV V P. Non-linear ramsey resonance in the optical region[J]. Applied Physics, 1976, 9(2): 171-173.
- [275] SALOUR M M, COHEN-TANNOUDJI C. Observation of Ramsey's Interference Fringes in the Profile of Doppler-Free Two-Photon Resonances[J]. Physical Review Letters, 1977, 38: 757-760.
- [276] BERGQUIST J C, LEE S A, HALL J L. Saturated Absorption with Spatially Separated Laser Fields: Observation of Optical "Ramsey" Fringes[J]. Physical Review Letters, 1977, 38: 159-162.
- [277] TEETS R, ECKSTEIN J, HÄNSCH T W. Coherent Two-Photon Excitation by Multiple Light Pulses[J]. Physical Review Letters, 1977, 38: 760-764.
- [278] BORDÉ C J, SALOMON C, AVRILLIER S, et al. Optical Ramsey fringes with traveling waves[J]. Physical Review A, 1984, 30: 1836-1848.
- [279] BORBELY J S, GEORGE M C, LOMBARDI L D, et al. Separated oscillatory-field microwave measurement of the $2^3\text{P}_1 - 2^3\text{P}_2$ fine-structure interval of atomic helium[J]. Physical Review A, 2009, 79: 060503.
- [280] VUTHA A C, HESSELS E A. Frequency-offset separated oscillatory fields[J]. Physical Review A, 2015, 92: 052504.
- [281] FABJAN C W, PIPKIN F M. Resonance-Narrowed-Lamb-Shift Measurement in Hydrogen, $n=3$ [J]. Physical Review A, 1972, 6: 556-570.